Magnetic Properties of Co and Ni doped SnO_2 Based Diluted Magnetic Semiconductors

A Thesis Submitted

By

Sunita Mohanty

In Partial Fulfillment of the Requirements for the Award of the Degree of

Doctor of Philosophy in Physics

Department of Physics
Indian Institute of Technology Guwahati,
INDIA

September 2012

Statement

The work contained in the thesis entitled "**Magnetic Properties of Co and Ni doped SnO_2 Based Diluted Magnetic Semiconductors**" has been carried out by me under the supervision of Prof. S. Ravi, Department of Physics, Indian Institute of Technology Guwahati. This work has not been submitted elsewhere for the award of any degree.

September 2012

(Sunita Mohanty)
Department of Physics
Indian Institute of Technology Guwahati
Guwahati - 781039

Certificate

It is certified that the work contained in the thesis entitled "**Magnetic Properties of Co and Ni doped SnO_2 Based Diluted Magnetic Semiconductors**" by Ms. Sunita Mohanty, a Ph.D. student of the Department of Physics, Indian Institute of Technology Guwahati, for the award of the degree of *Doctor of Philosophy* has been carried out under my supervision. This work has not been submitted elsewhere for the award of any degree.

September, 2012

(S. Ravi)
Professor
Department of Physics
Indian Institute of Technology Guwahati
Guwahati – 781 039

Dedicated to my Parents

Acknowledgements

The work presented in this thesis is by far the most significant scientific accomplishment in my life and it would have been impossible without the people who supported me and believed in me.

First of all I would like to like to express my gratitude to my research advisor Prof. S. Ravi for being extremely patient, and for supporting me with his valuable ideas and constructive criticism throughout my work. Without his encouragement, I would not have pursued a scientific career at this level. I consider him not only to be a good scientist, but equally importantly, a kind and down-to-earth person. His excitement about science and his trust in my abilities inspired me to set very high standards for myself. His drive for perfectionism has played a major role in my growth, both in research and personal realms. I am extremely grateful to him for the long painstaking hours that he squeezed out from his busy schedule to go through the manuscript of this thesis, and according my work his topmost priority.

I would also like to sincerely thank my doctoral committee members, Prof. A. Srinivasan, Prof. D. Pal and Prof. B. Mondal, for evaluating my annual progress reports and seminars during the course of my Ph.D. Their valuable suggestions and words of encouragement were truly inspirational for me.

I am grateful to the Prof. S. Basu Head, Physics Department, and Prof. S. Ravi, Prof. A. Khare, former Heads of the Department, for allowing me to use departmental facilities.

I would like to express my sincere thanks to Prof. M. Kar, Prof. D. Pamu, Prof. V. Manivanan, Mr. Himnashu for their help in preparing the thinfilm and nonopowder samples.

Thanks are also to all the staffs and scientific officer of Physics department and Central Instrument Facility (CIF).

Sincere thanks are also extended to my senior Mr. B. Samantaray, Mr. D. Mishra and other research scholars Ms. Trivedi, Mr. Bipul, Mr. Ranjan, Mr. P. Rajendra, Mr. Santosh, Mr. Akhilesh, Ms. Shyni, Mr. Bapaditya, Mr. Battakrishan, Mr. Bhagaban for their kind support and cooperation.

I take this opportunity to thank all my friends at IIT Guwahati, especially Ms. Arpita and Ms. Prangya who are very much affectionate and caring towards me and treat me as their younger sister. Also I am very much happy to have Ms. Rosalin, Ms. Archana, Ms. Anu, Ms. Pravati, Ms. Namita for creating a friendly and homely atmosphere and for always encouraging me when I am in difficulty.

I am forever indebted to my parents and brother, whose love, blessing and kind support made me what I am today. Therefore, no words are adequate to show my gratitude towards them. My heartiest thanks to my husband who not only supported me at every step of my carrier, but also has been a constant source of inspiration for me.

Last but not the least I am grateful to Indian Institute of Technology Guwahati and Ministry of Human Resource and Development for giving the financial support to carry out the present thesis work.

Sunita Mohanty

IITGuwahati, Guwahati
Assam, India

Abstract

Diluted magnetic semiconductors have evolved as a fascinating area of research for potential spintronics applications at practical temperature. The generic problem of resistance mismatch at metal-semiconductor interfaces hinders the effective spin injection therefore; much attention is being focused on the development of room temperature ferromagnetic semiconductors. If successful, we could have new generation devices having miniaturation, high energy efficiency, non-volatile memory, large Zeeman splitting and high speed devices e.g. the Spin-field effect transistors (SFET), Spin light emitting diode (SLED) etc. In order to bring these materials into practical application, we need a ferromagnetic semiconductor showing ferromagnetism above room temperature. In order to achieve this challenge, i.e. making a non-magnetic semiconductor into ferromagnetic semiconductor, several theoretical and experimental works are being carried out in this field. Several theoretical and experimental works have been done on Chalcogenides based magnetic semiconductors and transition element doped Group II-VI, Group III-V and Group IV-VI semiconductors. However in the above class of materials, the ferromagnetic transition temperature is quite below room temperature. Another interesting group of DMS materials are the transition element doped wide band gap oxide semiconductors.

The transition element doped oxide semiconductors such as TiO_2, ZnO and SnO_2 have potential applications in spintronics devices with room temperature ferromagnetism. They are generally called the oxide based diluted magnetic semiconductors (ODMS). However a few reports on thin film and bulk samples display other type of behaviors such as simple paramagnetism, antiferromagnetism (AFM), spinglass, etc. Giant magnetic moment as high as $7\mu_B$/TM-ion with high ferromagnetic transition temperature more than 600 K has been obtained in these ODMS.

The material preparation technique needs to be optimized for consistent results and the mechanism of magnetic interaction needs to be understood. Even though, several theoretical models have been proposed such as, bound magnetic polaron, polaron percolation, spin-split impurity band model, etc; the detailed investigations of experimental data in terms of available models are yet to be carried out.

At the beginning of the thesis work and as per literature survey, it was observed that, there were several reports on the TM doped ZnO and TiO_2 based DMS with room temperature

ferromagnetic. SnO_2 is one of the well known wide band gap semiconductors having wide range of applications in optoelectronic devices, solar cells, gas sensors, etc. Doping of trace amount of TM can gives rise to robust FM semiconductor for potential applications in optoelectronic and spintronic devices. Ogale *et al*. [*Phys. Rev. Lett. 2003. 91(7). p.077205*] have reported a giant magnetic moment of the order of 7.5 ± 0.5 μ_B/Co-ion and large Curie temperature as high as 650 K in Co-doped SnO_2 thin film. In view of the reported interesting giant magnetic moment in SnO_2 based thin film and due to the lack of detailed reports on bulk samples, I have taken up the preparation of Co and Ni doped bulk SnO_2 under different experimental conditions and the detailed study of magnetic properties.

Following samples were prepared for the present thesis work,

1) $Sn_{1-x}Co_xO_2$ (x = 0.0, 0.02, 0.05, 0.07, 0.10) samples by using solid state route and ball milling technique.
2) Pure and 2 at % Co-doped SnO_2 samples prepared by co-precipitation method.
3) $Sn_{1-x}Ni_xO_2$ (x = 0.0, 0.02, 0.05, 0.07, 0.10) samples by using solid state route and ball milling technique.

The above prepared samples were characterized by recording and analyzing room temperature powder X-ray diffraction patterns (XRD). The recording of microstructural images and compositional analysis were carried out by using LEO SEM machine equipped with energy dispersive X-ray spectroscopic (EDX) facilities. The microstructure and the composition at crystallites level were studied by recording TEM images using transmission electron microscope (TEM) coupled with an EDS analyzer. The samples were also characterized by recording Raman and FTIR spectra. The field variation of magnetization (M-H loop) was measured at different temperatures by using a Lakeshore make vibrating sample magnetometer (VSM). Temperature variation of magnetization was also measured to determine the Curie temperature. Electron spin resonance (ESR) spectra were recorded to study the presence of magnetic phase separation and magnetic clusters if any.

The Co-doped and Ni-doped SnO_2 samples were successfully prepared with room temperature FM. The role of particle size and oxygen vacancy on magnetic properties is discussed. Probably for the first time, we have carried out critical behavior studies in oxide based DMS, i.e. on Co-doped SnO_2. The critical exponents are found to be comparable to the mean field model.

The present thesis is divided into 5 chapters, namely, (1) Introduction, (2) Experimental Techniques, (3) Co-doped SnO_2, (4) Ni-doped SnO_2 and (5) Conclusions.

Introduction to DMS materials along with a brief review of basic concepts of various types of magnetic ordering, magnetic interaction and related phenomena are given in chapter 1. An overview of various theoretical models proposed in explaining the magnetic properties of DMS materials are also presented. Detailed experimental results on the magnetic properties of various oxide based DMS materials with special emphasis on SnO_2 based materials are presented.

Chapter 2 is devoted to experimental techniques. Here the detailed experimental techniques followed in material preparation and physical measurements are given. In addition to that brief details of working principle of various sophisticated instruments such as X-Ray diffractometer, scanning electron microscope, transmission electron microscope, Raman and FTIR spectrometer and vibrating sample magnetometer, are presented.

In Chapter-3, magnetic properties of Co-doped SnO_2 samples prepared by solid state route, co-precipitation method and mechanical alloying are discussed in detail.

$Sn_{1-x}Co_xO_2$ samples were prepared in single phase form up to x =0.10 by solid state route. The magnetic properties were studied from magnetization and electron spin resonance measurements. Large increase in magnetization by an order of magnitude has been observed on sample prepared by N_2 gas environment compared to air annealed sample. The M-H curves of air annealed samples recorded at three different temperatures could be analyzed based on bound magnetic polaron model**.** Temperature variations magnetization show clear paramagnetic to ferromagnetic transitions for all the Co doped samples. The susceptibility in the paramagnetic region could be fitted to Curie-Weiss law and the maximum Curie temperature was found to be 692K for x=0.02.

Nanocrystalline samples of pure and 2 at % Co-doped SnO_2 were prepared by a co-precipitation technique with average crystallite size of the order 10 nm. The homogeneity and single phase nature of the samples were confirmed by using various characterization techniques, such as X-ray diffraction, transmission electron microscope and Fourier infrared spectroscopy. Magnetization measurement shows a signature of room temperature FM. The observed reduction in magnetization value with decrease in crystallite size has been explained in terms of reduction in the range of bound magnetic polaron interaction. The samples prepared under nitrogen gas

environment exhibit an improvement in ferromagnetic behavior and enhanced electrical conductivity.

Pure SnO_2 based wide band gap semiconductors were prepared by mechanical alloying method by using steel and tungsten carbide (WC) vials. They were further annealed at 900^oC. The as milled powders obtained from both the vials were found to exhibit room temperature FM, i.e. without any transition element doping. However upon annealing, the FM was destroyed in one of the samples. The observed FM was explained in terms of oxygen vacancy induced defects. The FM T_c determined from the temperature variation of magnetization measurement is found to be 915 K. The initial magnetization data could be analyzed in terms of bound magnetic polaron model. A shift in the resonance field of electron spin resonance spectrum towards the lower field was observed on samples having strong FM interaction with larger T_c and is explained in comparison with magnetization measurement.

The Co-doped SnO_2 samples were also prepared by mechanical alloying followed by annealing at 900^oC. Room temperature FM was observed with a maximum saturation magnetization of 2.9emu/g for $Sn_{0.98}Co_{0.02}O_2$ sample and its value at 20 K was found to be 5.9emu/g (7.9μ_B/Co-ion). So, a giant magnetic moment of the order of 7.9μ_B/Co-ion was observed in bulk Co doped sample and this value is comparable to the giant magnetic moment (7.5μ_B/Co-ion) reported by Ogale *et al*. [*Phys. Rev. Lett. 2003. 91(7). p.077205*] in thin film sample of Co doped SnO_2. The magnetization data could be analyzed based on bound magnetic polaron model. Temperature variation of magnetization exhibits a clear paramagnetic to FM transition with a maximum T_c of 640 K for 2 at % Co-doped sample. Susceptibility in paramagnetic region could be fitted to modified Curie-Weiss law.

One of the Co-doped SnO_2 samples having relatively strong room temperature FM was taken up for detailed isothermal magnetization measurements in the vicinity of FM T_c. The critical behavior was studied by analyzing the magnetization data in terms of modified Arrott plot method and, independently by Kouvel-Fisher method. The sample is found to exhibit a second order phase transition. The critical exponents β, γ and δ corresponding to spontaneous magnetization, initial susceptibility and isothermal magnetization, respectively, were determined and the values are found to be comparable to the predicted values by the Mean field model. The critical exponent values are found to be consistent with the Widom scaling relation and the

universal scaling hypothesis. The temperature variation of effective critical exponent was determined and was found to show the characteristic behavior of disordered system.

In Chapter 4, the study magnetic properties of Ni-doped SnO_2 samples prepared by solid state route and ball milling method are presented.

The Ni-doped SnO_2 based diluted magnetic semiconductors were prepared in single phase form up to 10 at % of doping by solid state preparation technique. They exhibit room temperature FM with FM T_c as high as ~ 770 K. The initial M-H loops measured for the samples could be explained based on bound magnetic polaron model and the interaction between BMP and magnetic moments of matrix. Typical polaron size estimated at 80 K was found to be 60Å. The magnitude of electrical resistivity is found to decrease with increase in doping concentration and its temperature dependence could be explained based on variable range hopping mechanism.

Ni-doped SnO_2 samples up to the doping concentration of 10 at % were prepared by ball milling followed by annealing at 900^{o}C. All the prepared samples are found to be in single phase form. The Raman spectra showed the presence of disorder and oxygen vacancy related peaks for 7 at % Ni-doped sample. Room temperature FM was obtained in all the prepared samples. The maximum saturation magnetization, M_s value was found to be 1.3emu/g for 7 at % Ni-doped SnO_2. The M_s value was found to increase with increase in doping concentration up to a limit of 7 at % and beyond that it decreases. The observed FM was explained in terms of bound magnetic polaron model. The temperature variation of susceptibility in the paramagnetic region was fitted to modified Curie-Weiss law and the typical effective magnetic moment was found to be 3.7μ_B/Ni. It shows that doped Ni ions are mostly in high spin Ni^{2+} state.

To summarize, Co and Ni doped SnO_2 based DMS with room temperature FM were prepared successfully. The values of FM T_c were found to be quite large and much above the room temperature. The M_s value was found to depend upon the sample preparation techniques. The interaction mechanism prevailing in these compounds were explained in terms of the Bound magnetic polaron model. In addition to the transition element doping, the oxygen vacancy was found to play an important role in the observed FM behavior. The critical behavior was studied from the detailed magnetization measurement in the vicinity of transition temperature and the estimated critical exponents values were found to be comparable to the Mean Field model prediction. The summary of conclusions is presented in chapter 5.

List of Abbreviations

AFM	Antiferromagnetism (ic)
BMP	Bound magnetic Polaron
BSE	Back scattered electrons
DMS	Diluted magnetic semiconductors
DE	Double exchange
DM	Dzyaloshinsky-Moriya
EDS,EDX	Energy Dispersive Spectra(X-ray)
$\mathbf{E_{hop}}$	Hopping Energy
FTIR	Fourier Transmission Infrared
FM	Ferromagnetism (ic)
FWHM	Full width at half maximum
GPIB	General Purpose Instrumentation Bus
HF	High Field
$\mathbf{H_c}$	Coercive Field, Coercivity
IR	Infra Red
JT	Jahn-Teller
LF	Low Field
MAP	Modified Arrot Plot
$\mathbf{M_s}$	Saturation Magnetization
$\mathbf{M_o}$	Spontaneous magnetization
m_{eff}	effective spontaneous moment per bound magnetic polaron
$\mathbf{N\ (E_F)}$	Density of states in the vicinity of Fermi level
ODMS	Oxide based diluted Magnetic semiconductors
PM	Paramagnet (ic)
PID	Proportional–Integral–Derivative
RKKY	(Ruderman-Kittel-Kausya-Yosida)
$\mathbf{R_p}$	Profile Factor
$\mathbf{R_{hop}}$	Hopping Distance
RT	Room Temperature

SEM	Scanning Electron Micrograph
SFET	Spin Field effect Transistor
SLED	Spin Light Emitting Diode
SG	Spin Glass
T	Temperature
TEM	Transmission Electron Microscope
TM	Transition metal
T_c	Transition Temperature
WC	Tungsten Carbide
HRTEM	High Resolution transmission electron Microscope
SAD	Selected area diffraction
VRH	Variable Range Hopping
VSM	Vibrating Sample Magnetometer
XRD	X-ray Diffractometer
χ^2	Reduced chi-square
χ_m	Paramagnetic matrix
χ	Paramagnetic Susceptibility
θ_c	Curie Temperature
ρ	Resistivity

Table of Contents

Content **Page No.**

Statement ..... **i**
Certificate ..... **ii**
Dedication ..... **iii**
Acknowledgements ..... **iv**
Abstract ..... **vi**
List of Abbreviations ..... **xi**
List of Figures ..... **xvii**
List of Tables ..... **xxiv**

Chapter-1 Introduction..... 1

1.1 Diluted Magnetic Semiconductors in Spintronics…….....3
1.1.1 Enhanced Zeeman Splitting…….……3
1.1.2 Spin Field Effect Transistor(Spin FET).....…….....4
1.1.3 Photo Induced Ferromagnet.....……5
1.1.4 Spin-LED…….……6
1.2 Structural Properties……...7
1.2.1 Crystal Structure……7
1.2.2 Crystal Field Effect in TM-ion……..9
1.2.3 Jahn-Teller Distortion.....……..13
1.3 Magnetic Ordering……...16
1.3.1 Diamagnetism……16
1.3.2 Paramagnetism……....17
1.3.3 Ferromagnetism…….....18
1.3.4 Antiferromagnetism……20
1.3.5 Ferrimagnetism……...22
1.3.6 Spin Glass Behavior……23

1.4 Magnetic Interactions……...24
1.4.1. Magnetic Dipole-Dipole Interaction……24
1.4.2. Direct Exchange Interaction……24
1.4.3. Superexchange Interaction……...25
1.4.4 RKKY Interaction……27
1.4.5 Anisotropic Exchange Interaction……28
1.4.6 Double Exchange Interaction……29
1.5 Theoretical Models in DMS……33
1.5.1 Zener Model……...33
1.5.2 Bound Magnetic Polarons……..34
1.5.3 Spin Split impurity band model……38
1.6 Critical Exponents in Magnetic Transition……..40
1.7 Electrical Resistivity of Semiconductors……45
1.8 Experimental Work on Oxide based DMS……..48
1.9 Motivation of the present thesis work……..53

Chapter 2: Experimental Techniques……55

2.1 Sample Preparation……..55
2.1.1 Solid state reaction……56
2.1.2 Mechanical Alloying Technique……56
2.1.3 Co-precipitation Technique……...57
2.2. High Temperature Furnaces……58
2.3 X-ray Diffraction……59
2.4. Scanning Electron Microscope (SEM)……...62
2.5. Transmission Electron Microscope (TEM)……66
2.6 FTIR and Raman Spectroscopy……...69
2.6.1 FTIR Spectrometer……..70
2.6.2 Raman Spectrometer……...71
2.7 Vibrating Sample Magnetometer ……72

2.8 Electron Spin Resonance……74
2.9 Electrical Resistivity Measurements……77

Chapter 3: Co doped SnO_2 based DMS……80

3.1 $Sn_{1-x}Co_xO_2$ by solid state synthesis……82
3.1.1 Preparation and Characterization……82
3.1.2 Magnetic Properties……90
3.1.3 ESR Analysis……100

3.2 $Sn_{0.98}Co_{0.02}O_2$ by Co-precipitation……102
3.2.1 Preparation and Characterization……102
3.2.2 Magnetic Properties……108
3.2.3 Electrical Resistivity Measurement……109

3.3 Ball Milled Pure SnO_2 ……111
3.3.1 Sample Preparation and Characterization……111
3.3.2 Magnetic Properties……118
3.3.3 ESR Measurement……123

3.4 Co doped SnO_2 by Ball Milling……125
3.4.1 Preparation and Characterization……125
3.4.2 Magnetic Properties……132

3.5 Critical Behavior Studies……139
3.6 Summary……153

Chapter 4: Ni-doped SnO_2 Series ……155

4.1 Ni-doped SnO_2 by solid state route……156
4.1.1 Preparation and Characterization……156
4.1.2 Magnetic Properties……163
4.1.3 Resistivity Analysis……170
4.1.4 ESR Measurement……173

4.2 Ni-doped SnO_2 by ball milling……..176
4.2.1 Preparation and Characterization……..176
4.2.2 Magnetic Properties……..182
4.2.3 ESR Spectra……..190
4.3 Summary……191

Chapter-5: CONCLUSIONS……...192

References……..198
Publications…….....213

List of Figures

Page No.

Chapter-1

Fig. 1.1 Schematic representation of non-magnetic semiconductor (left), and a diluted magnetic semiconductor (right)……1

Fig. 1.2 Spin FET based on ZnO, (from ref. [1])……..4

Fig.1.3 A schematic representation of photo induced ferromagnet (ref.[1])…….5

Fig. 1.4 Schematic block diagram of Spin-FET from (ref.[2])…….6

Fig.1.5 Crystal structure of SnO_2. Here the bigger and smaller size atom represents Sn and respectively…….8

Fig. 1.6 The electronic distribution of 3-*d* orbitals. In the cubic crystal field, this fivefold degeneracy is lifted to two e_g orbitals (x^2-y^2 and $3z^2 - r^2$) and three t_{2g} orbitals (xy, yz and zx). (Reproduced from Tokura *et al.* [3])……10

Fig.1.7. Splitting of d-orbital in presence of different anion position configuration……11

Fig.1.8 TM-ion in **(a)** octahedral and **(b)** tetrahedral environment……...11

Fig.1.9 Electronic configuration of (a) high-spin (weak field) and (b) low-spin (strong-field) cases for $3d^7$ shell of TM ion……...12

Fig. 1.10: (a) Typical overlapping of one of the e_g orbitals ($d_{x^2-y^2}$) with p orbital of neighboring O in a two dimensional diagram. **(b)** One of the t_{2g} orbitals with p orbital. **(c)** The crystal field splitting of d shell in octahedral environment. The Jahn-Teller distortion leads to a further splitting of both t_{2g} and e_g states……..15

Fig. 1.11 Different types of antiferromagnetic arrangement in a unit cell……21

Fig.1.12 Schematic diagram showing the arrangement of spins and orbitals in **(a)** antiferromagnetic super-exchange interaction **(b)** ferromagnetic super-exchange interaction……..26

Fig. 1.13. The oscillatory part of RKKY interaction energy. x is proportional to the product of the Fermi wave vector and the distance from the localized moment……..27

Fig. 1.14 (a) Sketch of the double exchange mechanism which involves two Mn ions and one O

ion. (b) The mobility of e_g electrons is depicted for parallel alignment of localized spins. The transfer integral is shown in the Fig. (c)…….30

Fig. 1.15 A schematic electronic structure of TM at the tetrahedral substitutional site. The anti-bonding t_a states and non-bonding e_g-states appear in the band gap ref.[4]……32

Fig. 1.16 Schematic 3d orbital electronic configuration of TM-ions in presence of a tetrahedral environment. The + and – sign indicate the spin up and spin down states respectively (reproduced from ref. [4])……...32

Fig.1.17 Computed T_c values for 5 at % Mn doped semiconductors (ref.[5])……...34

Fig.1.18 The bound magnetic polaron model. The red circle shows a single polaron of radius a_B. (following ref. [6-9])……...36

Fig.1.19 Schematic of polaron pair model as per ref.[10]……...36

Fig.1.20 Schematic diagram of electronic structure of TM doped oxide semiconductor for (a) M = Ti, (b) M = Mn, and (c) M = Co. (reproduced from ref.[11])……..40

Fig.1.21 Scaling law for nickel sample using the data of Weiss and Forrer. The left side and right side curves correspond to $T < T_C$ and $T > T_C$ respectively. 't' denotes the reduced temperature $\varepsilon = (T - T_C)/T_C$ and M_1 is a constant. (Reproduced from Green *et al.* [12]……..42

Chapter-2

Fig. 2.1 (a) Photographic view of planetary ball mill and (b) schematic view of mechanical milling process……57

Fig. 2.2: Block diagram of the furnace with maximum operating temperature of 1200°C……..…59

Fig. 2.3 Ray diagram of X- ray diffractometer……..60

Fig. 2.4 Schematic view of scanning electron microscope……63

Fig. 2.5: (a) Electron and photon signals emanating from tear-shaped interaction volume during electron beam impingement on specimen surface, and (b) Energy spectrum of electrons emitted from the specimen surface……64

Fig.2.6 (a): Schematic diagram of transmission electron microscope **(b)** Schematic ray diagram for image mode (c) Schematic ray diagram for diffraction mode……...66

Fig.2.7 SAD pattern of single crystal Austenite……68

Fig. 2.8 Schematic block diagram for FTIR……..70

Fig. 2.9: Schematic diagram for Raman spectrometer……..72

Fig. 2.10 Block diagram of the vibrating sample magnetometer……..73

Fig. 2.11 Block diagram for ESR spectrometer……76

Fig. 2.12: Block diagram of APD Cryostat……...78

Fig. 2.13 Top view of sample holder for resistivity measurement……78

Fig.2.14 Block diagram of electrical resistivity measurement set-up……...79

Chapter 3

Fig.3.1 XRD patterns recorded at room temperature for $Sn_{1-x}Co_xO_2$ (x = 0.0, 0.02, 0.05, 0.07 and 0.10)……84

Fig.3.2(a) XRD patterns along with Rietveld refinement for x = 0.02 and 0.05……..85

Fig.3.2(b) XRD patterns along with Rietveld refinement for x = 0.07 and 0.10 samples. The circles represent experimental points and solid line represents Rietveld refined data. The dotted lines at the bottom show the difference between experimental and refined data……..86

Fig.3.3 Expanded view of (110) peak of XRD pattern……87

Fig.3.4 SEM images recorded for x= 0.02, 0.05 and 0.10 samples along with EDX spectra for x=0.10 Co-doped sample……..88

Fig.3.5 TEM, SAD and HRTEM image recorded for $Sn_{0.98}Co_{0.02}O_2$ sample annealed in air at 900^0C……89

Fig.3.6 Room temperature Raman spectra of $Sn_{1-x}Co_xO_2$ for x= 0.0, 0.02, 0.10 sample……..90

Fig.3.7 M-H loops recorded for $Sn_{1-x}Co_xO_2$ samples at (a) 85 K and (b) 400 K for x=0.02, 0.05, 0.07, 0.10……92

Fig.3.8 Magnetic hysteresis loop of nitrogen annealed $Sn_{0.98}Co_{0.02}O_2$ sample recorded at 400 K……93

Fig.3.9 (a) Magnetization versus field at 295K, for x= 0.02, 0.05, 0.07 and x=0.10 samples of $Sn_{1-x}Co_xO_2$. The solid lines represent the fit to Bound magnetic polaron model (eq.3.2).

Temperature variation of M-H loop **(b)** for x=0.05 and **(c)** 0.07 sample along with the BMP fit……94

Fig.3.10 The initial magnetization curve along with Brillouin function model fit for N_2 annealed x=0.02 sample……96

Fig.3.11 M-T plots for $Sn_{1-x}Co_xO_2$ (x=0.02, 0.05, 0.07 and 0.10)……98

Fig.3.12 Plots of χ^{-1} vs. T of solid state synthesized $Sn_{1-x}Co_xO_2$ (x = 0.02, 0.05, 0.07 and 0.10) samples along with the Curie-Weiss fit……...99

Fig.3.13(a). ESR spectra at room temperature for different samples of $Sn_{1-x}Co_xO_2$ and integrated ESR spectra for x=0.02(air annealed) sample recorded at (b) 295K, (c) 345 K, (d) 395 K, (e) 445 K respectively. The simulated data by using two overlapping Gaussian curves are also shown……...101

Fig.3.14. XRD patterns of $Sn_{0.98}Co_{0.02}O_2$ samples under different annealing conditions……...103

Fig.3.15. XRD patterns along with Rietveld refinement for the samples-3A and 3N……104

Fig.3.16 (a) TEM image of Sample-3N, (b) HRTEM image of the same sample, (c) SAD pattern, (d) EDX pattern of the Sample-3N……...106

Fig.3.17. FTIR spectra for N_2 annealed Co doped samples along with the parent SnO_2 for comparison ……107

Fig.3.18. Hysteresis loop recorded for air annealed and N_2 annealed samples at room temperature……108

Fig.3.19 Temperature variation of resistivity for samples 1N, 2N and 3N……109

Fig.3.20. Variation of resistivity with temperature for 400^oC N_2annealed $Sn_{0.98}Co_{0.02}O_2$ sample……..110

Fig. 3.21. XRD patterns recorded for samples T1, S1, T2 and S2 along with the un-milled commercial SnO_2. The star marks (*) represent WC impurity phase…….....112

Fig. 3.22 XRD patterns along with Rietveld refinement for samples T1 and S1……113

Fig. 3.23 XRD patterns along with Rietveld refinement for samples T2 and S2……114

Fig. 3.24 SEM imageS recorded for S2 and T2 samples along with their EDX spectra…….115

Fig.3.25. HRTEM and Selected Area Diffraction pattern images of samples T1 and S1. The inset shows the FFT image……116

Fig. 3.26 Raman Shift for T1, S1, T2 and S2 samples collected at room temperature……...117

Fig. 3.27 M-H curves recorded for samples T1, S1, T2 and S2 at 20 K and 300 K. The insets

show the initial curves along with the fit to BMP model……119
Fig. 3.28 Temperature variations of magnetization M, (**a, b** and **c**) and dM/dT **(d)** for samples T1, S1 and S2……122
Fig. 3.29 (a)ESR spectra recorded for T1, S1, T2 and S2 samples at room temperature. The inset shows the integrated intensity of ESR signal. **(b)** Integrated ESR pattern for sample S1 along with fitting to Gaussian functions with two different resonance fields…….124
Fig. 3.30 XRD patterns of $Sn_{1-x}Co_xO_2$ samples for x = 0.0, 0.02, 0.07 and 0.10 prepared by ball milling method. Star marked peaks correspond to spinel phase……..127
Fig. 3.31 XRD pattern along with Rietveld refinement for x=0.10 sample……128
Fig. 3.32 SEM images for x=0.02 and 0.10 with EDX spectra……...129
Fig. 3.33 TEM, HRTEM and SAD images of x=0.02 sample……130
Fig.3.34 Raman Spectra recorded for $Sn_{1-x}Co_xO_2$ x=0.0, 0.02, 0.07, 0.10 samples at room temperature……...131
Fig. 3.35 M-H loops of $Sn_{1-x}Co_xO_2$ samples for x = 0.0, 0.02, 0.07 and 0.10 samples at (a) 290 K and (b) 20 K……..132
Fig. 3.36(a) Initial M-H curve for x = 0 sample along with fit to eq. 3.6. (b) BMP model fit for x = 0.02, 0.07 and 0.10 sample……..134
Fig. 3.37 Temperature variations of magnetization M, (**a, b** and **c**) and dM/dT **(d)** for samples T1, S1 and S2……..138
Fig. 3.38 Temperature variation of magnetization for $Sn_{0.98}Co_{0.02}O_2$ sample……139
Fig. 3.39 Isothermal magnetization curves for $Sn_{0.98}Co_{0.02}O_2$ sample……141
Fig. 3.40 The Arrott plots (M^2 vs. H/M) for 2 at % Co-doped SnO_2 sample in the temperature range of 610-647 K……141
Fig.3.41 Modified Arrott plots, $M^{1/\beta}$ versus $(H/M)^{1/\gamma}$ with $\beta = 0.52$ and $\gamma = 1.1$…….143
Fig. 3.42 (a) The spontaneous magnetization (M_S) versus Temperature. **(b)** The plot in logarithmic scale along with fitted data……...144
Fig. 3.43 (a) The initial inverse susceptibility $1/\chi_0$ plotted against temperature for 2 at % Co-doped SnO_2 sample. **(b)** The plot in logarithmic scale along with fitted data……...145
Fig. 3.44. The critical isothermal magnetization at $T = T_C$ for 2 at % Co-doped SnO_2. (b) The plot in logarithmic scale, along with the fitted data shown as solid line……..146

Fig. 3.45 Scaling plot *of* $M\ |\varepsilon|^{-\beta}$ *versus* $H\ |\varepsilon|^{-(\beta+\gamma)}$ with β, γ and δ values from the final iteration for $Sn_{0.98}Co_{0.02}O_2$. Different symbols represent different temperatures. The inset reproduces plots in double logarithmic scale……..147

Fig. 3.46 Plot of $\chi_o^{-1}\left[\frac{d\chi_o^{-1}}{dT}\right]^{-1}$ versus temperature along with fitted data……..149

Fig. 3.47 Variation of γ_{eff} with reduced temperature ε……150

Chapter-4

Fig. 4.1. XRD patterns recorded at room temperature for x=0.0, 0.02, 0.05, 0.07 and 0.10 samples of $Sn_{1-x}Ni_xO_2$……157

Fig.4.2 (a) XRD patterns along with Rietveld refinement for x=0.02 and 0.05 samples……158

Fig. 4.2(b) XRD patterns along with Rietveld refinement for x= 0.07 and 0.10 samples……..159

Fig. 4.3 XRD patterns of x =0.0 and 0.07 samples with intensity in logarithmic scale……..160

Fig.4.4 SEM image and EDX spectrum of $Sn_{0.95}Ni_{0.05}O_2$……...161

Fig. 4.5 (a) TEM image of x=0.07 sample and the inset shows the selected area diffraction pattern. **(b)** HRTEM image showing the (110) plane. FFT image and inverse FFT image after filtering the background for (110) plane are shown in the top and bottom insets of the Fig (b).**(c)** EDS spectrum of x =0.07 sample showing the presence of Ni……...162

Fig.4.6 FTIR spectrum for x = 0.02 and 0.07 samples along with parent SnO_2 and NiO compounds for comparison……163

Fig.4.7 M-H loop recorded for x=0.02, 0.05, 0.07 and 0.10 samples at 300K and 80 K……164

Fig. 4.8 Magnetic hysteresis loops for x = 0.02, 0.05, 0.07 and 0.10 samples at 80 K and 300 K along with fit to BMP model……..…167

Fig.4.9. Temperature variation of magnetization for x=002, 0.05, 0.07 and 0.10 samples……168

Fig.4.10 paramagnetic susceptibility along with Curie-Weiss law fit for x = 0.02, 0.07 and 0.10 Ni doped SnO_2……169

Fig.4.11 Temperature variation of electrical resistivity for x=0.0, 0.02, 0.07 and 0.10 samples……..171

Fig. 4.12 ln ρ versus $(1/T)^{1/4}$ plots along with VRH model fit (solid line)……..…172

Fig.4.13 ESR data recorded for x = 0.02, 0.05, 0.07 and 0.10 at 295 K. ……..…..173

Fig. 4.14 ESR spectra recorded for x = 0.02, 0.07 and 0.10 samples at 295 K and 120 K. The experimental spectrum could be simulated with the help of two overlapping Gaussian profiles……..174

Fig. 4.15 XRD patterns recorded for ball milled x = 0.02, 0.05, 0.07, 0.10 samples……..178

Fig.4.16 XRD patterns of x=0.02, 0.05, 0.07 and 0.10 samples obtained by ball milling method along with the Rietveld refinement……...179

Fig.4.17 SEM and EDX images for x=0.02, 0.05 and 0.010 Ni doped SnO_2 along with the EDX spectra for x=0.10 sample……180

Fig.4.18 Raman spectra recorded for x=0.02, 0.05, 0.07 and 0.10 samples at room temperature…….....181

Fig.4.19 M-H loops recorded for x = 0.0, 0.02, 0.05, 0.07 and 0.10 samples at (a) 290 K and (b) 80 K……..…184

Fig. 4.20 Initial M-H curve of x =0.0 sample along with fit to eq. 3.6……...185

Fig. 4.21(a) Initial M-H curves of x =0.02, 0.05, 0.07 and 0.10 samples along with BMP model fit at **(a)** 300 K and **(b)** 80 K……..……186

Fig.4.22 (a) M-T curves for x=0.02, 0.05, 0.07 and 0.10 samples……..188

Fig.4.23 dM/dT plot for x = 0.02, 0.05, 0.07 and 0.10 samples……..188

Fig.4.24 Temperature variation of magnetization plot for x=0.05 and 0.07 samples alongwith Curie-Weiss fit in the paramagnetic region……..189

Fig. 4.25 ESR spectra and integrated ESR intensity for x=0.02, 0.05, 0.07 and 0.10 samples of Ni doped SnO_2……190

List of Tables

Chapter-1

Table-1.1: Atomic positions of SnO_2 in $P4_2/mnm$ space group……9

Table-1.2 Theoretical effective magnetic moment by considering Hund's coupling (P1) and orbital quenching (P2) along with experimental values for selected TM ions. (ref.[13])……13

Chapter-3

Table-3.1. List of parameters obtained from the Rietveld refinement and analysis of XRD patterns of $Sn_{1-x}Co_xO_2$ samples prepared by solid state route……87

Table-3.2 Cationic ratio obtained from EDX measurement for different Co-doped SnO_2 samples……88

Table-3.3 Coercive Field (H_c) and saturation magnetization (M_s) determined for $Sn_{1-x}Co_xO_2$ samples……91

Table-3.4 List of parameters obtained from the bound magnetic polaron model fit. M_0 is the spontaneous magnetization, χ_m is the susceptibility of the matrix and m_{eff} is the effective spontaneous moment per bound magnetic polaron……95

Table-3.5: Parameters obtained from Curie- Weiss fit. Here θ_c is the Curie temperature; μ_{eff} is the effective magnetic moment per Co-ion……99

Table-3.6 low field (LF) and high field (HF) resonance peak values in mT obtained from two peaks Gaussian model fit……100

Table-3.7. List of parameters obtained from the Rietveld refinement and analysis of XRD for 2 at % Co doped SnO_2 prepared by co-precipitation technique……105

Table - 3.8: List of parameters obtained from the analysis of XRD patterns, magnetization data and ESR spectra……115

Table-3.9: Cationic ratio obtained from EDX analysis for S1, T1, S2 and T2 samples……116

Table-3.10 List of parameters obtained from the bound magnetic polaron model fit. M_0 is the

spontaneous magnetization, χ_m is the susceptibility of the matrix and m_{eff} is the effective spontaneous moment per bound magnetic polaron……...121

Table-3.11. List of parameters obtained from the Rietveld refinement and analysis of XRD patterns……..…….....126

Table-3.12 Cationic ratio obtained from EDX measurement for x =0.0, 0.02, 0.07 and 0.10 samples…….130

Table-3.13 Coercive Field (H_c) and saturation magnetization (M_s) determined for various Co doped SnO_2 samples prepared by ball milling…….133

Table 3.14: List of parameters obtained from the analysis of M-H data by using BMP model. M_o is the spontaneous magnetization of the system, χ_m is the susceptibility of the matrix and m_{eff} is the effective magnetic moment per bound magnetic polaron……136

Table- 3.15. Comparison of Critical exponent values with different theoretical models for DMS and Ferrite samples……152

Chapter-4

Table-4.1 List of parameters obtained from the Rietveld refinement and analysis of XRD patterns…….160

Table-4.2 Cationic ratio obtained from EDX measurement for different Ni-doped SnO_2 samples……161

Table-4.3 Coercive Field (H_c) and saturation magnetization (M_s) determined for various Ni-doped samples from the magnetization measurements……165

Table 4.4: List of parameters obtained from the analysis of M-H data by using BMP model. M_0 is the spontaneous magnetization of the system, χ_m is the susceptibility of the matrix and m_{eff} is the effective magnetic moment for per BMP……..……..166

Table-4.5 Parameters obtained from Curie-Weiss fit. Where θ_c is the Curie temperature, μ_{eff} is the effective magnetic moment per Ni-ion……..169

Table-4.6 Parameters obtained from VRH model fit. Where ρ(RT) is the resistivity at room temperature. The density of states in the vicinity of Fermi level $N(E_F)$, hopping distance $R_{hop}(T)$ and hopping energy $E_{hop}(T)$……170

Table-4.7 Resonance fields (high field and low field) obtained from two overlapping Gaussian

models at 295 K and 120 K……175

Table-4.8 List of parameters obtained from the Rietveld refinement and analysis of XRD

patterns……180

Table-4.9 Cationic ratio obtained from EDX measurement for x =0.0, 0.02, 0.05, 0.07 and 0.10 samples……...……181

Table-4.10 M_s and H_c obtained from magnetization measurements……...185

Table-4.11 List of parameters obtained from the analysis of M-H data by using BMP model. M_o is the spontaneous magnetization of the system, χ_m is the susceptibility of the matrix and m_{eff} is the effective magnetic moment for per BMP……..187

Table-4.12 Parameters obtained from Curie-Weiss fit of susceptibility and ESR spectra. Where θ_c is the Curie temperature, μ_{eff} is the effective magnetic moment per Ni-ion. Resonance field and g values for ESR spectra……..189

Chapter 1

Introduction

The electronic industry is dominated by semiconductors, because their electrical conductivity could be tuned in a wide range by doping appropriate impurity at the desired level. It is known that their electrical properties are quite sensitive, even for doping at the level of 1 percentage per million. On the other hand, ferromagnetic materials are mostly metallic in nature but with an advantage of ability to polarize the spin of charge carriers. Diluted Magnetic semiconductors (DMS) are a special class of materials having the dual characteristics of semiconductor and a ferromagnet. Such materials facilitate one more degrees of freedom, i.e. spin polarization of charge carriers, in addition to the type and concentrations of charge carriers in tuning and controlling the electrical transport in devices. Devices having such extra degree of freedom regarding the spin polarization of electrons are called spintronic devices and they have potential applications in electronic circuits for high speed signal processing, miniaturization, low power consumption, etc. DMS materials are obtained by replacing a fraction of host ions in semiconductors with magnetic ions, such as transition or rare earth element as shown in Fig.1.1.

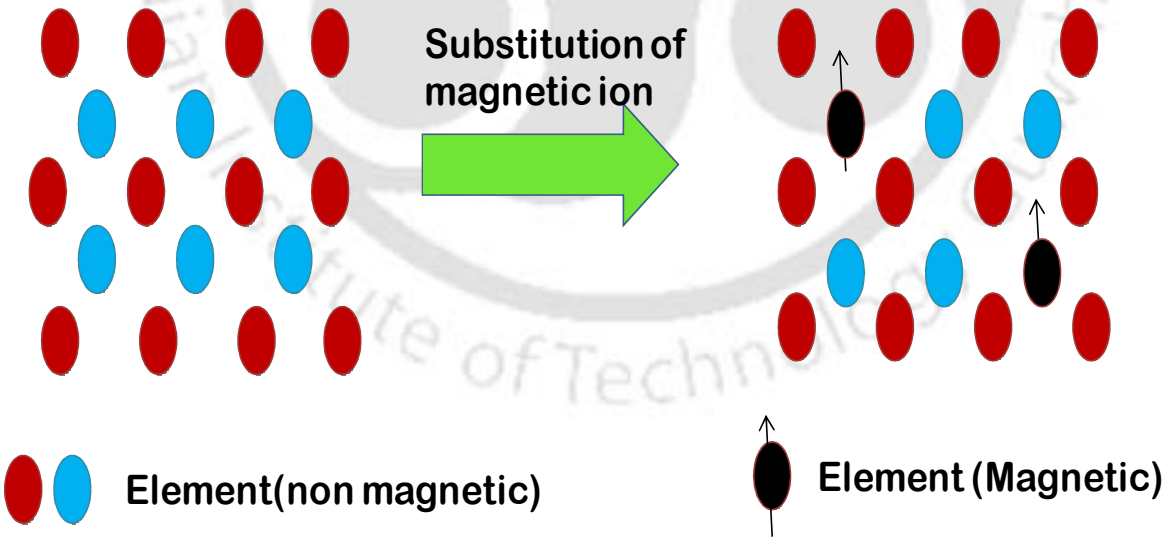

Fig. 1.1 Schematic representation of non-magnetic semiconductor (left), and a diluted magnetic semiconductor (right)

Following different types of DMS materials are studied in literature.

- Chalcogenides based magnetic semiconductors.
- Transition element doped Group II-VI, Group III-V and Group IV-VI semiconductors.
- Transition element doped wide band gap oxide semiconductors.

Europium chalcogenides EuX (X= O, S, Se) were known to exhibit ferromagnetic semiconducting properties but with a maximum transition temperature (T_c) of 69 K [14]. Transition element (TM = Ti, V, Cr, Mn, Fe, Co, Ni) doped Group II-VI semiconductors such as $Zn_{1-x}T_xS$, $Zn_{1-x}T_xSe$, $Cd_{1-x}T_xTe$ etc. are known to exhibit ferromagnetism (FM) with the highest T_c of 15K in $Zn_{1-x}Cr_xTe$ [5, 15-19]. Mn doped Group III-V semiconductors, such as (Ga,Mn)As, (In,Mn)As were studied extensively and the maximum FM T_c was reported to be 110 K [20-25]. The group IV-VI based semiconductors by transition element doping such as $Sn_{1-x}Mn_xTe$ and $Pb_{1-x}Mn_xTe$ have been studied by several authors [26-31]. Their magnetic properties are quite sensitive to charge carrier concentrations. Materials having charge concentrations in the range of 10^{17}-10^{19} cm^{-3} exhibit antiferromagnetism (AFM) and spin glass behavior down to liquid helium temperature and on the other hand FM with Curie temperature T < 30 K was observed in materials with charge concentrations of the order of 10^{21} cm^{-3} [26-31]. The FM ordering was due to RKKY type of interaction [26, 31]. The main drawback in the above type of DMS materials is the low FM T_c far below the room temperature. Moreover, it is quite difficult to prepare some of the above materials and to carry out the desired doping. For spintronic applications, the DMS materials should exhibit FM with T_c quite higher than room temperature.

Based on Zener model of FM [32], Dietl *et al.*[5] have predicted room temperature FM in Mn doped ZnO. Following this prediction, there were several experimental reports on room temperature FM in transition metal (TM) doped ZnO series. The TM doped oxide based semiconductors, such as TiO_2, SnO_2, In_2O_3 were also found to exhibit FM above room temperature [33-40]. Several theoretical models such as, charge carrier mediated RKKY type of interaction [41-43], bound magnetic polaron [10], polaron percolation theory [44], and spin-split impurity band in insulating oxides were used to explain the FM in DMS materials[11, 35]. In addition to that, the observed giant magnetic moment in some of the oxide based DMS was

explained in terms of oxygen defect and unquenched orbital magnetic moment [39, 45-47]. The exchange interaction mechanism prevailing in these materials is not yet understood clearly.

1.2 Diluted Magnetic Semiconductors in Spintronics

Type, mass and concentration of charge carriers in semiconductors play important role in electronic circuits. High frequency electronic devices made up of semiconductors with appropriate electron concentrations are used in integrated circuits for information processing and communications. The mass storage of data in information technology is achieved by the magnetic recording technique by using spin of the electrons in ferromagnetic metals. The performance of the devices can be enhanced, if the charge and spin of the electrons are utilized in a single device called spintronic device. This is possible by developing a new class of materials called magnetic semiconductors. Diluted magnetic semiconductors can be utilized for such applications.

Some of the properties of DMS materials, devices made up of DMS materials and their applications towards spintronic are discussed.

1.1.1 Enhanced Zeeman Splitting

Zeeman Effect is a well known phenomenon, which is observed in the presence of magnetic field. In the presence of an external magnetic field, the degeneracy of electrons is lifted due to the interaction between spin of electrons in the material and magnetic field. The spin magnetic moment parallel to the field direction will have lower energy than that of the spin magnetic moment opposite to the field direction. This difference in energy between the two spin-polarized electrons in opposite direction due to the external applied magnetic field is the well known Zeeman effect [48]. This energy difference is quite low for a wide band gap non-magnetic semiconductors. Now, if a magnetic element such as Mn^{2+} is doped in Group II-VI semiconductors, i.e. in case of $Cd_{1-x}Mn_xTe$, it exhibits FM and magnetic polarization in the presence of external magnetic field. Thus in this system, the magnetic field due to FM will also contribute for Zeeman splitting. This results in huge Zeeman splitting of the conduction electrons, which is quite large compared to the conventional Zeeman Effect in non-magnetic semiconductors[15, 48]. This effect has potential applications in diagnostic studies, optical devices etc. [15].

1.1.2 Spin Field Effect Transistor (Spin-FET)

Based on the ab-initio electronic structure calculation, Sato and Yoshida [1] proposed a design for spin-FET. The Mn-doped ZnO exhibits AFM spin glass state, but it becomes half metallic FM upon hole doping. Moreover the FM state of Co-, Ni- or Fe- doped ZnO becomes more stable upon electron doping. Using these properties of ZnO, one can fabricate the spin-FET as shown in Fig.1.2. The channel is made up of Mn-doped ZnO and the source and drain are made up of Co-doped ZnO. Here, when a negative voltage is applied to the gate terminal of Spin-FET, holes would be doped in the channel made up of Mn-dope ZnO. Because of the hole doping of Mn-ZnO, it is transformed from AFM spin glass state to half metallic ferromagnetic state and thereby introducing channel of spin polarized charge carriers. Upon biasing the source and drain, spin polarized electrons from the source due to the presence of Co ions are injected into the channel. The spin polarized charge carriers, whose spin alignment is parallel to those of polarized drain spins would feel no resistance and could be successfully collected at the drain. So, a realistic Spin-FET having 100% spin polarized electrons flowing through half-metallic channel made up of Mn-doped ZnO can be constructed. Since Co doped ZnO and Mn doped ZnO are used as spin injectors and channel respectively, there won't be any resistance mismatch and also it could be operated at room temperature as they exhibit FM with T_c above room temperature.

Similar type spin-FET was proposed by Datta and Das [49], where the drain and the source are made up of ferromagnetic material i.e. iron and the gate voltage was controlled by using narrow gap semiconductors such as InAlAs.

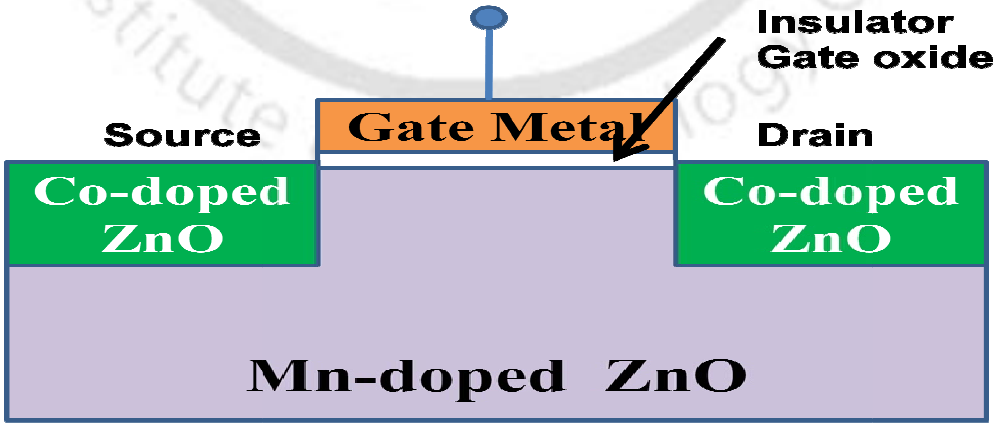

Fig. 1.2 Spin FET based on ZnO, (from ref. [1]).

1.1.3 Photo Induced Ferromagnet

According to Sato and Yoshida[1], photo induced ferromagnet can be obtained in ZnO based semiconductor. The Mn doped ZnO, (ZnO:Mn) is an insulator with spin glass state and on the other hand Cr or Fe doped ZnO (ZnO:Cr or ZnO:Fe) behaves like half metallic ferromagnets. One can make a mixture of Mn and Cr doping, such as $ZnO:Mn_{1-x}Cr_x$ and can be made into a paramagnet. The paramagnetic mixture on GaAs substrate could be grown as shown in Fig.1.3. Electrons and holes can be excited at GaAs and $ZnO:Mn_{1-x}Cr_x$ interface by photo-excitation by using photons of energy $h\upsilon > E_g$ of GaAs and $h\upsilon < E_g$ $ZnO:Mn_{1-x}Cr_x$. By biasing the junctions with appropriate voltage, the excited charge carriers can be introduced in the $ZnO:Mn_{1-x}Cr_x$ region and the system can be converted to half metallic ferromagnet. The ferromagnetically ordered state can be detected by using the technique of magneto optical effect by introducing another photon of energy $h\upsilon < E_g$ of ZnO. Optically turning on and off of FM in (III-Mn)V type of DMS have been reported by Koshihara *et al.*[50] and Munekata *et al.* [51].

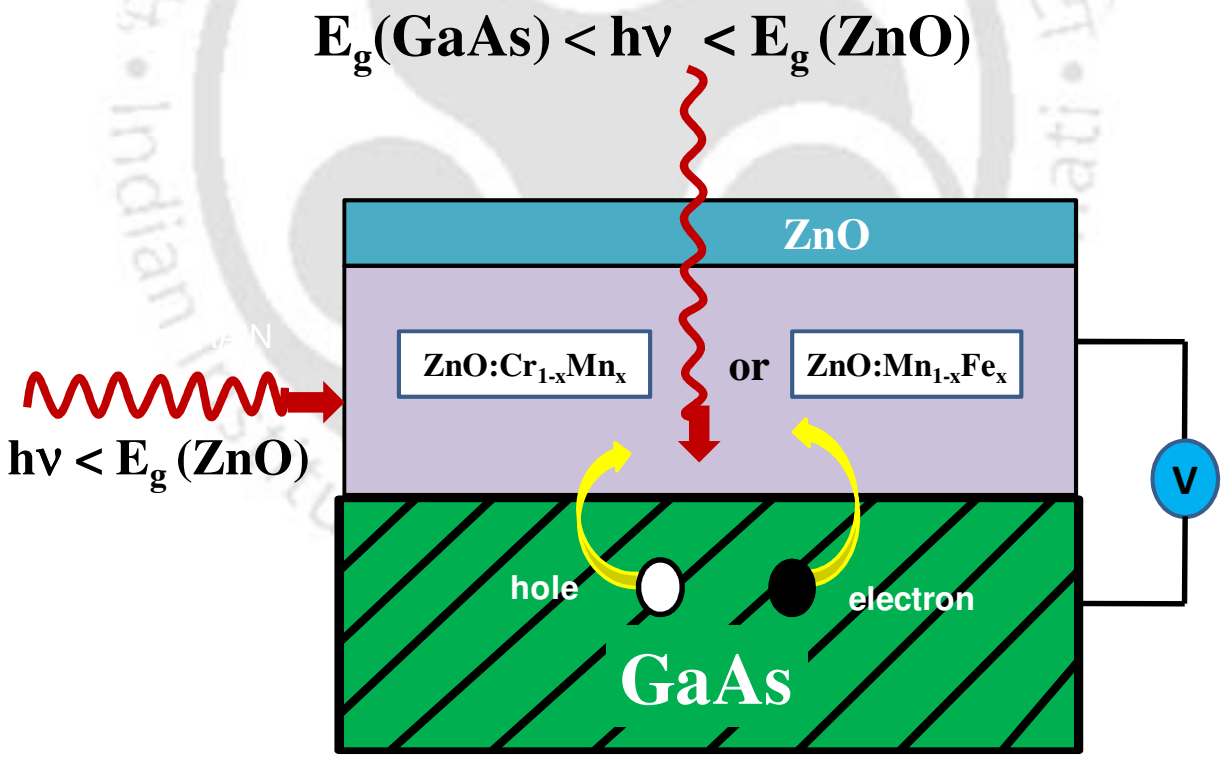

Fig.1.3 A schematic representation of photo induced ferromagnet (ref.[1]).

1.1.4 Spin-LED

Hono *et al.* [2] reported the fabrication of light emitting spintronic device using III-V based (GaMn)As DMS materials. Fig.1.4 shows the device structure grown by molecular beam epitaxy (MBE) method. Here n-type GaAs is used as substrate and over which n-type GaAs of 500 nm was grown as buffer layer. GaAs layer of 10 nm thin; InGaAs of 10 nm thin, GaAs spacer of thickness up to 220 nm and GaMnAs of 300 nm thick were grown over the substrate. Spontaneous magnetization will occur in p-type GaMnAs below the transition temperature as shown as black arrows in Fig.1.4. Under forward bias condition, the spin polarized holes from GaMnAs are allowed to pass through the GaAs spacer layer of thickness d and then injected into the InGaAs strained Quantum well (QW) which acts as a detector. The depth of the spin injection can be studied by placing the QW at different depth. Simultaneously the un-polarized electrons from the n-type GaAs substrate were allowed to inject into the InGaAs QW (hatched region). The spin polarization of the injected holes were directly determined from the polarization of emitted electroluminescence following the recombination of holes with the unpolarised elcectrons.

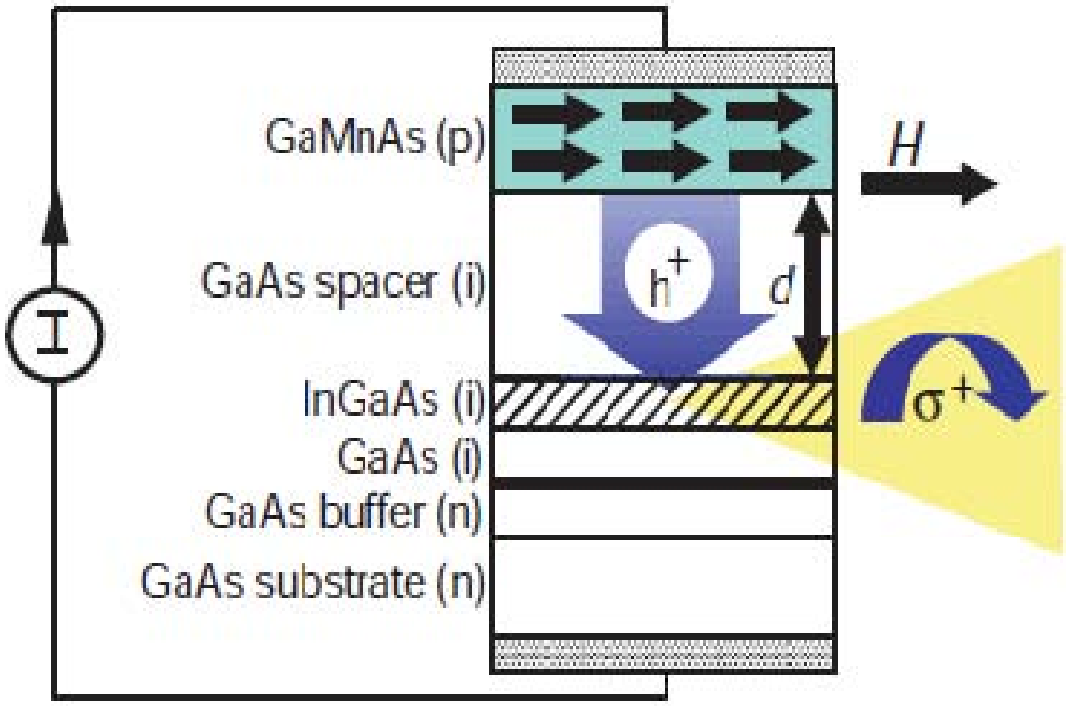

Fig. 1.4 Schematic block diagram of Spin-FET from (ref.[2])

1.3 Structural Properties

In this section, the crystal structure of wide band gap oxide semiconductors such as ZnO, TiO_2, SnO_2 are discussed. Other structural effects such as crystal field effect and Jahn Teller distortion are also given. Since DMS materials are prepared by transition element doping in oxide semiconductors, it is essential to understand their crystal structure.

1.3.1 Crystal Structure

ZnO mainly crystallizes in two different forms, namely the wurzite and the cubic zincblende structure. The wurzite structure is more stable and mostly forms in ambient preparation conditions, whereas the zincblende structure forms under hydrostatic pressure. The wurzite structure is mainly a hexagonal closed pack (hcp) system. It belongs to $P6_3mc$ space group with Zn atoms occupying the (0.667, 0.333, 0.000) position having a multiplicity factor of 2 and oxygen atoms occupying the (0.667, 0.333, 0.380) site with multiplicity factor 2. Thus there are two formula units per unit cell. The lattice parameters are given by a = b = 3.250 Å and c = 5.206 Å [52]. In both the cases Zn and O atoms have tetrahedral coordination.

TiO_2 mainly crystallizes into rutile, anatase and brookite structures. In addition to that, the pressure induced monoclinic baddeleyite and orthorhombic forms are also seen. The rutile state is found to be the most stable state. Upon heating, the anatase and brookite states are converted to rutile form. The rutile and anatase belong to the tetragonal crystal structure and brookite structure exhibits orthogonal cell. The rutile phase belongs to the $P4_2/mnm$ space group with lattice parameters a = b = 4.594 Å and c = 2.959 Å and z = 2 [53]. The anatase phase belongs to the $I4_1/amd$ space group with lattice parameters a = b = 3.785 Å and c = 9.514 Å and the number of formula units per unit cell z=4 [53]. The brookite phase belongs to the Pcab space group with Z = 8 and a = 5.456 Å, b = 9.182 Å, c = 5.143 Å.

SnO_2 is a mineral of cassiterite and exhibits rutile crystal structure similar to that of TiO_2. The Bravis lattice describing the SnO_2 is tetragonal closed packed structure. Here, the Sn atoms are six coordinated and oxygen atoms are three coordinated as shown in Fig.1.5. The space group for SnO_2 is $P4_2/mnm$ and two SnO_2 molecules are accommodated in a unit cell (Z=2). The lattice

parameters a = b = 4.737 Å and c= 3.185 Å [54], and bond angles α = β = δ= 90°. The atomic positions and their multiplicity factors are given in table-1.1.

SnO_2 is an n-type wide band gap semiconductor with band gap around 3.6eV. It is a diamagnetic solid having amphoteric nature. There has been a great deal of interest in the preparation of inexpensive thin films of SnO_2 because they are attractive from the scientific and technological point of view [55]. Several potential applications have been reported previously, such as, a transparent conductive electrode for solar cells [56-58], a gas sensing material for gas sensor devices [59], photochemical and photoconductive devices in liquid crystal display [60], gas discharge display and lithium-ion batteries. SnO_2 based varistors having highly nonlinear current–voltage characteristics similar to that of back-to-back Zener diodes but with much greater current and energy handling capabilities are also studied [61, 62].

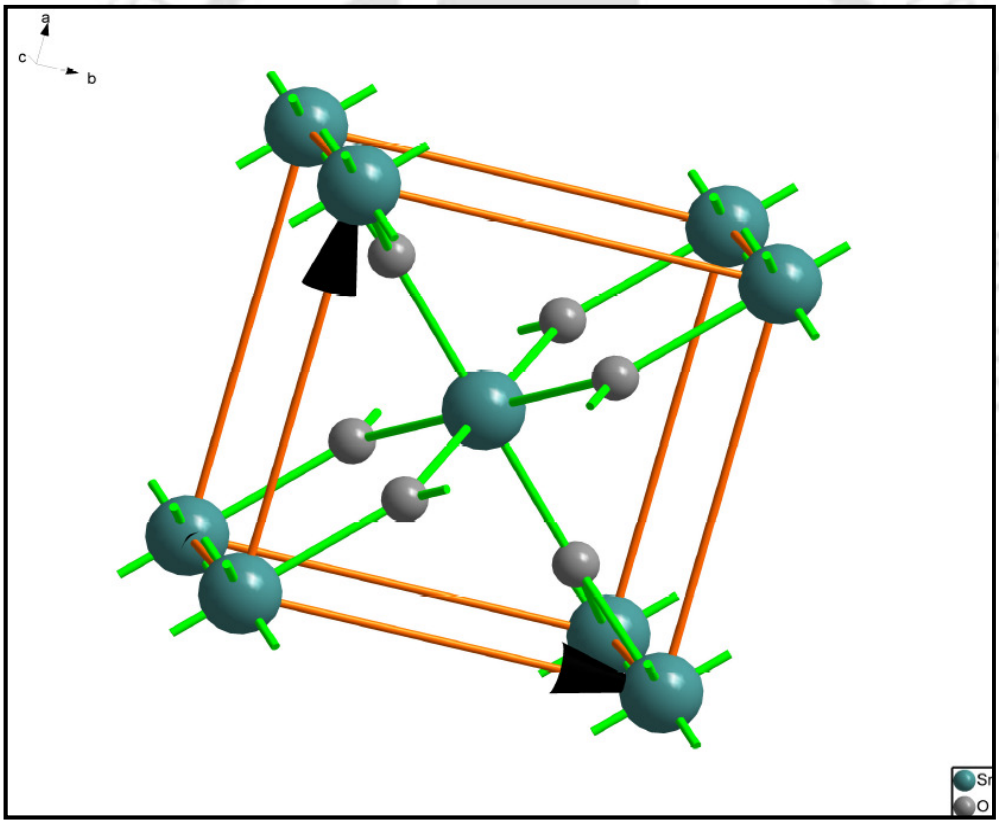

Fig.1.5 Crystal structure of SnO_2. Here the bigger and smaller size atom represents Sn and O respectively.

Table-1.1: Atomic positions of SnO_2 in $P4_2/mnm$ space group.

Ion	Site	(x, y, z)
Sn	2a	(0,0, 0)
O_1	4f	(x, x, 0) ≅ (0.3, 0.3, 0)

1.2.2 Crystal Field Effect in TM-ions

Atoms in a solid with a regular crystal structure are influenced by the electric field of the neighboring atoms. Such electric fields are called crystal field [13]. Crystal field depends upon the local environments, such as the nature of atomic co-ordination, etc. The crystal field effect on d orbitals can be illustrated by moving a set of negative point charges close to a metal ion. As one would expect, the energies of the d orbitals rise as the negative charges approach the metal ion, owing to the Coulomb repulsion between the d orbital electrons and the surrounding charges. The d shell has five orbitals, namely d_{xy} , d_{xz} , d_{yz} , d_{z^2} , and $d_{x^2-y^2}$; out of them, the first three are called t_{2g} orbitals and last two are called e_g orbitals. The electronic distributions of *d* orbitals are shown in Fig.1.6. In the absence of crystal field, all the five levels are degenerate. The t_{2g} orbitals point along in between x, y and z axes, but the e_g orbitals point along the direction of x, y and z axes. If the surrounding negative charge is spherically symmetric, all five d orbitals are equally affected. In practical cases, the surrounding negative charge is never spherically distributed, because the charge is associated with specific ions that occupy specific positions. The consequence is that each d orbital is affected differently, and how a particular d orbital is affected depends upon the geometry of the surrounding point charges. This effect is clearly seen in the splitting of the energy levels for the five d orbitals. The Crystal Field effects are summarized in the chart shown in Fig.1.7. Each geometry of point charges (linear, square planar, tetrahedral, or octahedral) produces a characteristic splitting pattern for the five d orbitals (*xy, xz, yz,* x^2-y^2*, and* z^2).

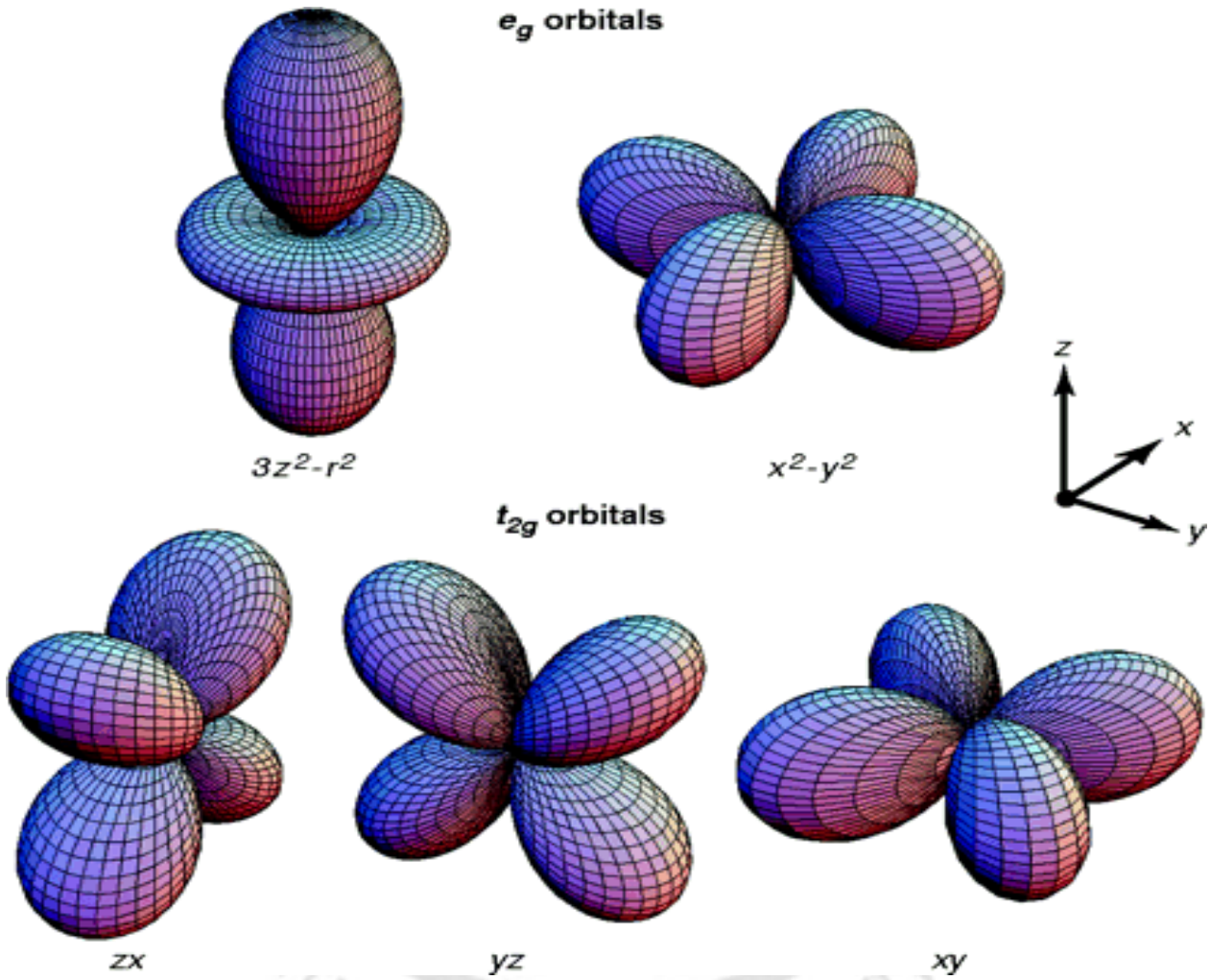

Fig. 1.6 The electronic distribution of 3-*d* orbitals. In the cubic crystal field, this fivefold degeneracy is lifted to two e_g orbitals (x^2-y^2 and $3z^2 - r^2$) and three t_{2g} orbitals (*xy*, *yz* and *zx*). (Reproduced from Tokura *et al.* [3])

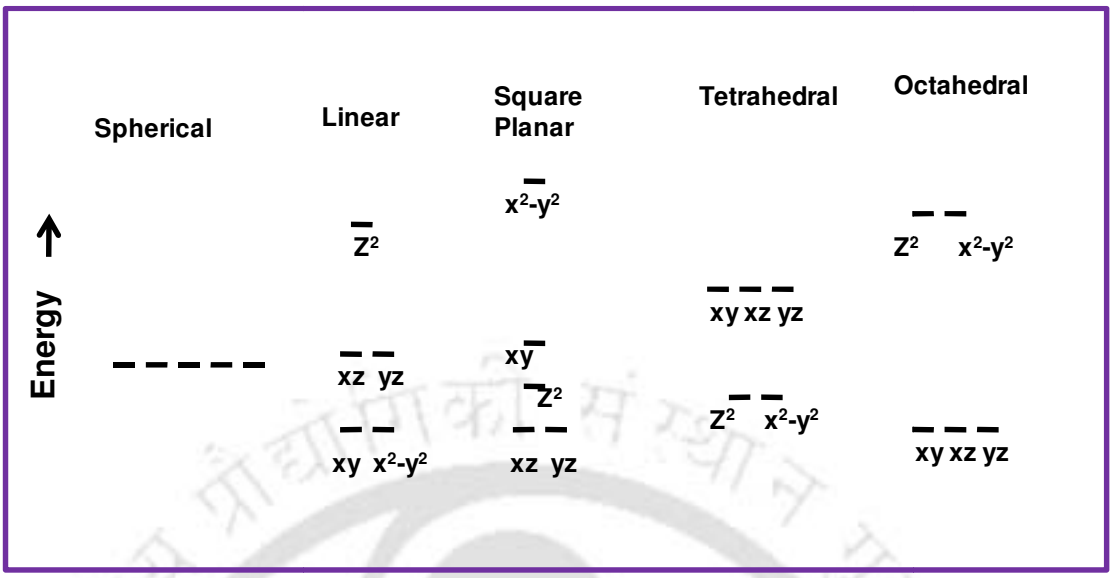

Fig.1.7. Splitting of d-orbitals in presence of different anion position configuration.

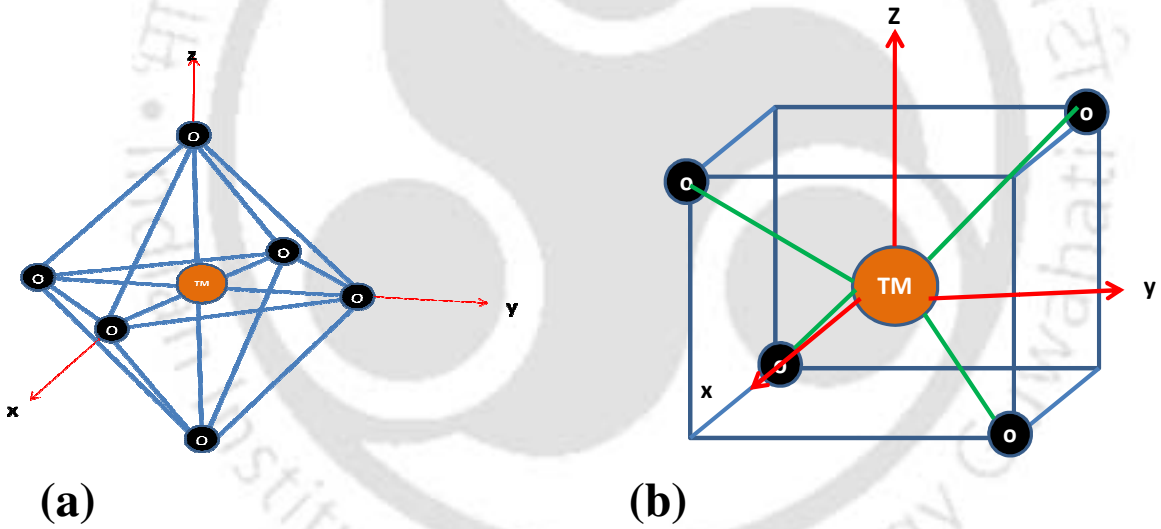

Fig.1.8 TM-ion in **(a)** octahedral and **(b)** tetrahedral environment.

High Spin and Low spin arrangement in TM-ion

In the case of octahedral environment as shown in Fig.1.8(a), the 3d electrons will first fill up the t_{2g} level before filling e_g. However the competition between the crystal field energy and pairing energy will decide the manner in which each orbital is filled up. In the presence of weak crystal field, the electrons filling in the orbitals will take place as per Hund's rule, i.e. electrons will singly occupy in each orbital followed by pairing of electrons with opposite spin in each orbital.

On the other hand, in the presence strong crystal field, where the crystal field energy dominates the Hund's energy, electrons will doubly occupy in some of the orbitals (t_{2g} or e_g) before the electrons are filled in the higher energy orbitals. For an example, Fig.1.9 shows the electronic arrangement in 3d shell of Co^{2+} ion under weak and strong crystal field cases. The net spin quantum number for the weak field case is found to be S=3/2, whereas S=1/2 for the strong field case.

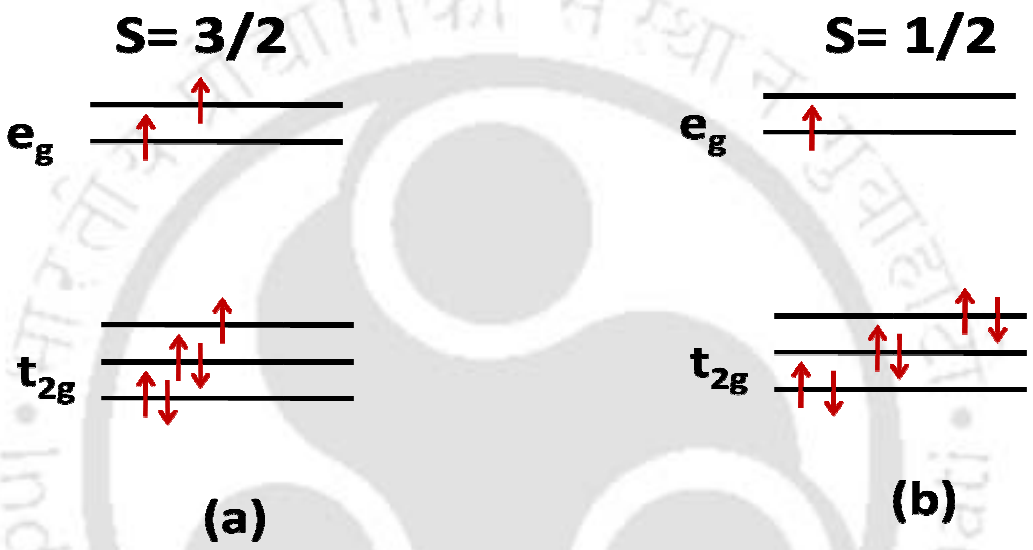

Fig.1.9 Electronic configuration of (a) high-spin (weak field) and (b) low-spin (strong-field) cases for $3d^7$ shell of TM ion.

Orbital quenching

In general, the effective magnetic moment of an ion is calculated by following the Hund's rule and taking the values of *S, L* and *J*. The formula is given by

$$\mu_{\text{eff}} = g\mu_B\sqrt{J(J+1)} \qquad \text{---------- (1.1)}$$

where μ_{eff} is the effective magnetic moment per magnetic ion. g is the Lande's g-factor whose value is equal to $g = 1+\frac{J(J+1)+S(S+1)-L(L+1)}{2J(J+1)}$ and $J=L+S$ is the total angular momentum quantum number. L and S are the orbital and spin angular momentum quantum number

respectively. In 3d shell of TM ions, the crystal field interaction is much stronger than the spin-orbit coupling interaction and as a result, the system chooses a ground state, such that $L = 0$. This is called quenching of orbital momentum and it leads to J = S and g = 2. Thus eq. 1.1 modifies to the following form.

$$\mu_{eff} = 2\mu_B[S(S+1)]^{1/2} \quad \text{---------- (1.2)}$$

The theoretically calculated μ_{eff} values for a few TM-ions by considering total angular momentum quantum number, J (P1) and independently by taking only spin quantum number S (P2) are tabulated in table-1.2. The experimental values are found to deviate from P1 but are comparable to P2 as shown in the table.

Table-1.2 Theoretical effective magnetic moment by considering Hund's coupling (P1) and orbital quenching (P2) along with experimental values for selected TM ions. (ref.[13]).

Ion	**Shell**	**S**	**L**	**J = L+S**	**g**	**P1=** $g\sqrt{J(J+1)}$ **(μ_B)**	**P2=** $2\sqrt{S(S+1)}$ **(μ_B)**	**P_{exp} (μ_B)**
Fe^{2+}, Co^{3+}	$3d^6$	2	2	4	3/2	6.70	4.9	4.82
Fe^{3+}	$3d^5$	5/2	0	5/2	2	5.92	5.92	5.82
Co^{2+}, Ni^{3+}	$3d^7$	3/2	3	9/2	1.33	6.63	3.87	4.90
Ni^{2+}	$3d^8$	1	3	4	5/4	5.59	2.83	3.12

1.2.3 Jahn-Teller Distortion

The observed degeneracy in crystal field splitting can be further broken by the lattice distortion. For example, in MnO_6 octahedral environment, the electrons in the 3d shell of Mn ions are under the Coulomb interaction of electrons from the *2p* shell of O ions. Since the p_x, p_y, p_z orbitals of O point along x, y and z directions respectively, there will be a overlapping with e_g orbitals of Mn ions ($d_{x^2-y^2}$, $d_{3z^2-r^2}$). So, the energy of e_g orbitals is raised compared to t_{2g} orbitals. Fig. 1.10(a) shows a two dimensional diagram of typical overlapping of one of the e_g orbitals ($d_{x^2-y^2}$) with *p* orbitals of neighboring O ions. On the other hand, we can see no such overlapping with a typical t_{2g} orbital (d_{xy}), as shown in Fig. 1.10 (b). In view of the above crystal field effect, the degeneracy in e_g orbitals and t_{2g} orbitals of d-shell are further lifted as shown in

Fig. 1.10 (c) for octahedral co-ordination [13]. Thus in addition to the splitting of d-orbitals into t_{2g} and e_g orbitals due to crystal field, there is further splitting of orbital within t_{2g} and e_g due to Jahn-Teller effect.

The oxygen ions are surrounded by Mn^{3+} ions. The readjustment of position of oxygen ions in MnO_6 octahedra can lead to asymmetry in MnO_6 octahedra. The above lattice asymmetry lifts the degeneracy of t_{2g} and e_g orbitals. The lifting of degeneracy due to orbital-lattice interaction is known as Jahn-Teller (JT) distortion. The Jahn-Teller distortion is significant for partially filled orbitals, where there is a net energy gain. This distortion leads to increase in elastic energy and decrease in electronic energy such that there is a net reduction in energy. Mn^{3+} ions are JT active, while Mn^{4+} ions are inactive for JT distortion in octahedral environment. Mn^{3+} ions have one e_g electron out of two e_g orbitals namely, $d_{3z^2-r^2}$ and $d_{x^2-y^2}$. The elongation of MnO_6 octahedra along z-axis gives rise to reduction in $d_{3z^2-r^2}$ level compared to $d_{x^2-y^2}$.level. Since, there is only one e_g electron, which occupies the $d_{3z^2-r^2}$ level, there is a reduction in electronic energy. The splitting of e_g and t_{2g} orbits due to JT distortion is shown in Fig. 1.10 (c). On the other hand, Mn^{4+} ion does not have any e_g electron, so reduction in electronic energy is not feasible and hence no JT distortion.

The TM-ion doped semiconductors are also affected by the Jahn-Teller distortion as estimated theoretically in Cr-doped Group II-VI based DMS by Blinowski *et al.*[18]. The susceptibility data obtained by Brumage *et al.* [63] on Cu-doped ZnO samples could be explained based on the crystal field effect and by incorporating the Jahn-Teller distortion, where the doped Cu was in Cu^{2+} state with electronic configuration $3d^9$.

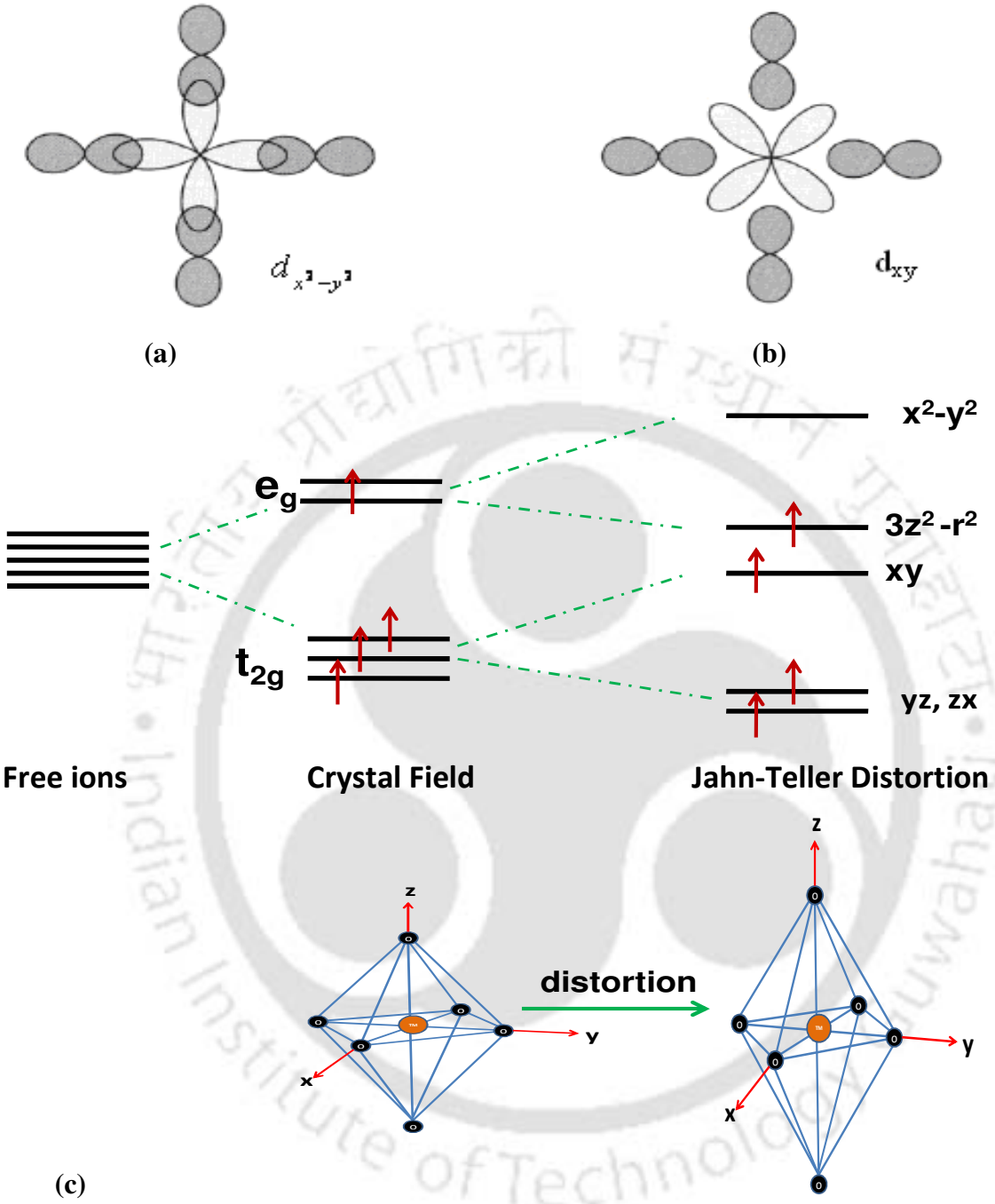

Fig. 1.10: (a) Typical overlapping of one of the e_g orbitals ($d_{x^2-y^2}$) with p orbital of neighboring O in a two dimensional diagram. **(b)** One of the t_{2g} orbitals with p orbital. **(c)** The crystal field splitting of d shell in octahedral environment. The Jahn-Teller distortion leads to a further splitting of both t_{2g} and e_g states.

1.4 Magnetic Ordering

Materials having appreciable magnetic moment in macroscopic scale are generally referred as magnetic materials. The fundamental parameter of magnetism is magnetic moment. The origin of magnetic moment of a material lies in the orbital and spin motion of electrons and how, the electrons interact with one another. The magnetism in microscopic scale depends upon how, atoms or group of atoms interact among themselves and to external field. The best way to introduce different types of magnetism is to describe, how materials respond to external magnetic field. The main distinction is that in some materials, there is no collective interaction of atomic magnetic moments, whereas in other materials there is a presence of very strong interaction between atomic moments [13, 64, 65]. The magnetic behavior of materials can be classified into the following major groups:

1. Diamagnetism, 2. Paramagnetism, 3. Ferromagnetism, and 4. Antiferromagnetism

Generally in the first two groups of materials, there is no collective magnetic interactions among the atomic or molecular moments, however they respond to applied magnetic field. Ferromagnetic materials are usually what we consider as being magnetic in macroscopic scale and they exhibit collective magnetic interaction among the dipoles in a long range such that the moments are aligned parallel to each other and the application of magnetic field enhances such alignment. Antiferromagnetism is exhibited by another class of materials, where there is a long range interaction among moments such that they align opposite to each other.

1.3.1 Diamagnetism

Diamagnetism is a fundamental property of materials, which try to oppose the applied magnetic field but it is usually very weak. It generally occurs in materials having completely filled electronic configuration. The atoms and molecules of diamagnetic substances do not posses any net magnetic moments (i.e. all the orbital shells are filled and there is no unpaired electron). However, when exposed to a magnetic field, the electrons orient themselves such that they try to oppose the applied magnetic field and hence they register negative magnetization and negative susceptibility. Most of semiconductors like ZnO, SnO_2 etc. are diamagnetic in nature.

1.3.2 Paramagnetism

Some of the atoms or ions in this class of materials have a net magnetic moment due to unpaired electrons in partially filled orbital. However, the individual magnetic moments do not interact magnetically, and like diamagnetism, the net magnetization is zero in the absence of external magnetic field. In the presence of an applied magnetic field, there is a partial alignment of atomic magnetic moments in the direction of the applied field, resulting in a net positive magnetization and hence positive susceptibility. The tendency of alignment of magnetic moments along the field direction is opposed by the thermal energy, which tries to randomize the spin orientation. So, they exhibit a temperature, (T) dependent susceptibility, χ known as the Curie Law,

$$\chi = \frac{C}{T} \qquad \text{---------- (1.3)}$$

with a Curie constant C [13].

In classical theory, each atomic moment is considered as magnetic dipole aligned in a particular direction with an angle θ with respect to applied field and the average magnetic moment along the field direction, z is written as, $< \mu^z > = \mu L(y)$. Here, μ is the magnetic moment of each dipole and L(y) is the Langevin function, $L(y) = Coth\ y - \frac{1}{y}$ and $y = \mu B/k_B T$. This function explains the magnetization of small particles made up of atomic clusters. For low applied field or at high temperature, such that y is small, L(y) tends to y/3. So, $< \mu^z > = \frac{\mu y}{3} = \frac{\mu^2 B}{3k_B T}$, or the magnetization $M=N< \mu^z >= \frac{N\mu^2 B}{3k_B T}$. So, the susceptibility $\chi = \frac{M}{H} = \frac{\mu_0 N \mu^2}{3k_B T} = \frac{C}{T}$ and the Curie law is obtained by the classical theory.

According to quantum mechanical treatment and by considering the quantization of total angular momentum of each atom, the average magnetic moment per atom aligned along the magnetic field direction, (i.e. z direction) of any paramagnetic sample can be written as [13, 64, 65]

$$\langle \mu_J^z \rangle = g\mu_B\, JB_J(x) \qquad \text{---------- (1.4)}$$

here, g is Lande's factor and it depends on spin-orbit coupling of electrons in each atom. J is the total angular momentum quantum number. $\mu_B = 9.27 \times 10^{-24}$ J/T is Bohr magnetron. $B_J(x)$ is Brillouin function, which can be written as,

$$B_J(x) = \frac{1}{J}\left[\left(J+\frac{1}{2}\right)Coth\left(J+\frac{1}{2}\right)x - \frac{1}{2}Coth\frac{x}{2}\right] \quad \text{---------- (1.5)}$$

here the variable $x = \frac{g\mu_B}{kT}B$, where k is the Boltzmann constant and T is the temperature. If N is the number of atoms per unit volume, the volume magnetization M can be written as,

$$M = N\langle\mu_J^z\rangle = Ng\mu_B JB_J(x) \quad \text{---------- (1.6)}$$

For the selection of magnetic field B and temperature T such that x is small, $B_J(x) \sim \frac{(J+1)}{3}x$.

Such assumption holds true for paramagnetic sample in a wide temperature region and for low applied field. So,

$$M = Ng\mu_B J\frac{(J+1)}{3}x = \frac{Ng^2\mu_B^2 B}{3kT}J(J+1) \quad \text{---------- (1.7)}$$

or, the susceptibility, $\chi = \frac{\mu_0 Ng^2\mu_B^2}{3kT}J(J+1)$ ---------- (1.8)

It is in the form of Curie law C/ T.

Thus the magnetic susceptibility based on Brillouin function expression reduces to Curie-law.

The examples of paramagnetic materials are W, Ce, Al, Li, Mg etc. with typical χ value of 6.8×10^{-5}, 5.1×10^{-5}, 2.2×10^{-5}, 1.4×10^{-5}, 1.2×10^{-5} respectively in SI unit[13].

1.3.3 Ferromagnetism

The property of parallel alignment of atomic moments due to their exchange interaction is called ferromagnetism. Unlike paramagnetic materials, the atomic moments in these materials exhibit very strong interactions. These interactions are produced by electronic exchange forces and result in a parallel alignment of atomic moments. The exchange force is a quantum mechanical phenomenon, due to the relative orientation of spins of two electrons. Ferromagnetic materials exhibit parallel alignment of moments resulting in large net magnetization even in the absence of external magnetic field. Two distinct characteristics of ferromagnetic materials are spontaneous magnetization and Curie temperature.

The spontaneous magnetization is the net magnetization that exists inside a uniformly magnetized microscopic volume called domain, even in the absence of external magnetic field.

All the magnetic moments align in a single unique direction. This effect is generally due to exchange interactions. The magnitude of this magnetization at 0 K, depends on the individual atomic magnetic moments in the magnetic domain. A related term is the saturation magnetization and it is the maximum induced magnetic moment per unit volume that can be obtained in a magnetic field (H_{sat}); beyond this field, no further increase in magnetization can occur. The difference between spontaneous magnetization and the saturation magnetization has to do with magnetic domains.

Even though the electronic exchange forces in ferromagnets are very large, thermal energy eventually overcomes the exchange interactions and produces a randomizing effect beyond a characteristic temperature called Curie temperature. When a FM material is heated, the thermal energy causes their magnetic moments to fluctuate. If the thermal energy becomes larger than the exchange energy, which keeps the moments parallel to each other, the materials tend to lose their magnetic ordering and behave like PM. The temperature at which this transformation occurs is called Curie temperature, (T_c). So, they undergo transition from ordered FM state to disordered PM state at T_c.

The phenomenon of ferromagnetism can often be well described by a mean field or molecular field model. The molecular field model simply assumes that all the interactions from the neighboring magnetic species can be described in terms of an effective internal or molecular field B_m, which is proportional to the magnetization, i.e. $B_m = \lambda M$, where λ is the Weiss molecular field constant. So, the total magnetic field experienced by each dipole is the sum of applied field B_a and the molecular field B_m. So, the expression for magnetization can be written by following eq. 1.6 with the modification that

$$x' = \frac{g\mu_B}{kT}\left(B_a + \lambda M\right) \qquad \text{---------- (1.9)}$$

$$M = Ng\mu_B\, JB_J\left(x'\right) \qquad \text{---------- (1.10)}$$

At temperature close to T_c, $B_J(x')$ is small and can be approximated to

$$B_J\left(x'\right) \rightarrow \frac{(J+1)}{3}x' \qquad \text{---------- (1.11)}$$

or, $$M = \frac{Ng^2\mu_B^2 J(J+1)}{3kT}\left(B_a + \lambda M\right) \qquad \text{---------- (1.12)}$$

or, $$\chi = \frac{C}{T - \theta_c}$$ ---------- (1.13)

The above equation is called Curie-Weiss law with the Curie temperature, $\theta_C = \frac{\lambda C}{\mu_0}$ and it is equivalent to ferromagnetic transition temperature. The examples of FM materials are Co, Fe, Ni, EuO with T_c 1388 K, 1043 K, 627 K, and 69 K respectively. The magnetic moment per formula unit for these materials are found to be 1.714, 2.22, 0.605 and 6.9 respectively in the unit of μ_B/formula unit[13].

1.3.4 Antiferromagnetism

In antiferromagnetic materials, the spins of electrons align in a regular pattern with neighboring spins pointing in opposite directions, below a certain temperature called Neel temperature. Above the Neel temperature, the material is typically paramagnetic. The magnetic susceptibility of antiferromagnetic material will appear to go through a maximum as the temperature is lowered. The antiferromagnetic ordering is possible based on different type of magnetic unit cell structures as shown in Fig. 1.11 except B type, which is a FM one.

In A-type structure, the magnetic ions are coupled ferromagnetically in each (001) plane but with alternate planes aligned in opposite spin orientation such that it they exhibit net anti-ferromagnetic interaction. B-type structure is a ferromagnetic one with all six nearest neighbor magnetic ions coupled ferromagnetically. In C-type structure, the atoms in (101) and $(\bar{1}10)$ planes are ferromagnetically aligned. Each atom has two ferro and four antiferromagnetic nearest neighbors such that there is a net antiferromagnetic unit cell.

In G-type structure, each ion is coupled antiferromagnetically to all its six nearest neighbors. Hence the atoms of positive and negative spins are arranged periodically. The other types of magnetic structures, D, E and F along with relative number of FM and AFM bonds are shown in Fig. 1.11. Some of the materials follow a structure which is a result of coupling of two types of magnetic structures. One such example is CE type, where there is coherent stacking of octants of C and E type structures. The examples of antiferromagnetic materials are MnF_2, MnO, CoO, FeO, Cr_2O_3, α-Fe_2O_3 with respective Neel temperature of 67 K, 116 K, 292 K, 116 K, 307 K and 950 K with θ_c of -80 K, -510 K, -330 K, -610 K, -485 K, -2000 K respectively[13].

Level	Cubic Octant of Magnetic Unit Cell	Relative no. of Bonds		Level	Cubic Octant of Magnetic Unit Cell	Relative no. of Bonds	
		FM	AFM			FM	AFM
A	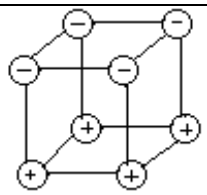	4	2	E	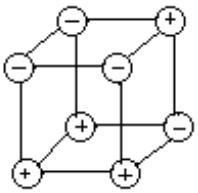	2	4
B	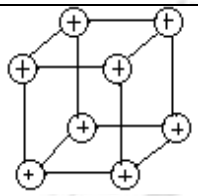	6		F	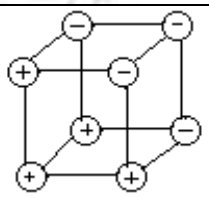	3	3
C	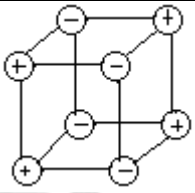	2	4	G	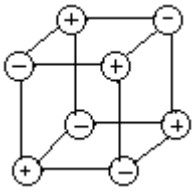		6
D	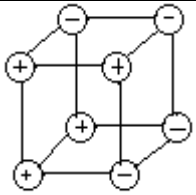	2	4				

Fig. 1.11 Different types of antiferromagnetic arrangement in a unit cell.

1.3.5 Ferrimagnetism

Ferrimagnetism is a special class of antiferromagnetism and for a long time it was mistaken for ferromagnetism. Here the magnetic moment of atoms in two sublattices A and B are not equal in magnitude. As a result, in antiparallel arrangement, there is a net non-zero magnetic moment. Ferrites are a family of ferrimagnet. Their general chemical formula is MFe_2O_4, where M is a divalent cation such as Zn^{2+}, Co^{2+}, Fe^{2+}, Ni^{2+}, Cu^{2+}, Sn^{2+}, Mn^{2+}, etc. They form spinel crystal structure, that contains two kinds of lattice sites; one is the tetrahedral site with four oxygen neighbors, and this is known as the A-site. The other one is known as the B-site or octahedral site, with six neighboring oxygen atoms. The B-sites accommodate twice the number of atoms compared to A site. In normal spinels, the M^{2+} ions occupy the A-site and Fe^{3+} ions occupy the B-site. In inverse spinels, the M^{2+} ions occupy half of the B-site. The other half of B site and the whole A-site were occupied by the Fe^{3+} ions. The atomic moments of Fe^{3+} cations in inverse spinel structure cancel each other because they equally occupy the A and B sites but opposite spin alignment. In this case, the net moment comes from the M^{2+} ions only.

The familiar example is magnetite, Fe_3O_4, where M^{2+} is Fe^{2+}. It exhibits all the hallmarks of ferromagnetic behavior such as spontaneous magnetization, Curie temperatures, hysteresis, and remanence. However, ferromagnet and ferrimagnet have very different magnetic ordering. Ferrimagnets are mostly ceramics in nature without any free electrons and this property has some practical applications. As the FM materials are mostly metallic in nature, they are not suitable for high frequency applications, where there is a presence of oscillating magnetic field. The rapidly changing magnetic field induces voltage, which results in eddy currents and heats up the metal. But by using the ferrimagnet, we can overcome such kind of problems. So they have a wide range of high frequency applications such as aerials, transformers, etc. which require high permeability and low energy loss. These ferrimagnets have corrosion resistance as they are already oxides.

1.3.6 Spin Glass Behavior

A frustrated magnetic system due to competing magnetic interactions undergoes a transition from disordered spin state to metastable frozen disordered state below a spin glass transition temperature T_g [66-70]. The frozen disordered state is known as spin glass. Here each spin is under the competing magnetic interactions with the nearest or next nearest ions. The spins cannot find a ground state by simultaneously minimizing their energy with each neighboring spins, so they are frozen in a metastable random direction to minimize the total energy. Unlike the other phase transitions, where a system undergoes transition from disordered to ordered state, here the system undergoes transition from one disordered state to another disordered state. The debate was, whether it is really a thermodynamic phase transition. More or less, it is agreed that spin glass is a phase transition because the high temperature disorder is due to random thermal fluctuations without any interaction between magnetic spins. On the other hand, the low temperature frozen disordered state is due to long range magnetic interaction of opposite signs. Conventional spin glass materials are basically the transition element doped metallic alloys known as diluted magnetic alloys, namely CuMn, AgMn, AuFe, etc. [66, 67]. The dc susceptibility of conventional spin glass materials exhibit bifurcation of zero field cooled (ZFC) and field cooled (FC) curves at T_f as reported by Nagata *et al.* [71].

Spin glass transition was reported on TM-doped DMS materials. Nagata *et al.*[72] found a spin glass behavior with T_c below T=10.9K in his work on (Hg,Mn)Te based DMS material. Also Chen *et al.* [73] found that the Fe-doped HgSe, CdS, ZnSe and ZnS group II-VI based DMS, exhibit typical spin-glass behavior. Here, the doped Fe concentration was found to be in the range 10 to 20 at %. The localized magnetic moments (resulting from localized d or f electrons) distributed randomly in nonmagnetic host lattice, are coupled by long range AFM interaction. This interaction yields frustration of magnetic moments, which is the possible reason for the observed spinglass behavior in these DMS materials. Moreover, the theoretical calculation of Marinari *et al.*[74] on II-VI based DMS suggests that a dilution beyond 80% leads to spin glass behavior. Shand *et al.* [75] studied the critical exponent corresponding to spin glass transition in II-VI based DMS and found that it obeys short range Heisenberg interaction. The critical exponent values were found to be $\gamma = 4.0\pm1.0$ and $\beta=0.8\pm0.2$[75].

1.4 Magnetic Interactions

1.4.1. Magnetic Dipole-Dipole Interaction

Magnetic dipole-dipole interaction [13] , also called dipolar coupling, refers to the direct interaction between two magnetic dipoles. The energy of the interaction is as follows:

$$H = -\frac{\mu_0}{4\pi r_{ij}^3}\left[3\left(\mu_i . \hat{r}_{ij}\right)\left(\mu_j . \hat{r}_{ij}\right) - \left(\mu_i . \mu_j\right)\right] \qquad \text{---------- (1.14)}$$

where, r_{ij} is a unit vector parallel to the line joining the centers of the two dipoles; μ_i and μ_j are the moments of two dipoles separated by a distance $|r_{ij}|$. This interaction is important in the properties of those materials, which order at milliKelvin temperature. The magnetic dipolar interaction is too weak to account for the ordering of most of the magnetic materials. There is a built in anisotropy to the dipolar interaction which can orient the spins either parallel (FM) or anti-parallel (AFM). If the spins are oriented along r_{ij}, they couple ferromagnetically and if they are oriented perpendicular to r_{ij}, they couple antiferromagnetically.

1.4.2. Direct Exchange Interaction

If the electrons of neighboring atoms interact directly to each other without any mediating ions, this is known as direct exchange. This is because the exchange interaction proceeds directly without the need for an intermediary. The direct exchange involves the overlapping of electronic wave functions of neighboring atoms and the Coulomb electrostatic repulsion. The Pauli's exclusion principle keeps the electrons with parallel spins away from each other to reduce Coulomb repulsion. So, mostly anti-parallel spin configuration is favored in direct exchange interaction. The wave functions of the magnetic 'd' or 'f' electrons decrease exponentially, thereby too small overlap of wave functions and the direct exchange interaction is very weak.

1.4.3. Superexchange Interaction

Kramer [76], Anderson and his group [77, 78] **,** Goodenough [79] and Kanamori [80] pointed out that ferromagnetic and anti-ferromagnetic interactions are possible by a mechanism called superexchange (SE) interactions. Here, two magnetic ions interact through an intermediate non-magnetic ion. This is a common interaction in insulating magnetic oxides, where the intermediate ion is O^{2-}. The basic interaction mechanism is as follows.

For example, consider two Mn^{4+} ions with an intermediate O ion. Let us discuss the case, where the unoccupied 3d orbital of Mn^{4+} ions point towards O-2p orbital as shown in Fig. 1.12(a). Due to this overlapping, the two spins of O-2p with opposite alignment likely to spend some time on the unoccupied 3d-orbitals and thus there is a simultaneous bond formation of the anion (O) with the cations (Mn^{4+}) on both sides. If the spins of the cations are anti-parallel, the positive spin of O-2p orbital forms the partial bond with the cation having positive spin and the negative spin of O-2p orbital forms the bond with the other cation having negative spin. So, there is FM coupling between electron of anion and cation and, this process leads net anti-ferromagnetic interaction between two Mn^{4+} ions as shown in Fig.1.12(a). Similar SE interaction is possible between two Mn^{3+} ions separated by O [79] . The above type of bond formation cannot occur if the spins of the cations are parallel.

According to Goodenough [79], the superexchange interaction in Mn-O-Mn network can be also ferromagnetic, if one of the Mn-O bonds is covalent, while the other Mn-O bond is ionic. Below the Curie temperature, the covalent bond becomes semi-covalence (bonding occurs between parallel spins) and the O^{2-} ion is left out with a single electron, since the other electron is associated with Mn ion in covalence bonding. There is a direct exchange interaction (AFM) between magnetic moment of anion (due to its isolate electron) and that of other Mn ion, which ionically bound to it. Thus two Mn ions are coupled FM as shown in Fig. 1.12(b).

Thus according to Goodenough, the superexchange between Mn^{3+}-O^{2-}-Mn^{3+} and Mn^{4+}-O^{2-}-$Mn^{4+}$are anti-ferromagnetic in nature, while Mn^{3+}-O^{2-}-Mn^{4+} is ferromagnetic. The superexchange interaction mainly leads to insulating behavior.

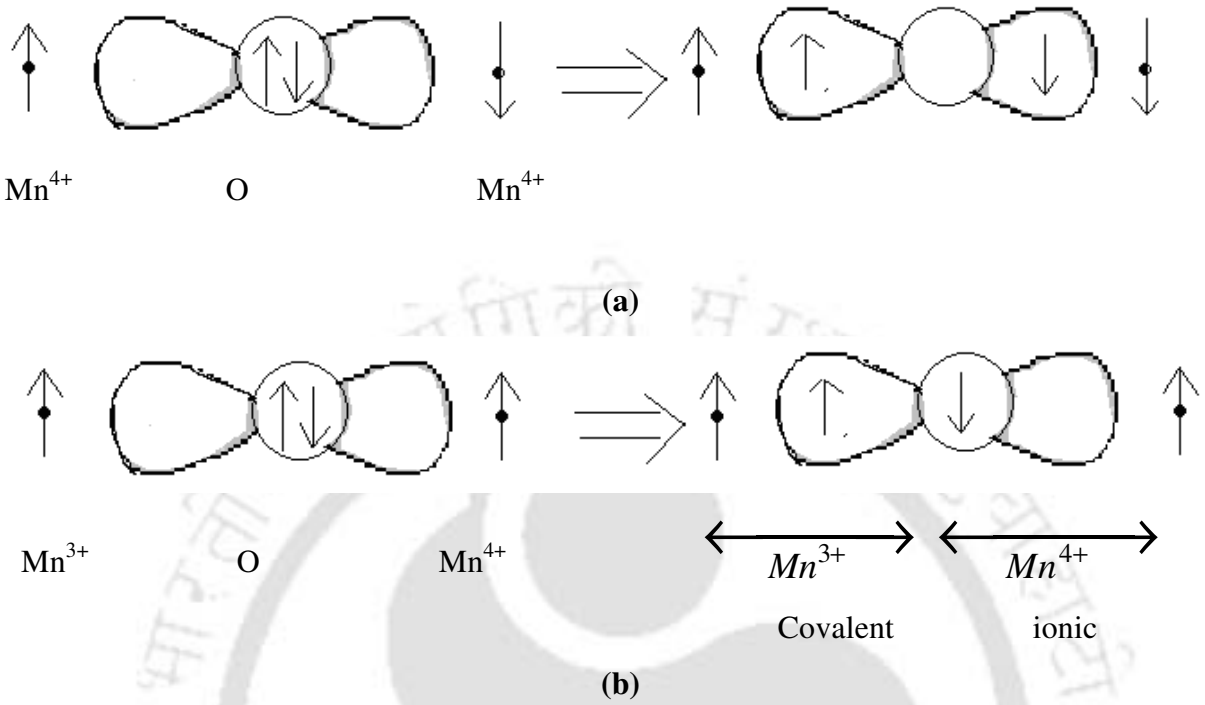

Fig.1.12 Schematic diagram showing the arrangement of spins and orbitals in **(a)** antiferromagnetic super-exchange interaction **(b)** ferromagnetic super-exchange interaction.

In many DMS materials, the SE interaction comes into picture at large concentrations of TM-ion. The First-principles study of the superexchange interaction in (Ga,Mn)*V,* (*V*=N, P, As, and Sb) by Chang *et al.* [81] reports that the short-range SE interaction is found to be AFM in nature and is found to be quite strong in (Ga,Mn)N, where as it is found to be weak in (Ga,Mn)As and (Ga,Mn)Sb. The SE interaction was found to be quite significant at large TM concentrations and it plays an important role in reducing the Curie temperature of ferromagnetic (Ga,Mn)N. The decrease in Curie temperature was attributed to the enhanced SE interaction due to Mn clustering. The lack of room temperature FM in $Ga_{1-x}Mn_xN$ is explained in terms of strong SE interaction which competes with carrier induced ferromagnetic interaction. The SE interaction mediated by anions is expected to be short range and strong between the nearest-neighbor Mn atoms.

1.4.4 RKKY Interaction

In rare earth metals, or in alloys of magnetic ions in a non-magnetic metallic host, the magnetic ions are placed too far away to interact with each other directly. Here the ferromagnetic ordering is due to the nonmagnetic conduction electron. The RKKY (Ruderman-Kittel-Kausya-Yosida) model [13, 82-84] explains the magnetic interaction between the localized single magnetic ion and the delocalized conduction electrons band. Here a localized magnetic moment spin-polarizes the conduction electrons and this polarization in turn couples to a neighboring localized magnetic moment at a distance r away. The exchange interaction is thus indirect because it does not involve direct coupling between magnetic moments. The coupling takes the form of an r-dependent exchange interaction $J_{ex}(r)$ given by

$$J_{ex}(r) = \frac{4\pi^2 m* k_F^4}{r^2} F(2k_F r) \qquad \text{---------- (1.15)}$$

m^* is the effective mass, k_F is the Fermi wave vector of the electron gas. The oscillating function is given as F(x) = $\frac{xcosx-sinx}{x^4}$ and is plotted in Fig.1.13 as a function of x.

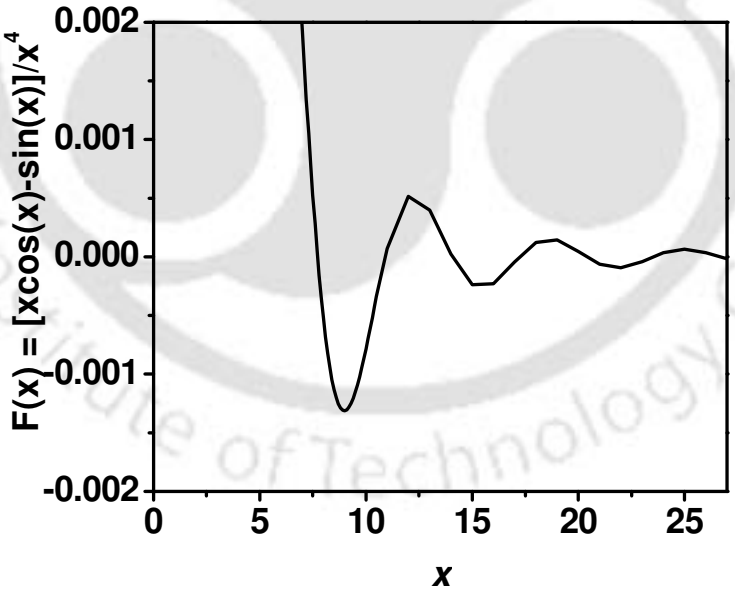

Fig. 1.13. The oscillatory part of RKKY interaction energy. F(x) is proportional to the product of the Fermi wave vector and the distance from the localized moment.

It is a long range interaction with oscillatory dependence on the distance between the magnetic ions. Hence, depending on the separation it may be either ferromagnetic or antiferromagnetic [85]. This model will be applicable in host materials having delocalized charge carriers.

RKKY interaction is also found to play a major role in many DMS materials when the solubility of carrier level is quite high [26, 31, 41]. The carrier concentration in such case is found to be quite high i.e. in the order of 10^{19} cm^{-3} to 10^{21} cm^{-3} and it correspond to about 60 at % of carrier doping in Group IV-VI based DMS [26, 31]. Evidence of magnetic phase transition from PM state to FM state with high carrier concentration has been observed experimentally. In DMS materials, doping of extra charge carriers along with magnetic ions, i.e. codoping gives rise to enhanced FM [42, 43, 86-90]. (Ga,Mn)As and (GaMn) alloys exhibit FM due to exchange interaction between Mn ions for a distance longer than the average Mn-Mn distance. In both of these alloys, exchange interactions are found to be oscillatory and are damped due to disorder. However, isolated Mn impurities in the semiconductor host with same number of valence holes exhibit un-damped RKKY type behavior [91-93].

1.4.5 Anisotropic Exchange Interaction

Anisotropic exchange interaction or magnetic anisotropy is the dependence of magnetic properties on the direction in which they are measured. The anisotropy could be intrinsic i.e. due to the sample crystal structure and could be also extrinsic, due to several factors such as shape of the sample, stress, preparation and annealing methods, plastic deformation etc. [48, 94, 95]. In general, isotropic exchange interaction is taken into account, where the exchange constant $J_{ij} = J\ (\vec{r_i} - \vec{r_j}) = J\ |(\vec{r_i} - \vec{r_j})|$, however it is valid only in highly symmetric system. In case of alloys and oxides with noncubic crystal structure, disordered and partially ordered magnets, magnetic nanostructures, and in multilayer, strong bond anisotropy was found. The bond anisotropy (exchange anisotropy) is different from that of relatively weak relativistic anisotropy. The relativistic anisotropy arises due to spin-orbit coupling and angle between magnetization and crystal axis. The examples of relativistic anisotropy are magnetocrystalline anisotropy, Dzyaloshinsky-Moriya (DM) interaction. The relativistic anisotropy contribution is quite less compared to Heisenberg contribution by a factor α^2, where α is the Sommerfeld's fine structure constant and given as $\alpha = 1/137$ [96, 97]. The magnetocrystalline anisotropy mainly arises in samples, exhibiting strong spin-orbit coupling. In order to orient the spins along the field

direction, additional energy is required to reorient the orbitals also due to strong spin-orbit coupling in some of the materials. In such case, one would expect large coercive field. However, in transition element based alloy the spin-orbit coupling is quite weak because of the strong crystal field effect and hence negligible magnetocrystalline anisotropy. The magnetocrystalline anisotropy also arises from the shape of the samples, which in turn depends on the demagnetization factor.

The DM interaction was independently developed by Dzyaloshinsky [98] and Moriya [99] in order to explain the weak FM occurring in α-Fe_2O_3, Co_3O_4, $MnCo_3$ etc. This also comes under relativistic anisotropic interaction, where the Hamiltonian is given by $H_{DM} = D_{ij}.\ S_1$ x S_2**.** Here the vector $D_{ij} = -D_{ji}$ and vanishes when the crystal field has inversion symmetry with respect to the centre between the two magnetic ions. However, in general it may not vanish and lie either parallel or perpendicular to the line connecting the two spins.

1.4.6 Double Exchange Interaction

The First principle electronic structure calculation of Sato and Yoshida [4] on tetrahedral coordinated TM-ion based DMS materials predicts that FM state was stabilized by double exchange interactions. In 1951, Zener presented a theory of indirect magnetic exchange between 3d atoms [32, 100]. Carrier electrons can hop between two ions only if the electron spins of the two ions are parallel and Zener showed that FM interactions are energetically favored when conduction electrons are present. To describe the exchange interaction between Mn^{3+} and Mn^{4+} ions via an oxygen ion, Zener introduced the concept of double exchange, i.e. simultaneous transfer of an electron from Mn^{3+} to oxygen and from the oxygen to Mn^{4+}. Two simultaneous motions are involved in this process, and so it is called double exchange (DE) interaction. The movement of electron can be shown as, $Mn^{3+}_{1\uparrow} O_{2\uparrow,3\downarrow} Mn^{4+} \rightarrow Mn^{4+} O_{1\uparrow,3\downarrow} Mn^{3+}_{2\uparrow}$, where the electron spins are labeled as 1, 2 and 3. Anderson and Hasegawa [77] presented the DE mechanism in detail by visualizing a second order process in which the electron transfer takes place as follows $Mn^{3+}_{1\uparrow} O_{2\uparrow,3\downarrow} Mn^{4+} \rightarrow Mn^{3+}_{1\uparrow} O_{3\downarrow} Mn^{3+}_{2\uparrow} \rightarrow Mn^{4+} O_{1\uparrow,3\downarrow} Mn^{3+}_{2\uparrow}$.

Double exchange is always ferromagnetic; if the spins of the d-electrons of the two manganese ions are parallel, the configurations Mn^{3+}-O^{2-}-Mn^{4+} and Mn^{4+}-O^{2-}-Mn^{3+} will be degenerated. If the manganese spins are not parallel, the electron transfer becomes more

difficult due to strong onsite Hund's coupling. The electron transfer will be more difficult if the Mn-O-Mn bonds are bent, i.e. deviated from 180°. The overlap of the manganese d-orbitals and the oxygen p-orbital is the largest and hence the interaction is strongest, where the bond angle is 180^{o}. It has been presented that, the effective hopping integral for the electron to move from one Mn site to another Mn site is proportional to the square of the hoping integral between p-oxygen and d-manganese orbitals. If the localized spins (t_{2g}, S = 3/2) are considered as classical objects and if they are canted with an angle θ between the nearest neighbor spins, the effective hopping integral would be proportional to cos(θ/2). For θ = 0, cos(θ/2) attains maximum value 1 and the hopping is maximum and, it corresponds to ferromagnetic interaction. If θ = 180^{0}, the cos(θ/2) becomes 0 and it corresponds to antiferromagnetic interaction [77].

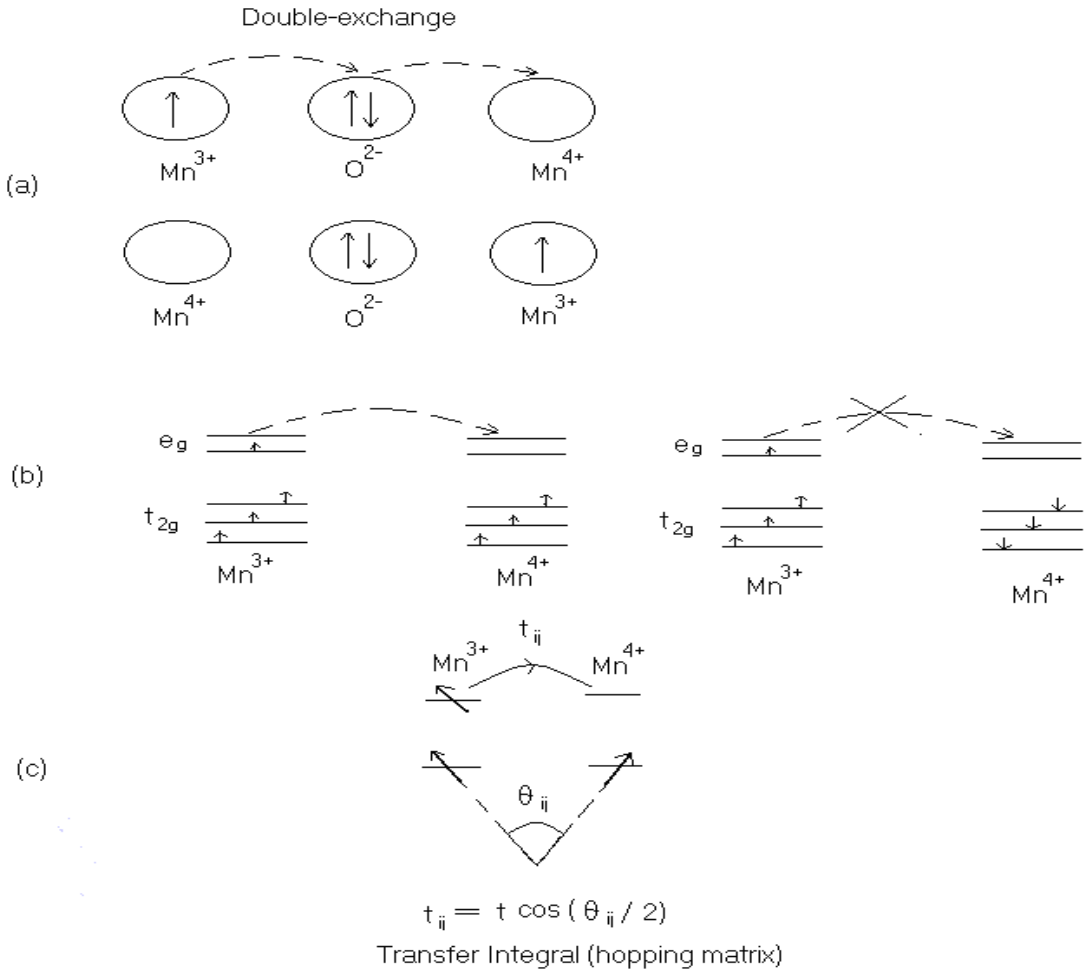

Fig. 1.14 (a) Sketch of the double exchange mechanism which involves two Mn ions and one O ion. (b) The mobility of e_g electrons is depicted for parallel alignment of localized spins. The transfer integral is shown in the Fig. (c).

Coming to the calculation done by Sato *et al*. [4], here the 3d levels of TM ions are split by crystal field into lower energy doublet e_g and higher energy triplet t_{2g} levels, as the TM ion lies in a tetrahedral environment. Again the spin-up (↑) and spin-down (↓) states are also split by exchange splitting. Here the spin-up 3d-states are lower in energy than the spin-down states. The wave functions of these t_{2g} states are extended to anions, therefore, t_{2g} states hybridize well with O-2p states which make the host valence band, so that bonding states (t_b) remain localized and anti-bonding (t_a) orbitals only contain electrons having itinerant characters, as schematically shown in Fig. 1.15(a). On the other hand, the wave functions of the e_g states are extended to the interstitial region, therefore, the hybridization of the e_g states with the host valence band is weak and e_g states remain as non-bonding localized states as shown in Fig. 1.15. If neighboring TM-ions of 2+ or 3+ states have parallel alignment of their magnetic moments, and the electrons from the partially filled t_{2g} orbital are allowed to hop from one ion to the other ion and stabilize the ferromagnetic ground state. Based on the above conditions, the 3d-orbital configuration which leads to FM or a spin glass behavior is shown in Fig. 1.16. Their results explain the observed magnetic behavior in group II-VI and III-V based DMS. But it contradicts with the observed FM in ZnO with Fe, Ni and Co. So, in the case of ZnO doped TM-ion, it is explained that the e_g state is extended well to the conduction band and so they contribute itinerant charge carriers.

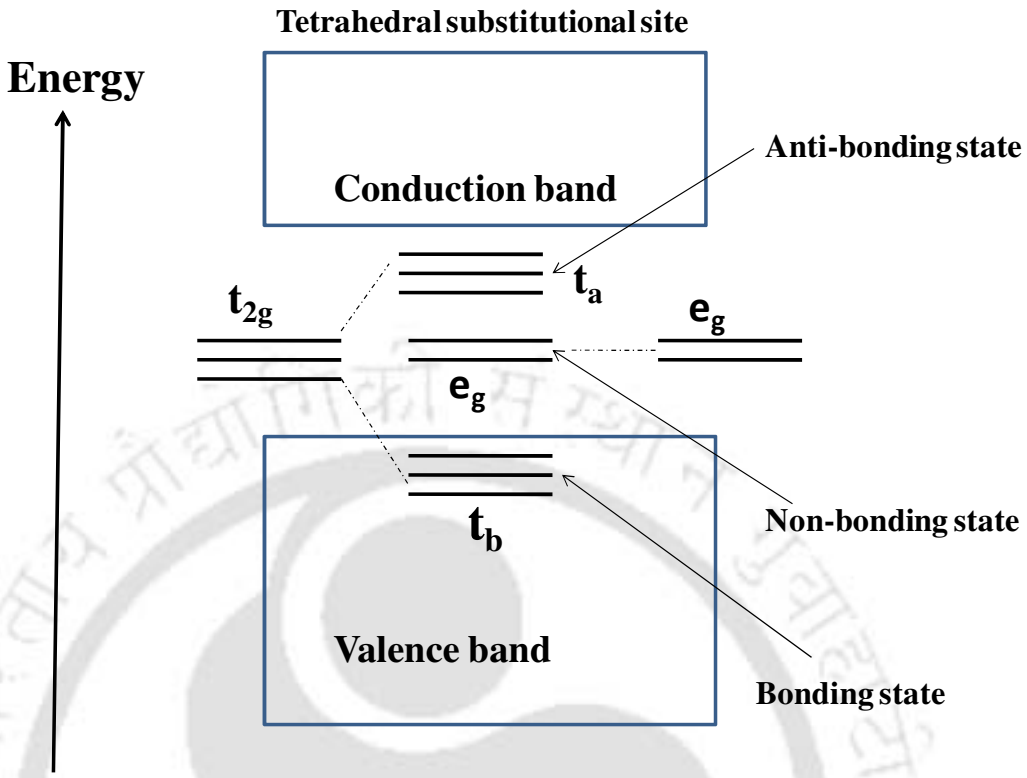

Fig. 1.15 A schematic electronic structure of TM at the tetrahedral substitutional site. The anti-bonding t_a states and non-bonding e_g-states appear in the band gap ref.[4].

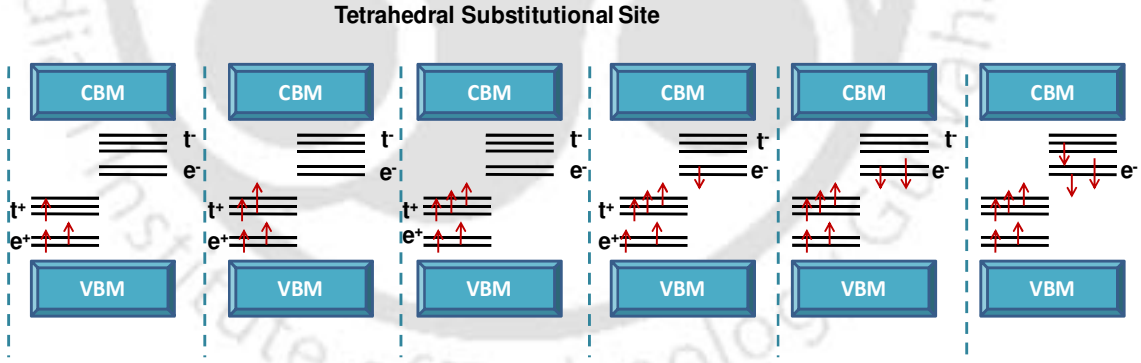

II-VI	V^{2+} ($3d^3$)	Cr^{2+} ($3d^4$)	Mn^{2+} ($3d^5$)	Fe^{2+} ($3d^6$)	Co^{2+} ($3d^7$)	Ni^{2+} ($3d^8$)
III-V	Cr^{3+} ($3d^3$)	Mn^{3+} ($3d^4$)	Fe^{3+} ($3d^5$)	Co^{3+} ($3d^6$)	Ni^{3+} ($3d^7$)	Cu^{3+} ($3d^8$)
Magnetic State	F	F	SG	SG	SG	F

Fig. 1.16 Schematic 3d orbital electronic configuration of TM-ions in presence of a tetrahedral environment. The + and – sign indicate the spin up and spin down states respectively (reproduced from ref. [4]).

1.5 Theoretical Models in DMS

Many theoretical models have been proposed in order to explain the FM ordering in DMS materials, but the complete understanding of origin of FM interactions prevailing in these DMS materials are yet to be understood. Here, some of the theoretical models most commonly used for explaining the FM in DMS materials are summarized.

1.5.1 Zener Model

The solubility limit of the dopant level is very low in Group III-V based DMS [21, 101, 102]. The observed FM in these materials was first explained by Dietl *et al.* [5] in Znic Blende $Ga_{1-x}Mn_xAs$ and their model is based on Zener's Model that was originally developed in 1950's. According to Zener model, the FM is driven by the exchange interaction between carriers and localized spins [32, 100, 103]. The Zener model explains that, direct exchange interaction between the adjacent d-shell atoms will leads to AFM in all circumstances, where as the itinerant carriers lead to FM ordering. According to Dietl *et al*.[5] the divalent magnetic ions such as Mn^{2+} in $Ga_{1-x}Mn_xAs$ provide a localized spins and at the same time act as acceptors. These Mn acceptors compensate the deep antisite donors present in GaAs and produce p-type conduction. In case of Zener model, the FM was mediated by the spin polarized conduction electrons, whereas in GaMnAs, the FM was due to the spin polarized free holes. Moreover RKKY and Zener Models lead to same value of predicted T_c in the mean field approximation [5] as long as the carrier concentration is lower than that of the localized spins. By determining, how the Ginzburg-Landau free energy F depends on magnetization, M and by minimizing the free energy with respect to M by considering F due to carriers, (F_c) and F due to localized spins, F_s. $F_c(M)$ was determined by considering the p-d exchange contributions and the spin-orbit splitting. $F_s(M)$ was determined by using the relation

$$F_s(M) = -\int_0^M dM_0 H(M_0) \qquad \ldots\ldots\ldots\ldots\ldots\ldots\ldots\ldots\ldots\ldots\ldots\ldots \qquad (1.16)$$

here $H(M_0)$ is the inverse function of experimental dependence of M_0 with H. By minimizing $F_c(M)+F_s(M)$ with respect to M at a given T and hole concentration p, they determined the FM T_c within the mean field approximation, which is valid quantitatively for long range exchange interaction.

The computed Curie temperature values for various semiconductors doped with 5 at % of Mn as shown by Dietl *et al*. [5] are reproduced in Fig.1.17. According to the above model, Mn doped GaN and ZnO are expected to be FM at RT.

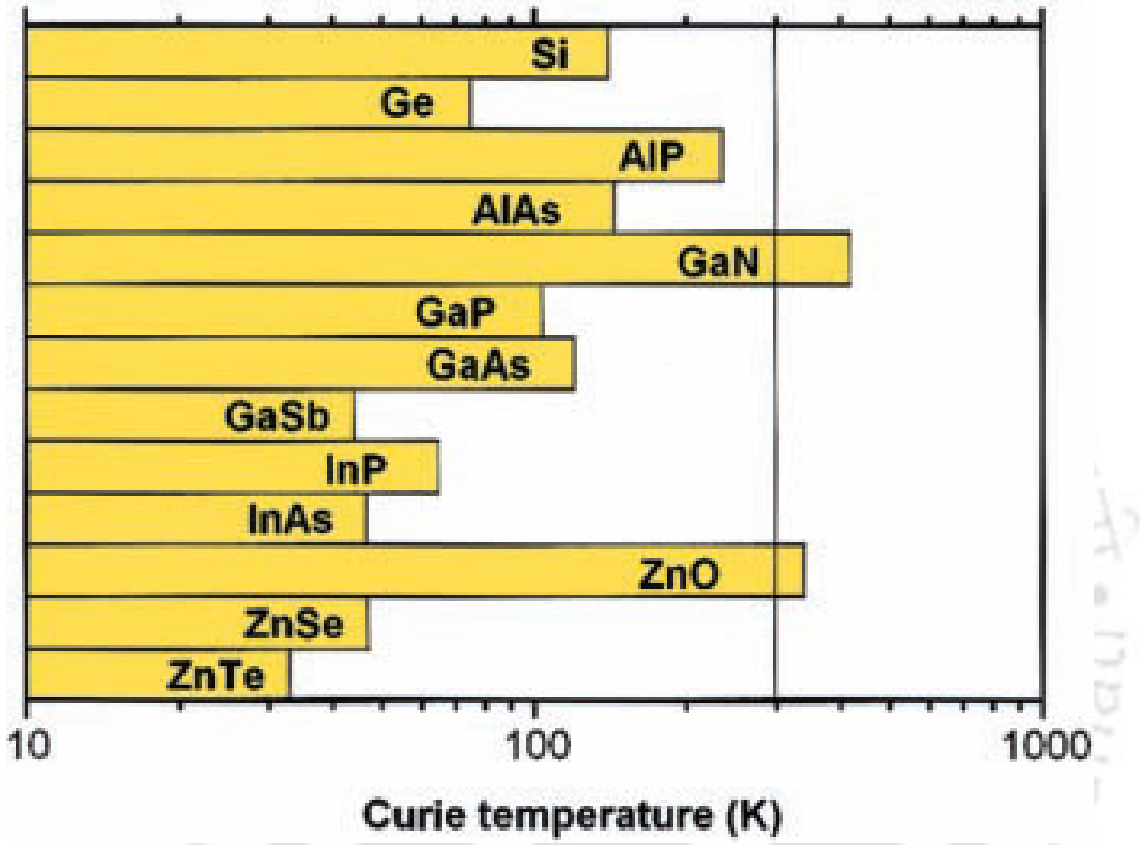

Fig.1.17 Computed T_c values for 5 at % Mn doped semiconductors (ref.[5]).

1.5.2 Bound Magnetic Polarons

The magnetic polaron in magnetic semiconductor was introduced by Kasuya *et al.* [104]. The concept of bound magnetic polaron (BMP) was introduced by Torrance *et al.* [105], while explaining the unusual electrical conductivity of EuO in the presence of magnetic impurity. According to them, the oxygen vacancies in EuO behave like shallow donors, i.e. one of the electrons is loosely bound. The electron in a large radius of molecular orbital around the oxygen vacancy interacts with the spin of localized magnetic impurity such that the magnetic spins are aligned parallel. Thus, the exchange interaction between localized carriers and magnetic ions within the carrier orbit leads to bound magnetic polaron.

Thus BMPs are entities, where the carrier spins couple to the localized spins of the magnetic elements through the exchange interactions [10, 104, 105]. BMP are produced in magnetic semiconductors by the exchange interaction between carrier spins and magnetic ion spins. At low temperatures, carriers bound to impurities align nearby magnetic ions, creating a finite local magnetization. The bound hole (electron) interacts with the spins of the magnetic ions within the sphere of Bohr orbit and tends to produce ferromagnetic alignment in those spins as shown in Fig.1.18. Thus, in a simple model, the material can be considered as an irregular assembly of ferromagnetic spheres in a matrix, which may be antiferromagnetic or paramagnetic, depending upon various conditions

The localization of these trapped (bound) charge carriers will increase their interaction with the surrounding (magnetic) environment. Due to the interaction, the magnetic spins can have a significant net FM alignment and in that case the BMP resembles a ferromagnetic bubble embedded in a PM matrix.

The ferromagnetic ordering of TM ions in DMS materials is also explained by the BMP model [6-9]. The effect of thermodynamic fluctuations on BMP was theoretically worked out by Dietl *et al.*[106]. According to them, the degree of spin alignment around the donor impurity depends not only the molecular field produced by the impurity electron but also by the thermodynamic fluctuations of magnetization.

The schematic representation of isolated polarons, polaron overlap and nearest neighbor antiferromagnetic interaction between impurity ions are shown in Fig. 1.18 by reproducing the plot reported by Coey *et al.*[35].

The observed magnetic behavior of transition element doped insulating DMS was theoretically explained by Durst *et al.*[10, 107] by BMP and interaction between polaron pairs as shown in Fig.1.19. According to their model, at low temperature, where the carrier ion exchange interaction becomes more significant, both polaron size and total intrapolaron exchange energy increase logarithmically with decrease in temperature in the range, $K^{/} << T << K$. Here $K^{/}$ is the ion-carrier exchange constant in the interstitial region (region between polaron pairs) and K is the intrapolaron ion-carrier exchange constant. At very high temperature, the spins within the system are not aligned and their model parameters yield a constant value. At high temperature, the intrapolaron ion-carrier exchange constant K is less than T ($K << T$). At very low temperatures, $T << K^{/}$, the interstitial parameters would become temperature dependent and for

reasonable carrier and ion densities, the polarons grow large enough size such that they touch each other and in such temperature region, the above model cannot be used.

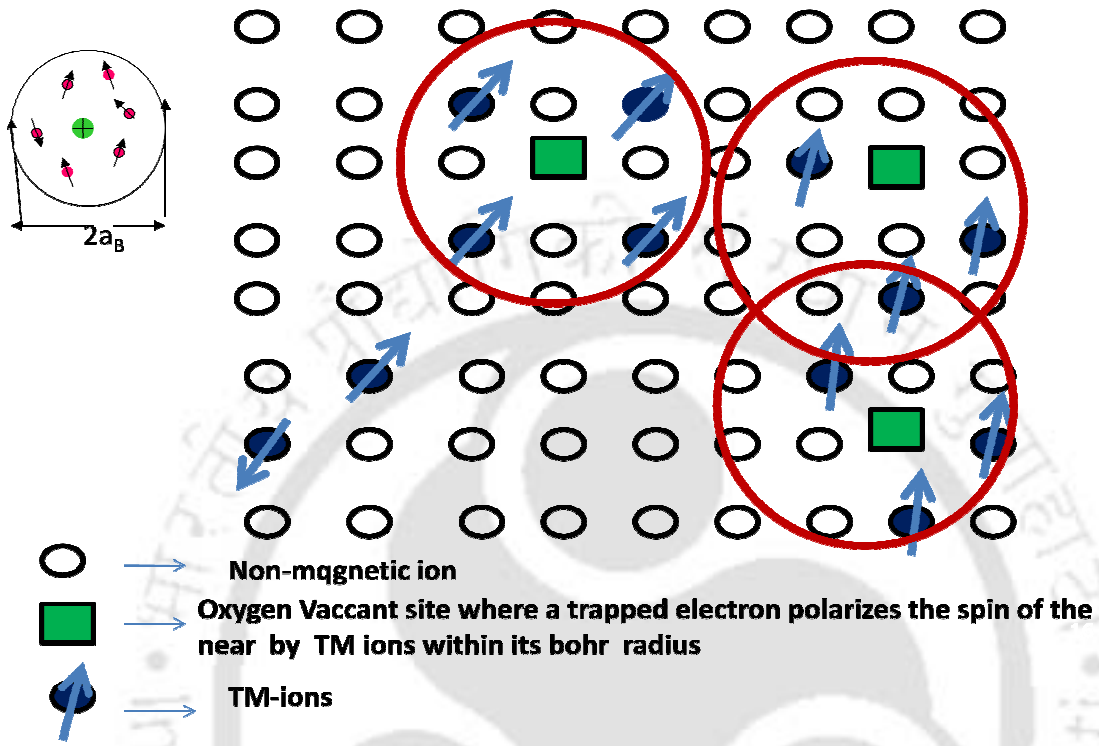

Fig.1.18 The bound magnetic polaron model. The red circle shows a single polaron of radius a_B. (following ref. [6-9])

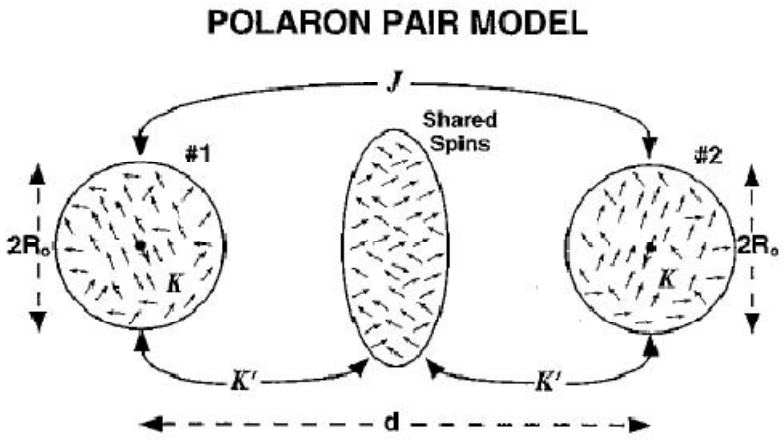

Fig.1.19 Schematic of polaron pair model as per (ref.[10]).

Kaminski and Das Sharma [44] have derived the analytical expression for FM T_c and temperature dependent magnetization of DMS by introducing polaron percolation model. They have assumed that holes (or electrons) are localized and the concentration of holes is smaller than magnetic impurity concentrations ($n_h << n_i$). The hole wave function was assumed to fall off exponentially away from the localization centers with decay length a_B. Because of low concentration of localized holes, the mean distance between localized holes is much longer than the hole localization radius. The FM T_c and the temperature at which two polarons correlate is given by,

$$T_c = sS|J_0|(a_B^3 n_h)^{1/3}\sqrt{\frac{n_i}{n_h}}exp\left(-\frac{0.86}{(a_B^3 n_h)^{\frac{1}{3}}}\right) \quad \text{----------} \quad (1.17)$$

Here s and S are spin of hole and magnetic impurity respectively. J_o is the exchange energy constant of impurity hole exchange interaction. The limit of applicability of the above equation is $a_B^3 n_h << 1$. The expression for magnetization as per polaron percolation theory is,

$$\frac{M(T)}{M(0)} = \gamma\left[0.86 + (a_B^3 n_h)^{1/3} ln\frac{T_c}{T}\right] \quad \text{----------} \quad (1.18)$$

Here the universal function γ is the infinite cluster volume in the model of overlapping spheres and it depends on the product of diameter of spheres and the cube root of their concentration. The theoretical M(T)/M(0) versus temperature curve is found to show a concave shape and is comparable to the experimental data of group III-V sample [108]. The above polaron percolation theory reduces to free carrier, Weiss molecular field theory at the limit $a_B^3 n_h$=1.

The experimental magnetization data recorded on several oxide based DMS materials are also analyzed in terms of BMP model [109-111].

McCabe *et al.* [112] analyzed the magnetization data in terms BMP model in the p-type magnetic semiconductor alloy $Cu_2Mn_{0.9}Zn_{0.1}SnS_4$. They showed that BMPs were present up to a temperature of about 60 K. According to them, the measured magnetization can be fitted to the following relation based on BMP model [112, 113].

$$M = M_0 L(x) + \chi_m H \quad \text{----------} \quad (1.19)$$

where, the first term is from BMP contribution and the second term is due to paramagnetic matrix contribution. Here $M_0 = Nm_s$, N is the number of BMPs involved and m_s is the effective spontaneous moment per BMP. $L(x) = \coth x - 1/x$ is the Langevin function with

$x = m_{eff} H /(k_B T)$, where m_{eff} is the true spontaneous moment per BMP and at higher temperature it can be approximated to $m_s = m_{eff}$. χ_m is the susceptibility of the matrix.

The magnetization data of several DMS samples could be explained in terms of BMP model [47, 109, 110, 114-117].

1.5.3 Spin Split impurity band model

The spin split impurity band model was developed by Coey *et al.* [35] in order to explain the interaction mechanism prevailing in diluted ferromagnetic oxides, that exhibit high Curie temperature and giant magnetic moment per TM-ion. The Oxide based DMS materials are known to exhibit high dielectric constant k and n-type semiconducting behavior. The conventional super-exchange interaction cannot account for the observed long range magnetic ordering, with a few percentage of the magnetic cation. Also there is no experimental evidence of presence of mixed valent TM ions such that they may lead to double exchange FM interaction. The model proposes that FM exchange is mediated by shallow donor electrons that form BMPs, which overlap to create a spin spilt impurity band.

The general formula for the oxides is,

$$(A_{1-x}M_x)\,(O\square_{\delta})_n \qquad \ldots\ldots\ldots\ldots\ldots\ldots\ldots\ldots\ldots\ldots \qquad (1.20)$$

where A is a non-magnetic cation, M is the magnetic ion, □- represents donor defect and n=1 or 2. The electron associated with a particular defect is confined within a hydrogenic orbital radius, $r_h = \varepsilon(m/m^*)a_o$, where ε is the dielectric constant, m- mass of electron, m^* effective mass of donor electron, a_o is the Bohr radius. With increase in donor concentrations, the impurity levels merge to form an impurity band. The donors tend to form a BMP, coupling the spin of 3d electrons of magnetic ions within their orbits. Such interaction can be written in terms of s-d exchange parameters $J_{sd,}$ i.e.

$$-J_{sd}\, S.s|\psi(r)|^2\Omega \qquad \ldots\ldots\ldots\ldots\ldots\ldots\ldots\ldots\ldots\ldots \qquad (1.21)$$

where S is the spin of 3d cations with volume Ω and s is the spin of donor electron.

As the density of defects $n_{\square}$ increases, the hydrogenic orbitals of donor electrons overlap and percolation occurs, when they fill 16 % space. The percolation threshold for long range FM ordering is $\gamma^3\delta=4.3$, where oxygen vacancy $\delta=n_{\square}/n_o$ (ratio of oxygen vacancy and oxygen concentrations) and γ is a constant. The Curie temperature as per molecular field approximation is,

$$T_c = \left[S(S+1)s^2 x\, n\, \frac{\delta}{3}\right]^{\frac{1}{2}} J_{sd}\, \frac{w_c}{k_B} \qquad \ldots\ldots\ldots\ldots\ldots\ldots\ldots\ldots\ldots\ldots \quad (1.22)$$

where x is the concentration of magnetic cations and it must lie below the percolation threshold, x_p to avoid antiferromagnetic interaction. Here w_c is the product of cation/anion volume ratio (~ 6%) and the oxygen packing fraction f_o, (~ 0.74). As per eq. 1.22, the Curie temperature for substituted ZnO, can be written as $T_c = 0.04[S(S+1)\delta x]^{\frac{1}{2}} \frac{J_{sd}}{k_B}$ and it is found to be 18 K[11]. However, the experimental T_c values are above the room temperature.

The only option to boost the theoretical T_c is to increase the donor concentration in the vicinity of magnetic impurity, i.e. to the level of 1 to 2 % electrons from the donor states to each magnetic ion. The electron transfer effect can be represented by introducing a factor $\left(\frac{r_c^{eff}}{r_o}\right)$in eq. 1.22 for T_c, i.e.

$$T_c = [(S+1)s^2 x\ \delta/3n]^{\frac{1}{2}} J_{sd} f_o \left(\frac{r_c^{eff}}{r_o}\right)^3 . \frac{1}{k_B} \qquad \ldots\ldots\ldots\ldots\ldots\ldots\ldots\ldots\ldots\ldots \quad (1.22)$$

The electronic structure required for high Curie temperature along with the electronic structure for low Curie temperature is shown in Fig. 1.20. High Curie temperature is expected whenever unoccupied 3d states overlap with impurity band. For light 3d elements such as Ti and V, 3d↑ states lie high within 2p(O)- 4s(Zn) gap, and overlapping the spin split donor impurity band, as shown in Fig.1.20(a). In the middle of the series, i.e. for TM = Mn, there is no overlap of 3d levels with spin split impurity band and the exchange interaction is weak as shown in Fig. 1.20(b). Towards the end of the series, the 3d↓ levels overlap with impurity band giving rise to high T_c, i.e. for TM = Co.

Thus the spin-split impurity band model explains the high T_c observed in TM doped oxide semiconductors [39, 118, 119].

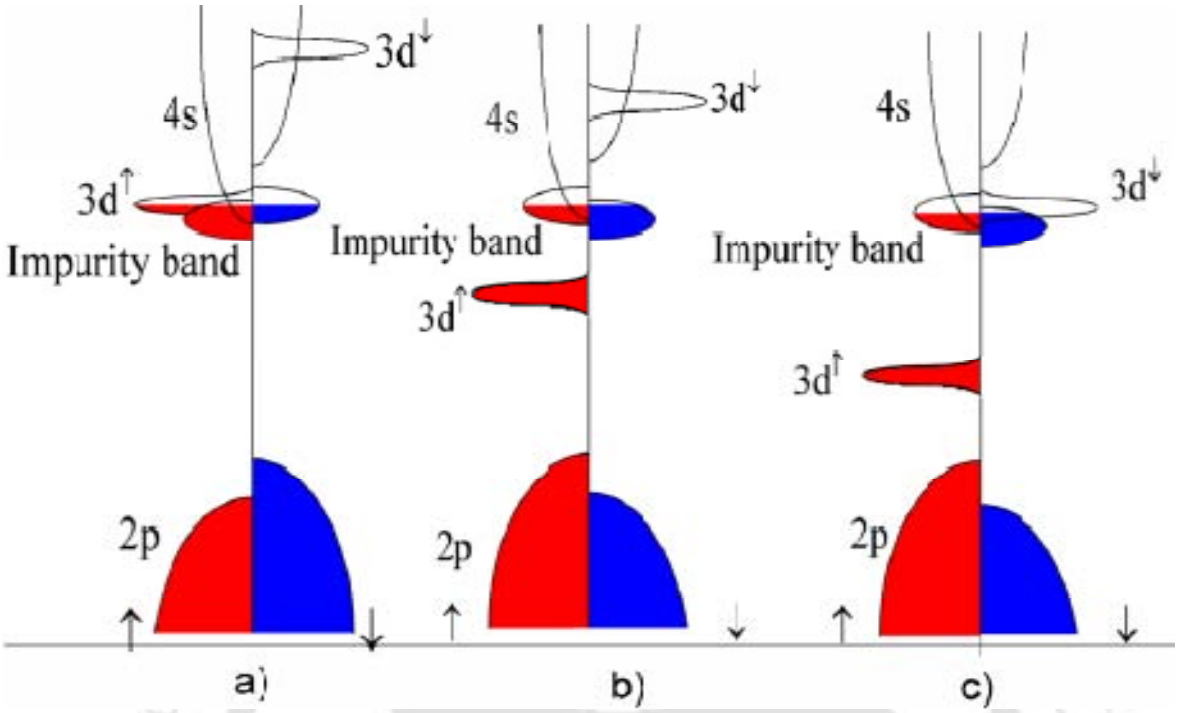

Fig.1.20 Schematic diagram of electronic structure of TM doped oxide semiconductor for (a) M = Ti, (b) M = Mn, and (c) M = Co. (reproduced from ref.[11]).

1.6 Critical Exponents in Magnetic Transition

The study of critical phenomena in the second order magnetic phase transition, i.e., close to FM T_C in amorphous and crystalline ferromagnets has been the field of interest for a long time to understand the type of magnetic interactions. The famous Landau theory for the second order magnetic phase transition assumed that the Gibb's free energy is a function of the order parameter and temperature dependent coefficients [120]. The Gibb's free energy G is written in terms of powers of order parameter. The magnetization M is taken as the order parameter. The expression for G as per Landau theory is given as,

$$G(T,M) = G_0 - MH + aM^2 + bM^4 + \cdots \quad \text{----------(1.23)}$$

Here, the coefficients a and b are temperature dependent parameters. The condition for minimum free energy in isothermal system, without any external influence can be written as ($\partial G/\partial M = 0$), and it gives rise,

$$\frac{H}{M} = 2a + 4bM^2 \quad \text{----------(1.24)}$$

According to eq. 1.24, a plot of M^2 versus H/M should be a straight line with a positive slope [121]. So, for a second order magnetic phase transition, the plot of M^2 versus H/M is expected to be a straight line, with a positive slope [122]. The spontaneous magnetization, $M_s(0, T)$, the inverse susceptibility, $\chi_0^{-1}(T)$ and the isothermal magnetization at the critical temperature $M(H, T=T_C)$ follow the power law behavior as given below [120],

$$M_S(T) \propto |\varepsilon|^{\beta} \qquad \varepsilon < 0 \qquad \text{----------(1.25)}$$

$$\chi_0^{-1}(T) \propto |\varepsilon|^{\gamma} \qquad \varepsilon > 0 \qquad \text{----------(1.26)}$$

$$M(H, T = T_C) \propto H^{\frac{1}{\delta}} \qquad \varepsilon = 0 \qquad \text{----------(1.27)}$$

Here β, γ and δ are critical exponents corresponding to M_S, χ_0 and isothermal magnetization at T_C and $\varepsilon = (T-T_C)/T_C$ is the reduced temperature. According to Arrott and Noakes [123], the mean-field relation (eq.1.24) can be modified for a more general case as given below,

$$\left(\frac{H}{M}\right)^{1/\gamma} = \frac{(T - T_C)}{T_1} + \left(\frac{M}{M_1}\right)^{1/\beta} \qquad \text{----------(1.28)}$$

where, T_1 and M_1 are material dependent constants. For the critical exponent values corresponding to the mean-field model, i.e., $\beta = 0.5$ and $\gamma = 1$, eq. (1.28) reduces to eq. (1.24). In the mean-field model (or molecular field model), the magnetic spins interact with one another through a molecular field proportional to the average magnetization. Here, the exchange interaction, J_{ij} between all the spins S_i and S_j is identical and independent of displacement. This model is appropriate, whenever the interaction is in long range. Chamberlin [124] has proposed the mean-field cluster model to explain the existence of long range interaction in different substances.

For high magnetic anisotropic materials, the critical exponents generally follow the Ising model. This model deals with only one component of the spins. In highly anisotropic materials, a stronger magnetic coupling is seen in one of the components of spin compared to other two components. The γ value corresponding to three dimensional Ising model is 1.25.

Heisenberg model is an isotropic model, where all components of spins play equal role in magnetic interactions. The magnetic interaction energy between spins S_i and S_j of atoms present at nearest neighboring positions i and j can be written as $U = -2 J S_i . S_j$, where, J is the exchange integral and is related to the overlap of the charge distributions of the atoms i, j. Such interaction takes place mostly with nearest neighbor magnetic ions and known as short range interaction.

The list of critical exponents γ, β and δ predicted by different theoretical models are given as follows.

3-D Heisenberg model	$\gamma = 1.336$,	$\beta = 0.365$	$\delta = 4.80$
3-D XY model	$\gamma = 1.30$,	$\beta = 0.34$	$\delta = 4.80$
3-D Ising model	$\gamma = 1.241$,	$\beta = 0.325$	$\delta = 4.82$
Mean-field model	$\gamma = 1.00$,	$\beta = 0.50$	$\delta = 3.0$
Tricritical mean-field	$\gamma = 1.00$,	$\beta = 0.25$	$\delta = 5.0$

The above critical exponents are related to each other by the Widom scaling relation [125], $\delta = 1 + \gamma/\beta$ and follow the static scaling hypothesis.

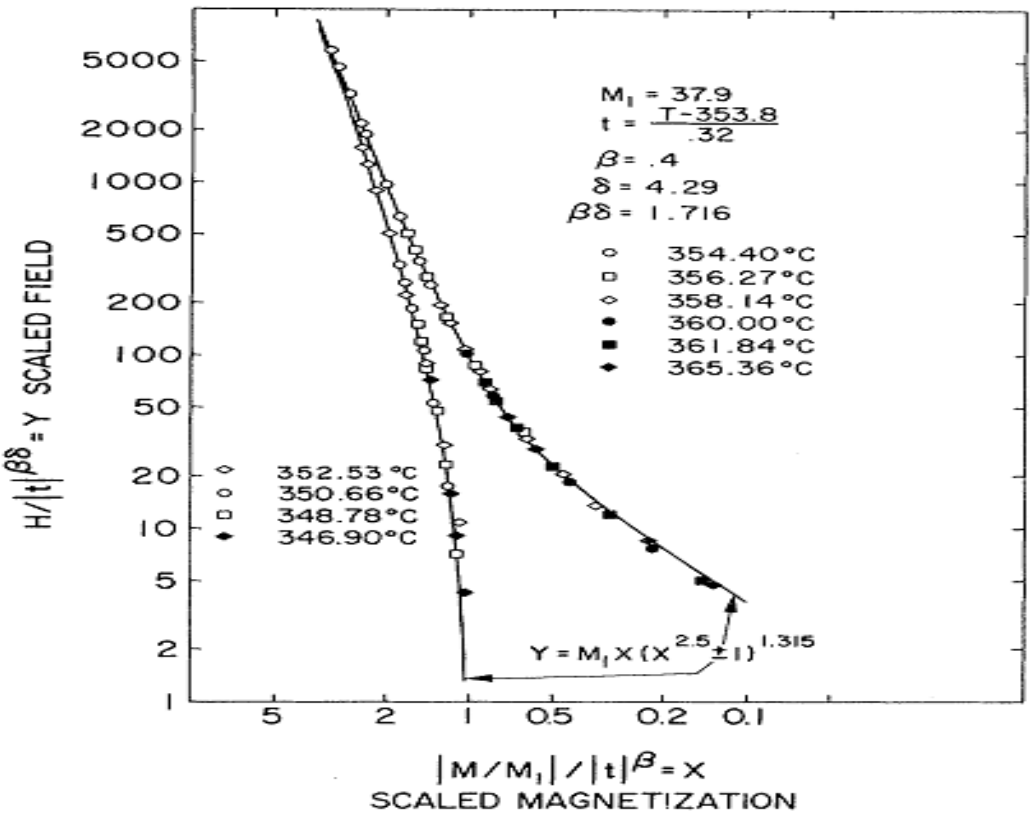

Fig.1.21: Scaling law for nickel sample using the data of Weiss and Forrer. The left side and right side curves correspond to $T < T_C$ and $T > T_C$ respectively. 't' denotes the reduced temperature $\varepsilon = (T - T_C)/T_C$ and M_1 is a constant. (Reproduced from Green *et al.* [12]

The static scaling hypothesis predicts that $M(H, \varepsilon)$ is an universal function of ε and H as given below,

$$M(H,\varepsilon)|\varepsilon|^{-\beta} = f_{\pm}\left(H|\varepsilon|^{-(\beta+\gamma)}\right) \quad \text{---------- (1.29)}$$

where, f_+ and f_- are regular analytical functions for $\varepsilon > 0$ and $\varepsilon < 0$, respectively. According to eq. (1.29), plots of $M(H, \varepsilon)|\varepsilon|^{-\beta}$ versus $H|\varepsilon|^{-(\beta+\gamma)}$ would lead to universal curves, one for temperatures $T > T_C$ $(\varepsilon > 0)$ and the other for $T < T_C$ $(\varepsilon < 0)$. A typical scaling hypothesis plot for Ni sample reported by Green *et al.*[12] from the experimental data of Weiss and Forrer [126] is shown in Fig.1.21. They used the exponent values of $\beta = 0.4$, $\gamma = 1.315$ with Curie temperature $T_C = 353.8$ °C.

To exclude the possibility of error in T_c obscuring the critical exponents, the χ_o data could be analyzed independently in terms of Kouvel-Fisher method [127] and according to that, the expression for susceptibility can be written in the following form

$$\chi_o^{-1}\left[\frac{d\chi_o^{-1}}{dT}\right]^{-1} = \frac{T-T_c}{\gamma} \quad \text{---------- (1.30)}$$

So, the plot of $\chi_o^{-1}\left[\frac{d\chi_o^{-1}}{dT}\right]^{-1}$ versus T is expected to exhibit a liner behavior with a slope $1/\gamma$ and the intercept in the T axis equal to T_c. Thus T_c and γ can be determined simultaneously.

Critical exponent analysis has been reported in many metallic alloys, metals and spinels such as Cu-Ni, Co-Ni, Fe-Ni, $Fe_{84}B_{16}$, FeZr, Fe, Co and Ni metal and also in ferrites such as Fe_3O_4, $TiFe_2O_4$, $MnFe_2O_4$ etc.[128-132]. Critical exponent analysis have carried out by Hiroyoshi *et al.* [129] in Ni and other metallic alloys. They have shown the linear behavior of $M^{2.5}$ vs $(H/M)^{0.75}$ for all the metallic and alloyed samples and it signifies that the type of interactions are same for all the FM alloys. The observed critical exponents were comparable to Heisenberg Model. Flores *et al.*[132] studied the phase transition in $Ti_{0.2}Fe_{2.8}O_4$ based ferrite samples by using Arrott plots and Kouvel-Fisher method and, the magnetic interaction was found to be short range Heisenberg type. The reported values of critical exponents on various perovskite colossal magneto-resistance materials have been found to be disparate with values corresponding to both long range and short range FM interactions. Motome *et al.* [133] estimated the value of β from the Monte-Carlo simulation and predicted that the above class of materials follow three dimensional (3D) Heisenberg model. Lofland *et al.* [134] and a few other research groups [135, 136] have observed long range interactions in (La, Sr)MnO_3 system, with estimated critical exponent values following the mean-field model. On the other hand, FM transitions in Sr, Ba and

Ag substituted La-Mn-O compounds have been found to follow either 3D Heisenberg [137-139] or 3D Ising [140] model. Venkatesh *et al.* [141] extracted the critical exponents from magnetization, ac susceptibility, resistivity and specific heat measurements on $Nd_{0.5}Sr_{0.5}MnO_3$ single crystalline sample. They reported that, the exponent values were all between mean-field and 3d-Heisenberg models.

Critical behavior of DMS materials such as $Ga_{1-x}Mn_xAs$ was studied theoretically by Priour *et al.*[142] using the large scale Monte Carlo calculation. They have modeled the magnetic transition in DMS materials in terms of strongly disordered Heisenberg model in 3D lattice. In the presence of strong disorder, there could be an apparent change in critical behavior especially at relatively large ε value. In such case, the expression for χ can be written by taking into account the correction to scaling as follows [142]

$$\chi = \chi_o (\varepsilon^{-\gamma} + B\ \varepsilon^{y_1} + C\varepsilon^{y_2} + \cdots) \quad \text{----------} \quad (1.31)$$

Where γ is the genuine critical exponent for χ_o and, y_1 and y_2 are the exponents for correction in the scaling relation. The effective critical exponent, γ_{eff} can be written as

$$\gamma_{eff}(\varepsilon) = \frac{\varepsilon}{\chi_o}\frac{d\chi_o}{dT} = \gamma\left[\frac{1+By_1\varepsilon^{y_1+\gamma}+Cy_2\varepsilon^{y_2+\gamma}}{1+B\varepsilon^{y_1+\gamma}+C\varepsilon^{y_2+\gamma}}\right] \quad \text{----------} \quad (1.32)$$

At $\varepsilon \to 0$, $\gamma_{eff} \to \gamma$, the genuine critical exponent of χ_o.

Fukuma *et al.*[143] studied the critical exponents behavior in $Ge_{1-x}Mn_xTe$ based DMS materials. The obtained parameters deduced from Modified Arrott plots and scaling behavior were found to be in good agreement with the theoretically predicted mean field model. However the values of critical exponents corresponding to (Cd,Mn)Sb and (Cd,Mn)Te [144, 145] show the nearest neighbor Heisenberg interaction.

1.7 Electrical Resistivity of Semiconductors

Electrical resistivity is a measure of the ability of a given material to oppose the flow of electric current. According to quantum mechanical treatment, the energy of an electron in an atom cannot take any arbitrary value and the energy states are quantized by specific energy values given by $E \approx \left(\frac{-13.6Z^2}{n^2}\right)$eV. Here n is a positive integer known as principal quantum number, and Z stands for atomic number. Conglomeration of such discrete energy levels results in an energy band. There can be many such energy bands in a material, depending on the atomic number and electron distribution. According to the band theory, the energy levels of semiconductors can be grouped into two bands, the valence band and the conduction band. For an electron to jump from the valence band to the conduction band, it requires a specific minimum amount of energy and the required energy varies depending on different materials. Electrons can gain enough energy to jump to the conduction band by absorbing either a phonon (heat) or a photon (light). In case of intrinsic semiconductors, the Fermi level lies in between the conduction band minimum and valence band maximum. Since the conduction band lies above the Fermi level, at 0 K, when no thermal excitations are available, the conduction band remains unoccupied. So conduction is not possible at 0K, and resistance is infinite. As temperature increases, occupancy of the conduction band goes up, thereby resulting in decrease of electrical resistance of the semiconductor. The temperature dependence of resistance follows an exponential relation, $R = R_0 e^{-\alpha/T}$. Here, R is the resistance of the material, $\alpha = E_{gap}/2k_B$, where E_{gap} is the bandgap energy and k_B is the Boltzmann constant. The resistivity is given by $\rho = R.A/l$, where A is the area of cross-section and l is the length of the sample.

Depending on the nature of hopping of the itinerant charge carriers, different models have been formulated in literature and are summarized below.

If the range of association of charge carriers to crystalline distortion is less than the size of the unit cell, they are called small polarons. In this case, the charge carriers are always found at the lattice site. The temperature variation of resistivity above as per small polaron model[146] is,

$$\rho = \rho_{sp} T^n \exp\left(\frac{E_{sp}}{k_B T}\right) \qquad \text{---------- (1.33)}$$

Here, E_{sp} is the hopping energy, T is the temperature. $n = 1$ corresponds to adiabatic small polaron hopping and $n = 3/2$ corresponds to non-adiabatic small polaron hopping. According to

adiabatic small polaron hopping, the charge carriers hop more rapidly and each time the carrier hops, the configuration of vibrating atoms in the adjacent site coincides with that of occupied state. In non-adiabatic case, the motion of small polaron is quite slow.

According to three dimensional Mott variable range hopping (Mott-VRH) model, the expression for electrical resistivity can be written as, [147, 148],

$$\rho = \rho_{0m} \exp\left(\frac{T_{0m}}{T}\right)^{1/4} \quad \text{---------- (1.34)}$$

Here, ρ_{0m} is the Mott residual resistivity and T_{0m} is the Mott characteristic temperature. The density of states in the vicinity of Fermi level, $N(E_F)$ and, hopping distance $R_{hop}(T)$ and hopping energy, $E_{hop}(T)$ can be written as,

$$N(E_F) = \frac{18}{k_B T_{0m} a^3} \quad \text{---------- (1.35)}$$

$$R_{hop}(T) = \frac{3}{8} a \left(\frac{T_{0m}}{T}\right)^{1/4} \quad \text{---------- (1.36)}$$

$$E_{hop}(T) = \frac{1}{4} k_B T^{3/4} T_{0m}^{1/4} \quad \text{---------- (1.37)}$$

Here a is the localization length. According to VRH model, the charge carriers hop from one localized state to another localized state having overlapping electron wave function. The energy required for such hopping is taken from phonon (lattice vibration). Efros and Skhlovskii (ES) [149] have modified the Mott-VRH model by taking into account the coulomb interaction between the charge carriers and the corresponding resistivity expression is,

$$\rho = \rho_{0s} \exp\left(\frac{T_{0s}}{T}\right)^{1/2} \quad \text{---------- (1.38)}$$

where, ρ_{0s} is the ES residual resistivity and T_{0s}, the ES characteristic temperature is defined as,

$$T_{0s} = \frac{\beta_1 e^2}{k_B a 4\pi\varepsilon_0\varepsilon_r} \quad \text{---------- (1.39)}$$

Here a is the localization length, ε_r is the dielectric constant and β_1 = 2.8 is a numerical constant.

Chou *et al.* [150] carried out the resistivity measurement in ZnO:Co based DMS materials. They prepared a series of Co doped ZnO thin films, under different atmosphere and annealing

conditions. Especially in order to introduce vacancy in the samples the films were grown in Ar atmosphere and annealed in vacuum. The resistivity data were analyzed based on the combination of both thermal excitation model and the Mott-VRH model.

The total conductivity, $\sigma(T)$ can be written as

$$\sigma(T) = A\ exp[-(C/T)^{1/4}] + B\ exp\ (-E_d/k_BT) \text{----------} \quad (1.40)$$

Here A and B are constants, E_d is the activation energy and C is a constant associated with the localized radius and hopping radius around localized states.

The thermal excitation term in eq. 1.40 describes about the thermal energy required by the localized charge carrier to overcome the bandgap and to reach the conduction band. They found that as the oxygen vacancy was increased in the system, the carrier concentration increases, which in turn decrease the activation energy.

Prathiba *et al*.[151] studied the transport properties in $SrSn_{0.9}Sb_{0.05}Fe_{0.05}O_3$ based oxide DMS and the obtained electrical conductivity could be well analyzed based on the Mott-VRH model. The localized radii of localized carriers (r_{VRH}) are found to be of the order of 2.32nm and it was found to be larger than the BMP radius which is of the order of 0.49nm. They suggested a concentric bounded model, where a larger VRH sphere surrounds the smaller BMP sphere[151, 152]. The long range FM ordering and electrical conduction in these oxide based DMS, evolves as a function of defect concentrations.

1.8 Experimental Work on Oxide based DMS

As discussed briefly in the beginning of this chapter, diluted magnetic semiconductors based on alloys such as, Group III-V, Group II-VI, etc. did not yield Curie temperature above room temperature, and the maximum T_c of 110 K was obtained in $Ga_{1-x}Mn_xAs$. Following the prediction of room temperature FM in Mn doped ZnO by Dietl *et al.*[5], there are several reports on the DMS based on oxide semiconductors. In this section, the experimental works carried out on ZnO, TiO_2 and SnO_2 based DMS are reviewed.

ZnO based DMS:

ZnO is one of the well known semiconductors with a wide band gap of 3.4eV. It forms in Wurtzite crystal structure with hexagonal symmetry, where each Zn atom is surrounded by four oxygen atoms in tetrahedral coordination[153]. ZnO has been the focus of research because of its applications such as light emitters, transparent conductor in electronic circuits, piezo electric transducer and window materials for display and solar cells[154, 155]. TM doped ZnO has been investigated to achieve room temperature FM and application towards spintronics [156-162]. Based on first principles calculations, Sato and Yoshida [163] showed that $Zn_{1-x}TM_xO$ compounds exhibit ferromagnetic ordering without any additional carrier doping for TM = V, Cr, Fe, Co and Ni. For TM = Ti and Cu, it results in paramagnetic state. Following the above reports, room temperature FM has been reported by several authors by doping the transition elements such as Ti [11, 35], V[118, 164, 165], Cr [11, 156, 164, 166], Mn [38, 86, 153, 167-173], Fe [111, 174-176], Co[11, 35, 42, 47, 177-189] etc.

Fukumura *et al.* [190] studied the Mn doped ZnO prepared by pulsed laser deposition technique on polished C-plane sapphire substrate. The substrate temperature was maintained at 600^{o}C and the oxygen partial pressure of 10^{-5} Torr. From magnetization measurement, they have observed a spin glass behavior with a freezing temperature of 13 K and with a strong AFM behavior. The solubility limit of Mn was reported to be up to 35 % due to the variation of thin film growth technique [165, 190-194]. The magnetic moment per Mn ion and the FM T_c were found to decrease with increase in Mn concentration [86, 153, 194, 195]. For example, by increasing Mn concentration from 2.2 to 30%, the magnetic moment per Mn atom was found to fall from 4.8μ_B to 0.02μ_B [193].The FM T_c was found to be above room temperature for Mn

concentration within 5 % [86, 153] and generally well below 100 K for higher concentration [194]. Bulk samples of Mn doped ZnO were studied by several authors and reported room temperature FM [196-198]. Theodoropoulou *et al.*[199] reported FM with T_c~ 250 K in Mn implanted (3%) single crystal sample of Sn doped ZnO. Mn (2 at %) doped ZnO sintered at temperature T < 700^{o}C was reported to exhibit FM with T_c > 420 K and M_s = 0.16 μ_B [37]. The strength of FM interaction was found to reduce with increase in Mn concentration. In contrast to the above report, a few authors have reported dominant AFM ground state in Mn doped ZnO samples [200, 201].

The first report of Co-doped ZnO thin film was from Ueda *et al.*[156], where they have reported room temperature FM for x = 0.05 to 0.25 in $Zn_{1-x}Co_xO_2$. Their x = 0.05 and x = 0.15 samples showed M_s values of 1.8 and 2.0μ_B with carrier concentrations $1.2x10^{18}$ and $2.9x10^{20}$ cm^{-3} respectively. The M_s and T_c values were found to increase with increase in doping concentration. The Co doped ZnO was studied by several authors [11, 182, 200, 202] and the stronger room temperature FM with magnetic moment per Co ion in the range of 1 to 6 μ_B/Co-ion were reported for Co concentration in the range of 3 to 5 at %. Giant magnetic moment of 5.9 μ_B/Co-ion and 2.6 μ_B/Co-ion were reported on 3 at % and 5 at % Co doped ZnO and these values are quite high even compared to M_s value of bulk Co metal, i.e. 1.7 μ_B/Co-ion[182, 203]. A giant magnetic moment of 6.1 μ_B/Co-ion with a high Curie temperature of 790 K was reported by Song et al.[47] on Co doped ZnO deposited on dielectric $LiNbO_3$. Due to the insulating nature of the sample, it was suggested that the magnetic coupling is not due to any carrier mediated exchange interaction but rather due to a super cooling mechanism based on bound magnetic polarons as result of magnetoelectric coupling between the substrate and $Zn_{1-x}Co_xO$ thin film.

Bulk polycrystalline samples of $Zn_{1-x}Co_xO$ for x = 0 to 0.15 were studied by Risbud *et al.*[89] and found that these materials exhibit nearest neighbor AFM interaction. Based on density functional calculation, they have suggested that the FM can occur only in the presence of additional hole doping. Liu *et al.*[90] reported that the FM coupling in Co:ZnO is induced through charge transfer between Co-3d and donor defect and it depends on the electron localization of oxygen defect. The distance between the Co atoms and oxygen vacancy plays important role in mediating FM coupling and is realized when the distance between Co atom and oxygen vacancy is less than 5Å. AFM coupling would be dominant, when the distance is larger than 5Å.

In addition to Mn and Co doping, other TM ions in ZnO was studied by several authors in thin film and bulk form [116, 204-207].

TiO_2 based DMS

TiO_2 is one of the interesting wide band gap semiconductors and occurs in different forms such as rutile, anatase and Brookite. Rutile is tetragonal with lattice parameters a = b = 4.59Å and c = 2.96Å with a band gap of 3.6eV and anatase phase also crystallizes in a tetragonal structure with lattice parameters a = b = 3.78Å and c = 9.52Å and, bandgap of 3.2eV [208].

The room temperature FM in Co doped TiO_2 thin film was first reported by Matsumoto et al.[33] for Co concentration up to 8 at %. They have used $LaAlO_3$ (001) and $SrTiO_3$ (001) substrates at oxygen partial pressure of 10^{-6} to 10^{-5} Torr and temperature of 680-720^oC. The M_s value was reported to be 0.32μ_B/Co-ion and the observed low M_s value was explained in terms of low spin state of Co. The resistivity and carrier concentration were 0.1-1 Ω-cm and 10^{18} cm^{-3} respectively. Following the above discovery, there are several reports on Co-doped TiO_2 by using various type of substrates, oxygen partial pressure and substrate temperature [34, 209-215]. Shinde *et al*.[209] reported FM T_c close to 650 K in Co:TiO_2 under low doped regime and explained that it is due to intrinsic DMS effect. FM T_c up to 400 K was reported by several other authors in Co:TiO_2 [33, 34, 209, 213]. The highest M_s value of 1.7μ_B/Co-ion was measured by Stampe *et al*.[211] in 7 at % Co doped sample on $LaAlO_3$ substrate. The M_s values in the range of 0.94μ_B/Co-ion to 1.4 μ_B/Co-ion were reported by several authors [33, 34, 209, 215].

Other transition element doping such as V, Cr, Fe, Ni in TiO_2 have been carried out by several authors. The solubility limit of Cr was found to be 16 at % [216-218] and its M_s value was found to vary from 2.9 μ_B/Cr-ion to 0.9 μ_B/Cr-ion with increase in Cr concentration from 0.06 to 0.12%. The Fe doping in TiO_2 was found to yield M_s value ranging from 0.14 μ_B/Fe-ion to 2.4 μ_B/Fe-ion [219-221]. Xiaoyan *et al*.[222] reported that ball milled α-Fe doped TiO_2 exhibits FM with T_c = 650 K and M_s = 0.15μ_B/Fe-ion. The observed FM was found to be an intrinsic property. Duhalde *et al*.[223] found RT FM in Cu doped TiO_2 where the observed FM was explained based on the formation of oxygen defects near the Cu ion.

SnO_2 based DMS:

SnO_2 is the first transparent semiconductor that was commercialized extensively. Extensive literature exists on preparation and electrical and optical properties of single crystal SnO_2 [224-227]. Under optimum condition of deposition, SnO_2 films are generally polycrystalline with grain size 200-300Å and retain tetragonal rutile structure of bulk SnO_2. It exhibits n-type conductivity and it is mainly due to non-stoichiometry. SnO_2 films are degenerate semiconductors with typical carrier concentrations N~10^{19}-10^{20} cm^{-3}, a mobility μ = 5-30 cm^2/V.s and resistivity ρ ~ 10^{-3}-10^{-2} Ω-cm[224]. Pure SnO_2 films exhibit direct optical band gap of 3.87 - 4.3 eV [224, 228].

Due to the interesting electrical and optical properties of SnO_2 and their applications in solar cells, gas sensors, as transparent conductors, etc., several authors have perused the research on TM doped SnO_2 to explore RT FM for spintronic applications. The RT FM with giant magnetic moment in SnO_2 was first reported by Ogale *et al.* [39] by depositing Co doped SnO_2 on R-plane sapphire substrate. They have grown the $Sn_{1-x}Co_xO_2$ films by PLD technique and keeping the substrate at 700°C in 10^{-4} Torr oxygen pressure. Giant magnetic moment of the order of 7.55±0.5μ_B/Co-ion was observed for 5 at % of Co doping. From magnetization measurement, the FM T_c was found to be 650 K. This moment is much larger than the moment of metallic Co or any other known Co oxides. Gopinadhan *et al.*[43] studied the $Sn_{1-x}Co_xO_2$ thin film prepared by spray pyrolysis technique. They have observed room temperature FM with increase in M_s value monotonically with Co concentration up to 0.10. The maximum carrier concentration and M_s values were reported to be 2.2x10^{19} cm^{-3} and 0.26 μ_B/Co-ion respectively. They have emphasized the role of carrier concentration in stabilizing the FM.

Bulk polycrystalline samples of Co doped SnO_2 were also found to exhibit room temperature FM with M_s = 0.13 μ_B/Co-ion [40]. The analysis of M-H data in terms of Brillouin function model gave an indication that the doped Co ions are in Co^{2+} state with effective magnetic moment, μ_{eff} ~ 4.57μ_B/Co-ion. Mn doped SnO_2 was also found to show FM behavior but with T_c above and below room temperature [229, 230]. However Duan *et al.*[198] observed AFM interaction in Mn doped SnO_2 and they have explained in terms of lack of free charge carrier density to induce RKKY type of FM interaction.

The theoretical calculation of Errico *et al.* [231] taking into consideration 25 at % TM-concentration in TiO_2 shows that the low spin state is more energetically preferable. In TM-ion

doped rutile crystal structure, the TM-ion is surrounded by the O atom in octahedral crystal field. The octahedral crystal field splits the d-orbital into lower energy triplet t_{2g} and higher energy doublet e_g states. The crystal field created by octahedral coordination of ligand field is twice as large as that created by tetrahedral coordination [232]. So, the crystal field dominates over the pairing energy. Thus low spin state is more preferable. Thus the resulting magnetic moment of 2.38μ_B/Fe-ion, 0.78μ_B/Co-ion etc. is expected in these compounds. As SnO_2 also has the same rutile structure as TiO_2 so, similar kind of result is expected.

Many TM-doped oxide based DMS, are found to be ferromagnetic insulating along with giant magnetic moment [47]. It is claimed that FM interaction prevailing in these insulating DMS is not carrier mediated. The other way of explanation is the defect mediated FM. Kilic and Zunger [233] predicted that even in pure SnO_2, oxygen vacancy has very low formation energy and would commonly exists. Moreover the ab-initio calculation of Errico *et al.* [231] on Co-doped TiO_2 and first-principle calculations on Co-doped SnO_2 by Wang *et al.* [45] predicted that there is a strong tendency of oxygen vacancy formation near the Co and Fe-ion. They found that the doped system is more energetically favorable than the undoped system for oxygen vacancy formation. As per the calculation of Wang *et al.* [45] the presence of vacancies increases the magnetic moment of the TM-ion. Also a sharp increase in magnetic moment was observed when the TM-ion and oxygen vacancy remain in the same octahedron, in which distance between TM ion and vacancy is 2.06Å [45]. This can be understood as follows. In order to have charge neutrality, the Co-ion replacing the Sn^{4+} ion must have the valence of Co^{4+} in Co-doped SnO_2 without introducing any defects. However, the Co^{4+} state is not energetically favorable and in order to maintain the charge neutrality an adjacent oxygen vacancy is created near the TM-ions [45]. Their results show that strong p-d coupling and hopping is possible in the Co and Fe-doped SnO_2. The calculations done by Wang *et al.* show that without the presence of oxygen vacancy, the magnetic moment in 12.5 at % of Co-doped SnO_2 is found to be of the order of 0.8μ_B/Co-ion and the value was found to be 2.3μ_B/Co-ion by including the vacancy in the system. Such oxygen vacancy mediated FM was reported in Fe doped SnO_2 [234].

In addition to that TM doping in a few other wide band gap semiconductor such as In_2O_3 and CeO_2, Cu_2O etc. were discussed in literature [46, 87, 117, 235-244].

Thus even though room temperature FM has been achieved in TM doped oxide semiconductors, the mechanism of FM is yet to be understood in detail.

1.9 Motivation of the present thesis work

At the beginning of the thesis work, and as per literature survey, it was observed that, there were several reports on the TM doped ZnO and TiO_2 based DMS with room temperature FM [33-38]. SnO_2 is one of the well known wide band gap semiconductors having wide range of applications in optoelectronic devices, solar cells, gas sensors, etc. Doping of trace amount of TM can gives rise to robust FM semiconductors for potential applications in optoelectronic and spintronic devices. Ogale *et al*.[39] have reported a giant magnetic moment of the order of 7.5 ± 0.5 μ_B/Co-ion and large Curie temperature as high as 650 K in Co-doped SnO_2 thin film. In view of the reported interesting giant magnetic moment in SnO_2 based thin film and due the lack of detailed reports on bulk samples, it was taken up for the preparation of Co and Ni doped bulk SnO_2 under different experimental conditions and the detailed study of magnetic properties.

Following samples were prepared for the present thesis work,

4) $Sn_{1-x}Co_xO_2$ for (x = 0.0, 0.02, 0.05, 0.07, 0.10) samples by using solid state route and ball milling technique.
5) Pure and 2 at % Co-doped SnO_2 samples prepared by co-precipitation method.
6) $Sn_{1-x}Ni_xO_2$ (x = 0.0, 0.02, 0.05, 0.07, 0.10) samples by using solid state route and ball milling technique.

The above prepared samples were characterized by recording and analyzing room temperature powder X-ray diffraction patterns (XRD). The recording of microstructural images and compositional analysis were carried out by using LEO SEM machine equipped with energy dispersive X-ray (EDX) facilities. The microstructure and the composition at crystallites level were studied by recording TEM images using transmission electron microscope (TEM) coupled with an EDS analyzer. The samples were also characterized by recording Raman and FTIR spectra. The field variation of magnetization was measured at different temperatures by using a Lakeshore make vibrating sample magnetometer (VSM). Electron spin resonance (ESR) spectra were recorded to study the presence of magnetic phase separation and magnetic clusters if any. The magnetic properties were studied by measuring magnetization versus field (M-H) loops at room temperature and a few selected low temperatures. Temperature variation of magnetization was also measured to determine the Curie temperature.

The Co and Ni doped SnO_2 based DMS with room temperature FM were prepared successfully. The FM T_c was found to be quite large and much above the room temperature. The M_s value was found to depend upon the sample preparation techniques. The interaction mechanism prevailing in these compounds were explained in terms of the Bound magnetic polaron formation. In addition to the transition element doping, the oxygen vacancy was found to play an important role in the observed FM behavior. Probably for the first time, we have carried out critical behavior studies in oxide based DMS, i.e. on Co-doped SnO_2. The critical behavior was studied from the detailed magnetization measurement in the vicinity of transition temperature and the estimated critical exponents values are found to be comparable to the Mean Field model prediction. The results of Co doped samples are reported in Chapter 3 and those of Ni doped samples are given in chapter 4.

Chapter 2

Experimental Techniques

It is essential to understand the principle and the mechanism of operation of various experimental facilities used in experimental research, in order to extract best possible and reliable experimental data and their meaningful interpretation. In this chapter, the experimental techniques used in material preparation, their structural characterization, electrical characterization and magnetic measurements are given. The samples for the current investigations were prepared by solid state route and ball milling technique. For heat treating the materials during the preparations, both homemade and commercial muffle furnaces were used. The prepared materials were studied by using X-ray diffractometer (XRD) to check their phase purity and crystal structure parameters, scanning electron microscope (SEM) to study the microstructure, energy dispersive spectrometer (EDS) for determining the sample composition and transmission electron microscope (TEM) to estimate particle size, to study the composition and the crystal structure at nano-crystalline level. Raman and Fourier Transform Infrared (FTIR) spectroscopic techniques were also employed to characterize the samples and to look for the presence of impurity if any. The electrical transport and magnetic properties were studied by carrying out temperature variations of electrical resistivity and dc magnetization measurements. Magnetization loops at different temperatures were also recorded. The experimental setup used for electrical transport and magnetic measurements are also discussed in this chapter.

2.1 Sample Preparation

Bulk samples of ceramics and oxides are generally prepared by solid state route. Solids do not usually react together at ambient temperature over laboratory time scales due to the lack of diffusion and mixing of constituent elements at the atomic scale. So, it is necessary to heat the reactants at high temperatures to overcome the kinetic barriers. The powders of stoichiometric ratio of starting compounds are often pressed into pellets before heating to high temperature in order to increase the contact between the particles. Reaction times are usually several days and it is best to repeat the process to ensure homogeneous samples. The starting materials are usually single cation oxides, carbonates, nitrates or hydroxides which decompose to form oxides when

heated. Samples used in the present thesis work were prepared by using different techniques such as solid state route, mechanical milling and by co-precipitation.

2.1.1 Solid state reaction

The stoichiometric ratios of starting compounds were weighed using an electronic balance supplied by Mettler Toledo model no. AG135 with an accuracy of ±0.01 mg. The weighed compounds were grinded under the medium of acetone (99%) using an agate mortar and pestle. The homogeneous mixture of starting compounds was transferred into an alumina crucible and was presintered at 400^{o}C for over 24 h followed by furnace cooling to room temperature. The presintered powder was grinded again to get a homogeneous mixture. The presintered powder was pressed into cylindrical shape pellets by using a 13 mm die and a hydraulic press supplied by Techno Search instruments, Thane, India with a maximum load capacity of 6 Ton/cm^2. The sintering in pellet form was carried out in a step by step process in air at different temperatures with several intermediate grindings and repelletizing. The final sintering temperature was 900^{o}C.

2.1.2 Mechanical Alloying Technique

Mechanical alloying (MA) of stoichiometric ratio of starting compounds was carried out by high-energy ball milling using a planetary ball mill (Insmart, India). The photographic view of a planetary ball mill, comprising of a horizontal support disc on which vials are mounted is shown in Fig. 2.1(a). The schematic view of MA process is shown in Fig.2.1(b). The vial rotates in a direction opposite to that of the disc, thereby simulating a planetary motion. This planetary motion result in a large centrifugal force acting on the balls kept inside the vial. This causes the balls collide with themselves and with the wall of the vial with high impact. The mixture of starting compounds along with balls in the vial are subjected to repeated cold welding and fracture at the surfaces of the balls and the vial. This process leads to the disintegration of the powders, resulting first in the refinement of crystallite size and ultimately in atomic level mixing of the elements and alloy formation. Hence, size refinement is a natural consequence of a MA process. The refinement and alloying processes are determined by the milling parameters such as the powder to ball weight ratio, ball size, rotation speed, milling time, etc. The nature of the milling vial, the balls and the milling media play an important role in the process of mechanical alloying.

In the present work, dry milling of high purity oxides such as SnO_2 and transition element oxides has been carried. The hardened steel vial and hardened steel balls were used for milling all the powder compositions. The ball to powder ratio of 10:1 and the rotating speed of 500 rpm were maintained during the milling process. In order to avoid excessive heating, it was programmed to stop for 10 minutes after every 15 minutes of continuous milling. For a comparison, we have also carried out the ball milling of selected samples by using tungsten carbide vial and balls with the help of a commercial ball mill.

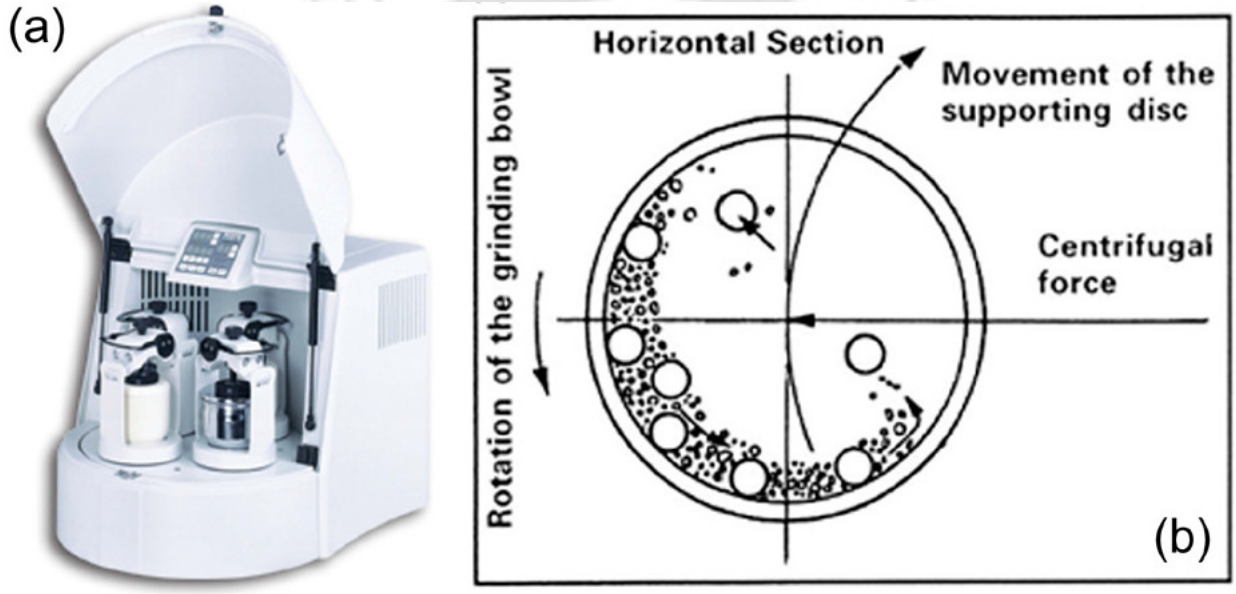

Fig. 2.1 (a) Photographic view of planetary ball mill and (b) schematic view of mechanical milling process

2.1.3 Co-precipitation Technique

Coprecipitation technique is a convenient method for preparing the highly homogeneous and stoichiometric composition. It is also relatively easy to prepare the materials in nanocrystalline form. Here the size of the nanoparticle depends upon various parameters such as, the type of salt used, reaction temperature, pH value, ionic strength of the system, etc. In a typical procedure, 1.48 mmol of $Co(NO_3)_2{\cdot}6H_2O$ and 82.5 mmol of $SnCl_2$ were dissolved in 150 mL of deionized water. To this pink solution, concentrated aqueous NH_3 was added drop wise with stirring, over

about 1 hr. The addition of NH_3 was stopped when the pH of the solution reached 12 and during this time the precipitation has ceased. Stirring was continued for another 2 hour and then the contents were left undisturbed. After 3 days, the solid Co doped SnO_2 was separated from the colorless supernatant layer using a centrifuge and washed with deionized water. Finally the crystalline Co doped SnO_2 powder was dried in oven at 80ºC for several hours. The same procedure was followed for obtaining pure/undoped SnO_2 from $SnCl_4$. The above product was heated at 200^{o}C for 12 hrs followed by grinding. The precursor powders thus obtained were divided into different batches and were annealed at 400^{o}C, 600^{o}C and 800^{o}C in air and N_2 gas atmosphere respectively.

2.2 High Temperature Furnaces

High temperature furnaces were used for material preparation. Homemade muffle furnaces with a maximum operating temperature of 1200°C and commercial high temperature furnaces with the maximum operating temperature of 1400°C were used for sintering the samples. The commercial furnaces were supplied by N. R. Enterprises and Bysakh & Company, Kolkata, India. The furnace supplied by N. R. Enterprises was powered by a thyristor unit of 30A rating. The temperature was controlled using; INDFURR make, PID programmable temperature controller (TAJE PFY-400). The platinum versus platinum-rhodium (Platinum + 10 % Rh) thermocouple was used for sensing the temperature. The heating elements were based on Si-Carbide rods. The temperature was controlled to an accuracy of ± 1°C. The furnace could be operated up to a maximum temperature of 1400°C. The other furnace supplied by Bysakh & Co. contains (1) a thyristor unit of 35 A rating, (2) a PID programmable temperature controller (model no. PRC-300) with 16 segment programming feature, (3) a platinum versus platinum-rhodium (Platinum + 13 % Rh) thermo couple wire, (4) Si-Carbide heating rods. The maximum operating temperature was 1450°C. The home made furnace (1200°C) consists of a cylindrical alumina muffle with an inner diameter of 5.8 cm and length 50 cm. Six Si-Carbide rods of 45 cm length each were used as heating elements. The muffle loaded with heating elements is housed in a cylindrical container of 50 cm diameter and 50 cm length and it is made up of galvanized aluminum sheet. It is filled with ceramic bricks and ceramic wools for thermal insulation. Measurement and controlling of temperature was carried out by using Chromel-Alumel (Cr-Al)

thermocouple and a commercial on/off type temperature controller. The input power to the furnace was regulated using a variac (dimmerstat) of 15 A capacity. An external on/off relay (15A capacity) was used for controlling the power supply to the heater wire. The relay was triggered using the temperature controller. The block diagram of the furnace is shown in Fig. 2.2. The furnace could be operated up to a maximum temperature of 1200°C. The temperature could be controlled with an accuracy of ± 5°C.

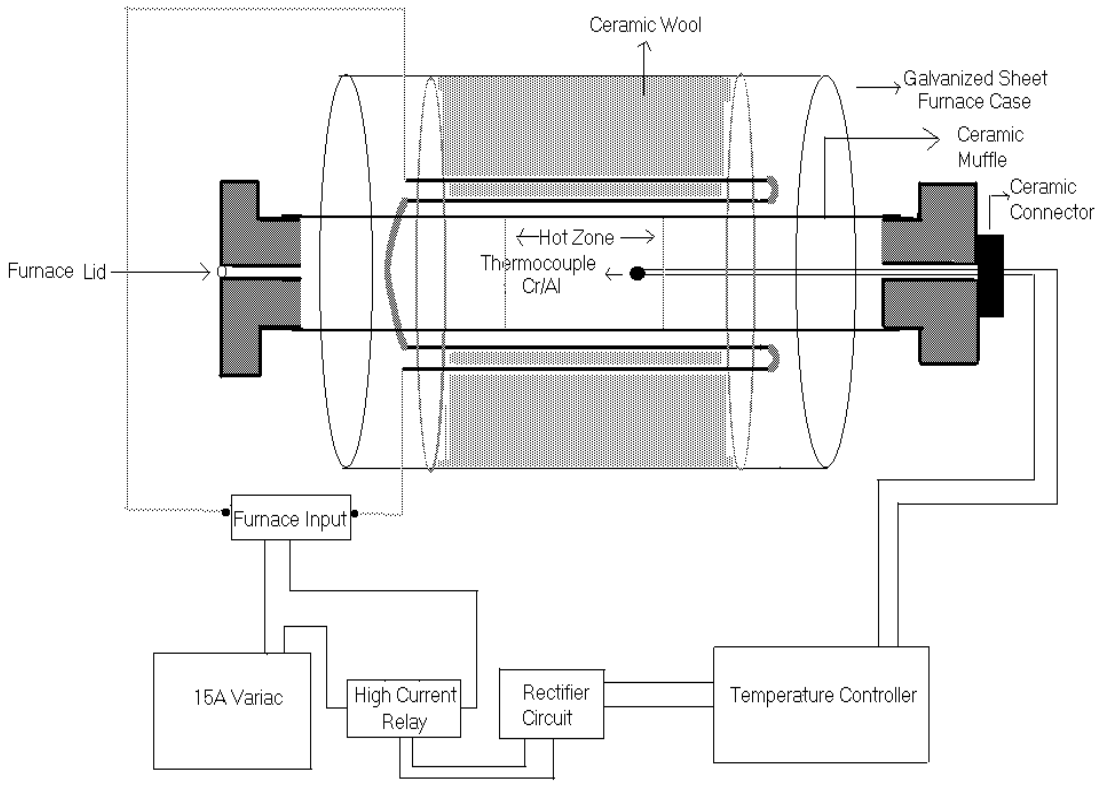

Fig. 2.2 Block diagram of the furnace with maximum operating temperature of 1200°C.

2.3 X-ray Diffraction

The X- ray diffraction technique has been used to study the phase purity and crystal structure of the prepared compounds. Powder X-ray diffraction (XRD) patterns were recorded at room temperature using commercial Seifert-model no. 3003TT or a Bruker model no. D8 X-ray diffractometer by employing CuK_{α} radiation (1.5418 Å). In the present investigation, all the XRD data were collected with the setting of 30 mA current and 40 kV voltage for X-ray generator. The instrument is based on the Bragg-Brentano geometry as shown in Fig. 2.3. In this

geometry, the source to sample distance and the sample to detector distance are kept equal. A perspex sheet with a rectangular groove was used for sample mount, where the powder sample was filled uniformly. The data were collected in θ-θ scan with an angular speed of 1-2°/minute and a step size of 0.03-0.05°.

The XRD patterns were analyzed with the help of Fullprof program by employing Rietveld refinement technique [245]. The background was refined using a polynomial function.

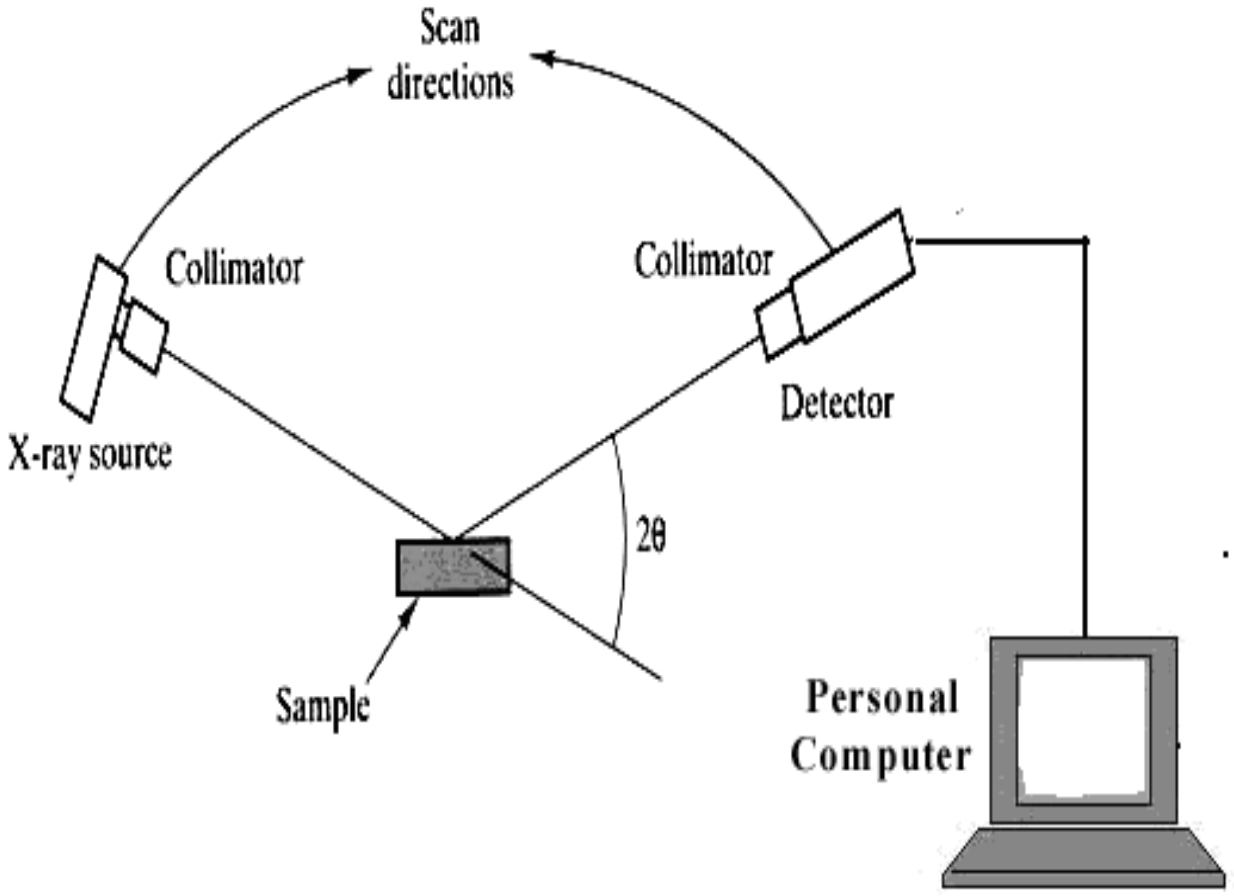

Fig. 2.3 Ray diagram of X- ray diffractometer.

Pseudo-Voigt function was chosen for peak shape. The global parameters, such as coefficients of background polynomial, scaling factor, half width parameters (u, v, w) and lattice parameters (a, b, c) were mainly varied during the refinement. In addition to that nuclear structure variables such as fractional atomic coordinates (x, y, z), isotropic displacement (temperature) parameters and occupancy values were varied. Here, occupancy is the chemical occupancy normalized to the multiplicity of the general position of the group. The occupancy of oxygen was taken as 1 for all the refinements and it was not varied during the refinement. The quality of the refinements are known based on the values of reliability factors such as, R_p, R_{wp}, R_{exp}, R_{Bragg}, R_F and χ^2 and they are defined as follows.

$$\text{Profile factor, } R_p = 100\frac{\sum_{i=1,n}\left|y_i - y_{c,i}\right|}{\sum_{i=1,n} y_i} \qquad \text{---------- (2.1)}$$

Here y_i is the observed point (experimental) and $y_{c,i}$ is the calculated point and n represents the number of data points.

$$\text{Weighted profile factor, } R_{wp} = 100\left[\frac{\sum_{i=1,n}\omega_i\left|y_i - y_{c,i}\right|^2}{\sum_{i=1,n}\omega_i y_i^2}\right]^{1/2} \qquad \text{---------- (2.2)}$$

Here $\omega_i = \frac{1}{\sigma_i^2}$, σ_i^2 is the variance of observation y_i.

$$\text{Expected weight factor, } R_{\exp} = 100\left[\frac{n-p}{\sum_{i=1,n}\omega_i y_i^2}\right]^{1/2} \qquad \text{---------- (2.3)}$$

Here $(n - p)$ is the number of degrees of freedom. n is the total number of experimental points and p is the number of refined parameters.

$$\text{Reduced chi-square, } \chi^2 = \left[\frac{R_{wp}}{R_{\exp}}\right]^2 \qquad \text{---------- (2.4)}$$

Bragg factor, $$R_B = 100 \frac{\sum_h \left| I_{obs,h} - I_{calc,h} \right|}{\sum_h I_{obs,h}}$$ ---------- (2.5)

Here h is the vector which levels the Bragg reflections. The $I_{obs,h}$ is the observed integrated intensities and $I_{calc,h}$ is the calculated intensities.

Crystallographic R_F factor, $$R_F = 100 \frac{\sum_h \left| F_{obs,h} - F_{calc,h} \right|}{\sum_h F_{obs,h}}$$ ---------- (2.6)

Here $F_{obs,h}$ and $F_{calc,h}$ are the observed and calculated structural factors respectively.

Inter atomic distances (bond length) were calculated using the refined fractional coordinates and lattice parameters by using Fullprof software.

The average crystallite size (S_C) has been calculated from the peak broadening by using the Scherrer's formula [246]

$$S_C = \kappa\lambda / \beta\cos\theta$$ ---------- (2.7)

where, constant k depends upon the shape of the particle(grain) size. Here it is taken as 0.89 by assuming the circular shape of the particle, β = Full Width at Half Maximum (FWHM) of intensity versus 2θ profile, λ is the wavelength of the CuK_α radiation and θ is the Bragg's diffraction angle. The instruments broadening effect has been taken into account.

2.4 Scanning Electron Microscope (SEM)

Recording of microstructural images and compositional analysis have been carried out by using LEO Scanning Electron Microscope (SEM, Leo 1430VP) equipped with Oxford energy dispersive spectrometer (EDS). Basic principles of SEM and EDS analysis are given briefly as follows. The scanning electron microscope (SEM) is a type of electron microscope that uses electrons to form an image of objects and to study surface morphology, fractured components, foreign particles and residues, etc. The schematic view of SEM is shown in Fig.2.4. The thermionically emitted electrons from a tungsten filament are drawn towards the anode and were focused by two successive condenser lenses into a beam with a narrow spot size (~50 Å). The shorter wavelength of electrons permits image magnifications up to 100,000 times in SEM. Pair of scanning coils located at the objective lens deflect the beam either linearly or in

raster fashion over a rectangular area of the specimen surface. These primary bombarding electrons on the surface of the specimen dislodge electrons from the specimen. Fig. 2.5 shows the interaction of electrons with the surface of the sample. Upon electron impinges on the surface, the interaction volume assumes a tear shape. These dislodged electrons are known as secondary electrons, which are attracted and collected by a positively biased grid or detector, and then translated into signals. These signals are then amplified, analyzed, and translated into images of the topography being inspected.

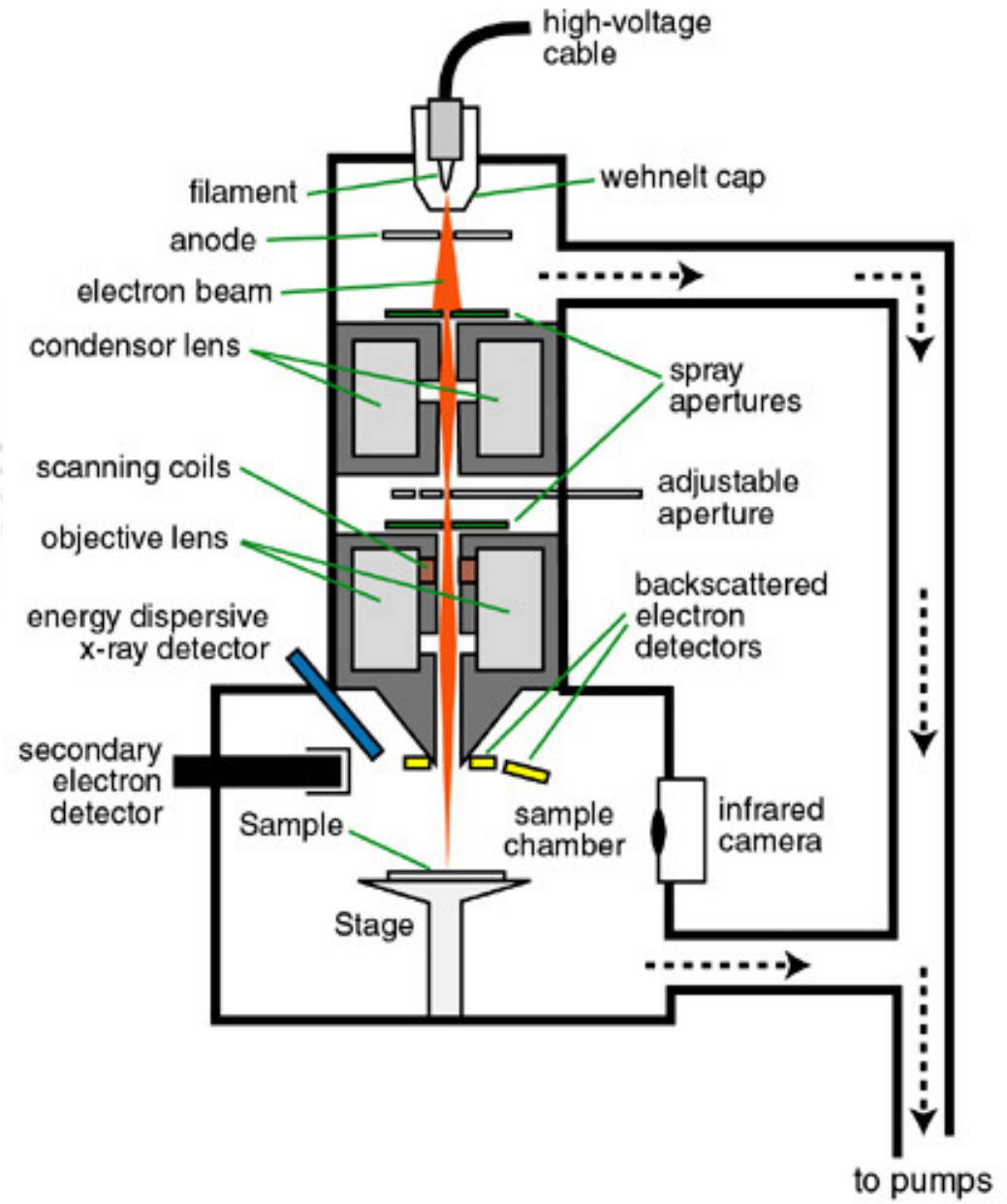

Fig. 2.4 Schematic view of scanning electron microscope.

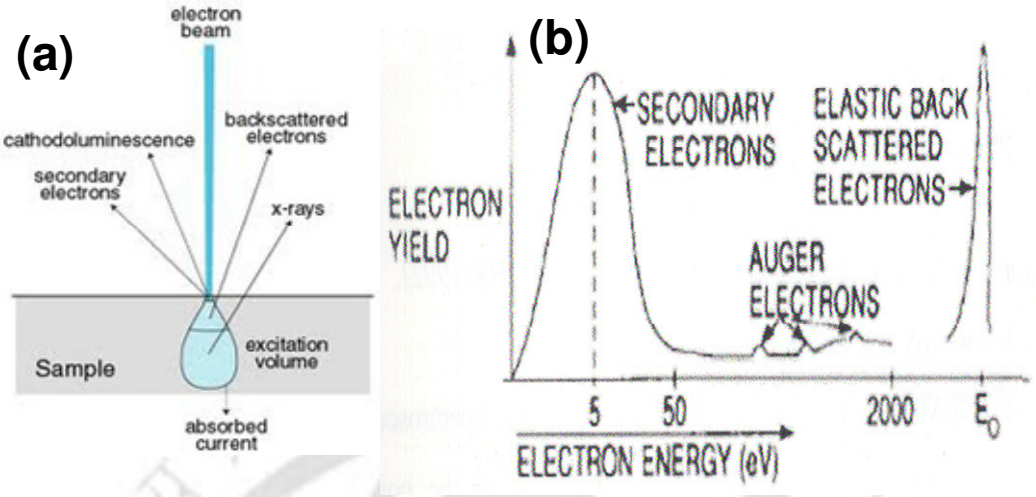

Fig. 2.5 (a) Electron and photon signals emanating from tear-shaped interaction volume during electron beam impingement on specimen surface, and (b) Energy spectrum of electrons emitted from the specimen surface.

Apart from secondary electrons, the back scattered electrons (BSE), characteristic x-rays, light (cathode-luminescence), specimen current and transmitted electrons are produced by SEM. These types of signal require specialized detectors and all such detectors are not present in a single machine. The primary electron beam results in the emission of BSE from the specimen. BSE possesses more energy than secondary electrons and have a definite direction. As such, they cannot be collected by a secondary electron detector, unless the detector is directly in their path of travel. All emissions above 50 eV are considered to be BSE. BSE imaging is useful in distinguishing one material from another, since the yield of the collected BSE increases monotonically with the specimen's atomic number Z (~ 0.05 $Z^{1/2}$). Backscattered imaging can distinguish elements with an atomic number difference of at least 3.

Energy dispersive X-ray spectroscopy (EDS or EDX) is an analytical technique used for the elemental analysis or chemical characterization of a sample. Its characterization capabilities originate from the fact that each element has a unique atomic structure, which emits its unique characteristic X-ray. To stimulate the emission of characteristic X-rays from a specimen, a high energy beam of charged particles such as electrons or protons, or a beam of X-rays, is focused into the sample being studied. At rest, an atom within the sample contains ground state (or

unexcited) electrons in discrete energy levels or electron shells bound to the nucleus. The incident beam may excite and eject an electron from an inner shell and it results in a hole or electron vacancy in the shell. An electron from an outer higher-energy shell then fills the hole, and the difference in energy between the higher-energy shell and the lower energy shell is released in the form of an X-ray. The atoms of every element release X-rays with unique amounts of energy during the above process. Thus, by measuring the value of energy of X-rays being released by a specimen during electron beam bombardment, the identity of the atoms present in the specimen can be established. Thus, we get the EDS spectrum, as an output and it is just a plot of how frequently an X-ray is received in each energy level. An EDS spectrum normally displays peaks corresponding to the energy levels for which the X-rays had been received. Each of these peaks is unique to an atom, and therefore corresponds to a single element. The intensity of the peaks depends on the concentration of the elements present.

In the present work, a thin solid pellet was mounted on carbon coated tape. Our samples are either semiconducting or insulators, so the direct SEM and EDS measurements could be not carried out without any metal coating. As the samples are semiconductors and insulating in nature, the electrons will get trapped in the surface and creates charge segregation which will not allow the further bombardment of electrons, for which the electrons cannot reach the detector. So a coating of metal layer serves our purpose.

2.5 Transmission Electron Microscope (TEM)

The TEM analysis was done in order to study the nanocrystalline microstructure of the samples by using JEOL Transmission electron microscope (TEM, JEOL 2100). Fig.2.6 shows the schematic diagram of TEM. Thermionically emitted electrons from the gun which is a tungsten filament are accelerated to 100 keV or higher and are first projected onto the specimen by means of the Condenser lens system.

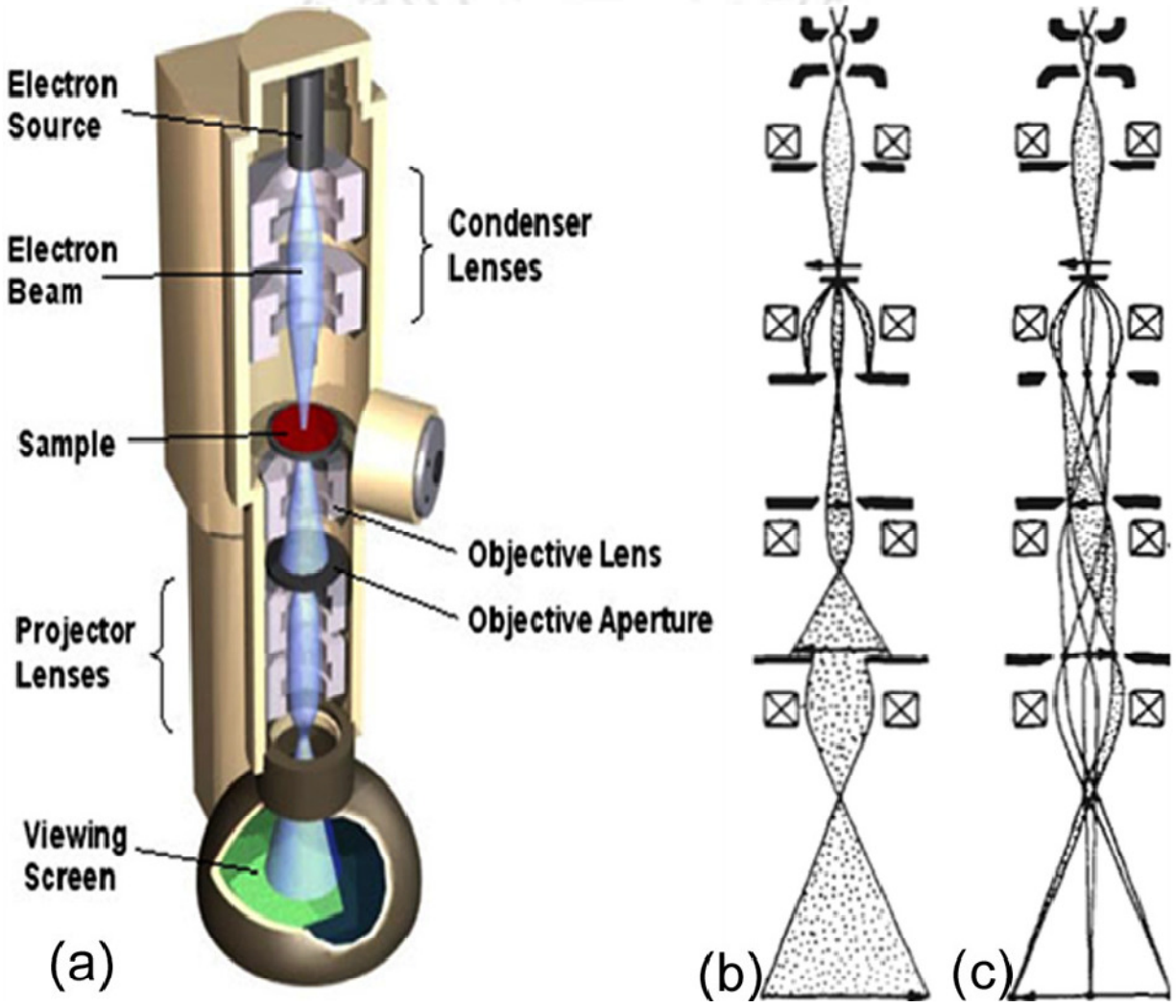

Fig. 2.6 (a) Schematic diagram of transmission electron microscope **(b)** Schematic ray diagram for image mode (c) Schematic ray diagram for diffraction mode.

The scattering process experienced by electrons during their passage through the specimen determines the kind of information obtained. Elastic scattering, involving no energy loss, when electrons interact with the potential field of the ion core, gives rise to diffraction patterns. Inelastic interactions between beam and matrix electrons at heterogeneities, such as grain boundaries, dislocations, secondary phase particles, defects, density variations, etc., cause complex absorption and scattering effects, leading to a spatial variation in the intensity of the transmitted beam. Images can be formed in a number of ways. The bright-field image is obtained by intentionally excluding all diffracted beams and only allowing the central beam through the specimen. This is done by placing suitably sized apertures in the back focal plane of the objective lens. Intermediate and projection lenses then magnify this central beam. Dark-field images are also formed by magnifying a single beam; here one of the diffracted beam is chosen by means of an aperture that blocks the central beam and the other diffracted beams. Fig.2.6(c) shows the schematic ray diagram for a diffraction mode. Fig. 2.7 shows the typical selected area (electron) diffraction (SAD or SAED) SAD pattern for a single crystal sample. We could see a long thin metal strip, the strip was placed in order to allow a small fraction of the beam, to enter into the sample and blocks the rest. The highly energetic electrons of the order of ~100 eV could easily pass through the samples having a thickness of few nanometers. The electron will behave like a wave and interact with the atoms and molecules more efficiently than visible and X-rays and gives rise to the diffraction pattern. We could observe a series of spot called as the selected area diffraction pattern, SADP, where each spot corresponds to a typical d_{hkl} value. If the same sample under illumination is tilted with some other angle, different diffraction conditions will be satisfied and the corresponding diffraction pattern can be seen. SAD is referred as selected because here we can easily choose any part of the specimen where we want to obtain the diffraction pattern.

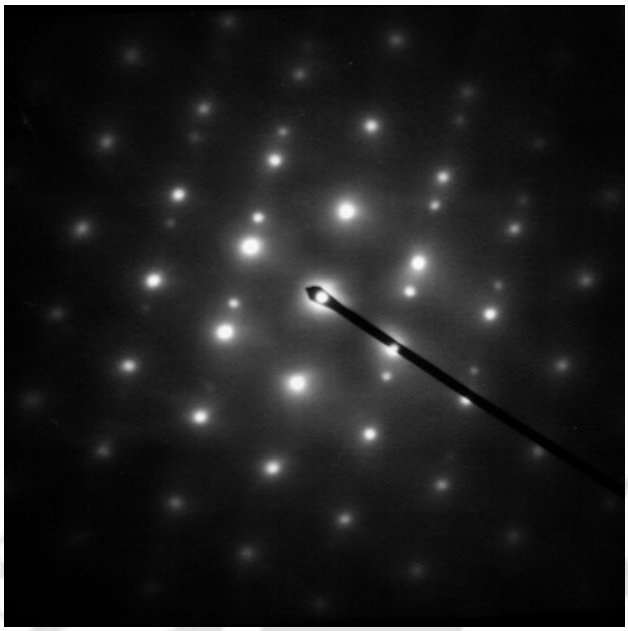

Fig.2.7 SAD pattern of single crystal Austenite.

SADP is used to identify crystal structures and examine crystal defects. It is similar to X-ray diffraction, but here the advancement is that we are able to select the areas in nanometer scale, whereas in X-ray diffraction several millimeters in size of the sample are required. The image obtained from the SAD patterns i.e. the obtained spots are basically in the k-space and in order to determine the d_{hkl} value in the real space we have used the imageJ software. Here, we could able to do the accurate centering of the diffraction ring and by choosing appropriate distance in nm^{-1} scale, the exact value of the d_{hkl} plane in the real space could be determined. Also the high resolution TEM (HRTEM) images were analyzed based on this software, to determine the corresponding d_{hkl} value for a particular crystal axis. We first do the fast Fourier Transform of the HRTEM image which converts the real space crystal planes to imaginary spots in the k-space, from that we could be able to determine the particular d_{hkl} plane.

In the present study the powdered sample was first dispersed in ethanol solution and then a drop of the liquid was placed on a carbon coated grid for the TEM observation.

2.6 FTIR and Raman Spectroscopy

Infrared and Raman spectroscopic techniques are basically related to vibrational spectroscopy and they give information about the vibrations of atoms of the constituent molecule and the nature of the atomic bonding. A molecule as a whole has constant translational and rotational motion. The frequency of the periodic motion is known as vibrational frequency. A non-linear molecule having N-atoms per primitive cell has 3N-6 normal modes of frequency of vibration. A linear molecule has 3N-5 normal modes of frequency because in this case, the rotation about the axis is not visible. At room temperature, all molecules are in their lowest energy levels with quantum no. n=0. For each normal mode, the most probable vibrational transition is from this level to the next higher level (n=0≥1) and they are called as the fundamental bands. For transitions into next higher levels such as for n≥2 are called overtone bands. The vibrational excitation occurs similar to that of the electronic excitation. Here the excitation particle is a phonon and its energy, a measure of vibrational energy is quantized. So it occurs in different energy states. Vibrational transitions are strongly related to photon-phonon coupling and follows the Franck-Condon selection rules [247]. The transition between the vibrational energy levels of molecules induced by the absorption of IR radiation and the resultant emission spectrum is known as IR spectroscopy. When the vibrational transition occurs during the scattering of light by molecule it comes under Raman spectroscopy. Depending on the nature of symmetry and asymmetry of a molecule, the mode of vibration can be either Raman active or IR active. In the case of IR active molecules, the dipole moment μ changes when the molecules vibrate whereas, the overall polarisabilty α changes in Raman active material. The asymmetric stretching and bending in a centre of symmetry molecule give rise to change in dipole moment and hence the molecule is IR active. The asymmetric stretching and bending in a centre of symmetric molecule do not give rise to change in polarizability and hence such molecules are Raman inactive. Whereas in symmetric stretching things will be just the opposite. Thus for a centre of symmetry molecule IR and Raman mode of vibrations are complementary to each other. However for molecules without having center of symmetry, the vibrational mode could be either IR active, Raman active, both, or neither.

2.6.1 FTIR Spectrometer

The Fourier transform infrared (FTIR) absorption spectra were recorded in the wave number range of 250-4000 cm^{-1} using model no. Spectrum BX, supplied by Perkin Elmer. The resolution of wave number was 2 cm^{-1}. Fig.2.8 (a) shows the block diagram of the FTIR spectrometer. The beam splitter divides the beam from the source into two parts. Half of the beam was reflected to a stationary mirror and come back to the splitter while the other half was reflected back by a movable mirror. Therefore the path length of this beam is variable. The two reflected beams recombine at the splitter and interfere. Constructive interference occurs for a path difference of zero or even multiple of wavelength and destructive interference occurs for half multiple of wavelength. The moving mirror should move smoothly. The position of the moving mirror is measured by using a laser as shown in Fig.2.8 (b). In the FTIR measurement, the sample is placed in between the interferometer and the detector. The sample absorbs a particular wavelength. Thus the output of the interferometer which is called as an interferogram contains the spectrum of the source minus the spectrum of the sample. A Fast Fourier Transform of the recorded interferogram changes the time domain to frequency domain.

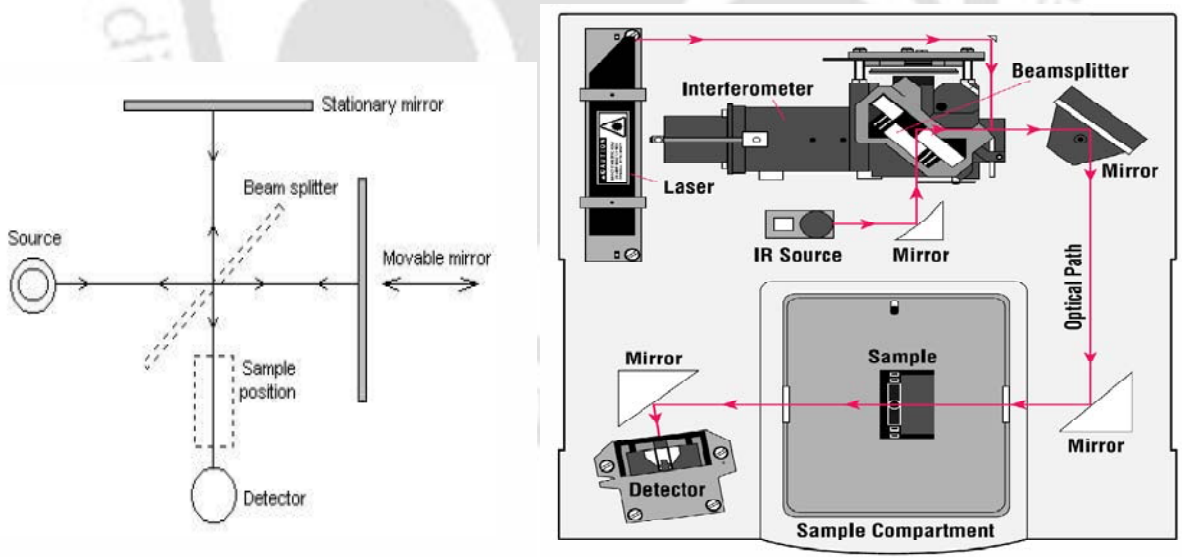

(a) **(b)**

Fig. 2.8 Schematic block diagram for FTIR

2.6.2 Raman Spectrometer

There are two types of scattering of light namely elastic and inelastic scattering. Elastic scattering is generally quite strong and the frequency of scattered light has the same frequency as that of the incident light (υ_o) and such scattering is generally known as Rayleigh scattering. In inelastic scattering, the frequency of scattered light can be either more or less than the incident wave. Raman scattering is a type of inelastic scattering and the scattered wavelengths fall in two categories namely antistoke lines and stokes lines. The Raman scattering phenomenon was first observed by Sir C.V. Raman in 1928, for which he got the Nobel Prize in 1930. In IR spectroscopy, a photon is completely absorbed to excite a molecular vibration, whereas in Raman spectroscopy quite high energy photons are used and some energy is lost from the photon to excite a vibration. The intensities and energy of the photons that have been lost energy to excite the vibrations are measured in order to get a spectrum. Fig. 2.9 shows the schematic diagram for the Raman spectrometer. The HR800 is an integrated Raman system used for all our samples to study the Raman spectra. The microscope is coupled confocally to a 800 mm focal length spectrograph equipped with two switchable gratings. The excitation photon can be supplied by using two sources namely HeNe laser of 20 mW power 632.817 nm wavelength or Argon laser of wave length 488 nm. If the particular sample used is fluorescence active to certain wavelength, then next higher wavelength is used, in order to observe the Raman spectra.

The laser beam is totally reflected by the beam splitter, which splits the beam into two equal parts. The beam was allowed to fall on the sample and it undergoes both Rayleigh and Raman scattering. The notch filter, allows only the Raman scattered wavelength while it blocks the incident wavelength. The inelastic scattered light was allowed to pass through the grating and etalon which in turn resolve the weak inelastic scattered wavelength coming from the sample more efficiently. Further the beam was allowed to enter into a charge couple device where it detects the change in polarisability of the sample from the change in wave length and converts into the intensity. We could see intensity vs. wave number graph in the computer screen.

.

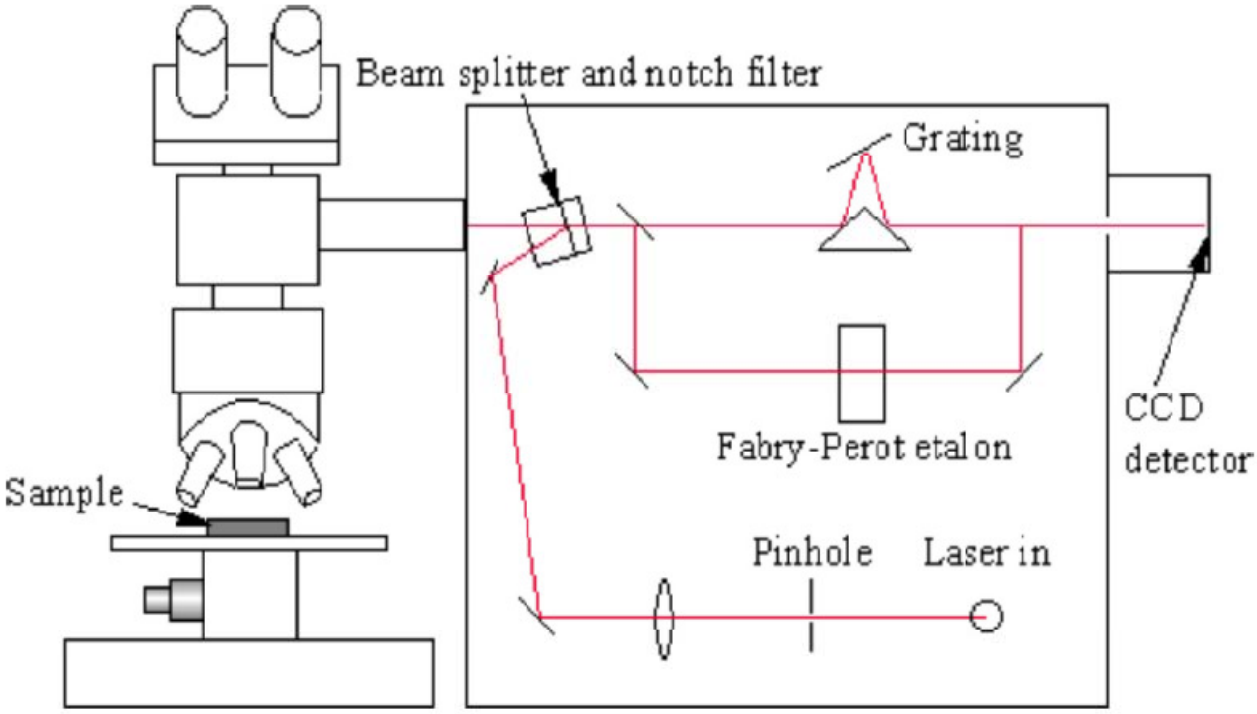

Fig. 2.9 Schematic diagram for Raman spectrometer.

2.7 Vibrating Sample Magnetometer

DC magnetization as a function of temperature and field was measured by using the vibrating sample magnetometer (VSM) (model no. 7410) made by Lakeshore.

The vibrating sample magnetometer (VSM) is an important equipment for the rapid and reliable measurement of the magnetic moment for a large variety of magnetic materials. The VSM developed originally by Foner [248] is widely used experimental set up for measuring temperature and field variation of magnetization of magnetic solids at ambient, higher and lower temperatures up to moderately high field. It has a flexible design and combines high sensitivity with ease of sample mounting and exchange. Samples can be changed rapidly, even at any operating temperature. Using a vibrating sample magnetometer, one can measure the DC magnetic moment as a function of temperature, magnetic field and time. So, it allows performing

susceptibility and magnetization studies. Magnetic moments as small as 5×10^{-5} emu are measurable with a VSM [248].

The temperature variations of magnetization (M) were measured by using a Lakeshore, model no. 7410 vibrating sample magnetometer. The temperature variation down to 20 K was achieved using an OXFORD make CCR cryostat (model X 74019-044) along with the temperature controller. The magnetic field was produced by using a 10 // electromagnet. The magnetization loop was measured by varying B up to 2 T. Calibration of the vibrating sample magnetometer was done by measuring the magnetic moment of a standard pure Ni sample. Block diagram of the vibrating sample magnetometer is shown in Fig. 2.10.

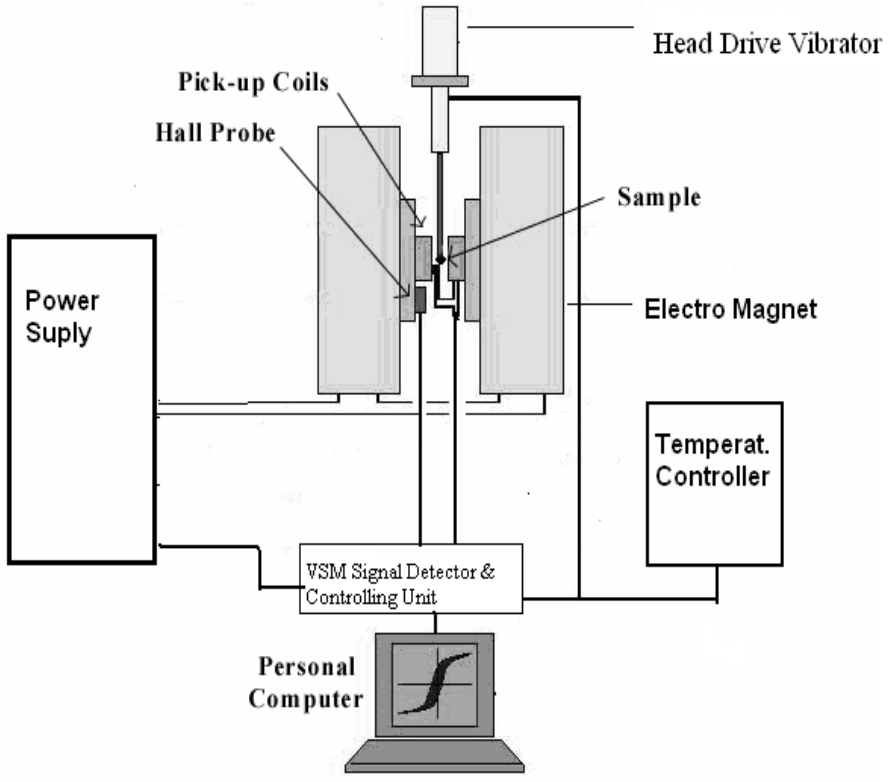

Fig. 2.10 Block diagram of the vibrating sample magnetometer.

The VSM is based upon Faraday's law, according to which an emf is induced in a conductor by a time-varying magnetic flux. If a sample of any magnetic material is placed in a uniform magnetic field, a dipole moment will be induced. If the sample vibrates with sinusoidal

motion, there is some magnetic flux change. This induces a voltage in the pick-up coils, which is proportional to the magnetic moment of the sample. Voltage, V (t) can be detected to a high resolution and accuracy by means of a suitable VSM signal detector (e.g. Lock in Amplifier).

2.8 Electron Spin Resonance

The Electron spin resonance (ESR) spectra could be understood as a consequence of Zeeman effect, where the splitting of energy levels of an atom occurs in the presence of an external magnetic field. The spectral term associated with an energy level is denoted by $^{2S+1}L_J$, where L, S and J are respective orbital angular momentum, spin angular momentum and the total angular momentum quantum numbers. In the presence of a magnetic field, the magnetic moment μ_J associated with J will be having a number of orientations represented by the quantum number m_J, where m_J= J, J-1,…… -J+1, -J. Different orientations of the magnetic dipole in the field B_0 correspond to different potential energies, so that the shift in energy of particular m_J level is given by

$$\Delta E = h\nu = g_J m_J \mu_B B_0 \quad \text{----------} \quad (2.8)$$

Where $g_J=1+\frac{J(J+1)+S(S+1)-L(L+1)}{2J(J+1)}$ is the Lande g-factor and μ_B=Bohr magneton = $e\hbar/2m_e$ = 9.2740 x 10^{-24} Am^2.

The g factor plays an important role in the ESR spectra and it gives us the idea about the nature of angular momentum state of the electron. It is different from the g_J.

The unpaired electron in an atom, not only get affected by the external magnetic field B_0, but also from the internal local magnetic fields associated with it. Therefore, the effective field B_{eff} felt by the electron was given by the eq.

$$B_{eff} = B_0 (1 - \sigma) \quad \text{----------} \quad (2.9)$$

Where σ includes the effects from the local fields which can be positive or negative, and therefore the resonance condition is satisfied when

$$\Delta E = h\nu = g_J\mu_B B_{eff} = g_J\mu_B B_0 (1 - \sigma) \quad \text{----------} \quad (2.10)$$

The quantity $g_J(1 - \sigma)$ is called the g factor, given the symbol g, so

$$\Delta E = h\nu = g\mu_B B_0 \quad \text{----------} \quad (2.11)$$

Using this equation, we can calculate the value of g from the ESR experiment by measuring the field B_0 and the frequency ν at which resonance occurs. The g-value depends on the nature of environment and interactions of electrons such as spin-orbit interaction in a crystal and it differs from the case of isolated electron having g value 2.0032.

Electron Spin Resonance (ESR) Spectrometer, JEOL JES-FA200 was used to carry out all the ESR measurements. Fig.2.11 shows the schematic diagram of ESR spectrometer. Here, the magnetic field is varied and a constant microwave source of frequency equal to 9.5 GHz (known as X-band microwave radiation) is used. The microwave can be amplified by the Klystron and is allowed to pass in one direction with the help of an isolator. Further, the power of the microwave can be decreased with the help of the attenuator. The desired microwave frequency is allowed to pass through the sample by passing the microwave into the microwave cavity. The cavity is placed in between the pole pieces of an electromagnet, and the magnetic field can be swept. The resonance occurs, when it satisfies the equation explained above. The observed signal is detected and amplified to give the ESR signal. The data were analyzed using the cW-ESR software.

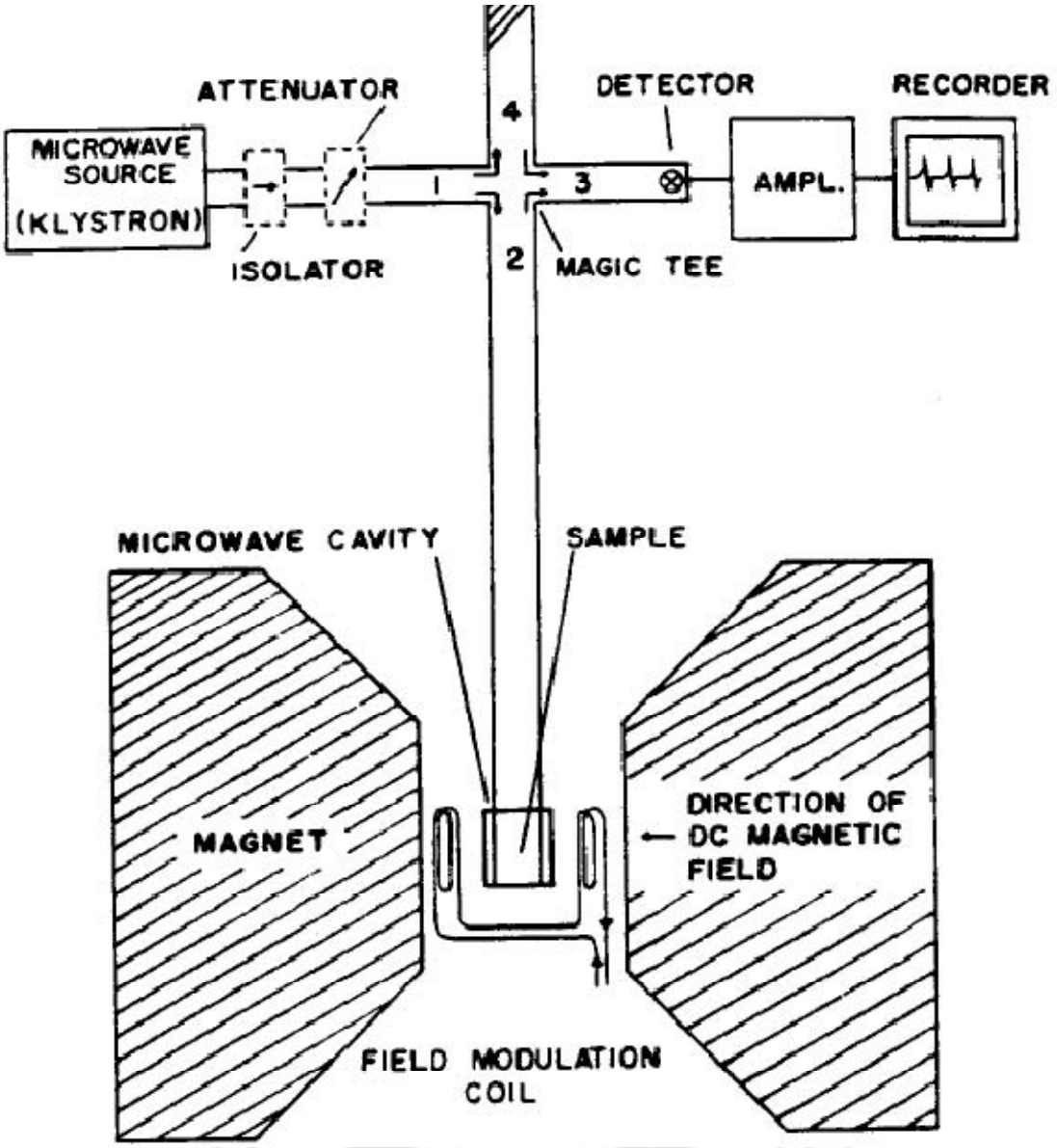

Fig. 2.11 Block diagram for ESR spectrometer.

2.9 Electrical Resistivity Measurements

Temperature variation of dc electrical resistivity measurements down to 20 K was carried out to study the electrical transport properties in the DMS materials. The low temperature was achieved by using a commercially supplied APD make CCR (closed cycle refrigerator). Fig.2.12 shows the schematic diagram of the Cryostat. The set up consist up of a copper sample holder (22x 22x6mm) which was mounted over the cold tip of the cryostat to load the sample. The temperature variation was achieved by using a heater wire in the vicinity of the cold tip.

The top view of the sample holder is shown in Fig.2.13. A groove of 10mm length and 3mm diameter was made in a copper block to mount the pt-100 sensor for sample temperature measurement. The controlling sensor is the Si-diode, which was mounted at the cold tip, where the heater wire of 37Ω resistance is installed. In order to mount the sample, electrically insulated from the copper sample holder, a thin mica sheet was used. Electrical contacts on the sample were made with the help of silver paint and /or Indium soldering. A printed circuit board (PCB) with four copper strips was mounted on the sample holder. The copper wires of 32SWG (0.2743mm) were used for electrical connection between PCB and sample. Standard two probe technique was used as most of our samples have high resistance. A programmable Keithley SourceMeter of model no.2410 was used for measuring the current (or voltage) as a function of temperature. The experimental data were collected using a personal computer equipped with GPIB board. The Fabricated sample holder attached to the CCR cryostat for resistivity measurement is shown in Fig.2.14. The necessary software in quick Basic language was developed for temperature controlling and data acquisition using a personal computer.

For the calculation of electrical resistivity, the dimension of the sample was determined by using a screw gauge and the distance between the voltage leads was measured by using a travelling microscope. The collected data were in the form of the temperature variation of current which was converted to resistance by dividing the constant voltage supplied by the source meter and hence the resistivity as a function of temperature was calculated by taking the sample dimensions.

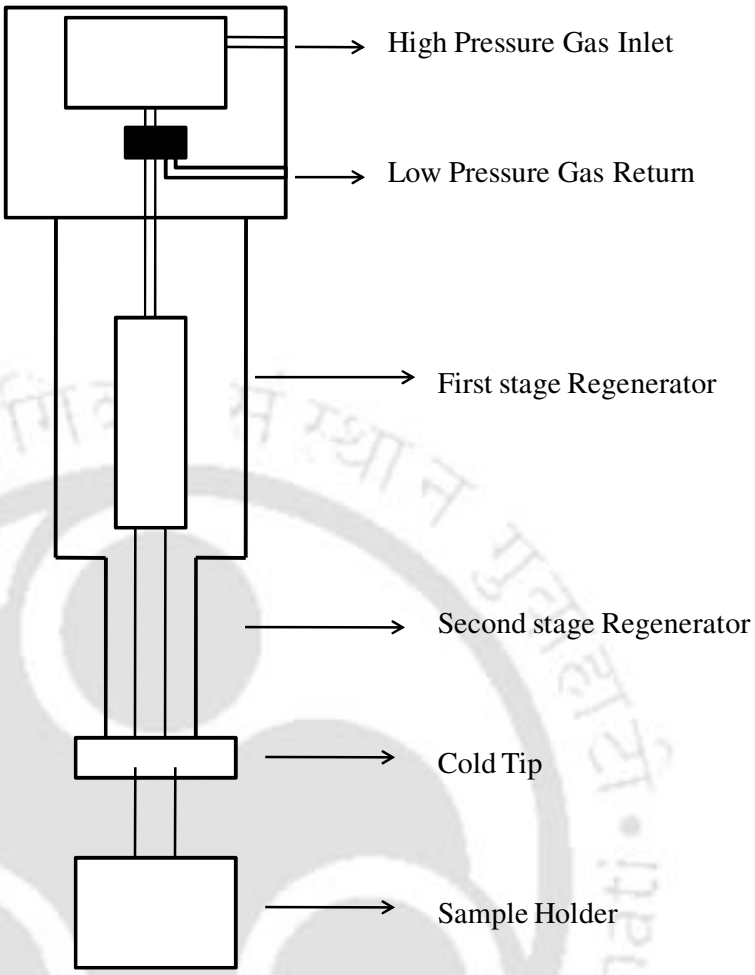

Fig. 2.12 Block diagram of APD Cryostat.

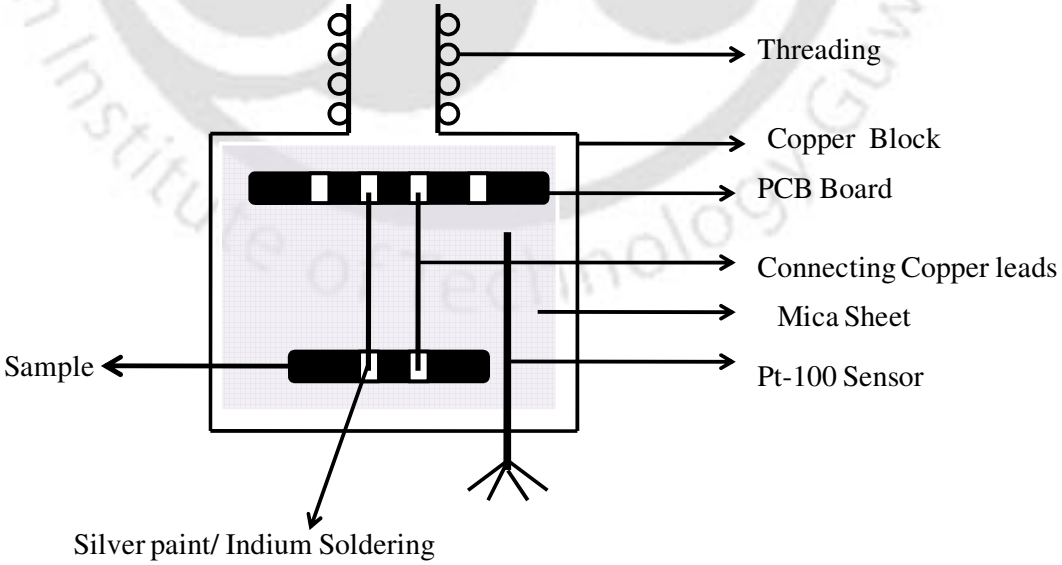

Fig. 2.13 Top view of sample holder for resistivity measurement.

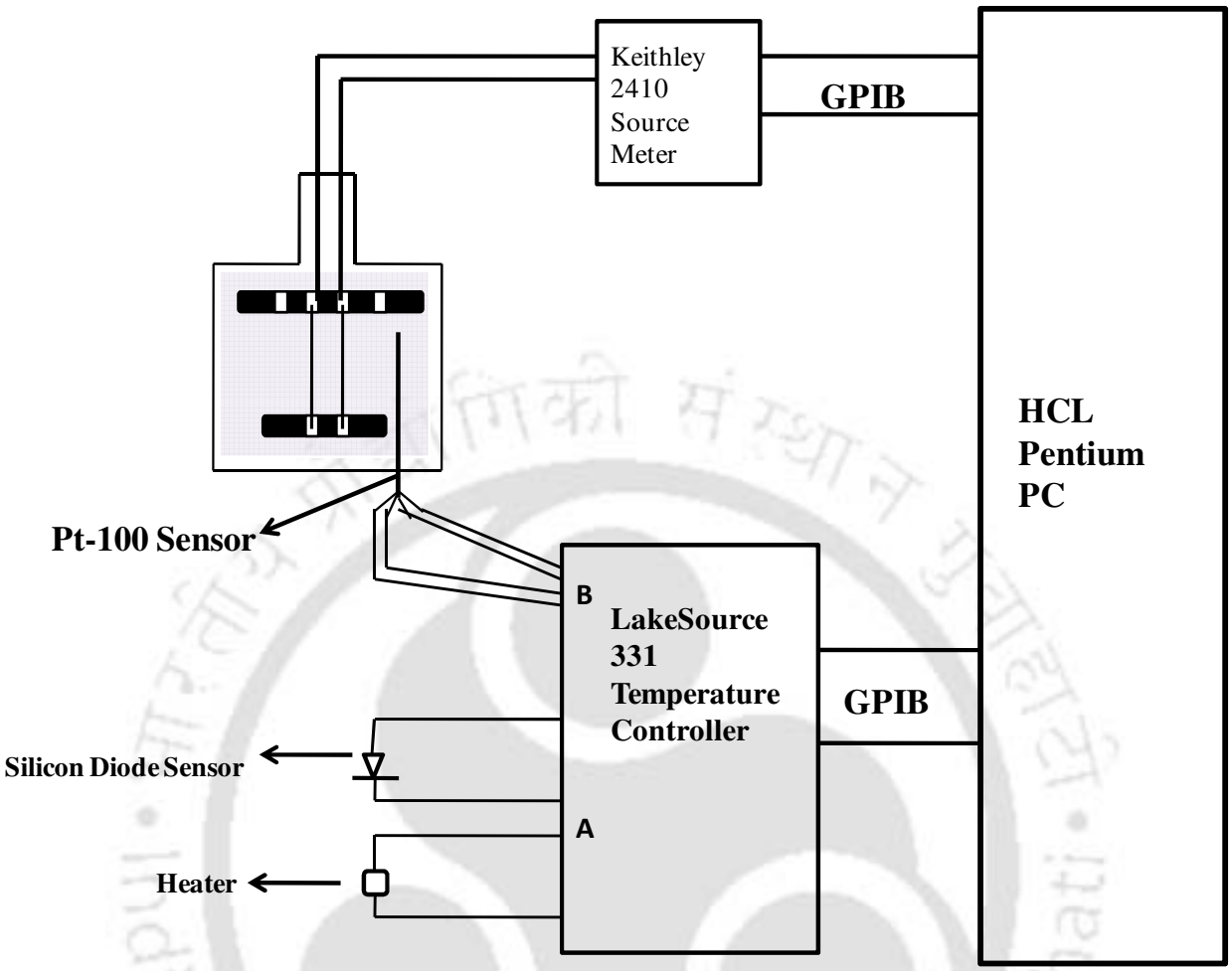

Fig.2.14 Block diagram of electrical resistivity measurement set-up.

To summarize, I have used various experimental facilities such as X-ray diffractometer, scanning electron microscope, transmission electron microscope, FTIR spectrometer, Raman spectrometer and ESR set up to characterize the samples. The detailed magnetization was measured by using a vibrating sample magnetometer as described above. The electrical resistivity as a function of temperature was measured by using linear two probe technique with the help of SourceMeter unit.

Chapter 3

Co doped SnO_2 based DMS

SnO_2 is an attractive semiconductor with wide band gap, E_g= 3.6 eV and optical transparency in the visible region. In an attempt to achieve spin controlled devices; it is first aimed at tailoring the material for reproducible room temperature ferromagnetism by doping transition elements in SnO_2. In thin film samples of Co doped SnO_2, Ogale *et al*.[39] reported giant magnetic moment of 7.55 μ_B/ion at room temperature. Subsequent to the above report, the room temperature ferromagnetism (FM) with saturation magnetic moment, m_s= 0.133 μ_B/Co-ion for x = 0.01 was obtained by Punnoose *et al*.[40] on polycrystalline $Sn_{1-x}Co_xO_2$. Gopinadhan *et al.* reported FM with $T_c > 573K$ and $m_s = 0.26\mu_B$/ion on thin film sample of 10 at % Co-doped SnO_2 [43]. Room temperature FM without any TM doping in wide band gap semiconducting oxides are also reported by a few authors [249, 250] and such phenomenon was explained in terms of defects, such as oxygen vacancy. However, antiferromagnetic (AFM) behavior has been observed by a few groups upon TM element doping in SnO_2 [198, 251].

In order to understand the magnetic behavior of Co doped SnO_2, without the influence of any substrate effect, bulk $Sn_{1-x}Co_xO_2$ for x = 0.02, 0.05, 0.07 and 0.10 were prepared by solid state route. It is found that, these materials exhibit ferromagnetism at room temperature with magnetic moment up to 0.34 μ_B/Co-ion, especially on material prepared under N_2 gas atmosphere. The magnetization data could be analyzed in terms of bound magnetic polaron model and for one of the samples, the magnetization data could be fitted to the Brillouin function model with ferromagnetic interaction.

To study the role of annealing conditions; crystalline size, etc. on the physical properties of Co doped SnO_2, we have prepared $Sn_{0.98}Co_{0.02}O_2$ by a co-precipitation technique. In this technique uniform distribution of Co ions and better control over its crystallite size are possible. They were annealed in air and N_2 atmosphere. We have found that the samples annealed in the presence of N_2 gas environment at 800^{o}C show relatively better room temperature ferromagnetic behavior in comparison to other air annealed samples.

In order to understand the defect induced room temperature FM in SnO_2, we have taken up mechanical milling of high purity SnO_2 without any TM element doping and using two different vials, namely steel and tungsten Carbide (WC). The milled powders were also annealed at 900^oC to study the effect of annealing on defects and the corresponding magnetic properties. Also, in order to study the role of defects and annealing conditions in these materials and in an attempt to have material with large M_s value, the Co doped SnO_2 samples were prepared by using ball-milling technique, followed by high temperature annealing.

Materials undergoing second order magnetic phase transition from paramagnetic (PM) to FM state are widely analyzed in terms of critical behavior of various thermodynamic parameters and the associated critical exponents can be determined in the vicinity of transition temperature [120, 128, 252]. Such critical exponents give an idea about the nature and type of magnetic interaction and in depth knowledge of magnetic phase transition. Even though, there are a couple of reports [142, 143, 145] on the critical behavior studies of alloy based DMS, there is no such report to the best of our knowledge on the critical exponent of oxide based DMS. Fukuma *et al.* [143] have studied the critical exponents of Group IV-VI based DMS alloys, i.e. $Ge_{1-x}Mn_xTe$ by recording isothermal magnetization and by analyzing the data, in terms of modified Arrott plot method. The critical exponents were found to follow the prediction of the mean field model. The presence of antiferromagnetic interaction was reported to have no influence on the observed critical behavior of FM transition. The DMS materials are generally characterized as strongly disordered magnetic system, due to the presence of random magnetic moments as a result of small concentrations of magnetic ion. Priour and Das Sarma [142] have studied theoretically, the effect of disorder on the critical behavior of the 3D Heisenberg model by using Monte-Carlo simulation. They have concluded that the strong disorder has no influence on the critical behavior of the 3D Heisenberg model, however, at large value of reduced temperature; the critical exponents get obscured due to the finite size correlation length effect. Hamedoun *et al.*[145] have reported that the critical exponent γ, associated with susceptibility was found to vary from the value corresponding to the Heisenberg model to that of the Ising model depending on the competitions between inter and intra sublattice interactions, especially in ferrites.

In the present thesis work, a detailed isothermal magnetization measurement and analysis on Co doped SnO_2 based DMS, exhibiting a strong room temperature FM have been carried out. The

analysis suggests the presence of long range magnetic interaction with critical exponents comparable to those of the mean field model.

3.1 $Sn_{1-x}Co_xO_2$ by solid state synthesis

Co doped SnO_2 samples were synthesized by solid state route. They were characterized by X-ray diffraction and by recording microstructural images. The detailed magnetization measurement and analysis are presented.

3.1.1 Preparation and Characterization

$Sn_{1-x}Co_xO_2$ samples for x = 0.0, 0.02, 0.05, 0.07 and 0.10 were prepared by following the standard solid state route. Stoichiometric ratio of SnO_2 and Co_3O_4 with 99.9% purity were weighed, mixed under acetone and were presintered at 400^{o}C. The final sintering in pellet form was carried out in air at 900^{o}C for 24 hr (air annealed). For a comparison, one of the pellets of *x* = 0.02 was annealed at 500^{o}C for 12 hr under flowing N_2 gas. X-ray diffraction (XRD) patterns were recorded at room temperature using Seifert 3003-TT XRD machine by employing Cu-Kα radiation. Fig.3.1 shows the XRD patterns recorded for $Sn_{1-x}Co_xO_2$ samples for *x* = 0 to 0.10 and they are found to be in single phase form. The patterns could be refined by using $P4_2/mnm$ space group with the aid of Rietveld refinement technique and Fullprof programme. Fig.3.2 shows the refined XRD patterns for all the Co doped SnO_2 samples. The obtained lattice parameters from the refinement are tabulated in table-3.1. The lattice parameters for pure SnO_2 are found to be a = b = 4.732 Å and c = 3.184 Å and they reduce to a = b = 4.712 Å and c = 3.142 Å for x = 0.10. The lattice parameters are found to decrease marginally with increase in doping concentration and it can be understood in terms of Co^{2+} or Co^{3+} replacing Sn^{4+}ions. The lattice parameters are comparable to those reported by Duan *et al.* [198] for Mn doped SnO_2. The expanded view of (110) peaks are shown in Fig.3.3, where one can see the shift in peak position towards higher 2θ value with increase in doping concentration. The above observation substantiates the argument of lattice parameter variation due to Co-ions replacing Sn ions.

The average crystallite size was calculated using the Scherrer's formula

$S=\lambda k/\beta \cos\theta$ ..... (3.1)

where constant k depends upon the shape of the grain size and is taken as 0.89 by assuming the circular grains, λ=1.5406 Å for $Cu K\alpha$ radiation, β is the full width at half maximum (FWHM) of diffraction peaks and θ is the glancing angle. The experimental β value was corrected for instrumental broadening using the relation $\beta^2 = \beta_m^2 - \beta_{ins}^2$. Here β_m is the measured FWHM of the XRD peak and β_{ins} is the instrumental broadening. The crystallite sizes for various samples are given in table-3.1. The average crystallite size was found of the order of 60 nm.

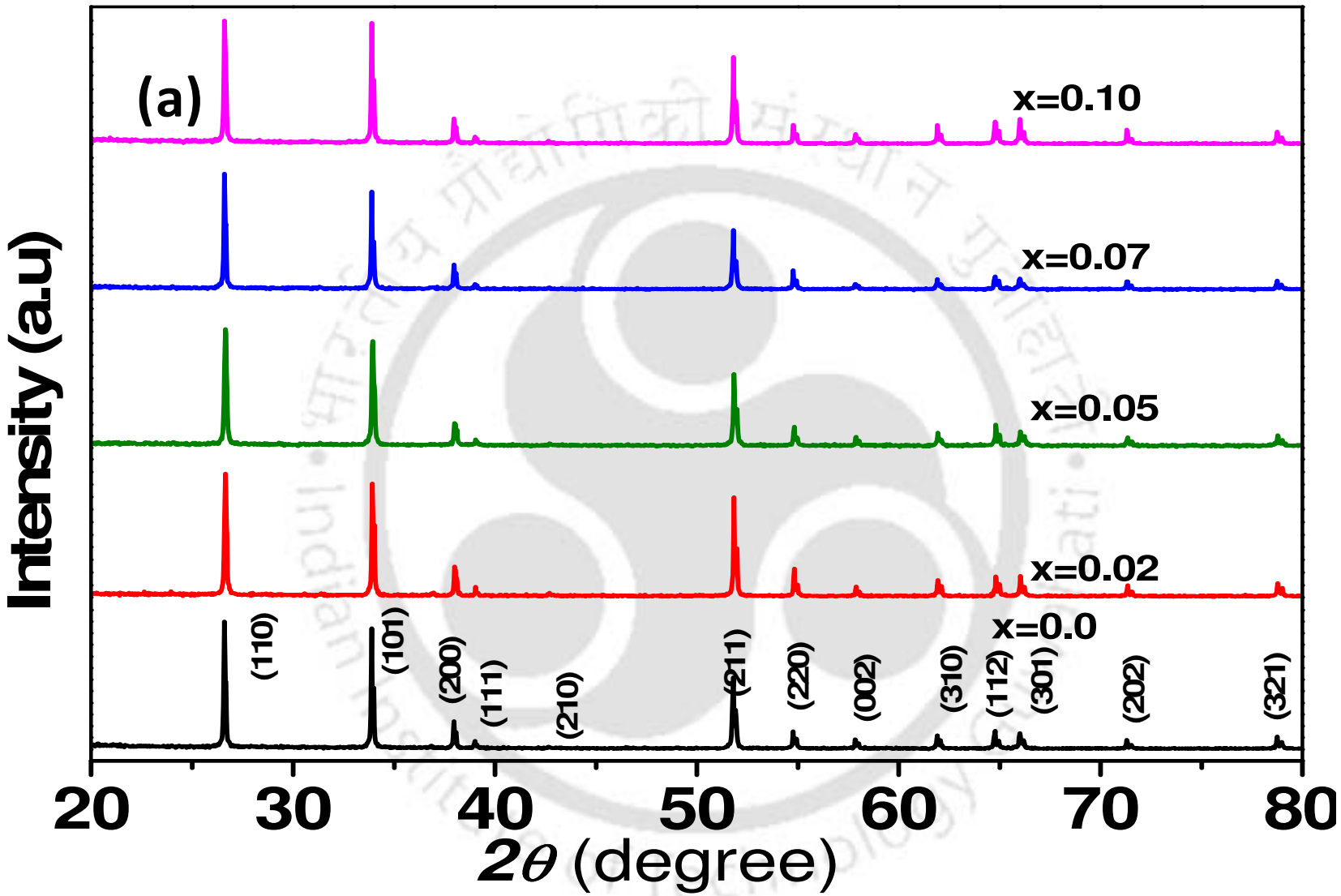

Fig.3.1 XRD patterns recorded at room temperature for $Sn_{1-x}Co_xO_2$ (x = 0.0, 0.02, 0.05, 0.07 and 0.10).

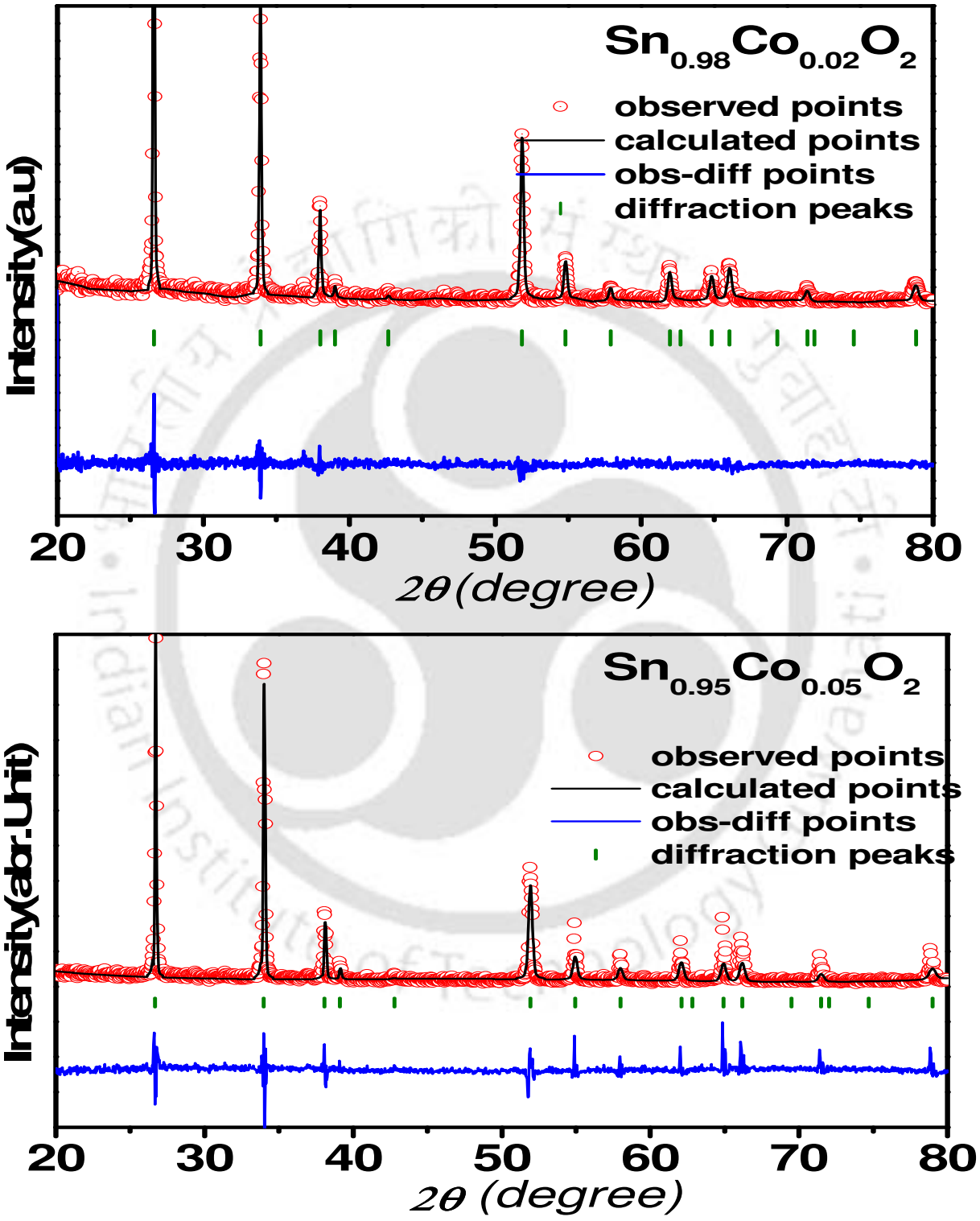

Fig.3.2(a) XRD patterns along with Rietveld refinement for x = 0.02 and 0.05.

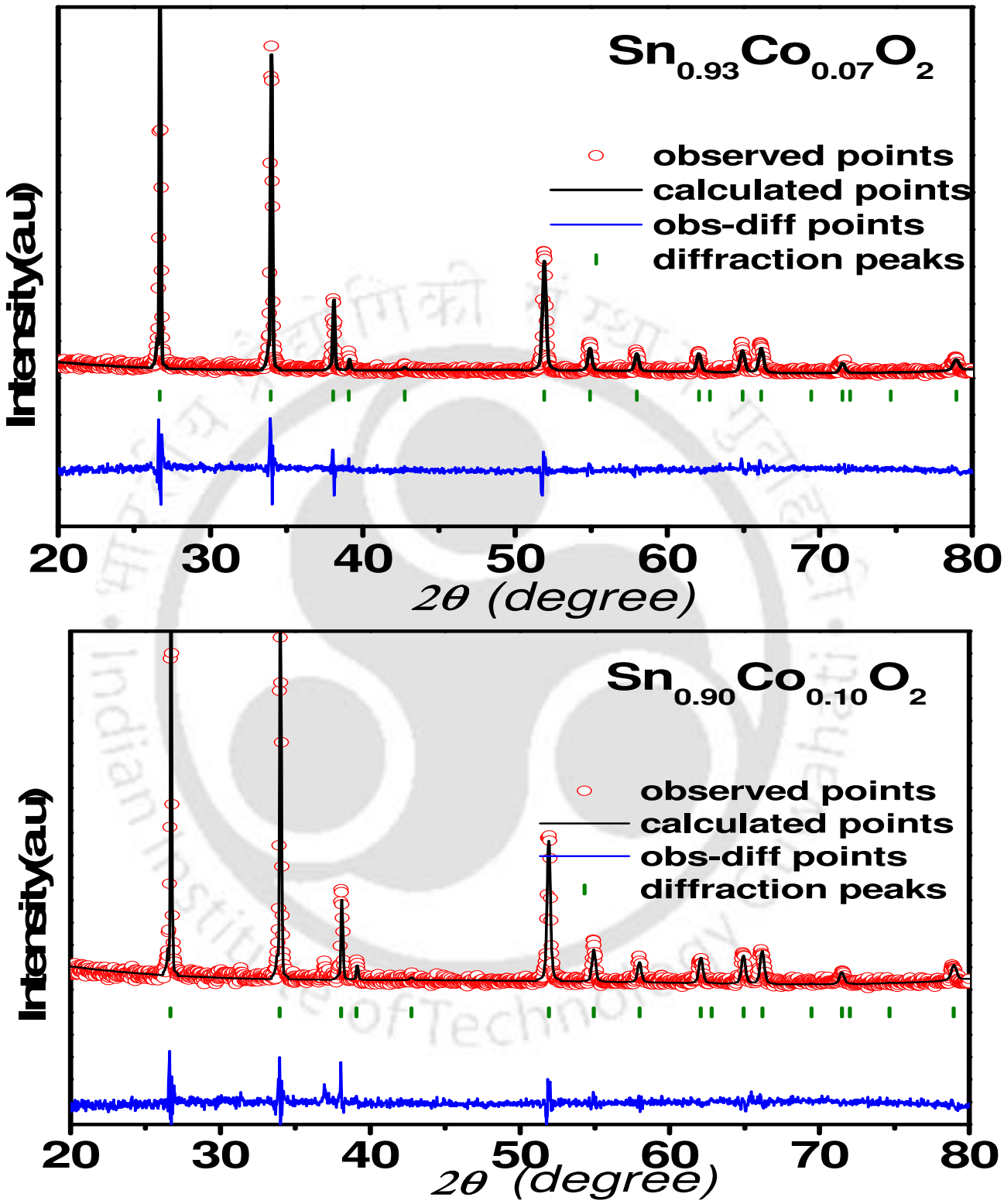

Fig.3.2(b) XRD patterns along with Rietveld refinement for x = 0.07 and 0.10 samples. The circles represent experimental points and solid line represents Rietveld refined data. The dotted lines at the bottom show the difference between experimental and refined data.

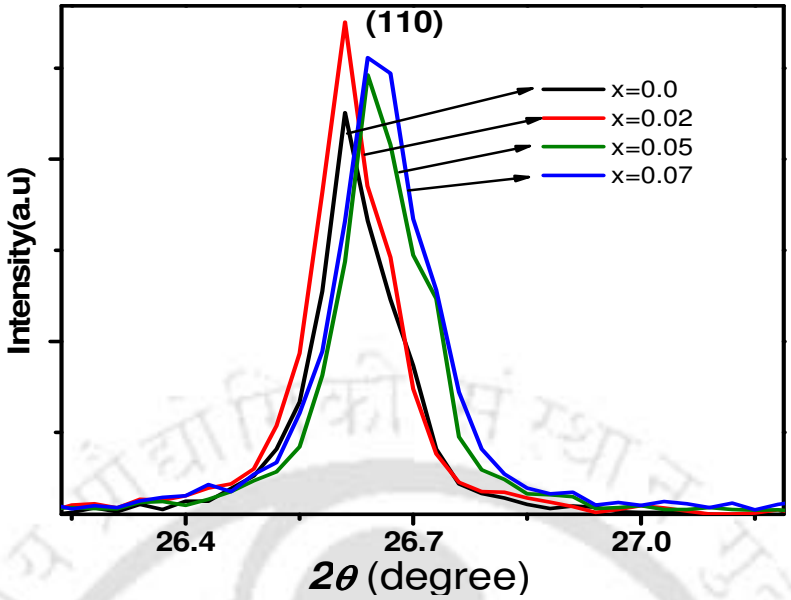

Fig.3.3 Expanded view of (110) peak of XRD pattern.

Table-3.1. List of parameters obtained from the Rietveld refinement and analysis of XRD patterns of $Sn_{1-x}Co_xO_2$ samples prepared by solid state route.

Sample/Parameters	**x = 0.0**	**x = 0.02**	**x = 0.05**	**x = 0.07**	**x = 0.10**
Space group	$P4_2/mnm$	$P4_2/mnm$	$P4_2/mnm$	$P4_2/mnm$	$P4_2/mnm$
a = b (Å)	4.732	4.731	4.723	4.717	4.712
c (Å)	3.184	3.182	3.178	3.164	3.142
Volume ($Å^3$)	71.3	71.2	70.9	70.4	69.8
χ^2 (%)	3.17	1.38	2.26	1.87	1.95
R_p (%)	28.1	19.9	20.0	18.5	16.7
Crystallite Size(nm)	66	68	66	65	63

The microstructure and compositional analysis were studied by using LEO SEM machine with energy dispersive X-ray spectrum (EDX) facilities. The SEM images show uniform surface morphology. The cation ratio obtained from EDX analysis are given in table-3.2 and are found to be comparable to that of nominal starting composition.

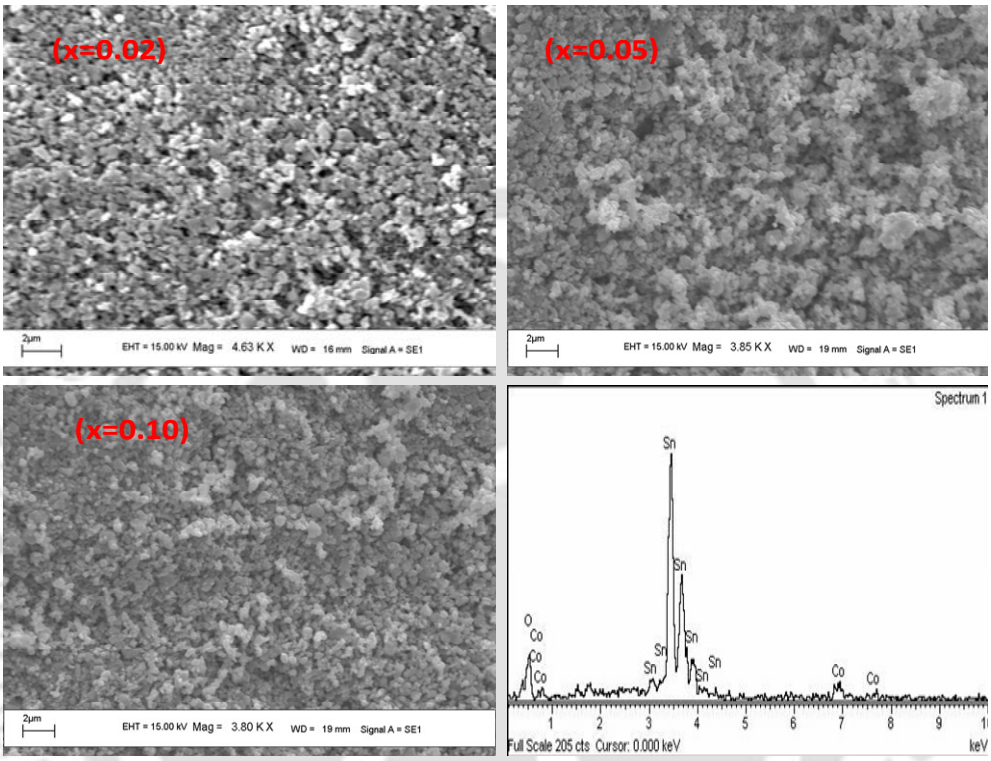

Fig.3.4 SEM images recorded for x= 0.02, 0.05 and 0.10 samples along with EDX spectra for x=0.10 Co-doped sample.

Table-3.2 Cationic ratio obtained from EDX measurement for different Co-doped SnO_2 samples.

Sample	**Calculated Cationic Ratio from EDS**	
	Sn	**Co**
x=0.02	0.97	0.03
x=0.05	0.94	0.05
x=0.07	0.92	0.08
x=0.10	0.87	0.12

Fig. 3.5 shows the TEM images of x = 0.02 sample taken in a carbon coated copper grid. The average particle size is found to be around 50 nm. Fig. 3.5(b) shows the selected area electron diffraction pattern and it depicts the polycrystalline behavior of the sample. The absence of ring like pattern suggests that the crystalline grains are in some preferred orientation.

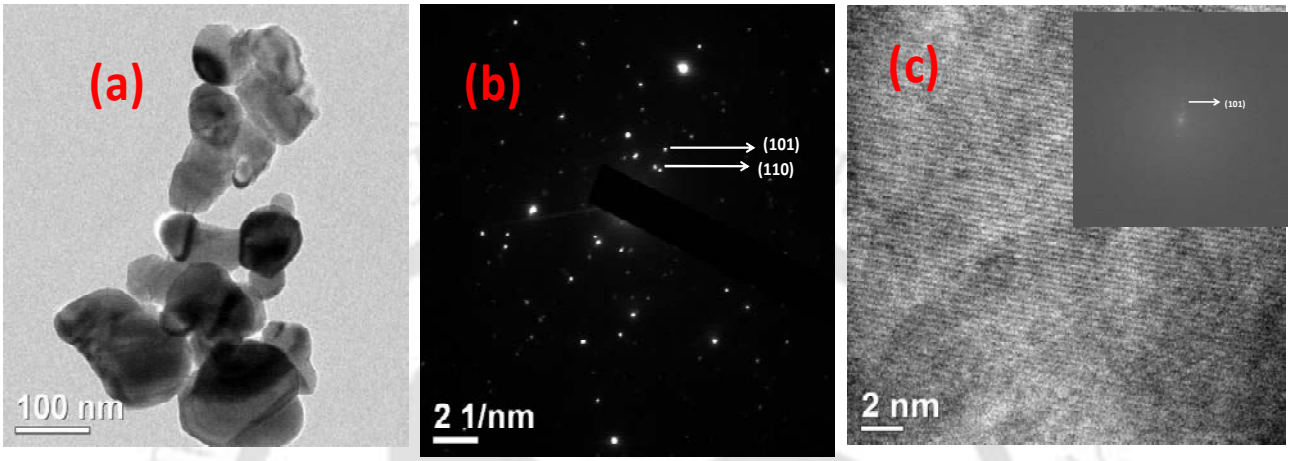

Fig. 3.5 TEM, SAD and HRTEM image recorded for $Sn_{0.98}Co_{0.02}O_2$ sample annealed in air at 900^0C.

The EDS measurement using TEM facility was carried out and it showed the presence of Co within the crystallites. The high resolution transmission electron microscope (HRTEM) image recorded at different locations shows continuous (101) atomic plane as can be seen in Fig.3.5(c). The Fast Fourier Transform (FFT) image is shown in the inset of Fig. 3.5(c), where we can see the uniform (101) plane.

The samples were also characterized by recording Raman spectra by using LabRam HR 800 spectrometer. The typical Raman spectra recorded for x=0.0, 0.02 and 0.10 samples are shown in Fig.3.6. The main peak at 633 cm^{-1} corresponds to A_{1g} mode, i.e. symmetric Sn-O stretching. The observed minor peak at ~693 cm^{-1} can be compared to the reported Raman spectrum in literature for SnO_2 [253, 254]. It may be noted that other than reduction in intensity no additional peak has been observed. So, the samples are basically free from Co_3O_4 and other related impurity phases.

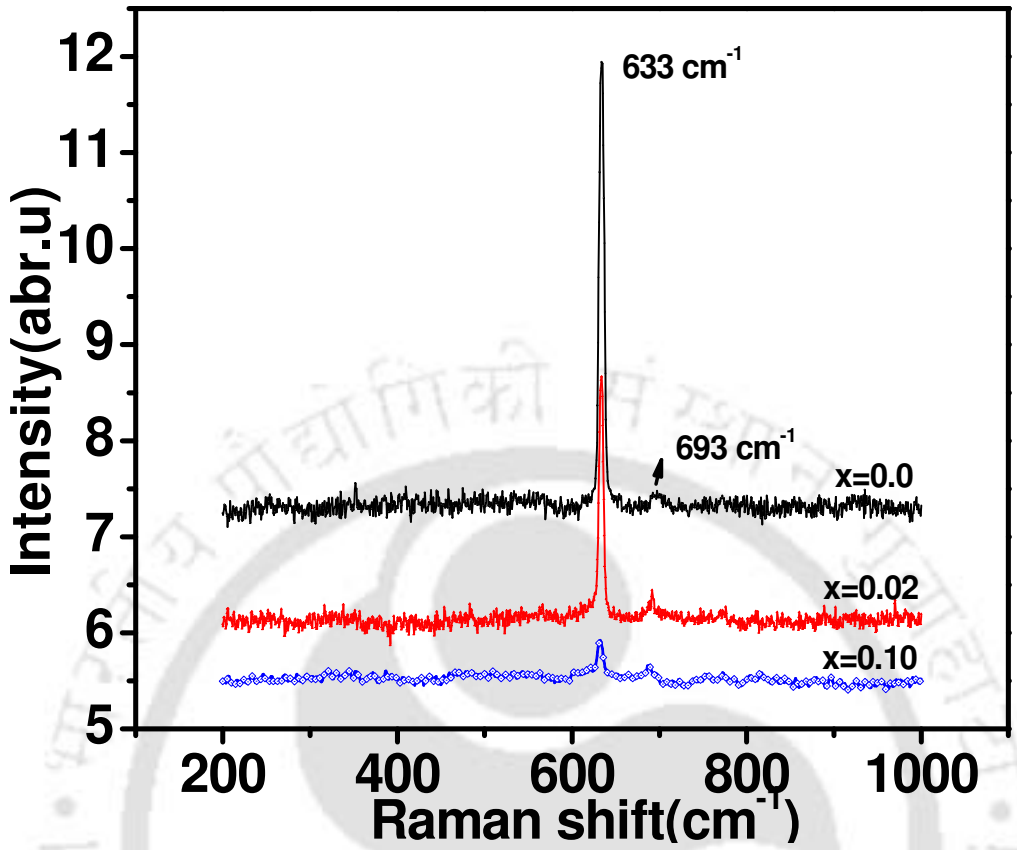

Fig.3.6 Room temperature Raman spectra of $Sn_{1-x}Co_xO_2$ for x= 0.0, 0.02, 0.10 sample.

3.1.2 Magnetic Properties

The field variation of magnetization at different temperatures and temperature variation of magnetization in the temperature range of 400 K to 1000 K were measured by using Lakeshore model no.7410 vibrating sample magnetometer (VSM). Typical magnetization loops recorded at two different temperatures namely 85 K and 400 K are shown in Fig.3.7 for all the Co doped samples. The magnetization data are expressed in the unit of μ_B/Co-ion, and it was calculated from emu/mole by taking into account the actual Co concentration in the material. They all exhibit ferromagnetic behavior even at 400 K. The 2 at % Co-doped sample exhibits magnetic saturation with its magnitude considerably larger than that of other higher concentration of Co doped samples. In addition to the FM behavior, considerable linear contribution can be seen especially for $x \geq 0.05$ at low temperature and it suggests the presence of considerable

paramagnetic matrix in the system. The saturation magnetization M_s and coercivity H_c values for all the Co-doped samples are given in table-3.3.

The saturation moment of 0.036 μ_B/Co-ion (0.19emu/cm^3) has been observed for x = 0.02 at 400 K and it enhances to 0.055 μ_B/Co-ion (0.28emu/cm^3) when the temperature is reduced to 85 K. As the temperature is reduced, there is a considerable increase in hysteresis loss due to the possible enhancement in magnetic anisotropy or other competing magnetic interaction. The M-H curve of N_2 annealed x = 0.02 sample is shown in Fig.3.8 and we can see a large increase in magnitude of magnetization compared to air annealed material. The N_2 annealing is expected to reduce the oxygen content in the sample and that leads to electron doping in the material. In other words, there would be an increase in electron concentration with N_2 annealing. Thus enhanced carrier concentration plays an important role in ferromagnetic interaction.

Table-3.3 Coercive Field (H_c) and saturation magnetization (M_s) determined for $Sn_{1-x}Co_xO_2$ samples.

Sample/Parameters	**x = 0.0**	**x = 0.02**	**x = 0.05**	**x = 0.07**	**x = 0.10**
H_c Oe (85 K)	diamagnetic	4100	3776	3434	2975
H_c Oe(400 K)	----------	529	929	499	887
M_s emu/gm(85 K)	----------	0.042	0.047	0.016	----------
M_s emu/gm(400 K)	----------	0.022	0.024	0.028	0.019

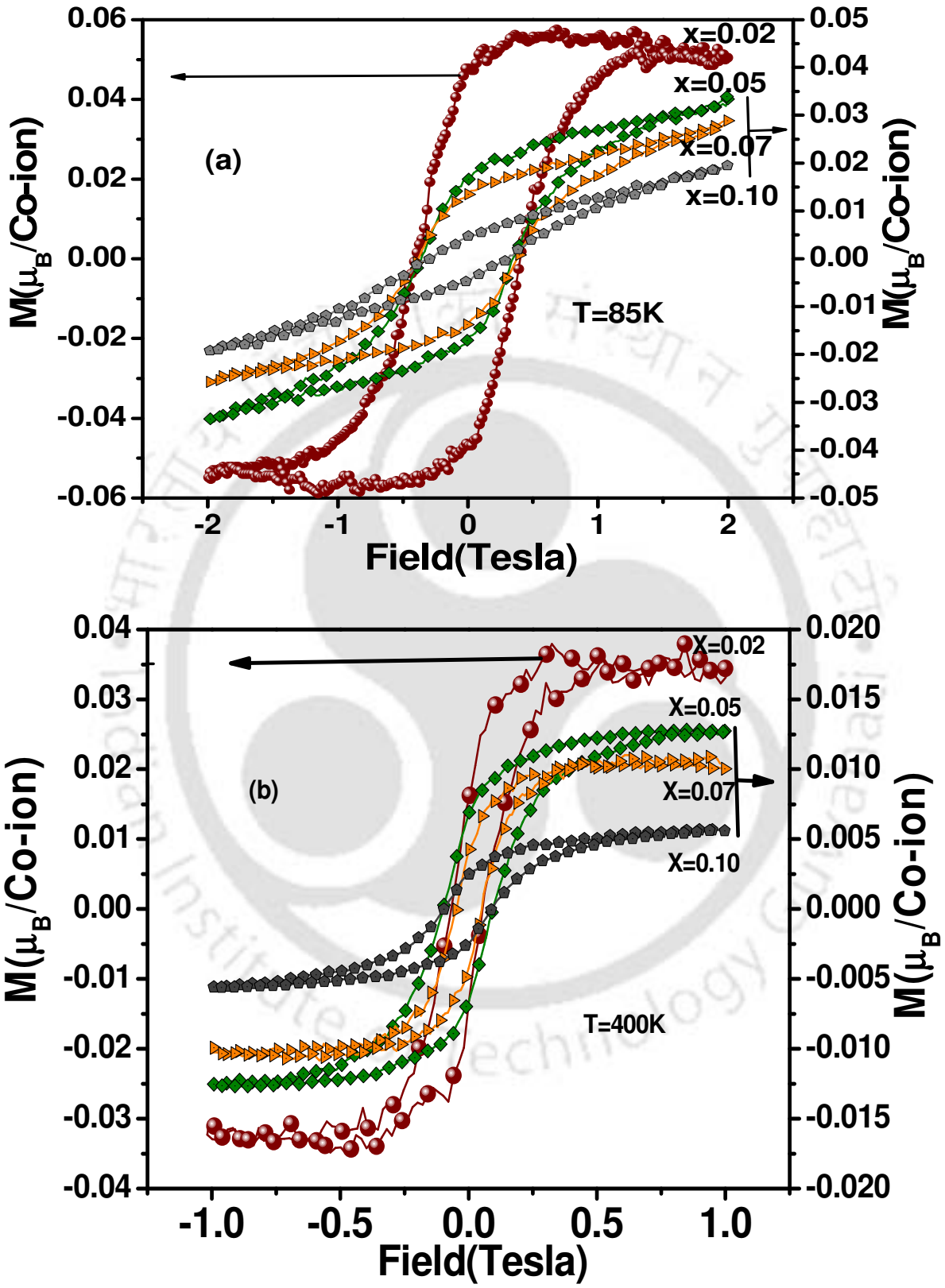

Fig.3.7 M-H loops recorded for $Sn_{1-x}Co_xO_2$ samples at (a) 85 K and (b) 400 K for x=0.02, 0.05, 0.07, 0.10.

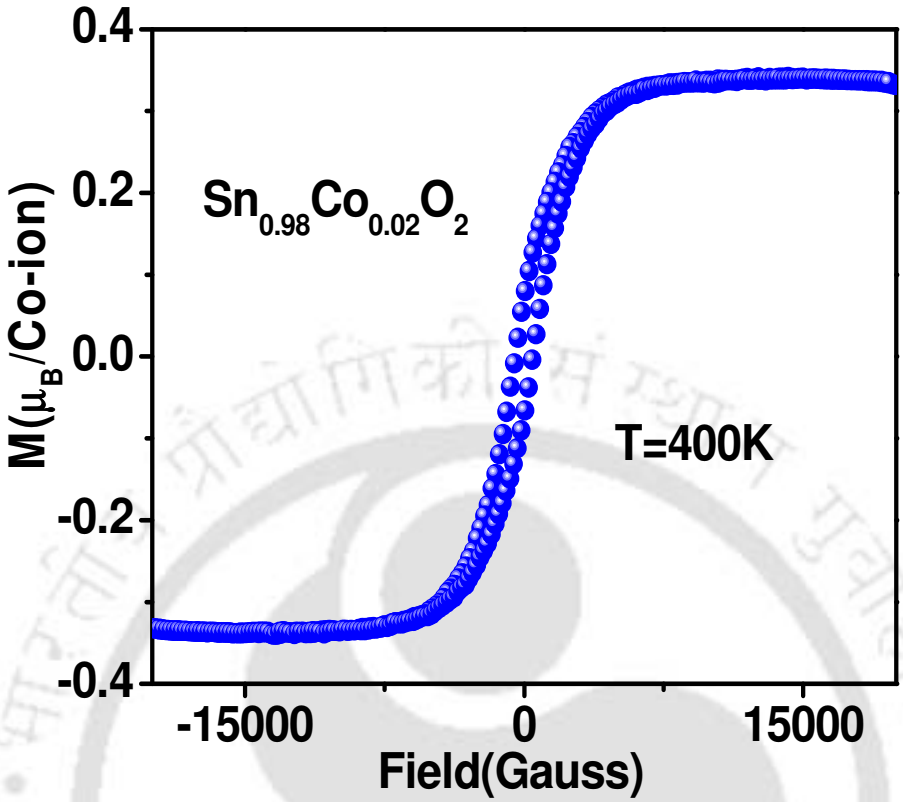

Fig.3.8 Magnetic hysteresis loop of nitrogen annealed $Sn_{0.98}Co_{0.02}O_2$ sample recorded at 400 K.

In order to further understand the magnetic properties, we have analyzed the measured initial M-H curves of the air annealed samples in terms of bound magnetic polaron (BMP) model by following refs [112, 113, 255] i.e.

$$M=M_0L(x) + \chi_m H \quad \text{.....} \quad (3.2)$$

Here the first term is from BMP contribution and the second term is due to paramagnetic matrix. Here $M_0=Nm_s$, N is the number of BMPs involved and m_s is the effective spontaneous moment per BMP. $L(x) = cothx-1/x$ is the Langevin function with $x = m_{eff}H/(k_BT)$, where m_{eff} is the true spontaneous moment per BMP. At relatively high temperature, where the interaction between BMPs can be ignored; $m_s = m_{eff}$ can be taken [112]. However at sufficiently high temperature, where there is a considerable mobility of charge carriers, so, eq.3.2 cannot be used due to the lack of BMP. χ_m is the susceptibility of the matrix. The M-H curves recorded at three different temperatures namely 85 K, 295 K and 400 K could be fitted to eq.3.2 for samples with $x \geq 0.05$. Intial M-H curves of different samples measured at 295 K along with BMP model fit are shown

in Fig.3.9(a). BMP fit of magnetization measured at different temperatures for x = 0.05 and 0.07 samples are shown in Fig. 3.9(b) and (c) respectively. The fitted parameters M_0, χ_m and m_{eff} are given in table-3.4.

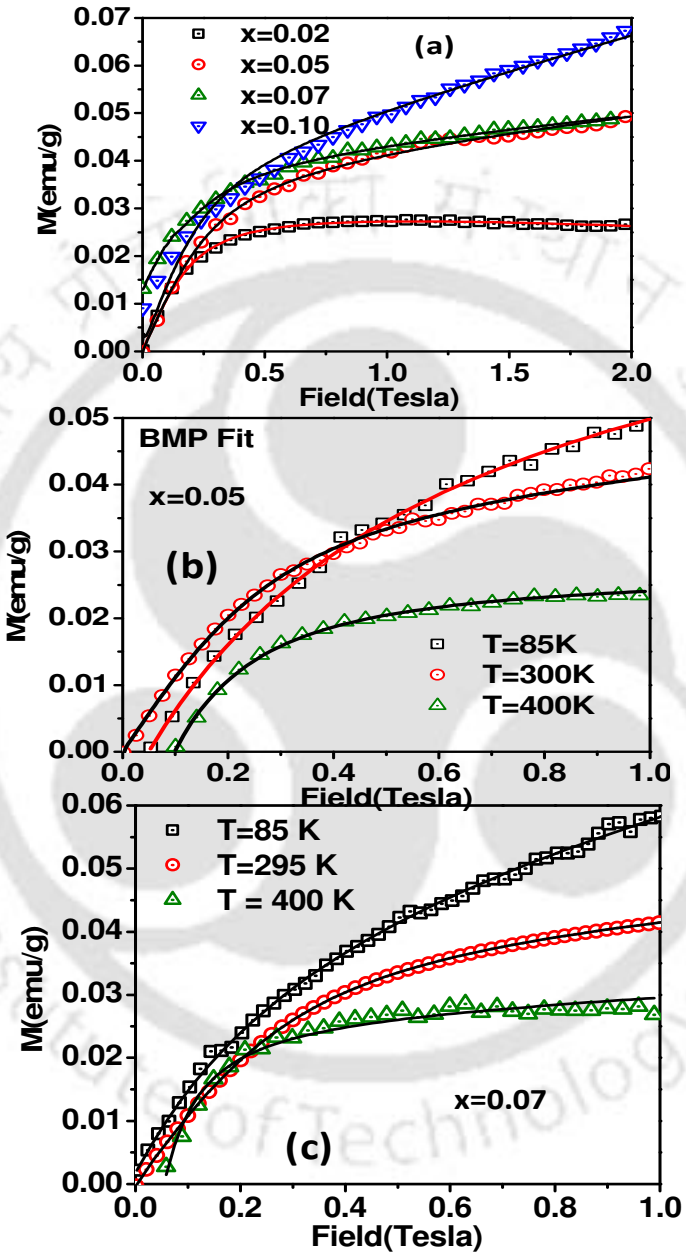

Fig.3.9 (a) Magnetization versus field at 295K, for x= 0.02, 0.05, 0.07 and x=0.10 samples of $Sn_{1-x}Co_xO_2$. The solid lines represent the fit to Bound magnetic polaron model (eq.3.2). Temperature variation of M-H curves **(b)** for x=0.05 and **(c)** 0.07 samples along with the BMP fit.

Table 3.4: List of parameters obtained from the bound magnetic polaron model fit. M_0 is the spontaneous magnetization, χ_m is the susceptibility of the matrix and m_{eff} is the effective spontaneous moment per bound magnetic polaron.

Sample/ parameter	***x=0.05***			***x=0.07***		***x=0.10***		
Temperature (K)	85	295	400	85	295	85	295	400
M_0(emu/g)	0.06	0.04	0.02	0.06	0.04	0.05	0.04	0.02
χ_m(10^{-4} cgs)	0.03	0.03	0.002	0.09	0.03	0.12	0.11	0.003
m_{eff}(10^{-17} emu)	0.42	3.8	5.2	0.41	3.3	0.22	2.7	4.5
BMP radius (Å)	38	72	80	31	61	22	51	80

For a given doping concentration, the M_0 values are found to decrease with increase in temperature and this can be understood as a result of the decrease in ferromagnetic interaction with increase in temperature. On the other hand, M_0 value is found to decrease with increase in doping concentration and such a decrease in ferromagnetic interaction with increase in doping concentration has been reported in Mn-doped SnO_2 based diluted magnetic semiconductor [198]. It is mainly due to a reduction in average Co-Co inter-atomic distance, which might contribute to nearest neighbor antiferromagnetic interaction at the expense of ferromagnetism. The paramagnetic susceptibility χ_m is found to decrease with increase in temperature as expected for any paramagnetic matrix and its value marginally increases with increase in doping concentrations. The spontaneous moment per BMP, m_{eff} is found to increase with temperature and such a variation of m_{eff} is in contradiction to the variation of M_0 and it can be understood as a result of increase in size of BMP with temperature. At higher temperature, even though the magnetic moments are aligned parallel within each BMP, the overall alignment of BMPs along the applied field may not be complete due to the increase in thermal energy. The value of m_{eff} is found to be in the order of 10^{-17} emu (10^{-20} J/T) and it is comparable to that reported by Quintero *et al.* [114] in p-type $Cu_2FeGeTe_4$. However, the present m_{eff} value is found to be one order of magnitude larger than that reported in $Cu_2Mn_{0.9}Zn_{0.1}SnS_4$ and $Y_{0.9}Ce_{0.1}MnO_3$ [112, 256]. In the present series of samples, the parameter M_0/m_{eff} is found to vary with temperature, so in such condition, one cannot assume $m_s = m_{eff}$. In view of above the restriction, we could not estimate N, the number of BMP per unit volume. The average radius of the BMP was estimated from the

fitted value of m_{eff} and by assuming a spherical shape of BMP. The typical radius of BMP for x=0.05 sample is found to be 38 Å. Our result is comparable to that reported by Dietl *et al.* [6] in CdMnSe based DMS, where the radius was determined to be 40 Å. The BMP radius at different temperatures and doping concentrations are given in table-3.4

The magnetization data of N_2 annealed sample could not be fitted to BMP model; on the other hand it could be fitted to the Brillouin function model by taking into account the ferromagnetic contribution.

$$M = M_S B_J(x) \quad \text{..... (3.3)}$$

$$M_S = ng\mu_B S \text{ and } B_J(x) = \frac{1}{S}\left[\left(S+\frac{1}{2}\right)\coth x\left(S+\frac{1}{2}\right) - \frac{1}{2}\coth\frac{x}{2}\right]$$

Here n is the number of magnetic atoms per unit volume, S is the magnetic spin quantum number and $x = \frac{g\mu_B B}{kT}$. The fitted data are shown as solid line in Fig.3.10, which closely follow the experimental data. The values of S and M_s are found to be 1.38 and 0.23 emu/g respectively. The S value suggests the presence of Co^{2+} ions in high spin state and however, we cannot rule out the presence of Co^{3+} ions. The magnetization data of air annealed x=0. 02 sample could not be fitted to the Brillouin function model due to the weak signal.

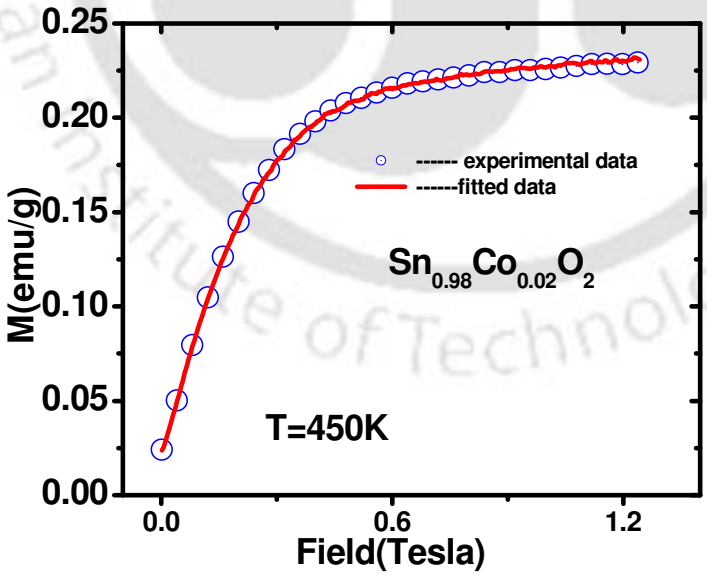

Fig.3.10 The initial magnetization curve along with Brillouin function model fit for N_2 annealed x=0.02 sample.

In order to study the ferromagnetic transition, the temperature variation of magnetization was measured in the temperature range 400 to 1000 K for an applied field of H=0.2T. The M-T curves for all the Co-doped samples are shown in Fig.3.11, where a clear paramagnetic to ferromagnetic transition can be seen. The magnetization is found to increase gradually with decrease in temperature. The paramagnetic susceptibility was fitted to Curie-Weiss law,

$$\chi = \frac{C(x)}{T - \theta_c} \quad \ldots\ldots\ldots\ldots\ldots\ldots\ldots\ldots\ldots\ldots\ldots\ldots\ldots\ldots\ldots\ldots\ldots\ldots\ldots\ldots\ldots\ldots \quad (3.4)$$

where, $C(x) = xC_0 = xn\mu_{eff}^2/3k_B$ is the Curie constant, where x is the concentration of doped Co, θ_c is Curie temperature. The Curie temperature is found to be 692 K for x = 0.02 and it gradually decreases to 582 K for x = 0.10 sample as shown in Fig. 3.12. The effective magnetic moment μ_{eff} estimated from Curie constant is found to vary from 1.3μ_B/Co-ion to 1.9μ_B/Co ion which suggests that the Co-ions are mostly in the Co^{2+} lowspin state. The theoretical effective magnetic moment of Co^{2+} ion in the low spin state is μ_{eff}^{th} = 1.73. The Curie temperature and the effective magnetic moment values for all the Co-doped samples are given in table-3.5

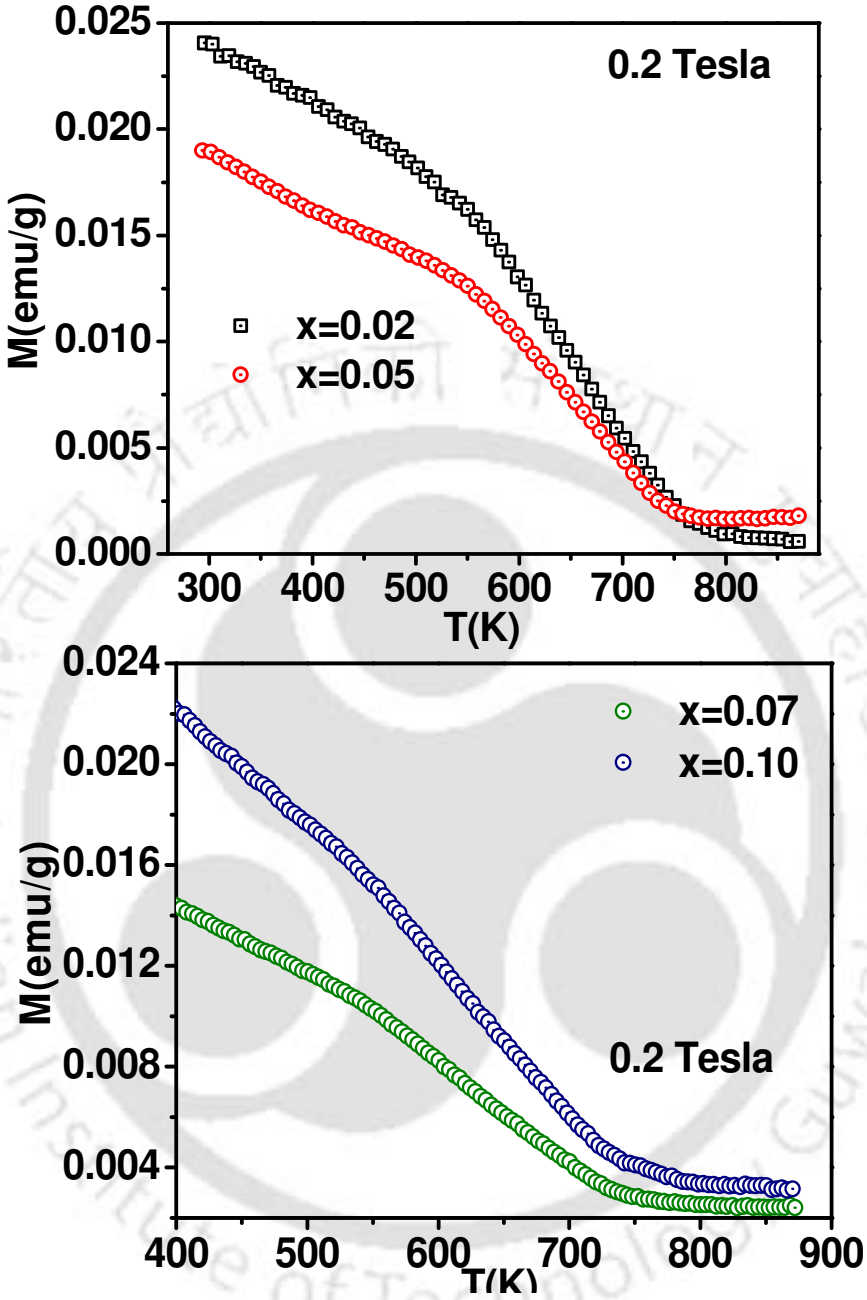

Fig.3.11 M-T plots for $Sn_{1-x}Co_xO_2$ (x=0.02, 0.05, 0.07 and 0.10).

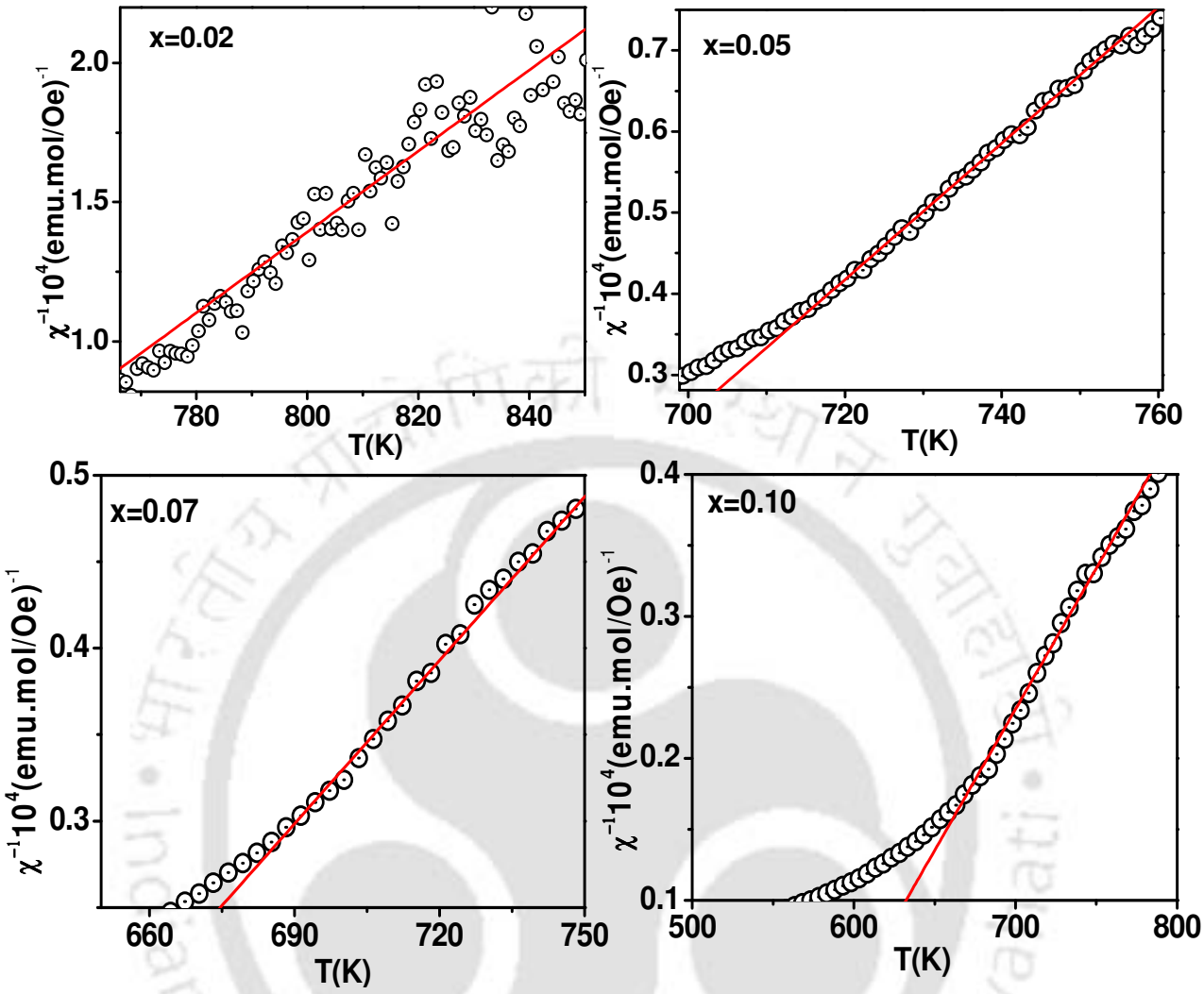

Fig.3.12 Plots of χ^{-1} vs. T of solid state synthesized $Sn_{1-x}Co_xO_2$ (x = 0.02, 0.05, 0.07 and 0.10) samples along with the Curie-Weiss fit.

Table-3.5: Parameters obtained from Curie- Weiss fit. Here θ_c is the Curie temperature; μ_{eff} is the effective magnetic moment per Co-ion.

Sample/Parameters	x=0.02	x=0.05	x=0.07	x=0.10
θ_C (K)	696	670	595	582
μ_{eff} (μ_B)	1.65	1.37	1.9	1.92

3.1.3 ESR Analysis

ESR spectra in the temperature range of 295 K to 445 K were recorded on $Sn_{1-x}Co_xO_2$ samples of solid state route. ESR spectra for x=0. 02, 0.07, 0.10 samples are shown in Fig.3.13 (a). We can see a shift in the resonance field towards the higher field with increase in doping concentration and it supports the magnetization results of decrease in FM interaction. In order to study the variation of ESR signal intensity with temperature, ESR signal were recorded at different temperature for x = 0.02, 0.05, 0.07 and 0.10 samples (air annealed). The spectra of integrated ESR signals at different temperatures for x = 0.02 sample are also shown in Fig.3.13. The observed increase in intensity with temperature can be explained as a result of increase in paramagnetic signal as it approaches towards Curie temperature. The observed low field shoulder in the above curves signifies the presence of ferromagnetism even above room temperature. The observed ESR signal could be simulated by using two Gaussian curves as shown as dashed lines in Fig. 3.13(b). The low field (LF) and the high field (HF) resonance peak values for all the samples with temperature variations are tabulated in table-3.6. As the temperature approaches 445 K, the signal could be reproduced by using single Gaussian function, where the material is close to the paramagnetic state.

Table-3.6 low field (LF) and high field (HF) resonance peak values obtained from two peaks Gaussian model fit.

Sample/ Temperature(K)	**x=0.02**		**x=0.05**		**x=0.07**		**x=0.10**	
	LF(mT)	**HF(mT)**	**LF(mT)**	**HF(mT)**	**LF(mT)**	**HF(mT)**	**LF(mT)**	**HF(mT)**
295	29±2	274±0.5	33±3	285±0.5	112±2.2	285±0.1	---------	294±0.1
345	65±4	286±0.9	75±5	285±0.7	165±3	284±0.3	---------	294±0.2
395	77±2	273±0.5	149±2	286±0.1	------	285±0.1	---------	295±0.1
445	-----	276±0.4	-----	286±0.2	-------	285±0.2	---------	295±0.3

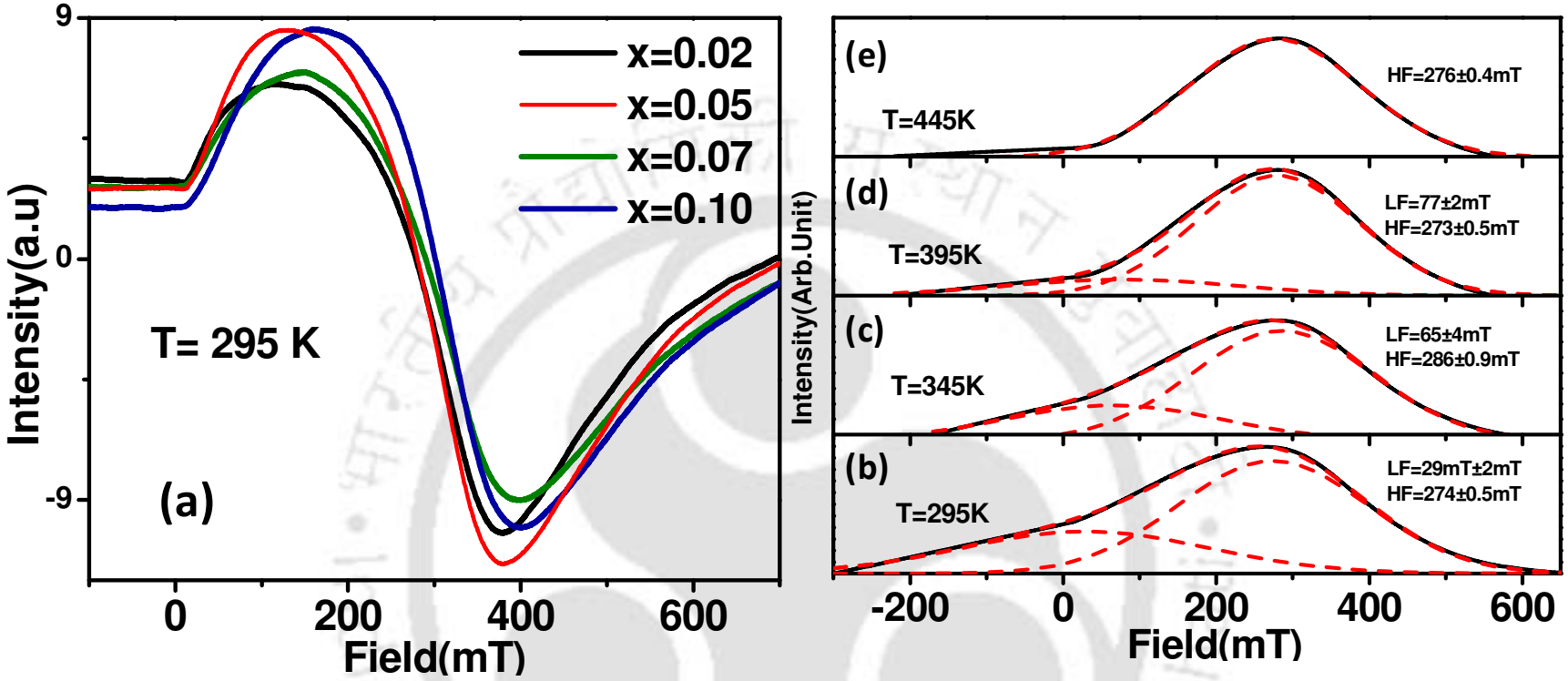

Fig.3.13(a). ESR spectra at room temperature for different samples of $Sn_{1-x}Co_xO_2$ and integrated ESR spectra for x=0.02(air annealed) sample recorded at (b) 295K, (c) 345 K, (d) 395 K, (e) 445 K respectively. The simulated data by using two overlapping Gaussian curves are also shown.

3.2 $Sn_{0.98}Co_{0.02}O_2$ by Co-precipitation

3.2.1 Preparation and Characterization

A Co doped (2 at % of cobalt) SnO_2 material was synthesized by co-precipitation technique. Here 1.48 mmol of $Co(NO_3)_2 \cdot 6H_2O$ and 82.5 mmol of $SnCl_2$ were dissolved in 150 mL of deionized water. To this pink solution, concentrated aqueous NH_3 was added drop wise with stirring, for about 1 hour. During this time the precipitation has ceased. Addition of NH_3 was stopped when the pH of the solution has reached about 12. Stirring was continued for another 2 hours and then the contents were left undisturbed. After 3 days, the solid Co-doped SnO_2 was separated from the colorless supernatant layer using a centrifuge and washed with deionized water. The crystalline Co-doped SnO_2 powder was dried in an oven at 80ºC for several hours. The same procedure was followed for obtaining pure/undoped SnO_2 from $SnCl_4$. The above product was heated at 200^{o}C for 12 hr followed by grinding. The precursor powder thus obtained was divided into different batches and were annealed at 400^{o}C, 600^{o}C and 800^{o}C in air and N_2 gas atmosphere respectively. Fig.3.14 shows the XRD patterns for different samples annealed under air and N_2 gas environment at atmospheric pressure. The air annealed samples at 400^{o}C, 600^{o}C, 800^{o}C are named as Sample-1A, Sample-2A and sample-3A respectively. Similarly the N_2 annealed samples at the corresponding temperature are named as Sample-1N, Sample-2N and Sample-3N respectively. The crystalline behavior is found to be enhanced with increase in annealing temperature. The XRD patterns could be refined to $P4_2/mnm$ space group by using the Reitveld refinement technique with the help of FullProf program. The typical XRD pattern, along with the refinement is shown in Fig.3.15 for the sample-3A and 3N, where all the observed peaks could be refined. The typical lattice parameters for SnO_2 and 2 at % Co-doped Sample-3N are a = b = 4.745Å, c = 3.192Å and a = b = 4.725 Å, c = 3.182 Å respectively. The lattice parameters are comparable to those reported by Bouaine *et al.* [253] in Co-doped SnO_2. The lattice parameters obtained from the refinement are tabulated in table-3.7. The lattice parameters are found to decrease with the introduction of Co ion and it indicates the incorporation of smaller ionic sized Co ions into the Sn sites. Similar kind of decrease in lattice parameters was observed in Co-doped SnO_2 samples prepared by solid state route (section 3.1.1).

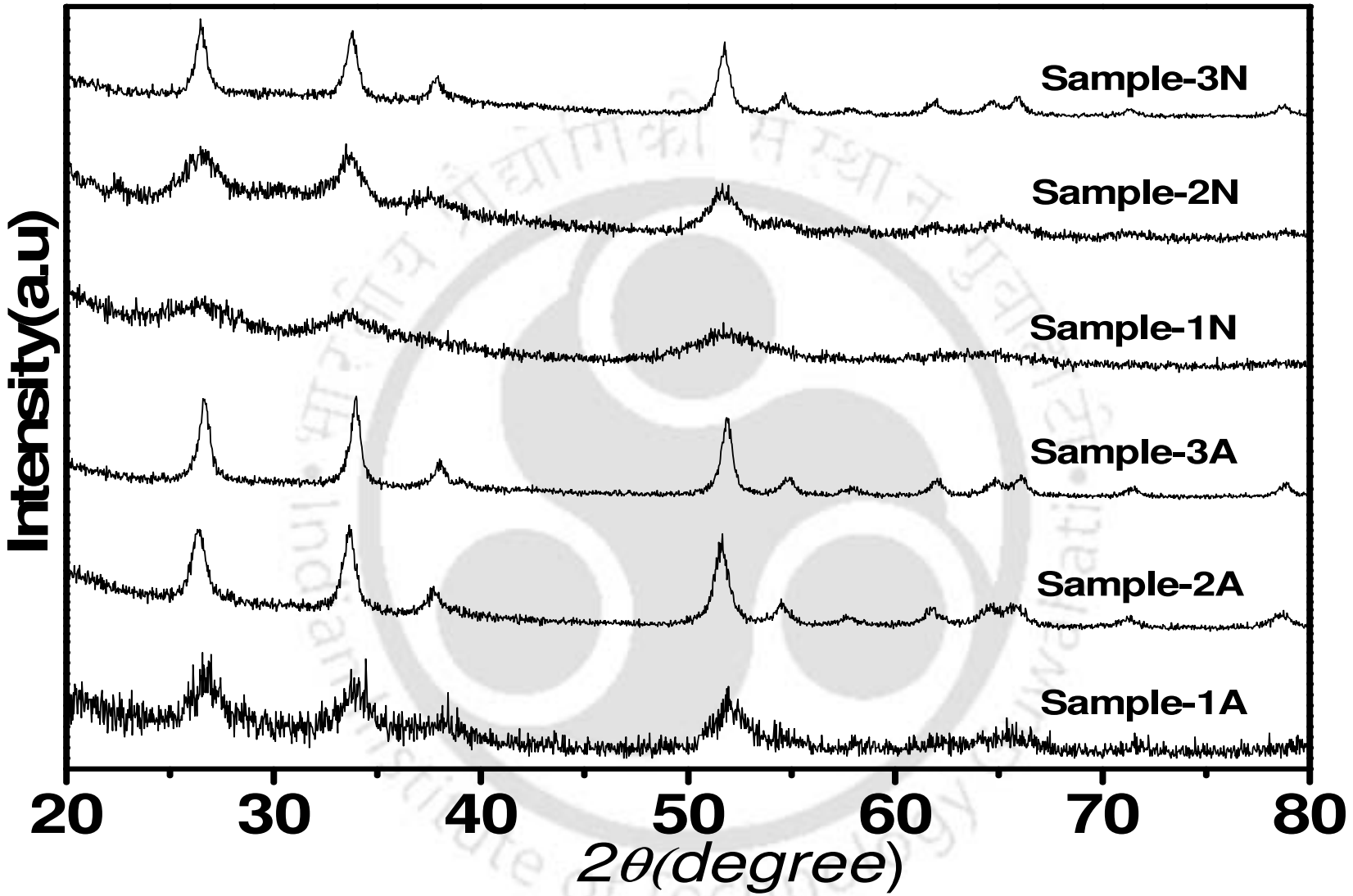

Fig.3.14. XRD patterns of $Sn_{0.98}Co_{0.02}O_2$ samples under different annealing conditions

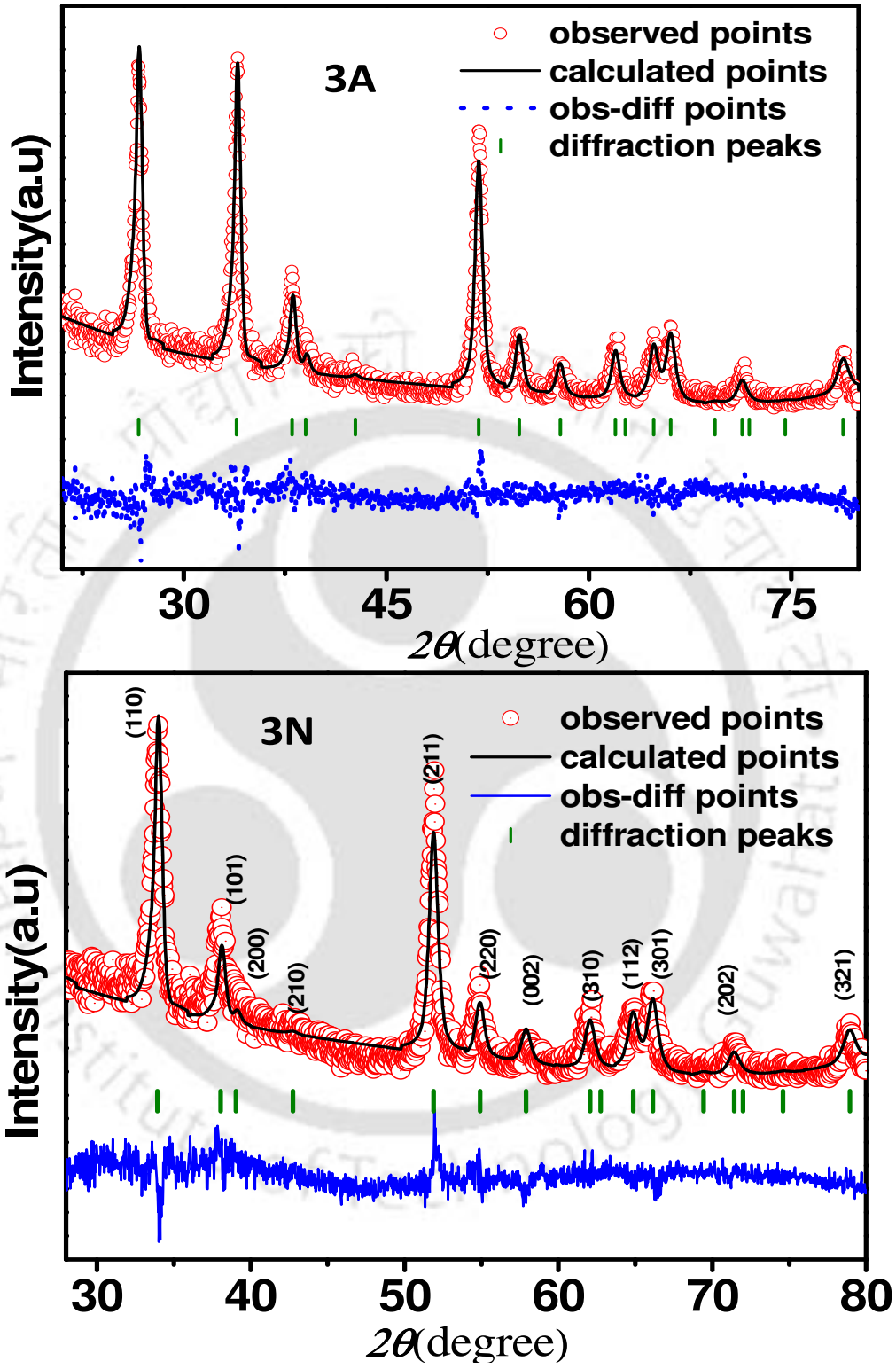

Fig.3.15. XRD patterns along with Rietveld refinement for the samples-3A and 3N.

The average crystallite size was calculated using the Scherrer's formula by using eq.3.1. The crystallite sizes for various samples are given in table-3.7. They depict the nanocrystalline phase of the prepared materials. The crystallite size is found to increase with annealing temperature. In comparison to our solid state route prepared Co doped SnO_2, where the crystallite size was of the order of 60 nm as given in table-3.1, here the highest crystallite size is found to be 15 nm.

Table-3.7. List of parameters obtained from the Rietveld refinement and analysis of XRD for 2 at % Co doped SnO_2 prepared by co-precipitation technique.

Sample/Parameters	**SnO_2**	**1A**	**2A**	**3A**	**1N**	**2N**	**3N**
Space group	$P4_2/mnm$	$P4_2/mnm$	$P4_2/mnm$	$P4_2/mnm$	$P4_2/mnm$	$P4_2/mnm$	$P4_2/mnm$
a = b (Å)	4.745	4.706	4.724	4.731	4.733	4.731	4.723
c (Å)	3.192	3.181	3.181	3.184	3.198	3.188	3.182
Volume ($Å^3$)	71.86	70.44	70.99	71.24	71.63	71.34	71.24
χ^2 (%)	3	2.63	2.18	1.80	2.44	4	1.8
R_p (%)	17	31	15	12	17	30	12
Crystallite Size(nm)	40	6	12	15	5	7	14

In order to confirm the absence of impurity phase or any clustering, we have carried out high resolution TEM analysis. Fig. 3.16 shows the images of Sample-3N taken in a carbon coated copper grid. The TEM image of particles and HRTEM image are shown in Fig.3.16 (a) and (b), where the (110) and (101) planes can be seen. Fig.3.16(c) shows the selected area diffraction (SAD) pattern. We have observed a faint ring pattern along with many bright spots and it suggests the polycrystalline nature of the particle. Many regions of the sample were searched; no trace of Co clustering has been detected from the EDS measurement done at different crystallites and it shows the substitution of Co-ions into the lattice and their uniform distribution. The Sn:Co atomic ratio was found to be 0.98: 0.015.

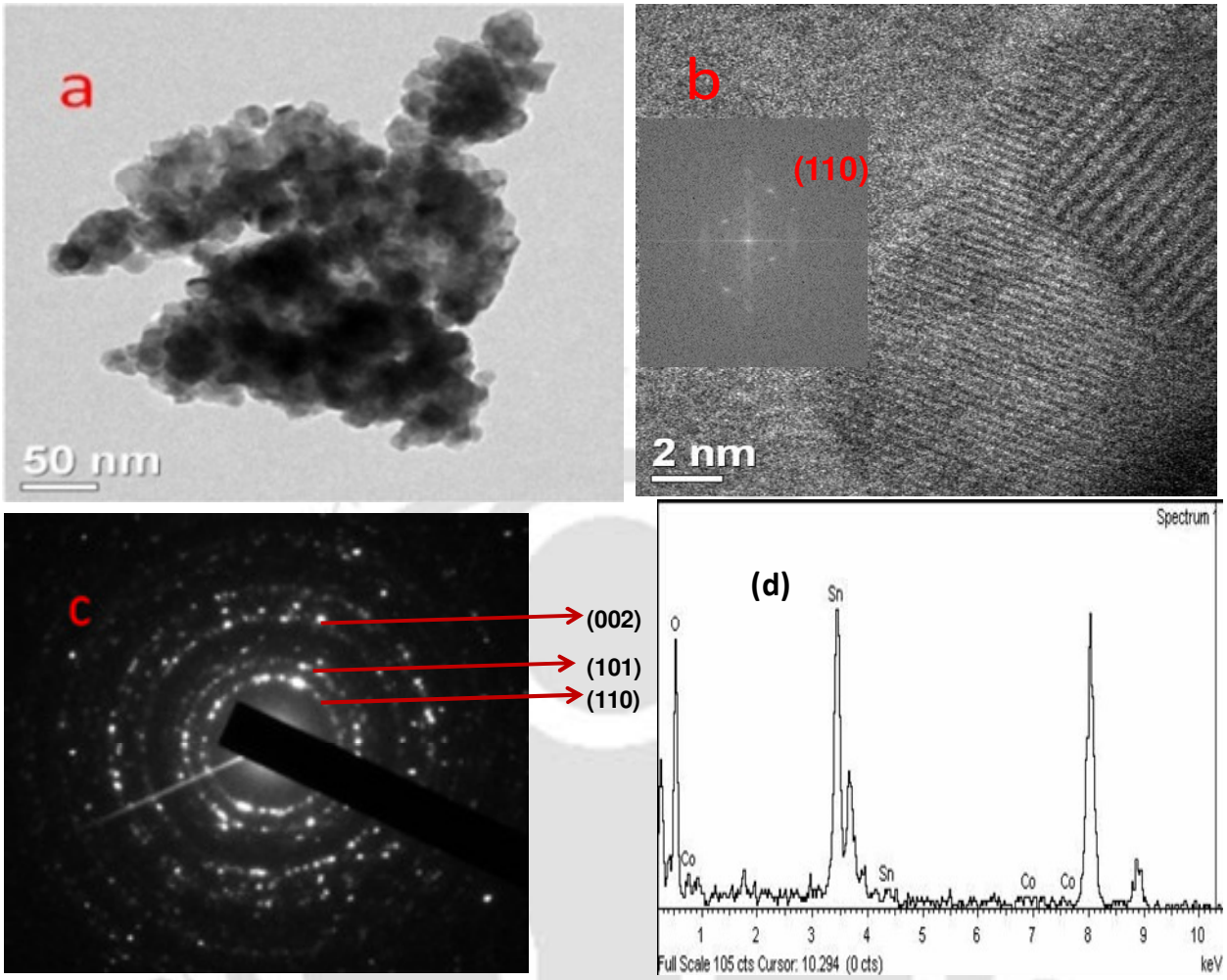

Fig.3.16 (a) TEM image of Sample-3N, (b) HRTEM image of the same sample, (c) SAD pattern, (d) EDX pattern of the Sample-3N.

Fourier transform infrared (FT-IR) spectrum in the wave number range of 400 to 4000 cm^{-1} was recorded for all the samples. Fig.3.17 shows the typical FTIR spectra for a few samples along with the parent SnO_2. The absorption band at around 3400 cm^{-1} and 1640 cm^{-1} are associated with the oxide surface hydroxyl group which is in O-H mode. The weaker band at, 1370 and 1130 $cm^{-1}$are because of the C-H vibrations, due the reaction between CO_2 from atmosphere with H_2O as reported in[257]. The bands at around 530 and 680 cm^{-1} correspond to Sn-O and Sn-O-Sn vibrations of SnO_2. So, it is evident from Fig.3.17 that the prepared samples exhibit pure rutile structure without any significant change in crystal structure due to Co substitution. We have not observed any peak due to Co_3O_4 or related compounds, so the doped Co ions are expected to replace the Sn^{4+} without forming any clustering. If we observe the sharpness of the

peaks, it increases with increase in annealing temperature because of the increase in crystalline behavior, which is in good agreement with the XRD data.

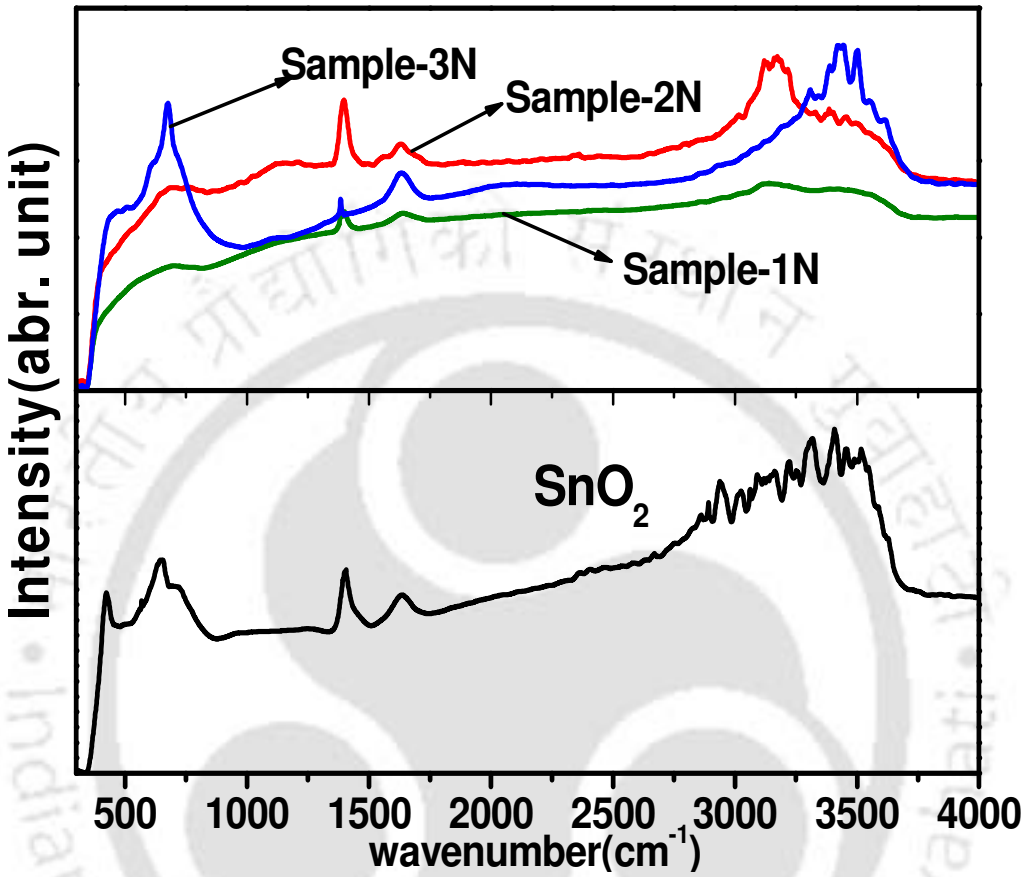

Fig.3.17. FTIR spectra for N_2 annealed Co doped samples along with the parent SnO_2 for comparison.

3.2.2 Magnetic Properties

Fig.3.18 shows the M-H loops recorded for all the samples. The nitrogen annealed samples exhibit improvement in ferromagnetism compared to air annealed samples, although having a weak magnitude. From Fig.3.18, we can infer that as the annealing temperature is increased, the magnitude of magnetization increases. Such phenomenon can be explained as a result of the increase in oxygen vacancy, which encourages the formation of bound magnetic polaron and ferromagnetic interaction. Moreover the crystallite size may also play a role in restricting the range of BMP interaction leading to FM. In materials prepared under normal conditions with relatively large crystallite size of the order of 40nm, the magnetization value was found to be larger as discussed in (section 3.1.2).

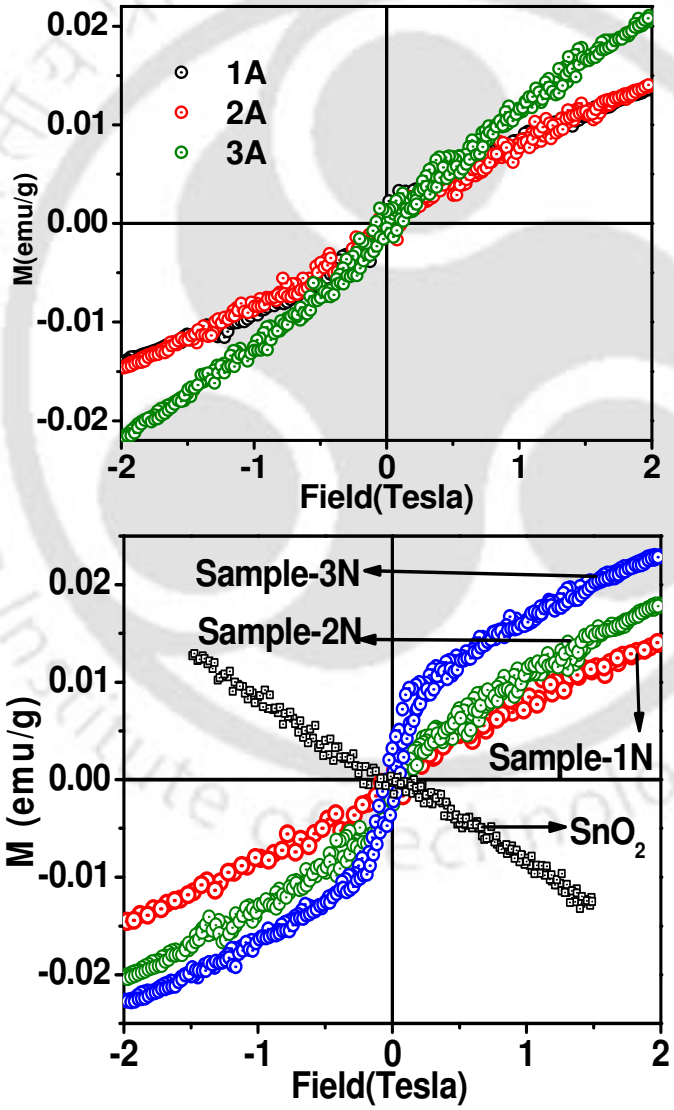

Fig.3.18. Hysteresis loop recorded for air annealed and N_2 annealed samples at room temperature.

3.2.3 Electrical Resistivity Measurement

The temperature variation of electrical resistivity was measured by using two probe technique. The electrical resistivity of air annealed samples at room temperature are found to be in the order of 10^9 Ω-cm, and their temperature variation could not be measured because of large resistance beyond the measuring limit of the instrument used. On the other hand, the electrical resistivity of nitrogen annealed samples are found to be about two orders of magnitude smaller than that of the air annealed material. Fig. 3.19 shows the resistivity vs. temperature plot for the N_2 annealed samples. The values of resistivity at 70 K for 1N, 2N and 3N samples are found to be 8 x 10^7Ω-cm, 3.4 x 10^7Ω-cm and 3 x 10^7Ω-cm respectively and it reduces to 0.03 x 10^7Ω-cm, 0.02 x 10^7Ω-cm and 0.1 x 10^7Ω-cm respectively at 300 K.

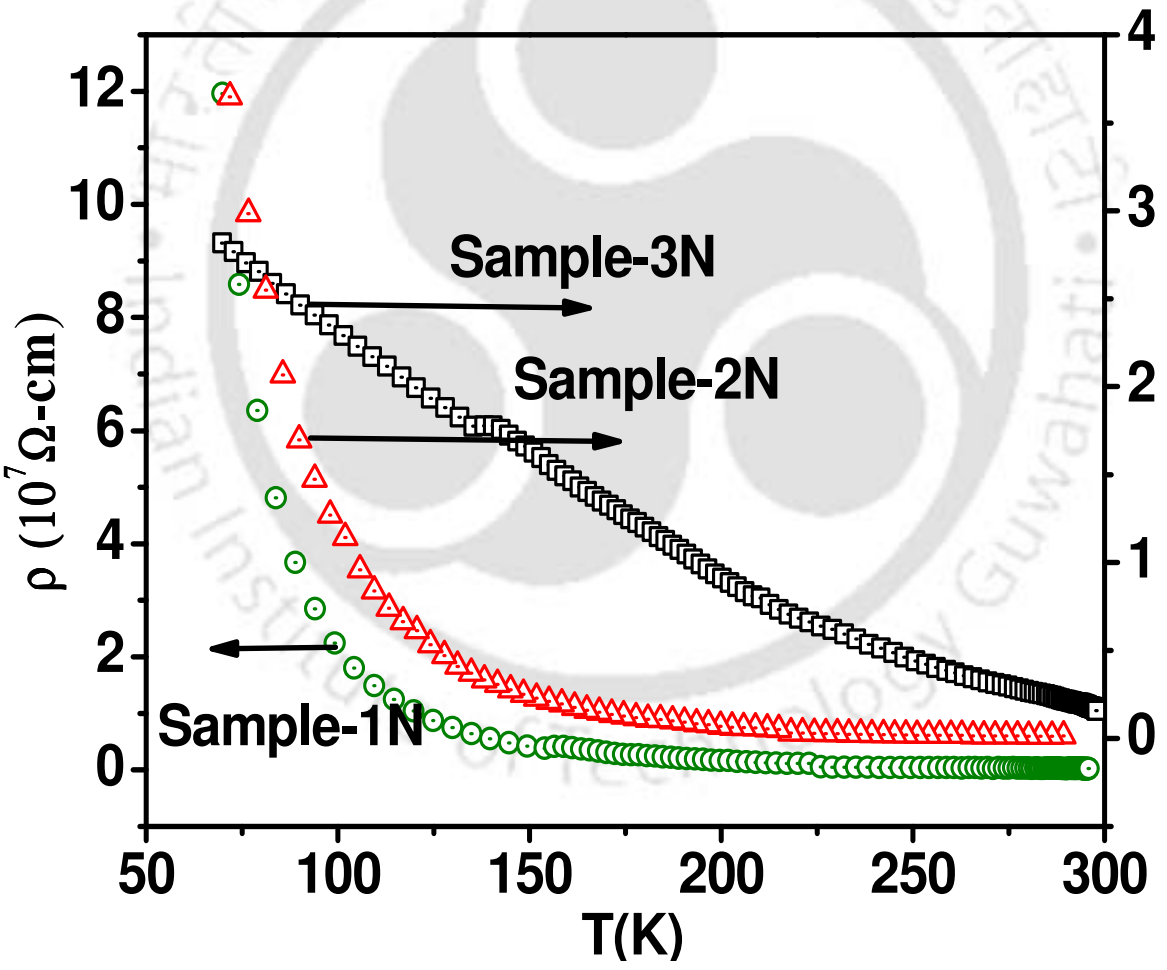

Fig.3.19 Temperature variation of resistivity for samples 1N, 2N and 3N.

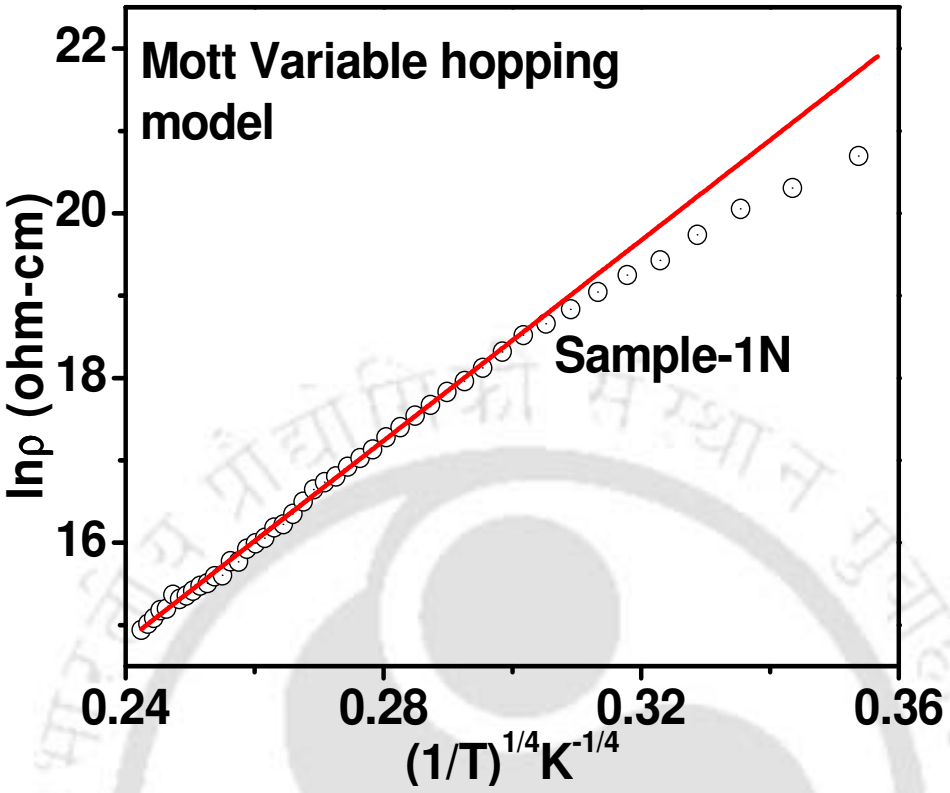

Fig.3.20. Variation of resistivity with temperature for 400°C N_2 annealed $Sn_{0.98}Co_{0.02}O_2$ (sample-1N).

The resistivity data of N_2 annealed sample could be analyzed based on the Mott variable hopping range model (VRH) using the eq.3.5 [148]

$$\rho = \rho_o \exp [T_o/T]^{1/4} \quad \ldots\ldots\ldots\ldots\ldots\ldots\ldots\ldots\ldots\ldots\ldots\ldots\ldots\ldots\ldots\ldots\ldots\ldots \quad (3.5)$$

Where ρ is the resistivity of the sample, ρ_o and T_o are constants.

Fig.3.20 shows the typical plot of ln (ρ) versus $(1/T)^{1/4}$ for Sample-1N, where the solid line is the fit to VRH model. From the fitted value of T_o and ρ_o, the density of states in the vicinity of Fermi level, $N(E_F)$, hopping distance $R_{hop}(T)$ and hopping energy $E_{hop}(T)$ are determined following ref. [148] and using eq.3.5. The density of states, hopping distance and hopping energy are found to be 1.67×10^{26} $eV^{-1}m^{-3}$, 25Å and 94meV respectively. The resistivity data for 2N and 3N samples could not be fitted based on the above model.

Thus the 2 at % Co doped SnO_2 samples prepared by co-precipitation technique exhibit weaker FM compared to the sample obtained from solid state route for the same composition. This can be explained in terms of reduced crystallite size and limited range of BMP interaction. N_2 annealing is found to show enhanced FM and electrical conductivity.

3.3 Ball Milled Pure SnO_2

3.3.1 Sample Preparation and Characterization

Two batches of commercially available SnO_2 (diamagnetic) of 99.9% purity were separately milled for 10hr by using steel and tungsten carbide (WC) vials respectively. The milling speed and balls to powder ratio were kept same for both the batches; the milling speed was 500 rpm and the ball to powder weight ratio was kept as 10:1. The as-milled samples on steel and WC vials are represented as samples S1 and T1 respectively. A part of the milled powder from each batch was pressed into cylindrical pellets and were annealed in air at 900^{o}C for 10 hrs. These annealed samples originated from steel vial milling and WC vial milling are represented as S2 and T2 respectively. XRD patterns of as milled samples T1 and S1 and annealed samples T2 and S2 along with commercial SnO_2 powder are shown in Fig. 3.21. XRD pattern of sample T1 shows the presence of minor impurity peaks corresponding to WC. However, upon annealing, i.e. sample T2 doesn't show any WC impurity. XRD patterns of samples S1 and S2 are found to be comparable to the commercial SnO_2 powders except that the widths of the peaks are quite broad in the prepared samples due to reduced crystallite sizes. XRD patterns were refined by choosing $P4_2/mnm$ space group in tetragonal cell. All the observed peaks in samples S1, S2 and T2 could be refined; the minor impurity peaks observed in T1 sample were excluded in the refinement. The XRD patterns for samples T1, S1, T2 and S2 along with Rietveld refinement are shown in Fig. 3.22 and Fig.3.23, where we can see the refined pattern closely following the experimental data. The lattice parameters obtained from the above analysis are given in table-3.8, they are comparable to the reported values in literature [250]. The lattice parameters of as-milled powders are found to relatively large compared to the commercial and annealed samples. This property can be easily correlated with nanocrystalline behavior of as-milled samples. The average crystallite size was estimated using the Scherrer's formula $S = \lambda k/\beta \cos\theta$. The average crystallite size values are found to be around 15 nm for as milled samples S1 and T1 and it is found to increase upon annealing as shown in table-3.8.

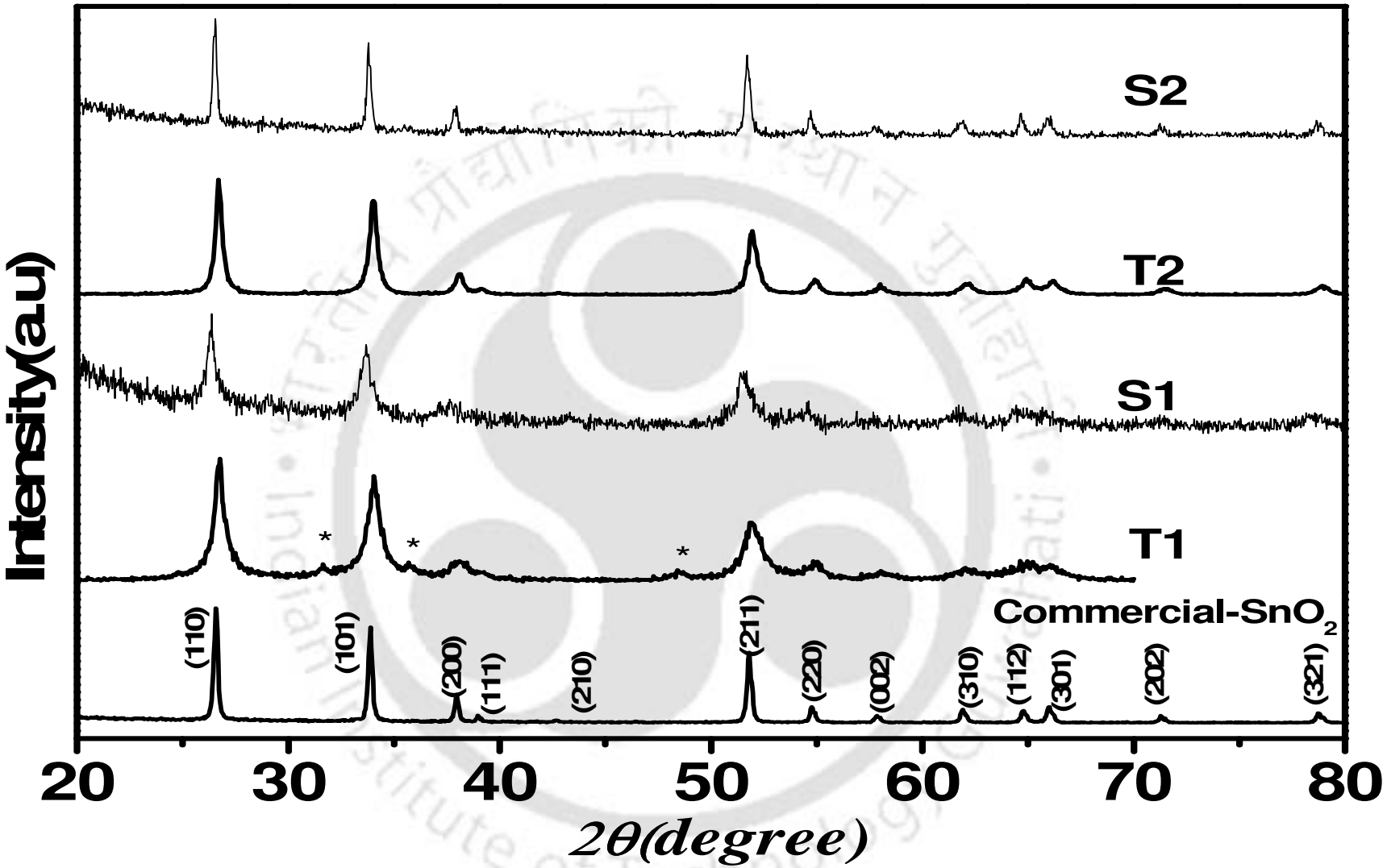

Fig. 3.21. XRD patterns recorded for samples T1, S1, T2 and S2 along with the un-milled commercial SnO_2. The star marks (*) represent WC impurity phase.

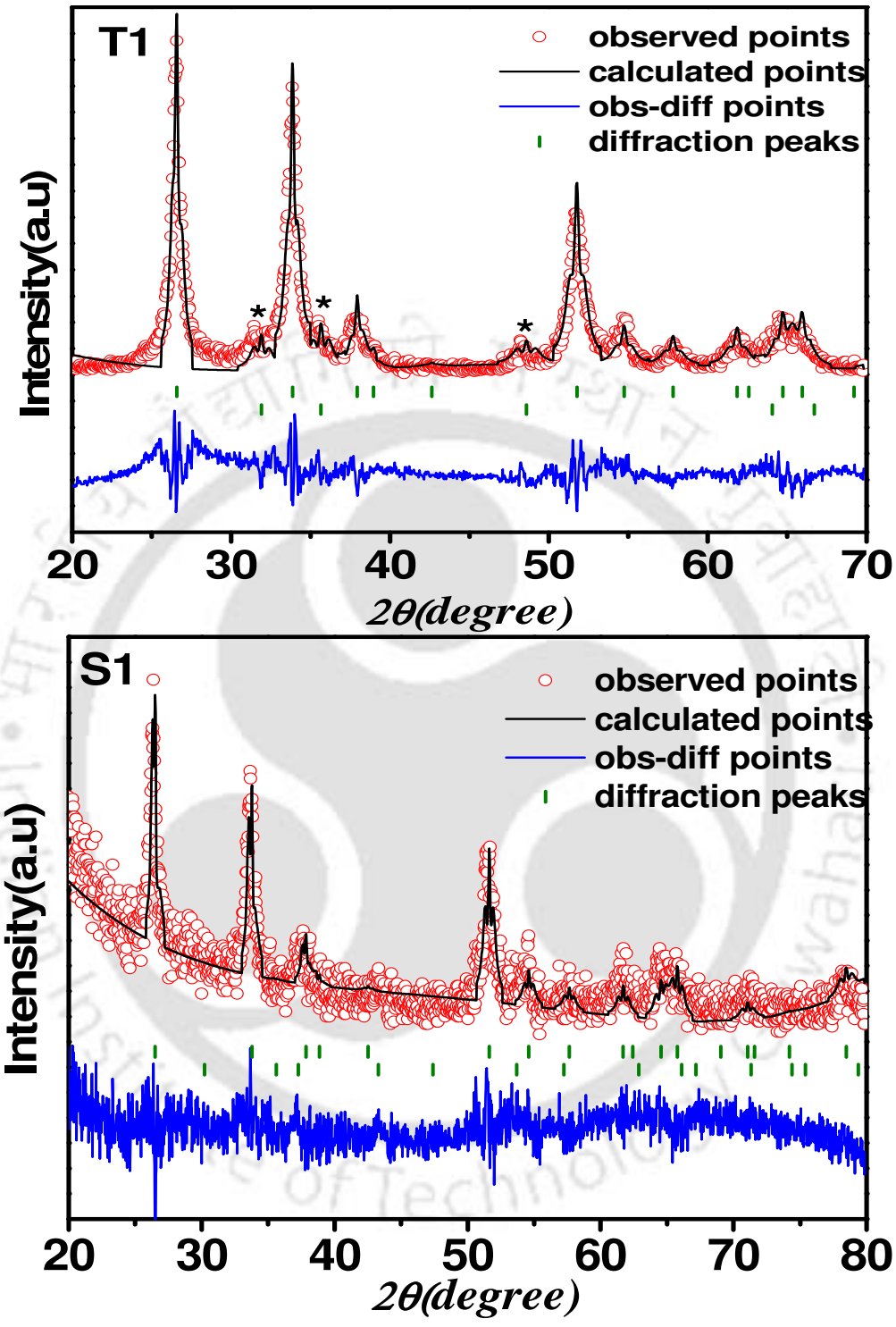

Fig. 3.22 XRD patterns along with Rietveld refinement for samples T1 and S1.

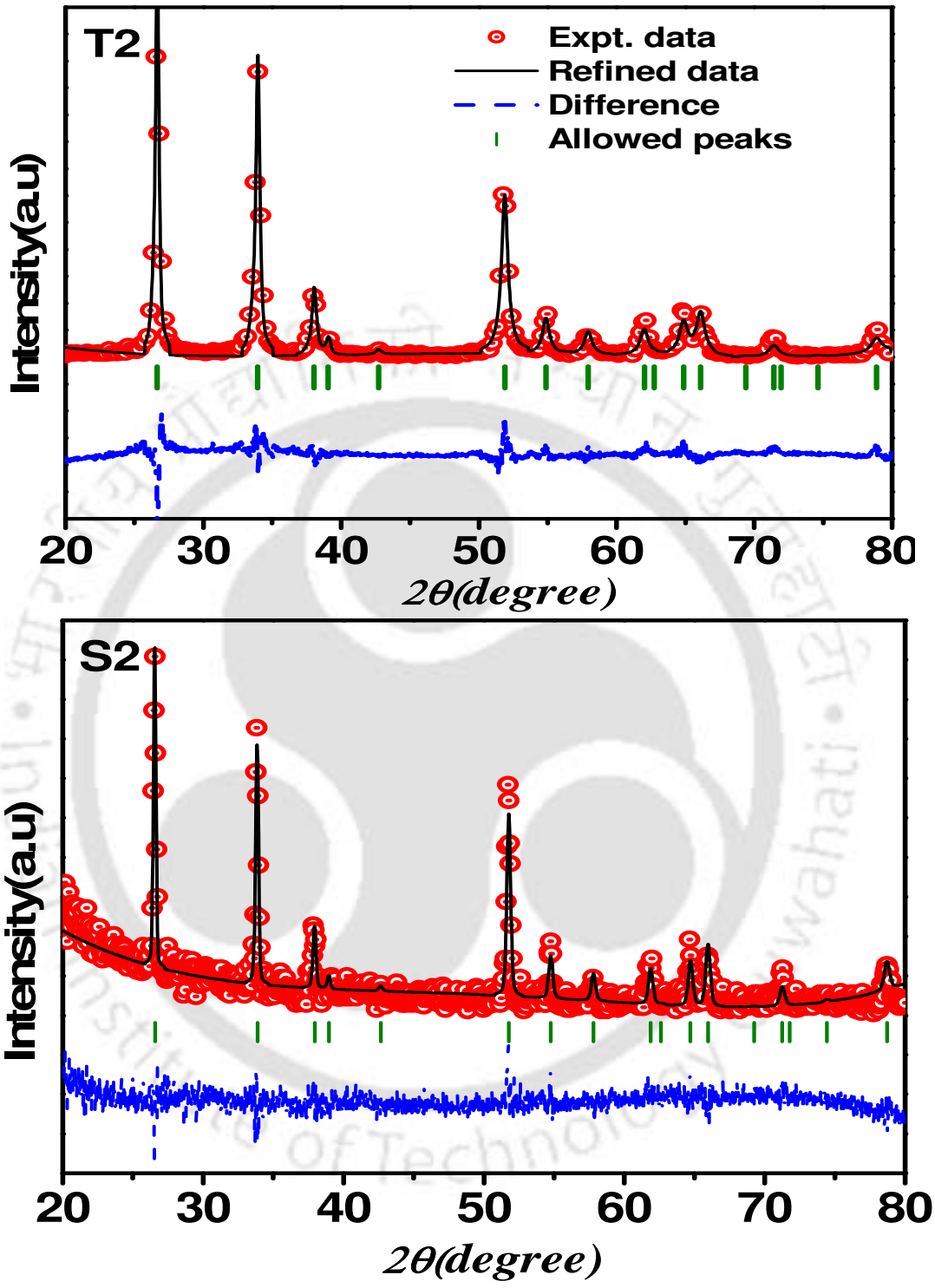

Fig. 3.23 XRD patterns along with Rietveld refinement for samples T2 and S2.

Table - 3.8: List of parameters obtained from the analysis of XRD patterns, magnetization data and ESR spectra.

Samples/Parameters	Commercial SnO_2	T1	S1	T2	S2
a=b(Å)	4.7311	4.737	4.749	4.7288	4.732
c(Å)	3.1826	3.185	3.195	3.181	3.185
χ^2(%)	1.39	2.42	1.99	3.24	1.31
R_p (%)	13.4	22	20.5	21.4	14.9
Crystallite Size(nm)	40	15	18	22	40
M_s(300K) emu/g	-	0.11	0.95	-	0.9
M_s(20K) emu/g		0.13	1.68		1
H_c(300K)Oe	-	841	430	-	440
H_c(20K)Oe		936	650		590
Resonance Field (mT)	-	106±0.3	H_l=101±0.5 H_h=269±0.4	-	293±0.5

Fig. 3.24 shows the typical SEM images of S2 and T2 samples along with their EDX pattern. The SEM images show uniform surface morphology. The EDX images show the presence of small fraction of Fe peaks along with Sn and O, for S1 and S2 samples and W related peaks for T1 and T2 samples respectively. The cation ratio obtained from EDX analysis are given in table-3.9.

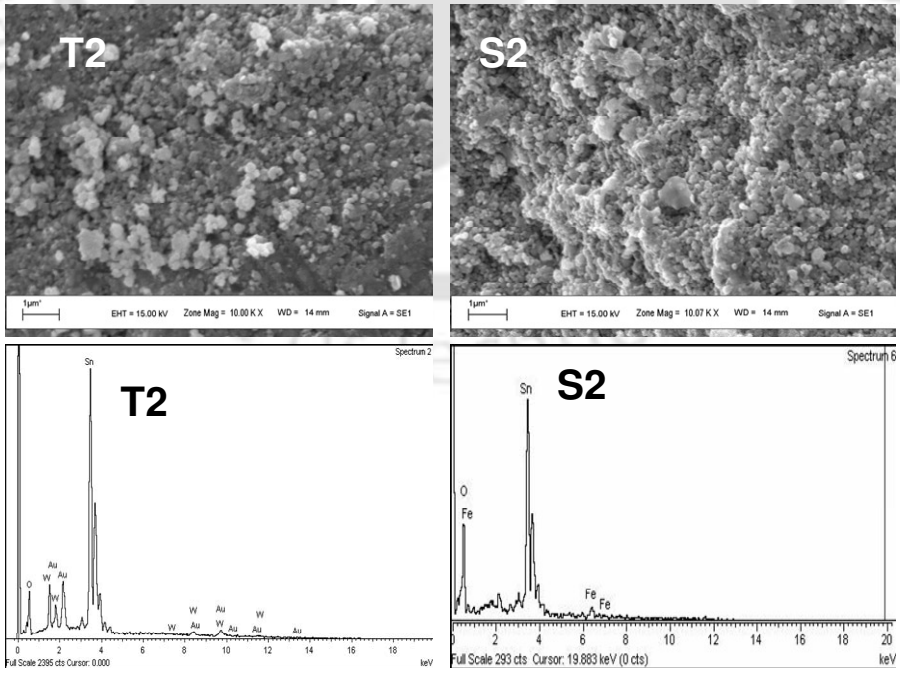

Fig. 3.24 SEM imageS recorded for S2 and T2 samples along with their EDX spectra.

Table-3.9: Cationic ratio obtained from EDX analysis for S1, T1, S2 and T2 samples.

Sample	Calculated Cationic Ratio from EDS		
	Sn	Fe	W
S1	0.94	0.05	------
T1	0.96	-----	0.03
S2	0.93	0.06	-----
T2	0.95	-----	0.04

The microstructure and the composition at crystallites level were studied by recording TEM images using JEOL-JEM 2100 transmission electron microscope (TEM) coupled with an EDS analyzer. Typical High resolution TEM image (HRTEM) and selected area diffraction pattern for samples T1 and S1 are shown in Fig.3.25. The HRTEM image shows the presence of (101) plane and the inset shows the Fast Fourier Transform (FFT) image. The d-values obtained from SAD pattern are found to agree with those of XRD analysis.

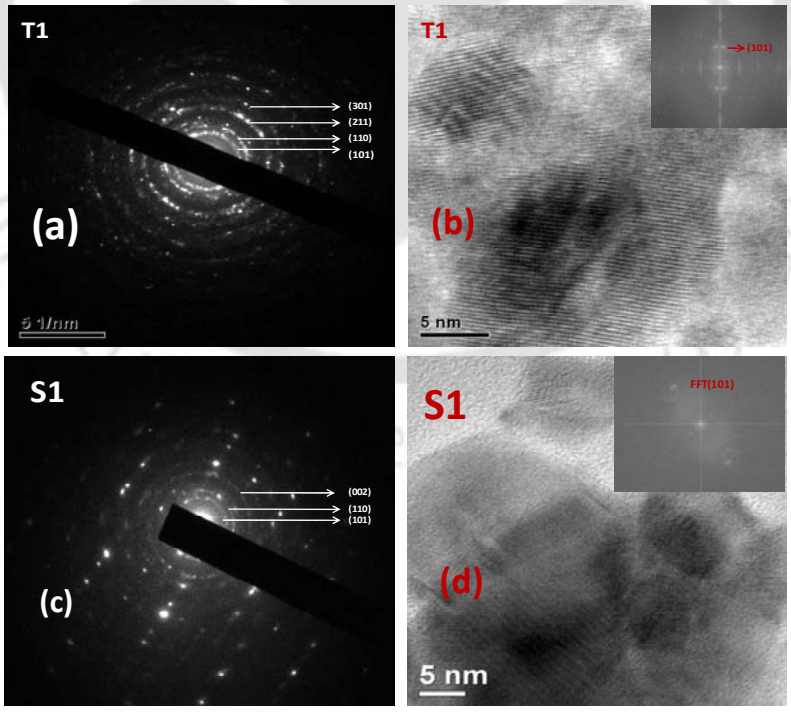

Fig.3.25. HRTEM and Selected Area Diffraction pattern images of samples T1 and S1. The inset shows the FFT image.

The samples were also characterized by recording Raman spectra using LabRam HR800 spectrometer. The Raman spectra recorded for T1, S1, T2 and S2 samples are shown in Fig.3.26. SnO_2 has the tetragonal rutile structure (space group D_{4h}^{14}, $P4_2/mnm$) with two SnO_2 molecules per unit cell. The number of allowed modes of vibrations is 15, the irreducible representations of the optic modes are

$$\Gamma = \Gamma_1^+(A_{1g}) + \Gamma_2^+(A_{2g}) + \Gamma_3^+(B_{1g}) + \Gamma_4^+(B_{2g}) + \Gamma_5^-(E_g) + \Gamma_1^-(A_{2u}) + 2\Gamma_4^-(B_{1u}) + 3\Gamma_5^-(E_u).$$

The 5 modes of A_{1g}, B_{1g}, B_{2g}, E_g are Raman active, 7 modes of A_{2u} and $3E_u$ are IR active and 2 modes of A_{2g} and B_{1u} are inactive [258, 259]. All the samples show the Raman shift at ~ 640 cm^{-1} which corresponds to A_{1g} (symmetric Sn-O stretching). This indicates the tetragonal rutile structure. The other peak observed at 693 cm^{-1} for S1 and S2 is because of the A_{2u}(LO), LO=longitudinal optic mode; which is basically IR-active but because of some disorder this become Raman active [259-261]. T1 and S1 samples exhibit the peak broadening effect and it depicts the presence of some amorphous phase. The peaks become sharper for T2 and S2, which depicts the improved crystalline nature of the samples upon annealing. The observed peak at 475 cm^{-1} for samples T1 and S1 corresponds to the E_g mode of vibration. However such peak was not observed for sample T2 and weak broad peak like feature can be seen for sample S2. As the E_g mode is the result of two oxygen atoms vibrating parallel to the c axis, but in opposite direction; it is more sensitive to oxygen vacancies than other modes[262]. So the vacancy related defects are dominant in samples T1 and S1.

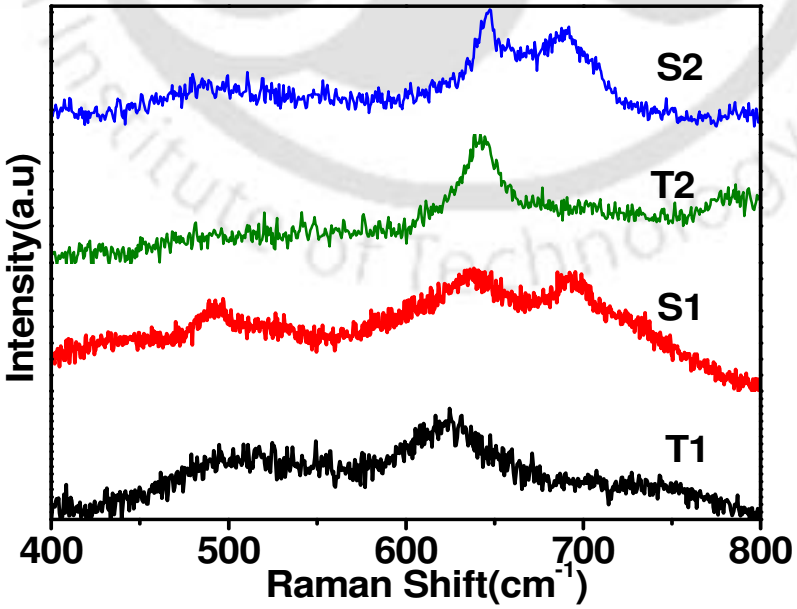

Fig. 3.26 Raman Shift for T1, S1, T2 and S2 samples collected at room temperature.

3.3.2 Magnetic Properties

The field variation of magnetization at different temperatures and the temperature variation of magnetization in the temperature range of 20 K to 1000 K were measured by using a Lakeshore vibrating sample magnetometer (VSM) of model no.7410.

The M-H loops were recorded at room temperature (300 K) and at T = 20 K. Fig.3.27 shows the M-H loops of as milled (T1 and S1) and annealed samples (T2 and S2). Surprisingly both the as milled samples T1 and S1 show room temperature FM without any transition element doping. Even though, sample T1 was milled by using non-magnetic WC vial and still room temperature FM has been observed. Both samples exhibit increase in hysteresis loss and saturation magnetization, M_s at low temperature. In addition to that, M-H loops at T = 20 K exhibit considerable linear behavior and it can be explained in terms of the presence of strong magnetic anisotropy or competing antiferromagnetic interaction. The values of the M_s and coercive field H_c are given in table-3.10. The H_c value is found to increase appreciably with decrease in temperature. The M-H curve of annealed sample T2 shows a diamagnetic behavior similar to that of commercial SnO_2. So, upon annealing the FM is destroyed.

The oxygen vacancy induced localized electron spin moments and their exchange interaction are known to play a role in room temperature ferromagnetism [249]. Theoretical calculations of Kilic and Zunger [233] suggest that oxygen vacancy has very low formation energy and would commonly exist in non-stoichiometric SnO_2. So, the observed FM in as milled sample T1 and its disappearance upon annealing, (T2) can be explained in terms of ferromagnetism originating from oxygen vacancy or other defects related mechanism. On the other hand, the annealed sample S2 shows FM but with reduced M_s value compared to the as milled sample S1. Another notable difference is that the presence of linear behavior of the magnetization curve observed in sample S1 has disappeared upon annealing and a complete saturation behavior is observed as shown in Fig. 3.27(d) for sample S2. No appreciable difference between the M_s value of T = 300 K and 20 K was observed. The reduction in M_s value of sample S2 compared to that of S1 can be understood in terms of reduced oxygen vacancy and defects upon annealing. Moreover, the presence of FM in sample S2, even after the annealing can be understood in terms of inadvertent doping of Fe in SnO_2 due to the contamination from steel vial.

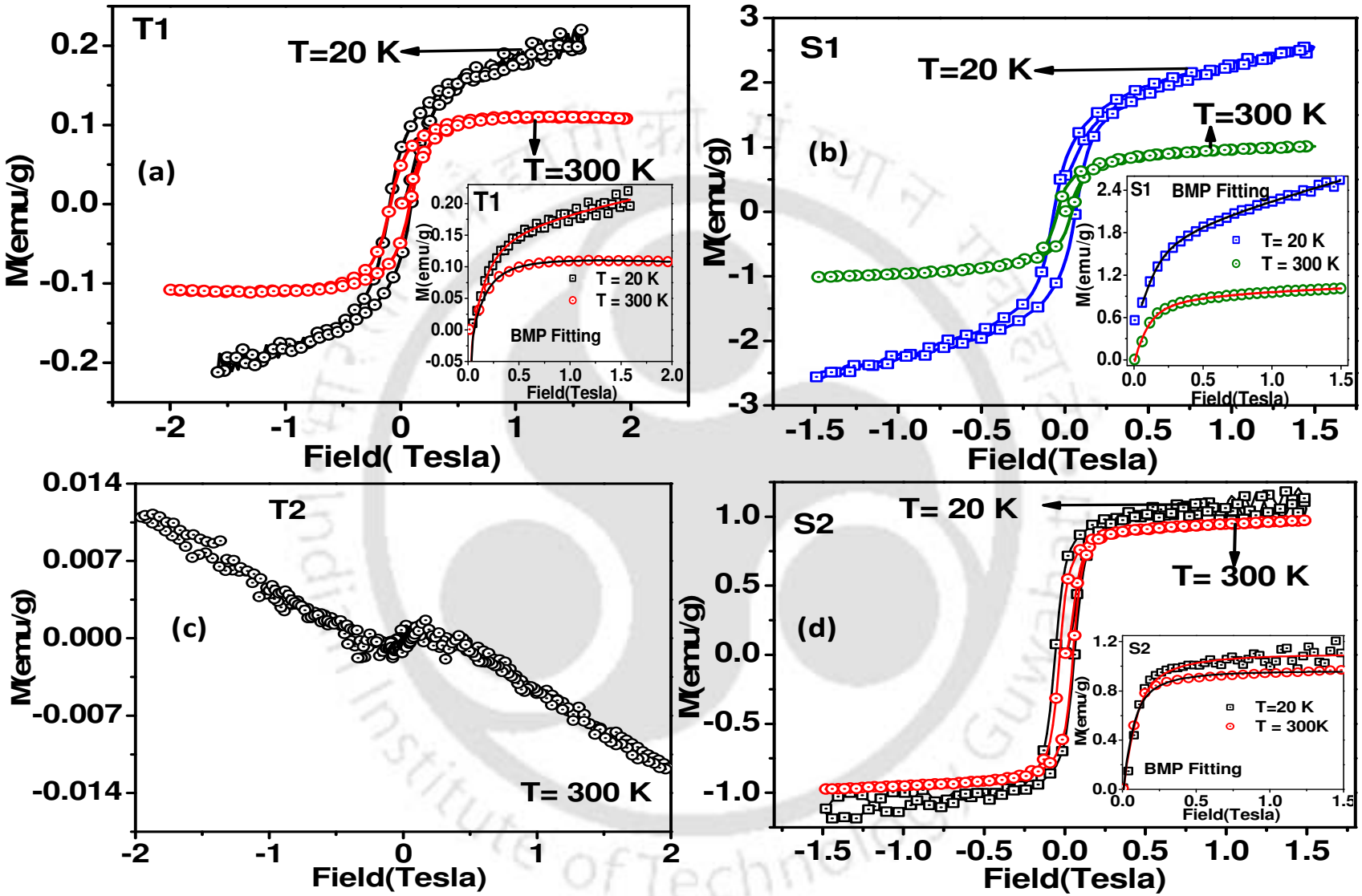

Fig. 3.27 M-H curves recorded for samples T1, S1, T2 and S2 at 20 K and 300 K. The insets show the initial curves along with the fit to BMP model.

The magnetization data were further analyzed in terms of bound magnetic polaron (BMP) model [112, 113, 255], i.e. by fitting the initial M-H curves to eq. 3.2. The parameters M_o, m_{eff}, χ_m were varied during the fit. The initial magnetization curves of T1, S1 and S2 at 20 and 300 K along with the fitted data are shown in the respective inset of Fig.3.27. The fitted data closely follow the experimental data and the fitted parameters M_o, m_{eff} and χ_m are given in table-3.10. The χ_m is found to increase with decrease in temperature. The spontaneous moment per BMP, m_{eff} is found to increase with increase in temperature and such a variation of m_{eff} is in contradiction to the variation of M_o and it can be understood as a result of increase in size of BMP with temperature. At higher temperature, even though the magnetic moments are aligned parallel within each BMP, the overall alignment of BMPs along the applied field may not be complete due to the increase in thermal energy. The value of m_{eff} is found to be in the order of 10^{-17} emu and it is comparable to that reported by Quintero *et al*.[114] in p-type $Cu_2FeGeTe_4$ based DMS. The present M_o is found to be one order of magnitude larger than that of the solid sate route prepared Co doped SnO_2 as given in table-3.4, whereas the m_{eff} varies with the same order of magnitude. In the present series of samples, the parameter M_0/m_{eff} is found to vary with temperature, so in such condition, one cannot assume $m_s = m_{eff}$. In view of above the restriction, we could not estimate N, the number of BMP per unit volume.

In order to determine the FM transition temperature, we have measured the temperature variation of magnetization of samples T1, S1 and S2 for an applied field of H = 0.2 T.

Fig. 3.28 (a) shows the M-T plot of T1 sample, where we can see a clear paramagnetic (PM) to FM transition with T_c at 915 K. For $T < T_c$ the magnetization is found to be almost constant and suggests the presence of long range magnetic ordering. The M-T plot of sample S1 shows two transitions. The main transition observed at 911K is found to be quite close to that observed in T1 sample and a secondary transition with onset at around 700 K was observed. The T_c of sample T1 and the high temperature T_c of sample S1 are found to be comparable and it suggests that even though these two samples were alloyed by using different type of vials, they have the same origin of FM, i.e. oxygen vacancy or defect induced FM. The two transitions observed in sample S1 suggest that there is more than one mechanism responsible for FM. Interestingly upon annealing, i.e. in sample S2, the high temperature T_c disappears and the low temperature T_c remains same without any appreciable shift. It closely supports the argument of defect or oxygen vacancy induced FM in as milled samples. In samples S1 and S2, the low temperature FM could

be due to the doping of Fe ions into Sn site of SnO_2 due to the contamination from the steel vial. The low temperature T_c of S1 sample is comparable to the 2 at % Co doped SnO_2 sample prepared by solid state route. Thus the mechanism of FM ordering at T_c~700K can be attributed to the transition element doping in SnO_2. Thus transition element doping and oxygen vacancy give rise to FM at two different temperatures. Since no FM was observed in sample T2, we have not carried out any M-T measurement. The dM/dT versus T plots for the above samples are shown in Fig. 3.28 (d). We can see that both samples T1 and S1 show prominent negative peaks at around 915 K and it is attributed to the FM transition originating from oxygen vacancy or defect. For sample S1, in addition to the high temperature negative peak, a broad negative peak like structure is observed at T< 700 K. The low temperature transition is smeared due to the presence of dominant high temperature transition and their possible overlapping. The sample S2 shows a sharp negative peak at 690 K and it is comparable to the low temperature transition observed at sample S1, the sample S2 does not show any high temperature peak. This clearly indicates the suppression of FM due to oxygen vacancy upon annealing. This is consistent with complete destruction of FM in sample T2.

Table-3.10 List of parameters obtained from the bound magnetic polaron model fit. M_0 is the spontaneous magnetization, χ_m is the susceptibility of the matrix and m_{eff} is the effective spontaneous moment per bound magnetic polaron.

Samples/Parameters	T1	S1	T2	S2
M_o (300 K)emu/g	0.131	0.9	-	1
M_o (20 K)emu/g	0.167	1.8		1.15
$\chi_m(10^{-6}emu/g.Oe)$ 300K	0.6	3.1	-	1.4
$\chi_m(10^{-6}emu/g.Oe)$ 20K	3	5		1.6
$m_{eff}(10^{-17}emu)$ 300K	4.4	7.2	-	10.4
$m_{eff}(10^{-17}emu)$ 20K	0.3	0.4		0.5

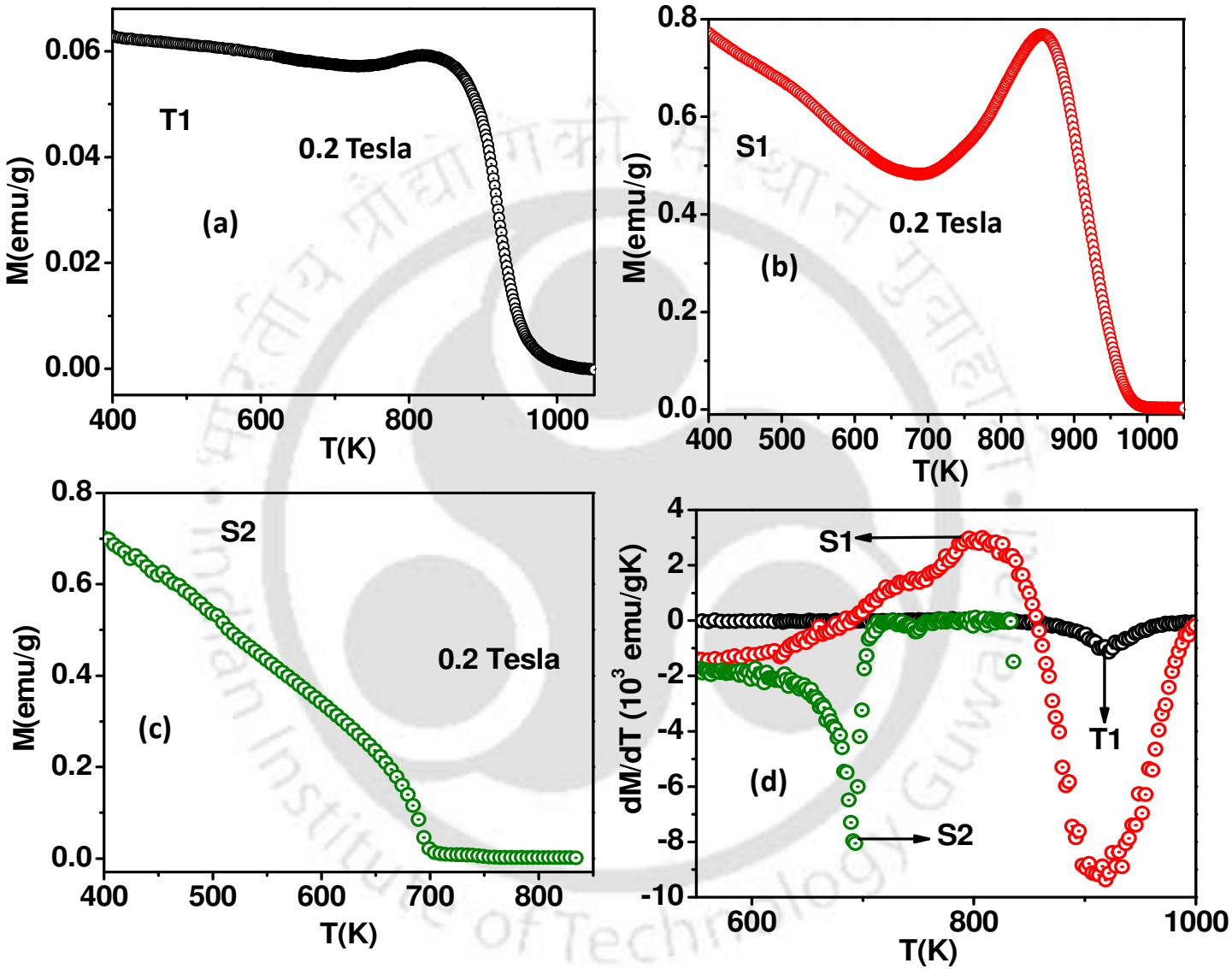

Fig. 3.28 Temperature variations of magnetization M, (**a, b** and **c**) and dM/dT **(d)** for samples T1, S1 and S2.

3.3.3 ESR Measurement

In order to further understand the magnetic properties, room temperature ESR spectra for all the samples were measured and are shown in Fig. 3.29. The inset shows the integrated intensity of ESR signal. The resonance field values are tabulated in table-3.8. The T2 sample doesn't show any ESR spectrum, which can be well understood from the observed diamagnetic property of the material. The observed ESR signal in T1 and S1 could be due to the polarized electron spins at the oxygen vacancy site. The observation of the ESR signal due to oxygen vacancy has been also reported in the literature on nanocrystalline SnO_2 [233]. The shift in the resonance field towards higher field for sample S2 can be understood in terms of reduced T_c. The integrated intensity of ESR signals is shown in the inset of Fig. 3.29(a), where we can see that the samples S1 and T1 exhibit a broad peak. Careful investigation of the spectrum of samples S1 shows a step like behavior below the resonance field and it is due to the mixture of two ESR signals. So, the integrated intensity of sample S2 was fitted to two Gaussian peak model and is shown in Fig. 3.29(b). So, it is basically a mixture of two ESR signals with resonance fields at H_l = 101± 0.5 mT and H_h= 269 ± 0.4 mT respectively. The H_l value is found to be comparable to the resonance field of sample T1 and similarly H_f value is found to be comparable to the resonance field of sample S2, so it clearly depicts the resonance field originating from high T_c and low T_c FM phases respectively. Higher FM T_c, larger the exchange interaction and hence larger molecular field is expected. Due to the presence of large molecular field, the resonance occurs at low applied field.

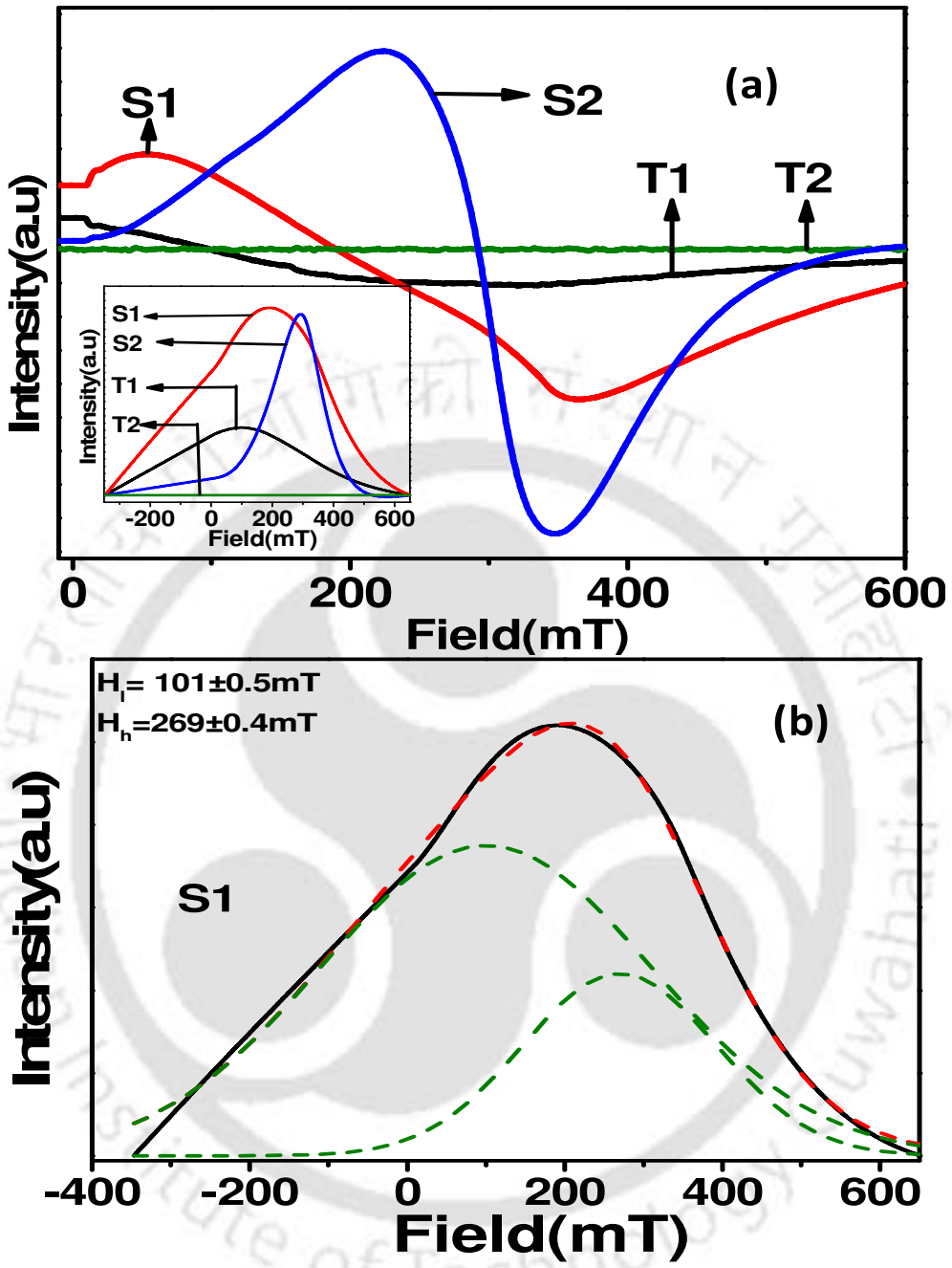

Fig. 3.29 (a)ESR spectra recorded for T1, S1, T2 and S2 samples at room temperature. The inset shows the integrated intensity of ESR signal. **(b)** Integrated ESR pattern for sample S1 along with fitting to Gaussian functions with two different resonance fields.

3.4 Co doped SnO_2 by Ball Milling

3.4.1 Preparation and Characterization

.

$Sn_{1-x}Co_xO_2$ samples for x = 0.0, 0.02, 0.07 and 0.10 were prepared by mechanical alloying method. The stoichiometric ratio of SnO_2, Co_3O_4 with 99.9% purity were weighed and mixed and, then ball milled using a hardened steel vial containing steel balls of 8 mm diameter and weight of each ball is approximately 2.1g. The weight of the vial is 15.5kg with a volume of 203cm^3. The milling speed was 500 rpm and ball to powder weight ratio was 10:1. The milling was carried out for duration of 10 hrs. The milled powders were pressed into cylindrical pellets and were annealed in air at 900^oC for 10 hrs.

XRD patterns of ball milled $Sn_{1-x}Co_xO_2$, for x = 0.0, 0.02, 0.07 and 0.10 are shown in Fig. 3.30. In addition to the allowed XRD peaks for tetragonal rutile structure of SnO_2, a minor XRD peak at $2\theta \approx 35.5^o$ is observed. The origin of the minor extra peak was found to be from Fe_3O_4 or $SnFe_2O_4$ based spinel structure. Since, no Fe was doped in the above samples; we can infer that the contamination from the steel vial could be the source of the spinel structure. So, the patterns were refined to the two phase model of crystal structure corresponding to $Sn_{1-x}Co_xO_2$ and the spinel phase by using Rietveld refinement technique and Fullprof programme. The refinements were carried out by choosing $P4_2/mnm$ space group for $(Sn,Co)O_2$ and Fd3m space group for the spinel phase. Typical XRD pattern for x = 0.10 sample along with Rietveld refined data are shown in Fig. 3.31. The volume fraction of the spinel phase obtained from the XRD refinement was found to around 6 %, without any appreciable variation with increase in doping concentration. From the obtained value of volume fraction of spinel phase and by taking the theoretical density, the weight % of spinel phase was determined for different samples and the values are found to be close to 4.5 wt %. The lattice parameters and particle size values determined from XRD analysis are given in Table-3.11. We can see that the values of the lattice parameters decrease marginally up to 7 % of Co-doping and can be explained in terms of Co^{3+} (0.61 Å) replacing some of Sn^{4+} (0.69 Å) ions. The above variation of lattice parameters is comparable to those of Co doped SnO_2 samples prepared by conventional solid state route as discussed in section 3.1.2. The refined occupancy values of Sn and Co are found to be comparable to the nominal starting composition. Typical values of Sn/Co occupancy are

0.923/0.077 for x=0.07 sample. The lattice parameters of spinel structure phase is found to be around 8.40 Å, and is comparable to the reported value of ferrites [263]. The crystallite size values are found to be close to 40 nm for all the samples.

Table-3.11. List of parameters obtained from the Rietveld refinement and analysis of XRD patterns.

Samples/Parameters	**x=0.0**	**x=0.02**	**x=0.07**	**x=0.10**
a=b(Å)	4.7322	4.7327	4.7310	4.7329
c(Å)	3.1848	3.1836	3.1824	3.1830
χ^2(%)	1.31	1.9	2.2	2.21
R_p (%)	14.9	19.9	18.5	17.7
Crystallite Size(nm)	40	39	42	41

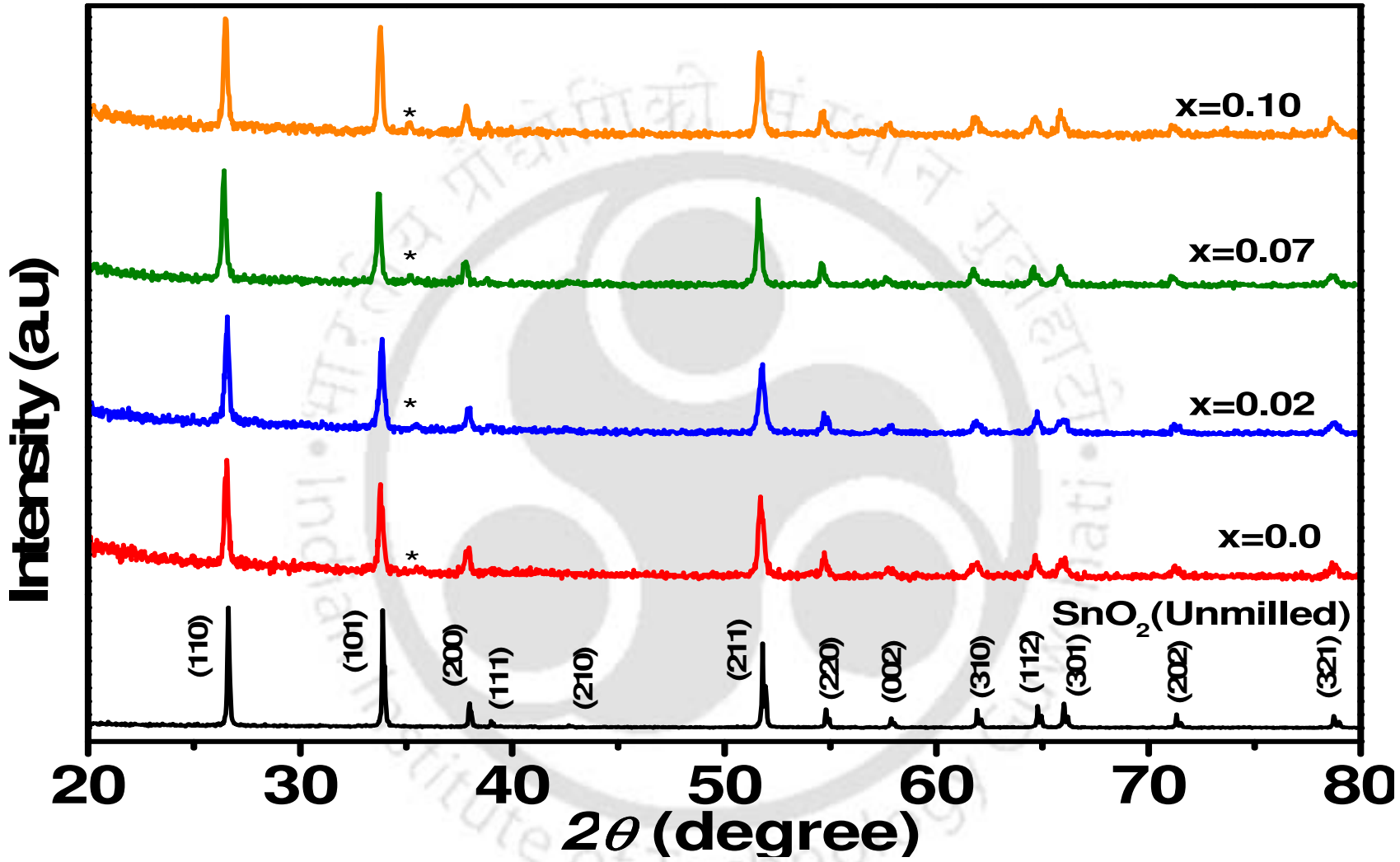

Fig. 3.30 XRD patterns of $Sn_{1-x}Co_xO_2$ samples for x = 0.0, 0.02, 0.07 and 0.10 prepared by ball milling method. Star marked peaks correspond to spinel phase.

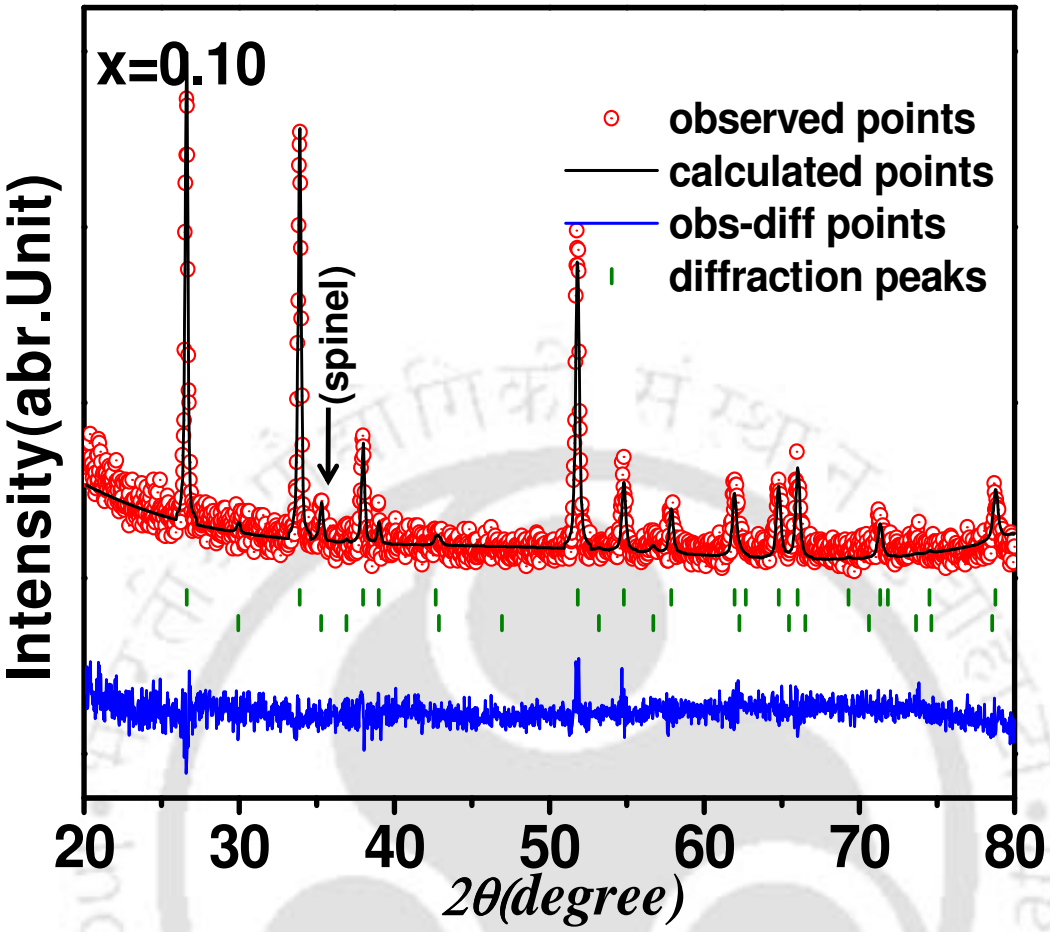

Fig. 3.31 XRD pattern along with Rietveld refinement for x=0.10 sample.

The EDX spectra recorded for the pure and the Co-doped samples show the presence of Fe along with Co, Sn and O peaks as shown in Fig.3.32. This can be understood in terms of Fe contamination due to the ball milling process using the steel vial. It is also in agreement with the observed spinel phase from XRD analysis. Similar Fe contaminations were also reported in Co-doped ZnO based materials prepared by mechanical synthesis route [264]. The EDX spectra analyses for all the samples are tabulated in table-3.12. From the observed Fe content in EDX analysis and by assuming that they are from the spinel phase, the weight percentage of spinel phase was estimated by taking the theoretical densities of $(SnCo)O_2$ and Fe_3O_4 and by normalizing them, the value was found to be close to 6 wt %. They are comparable to the results of XRD analysis.

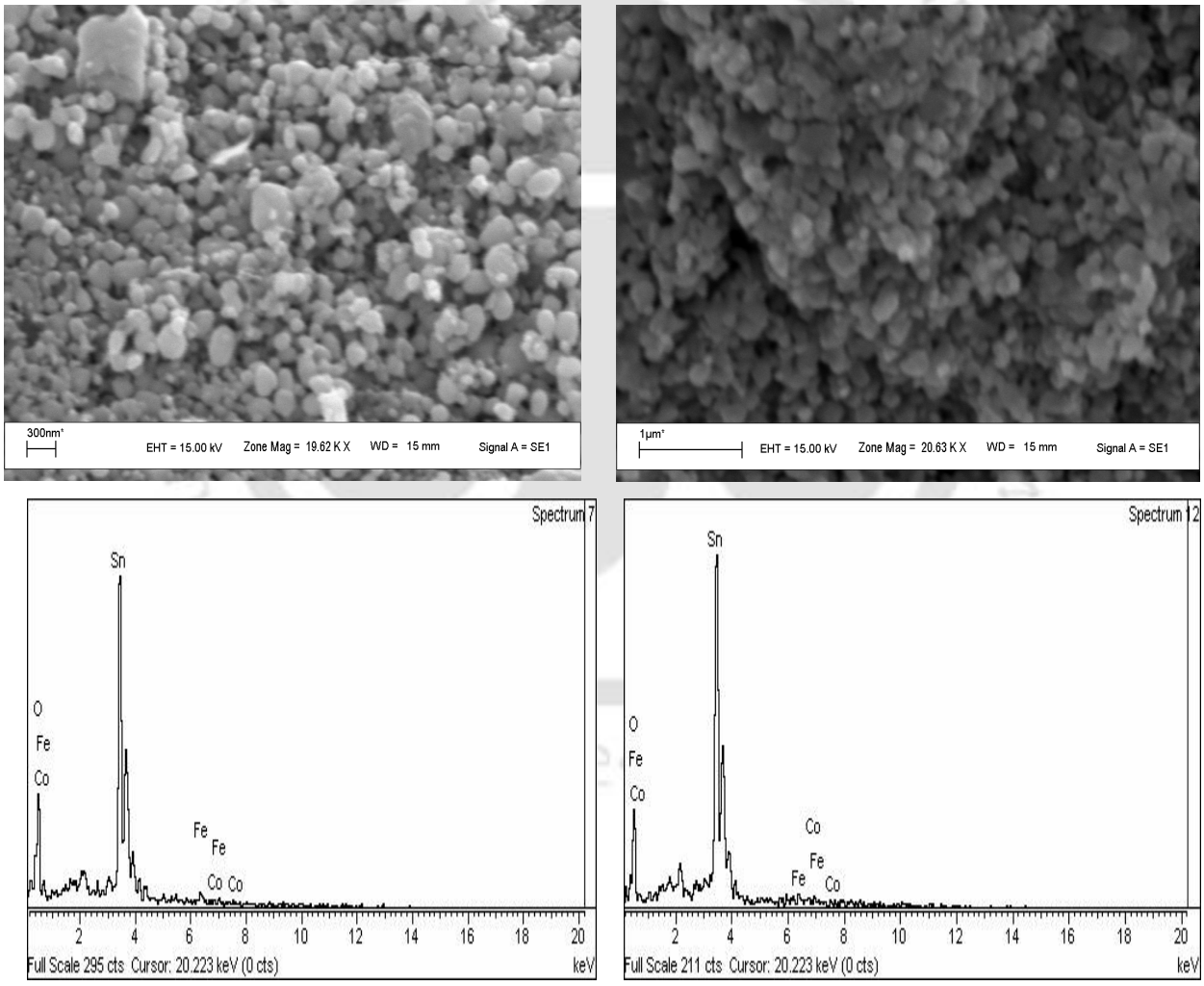

Fig. 3.32 SEM images for x=0.02 and 0.10 with EDX spectra.

Table-3.12 Cationic ratio obtained from EDX measurement for x =0.0, 0.02, 0.07 and 0.10 samples.

Sample	Calculated Cationic Ratio from EDS		
	Sn	Co	Fe
x=0.0	0.93	-----	0.06
x=0.02	0.91	0.023	0.077
x=0.07	0.87	0.067	0.072
X=0.10	0.74	0.098	0.062

Typical TEM image of x = 0.02 sample is shown in Fig. 3.33, where we can see the nanometric size of the particles. The high resolution TEM (HRTEM) images recorded at different locations show the presence of (110) plane as shown in Fig. 3.33(b). The respective Fast Fourier Transform (FFT) image is shown in the inset of Fig. 3.33(b). Typical selected area diffraction pattern (SAD) recorded for x = 0.02 sample is shown in Fig. 3.33(c), where a regularly arranged bright spots are observed and it highlights the single crystalline nature of the particle. The crystal structure observed at the microscopic scale was found to be comparable to the bulk crystal structure obtained from XRD analysis.

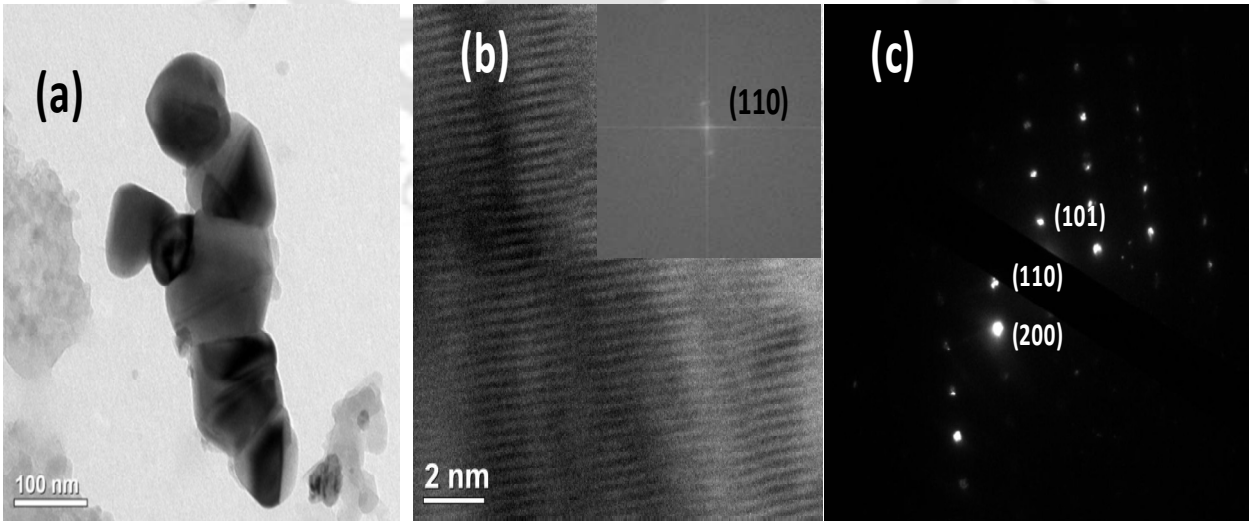

Fig. 3.33 TEM, HRTEM and SAD images of x=0.02 sample.

The Raman spectra recorded for all the Co-doped samples are shown in Fig.3.34. All the samples show the Raman shift at ~ 640 cm^{-1} which corresponds to A_{1g} (symmetric Sn-O stretching). This indicates the tetragonal rutile structure. The other peak observed at 693 cm^{-1} is because of the A_{2u}(LO), LO=longitudinal optic mode; which is basically IR-active but because of some disorder this become Raman active [259-261]. The samples exhibit the peak broadening effect and it depicts the presence of some amorphous phase. The observed peak at 475 cm^{-1} corresponds to the E_g mode of vibration. As the E_g mode is the result of two oxygen atoms vibrating parallel to the c axis, but in opposite direction; it is more sensitive to oxygen vacancies than other modes[262]. So the vacancy related defects are dominant in the samples.

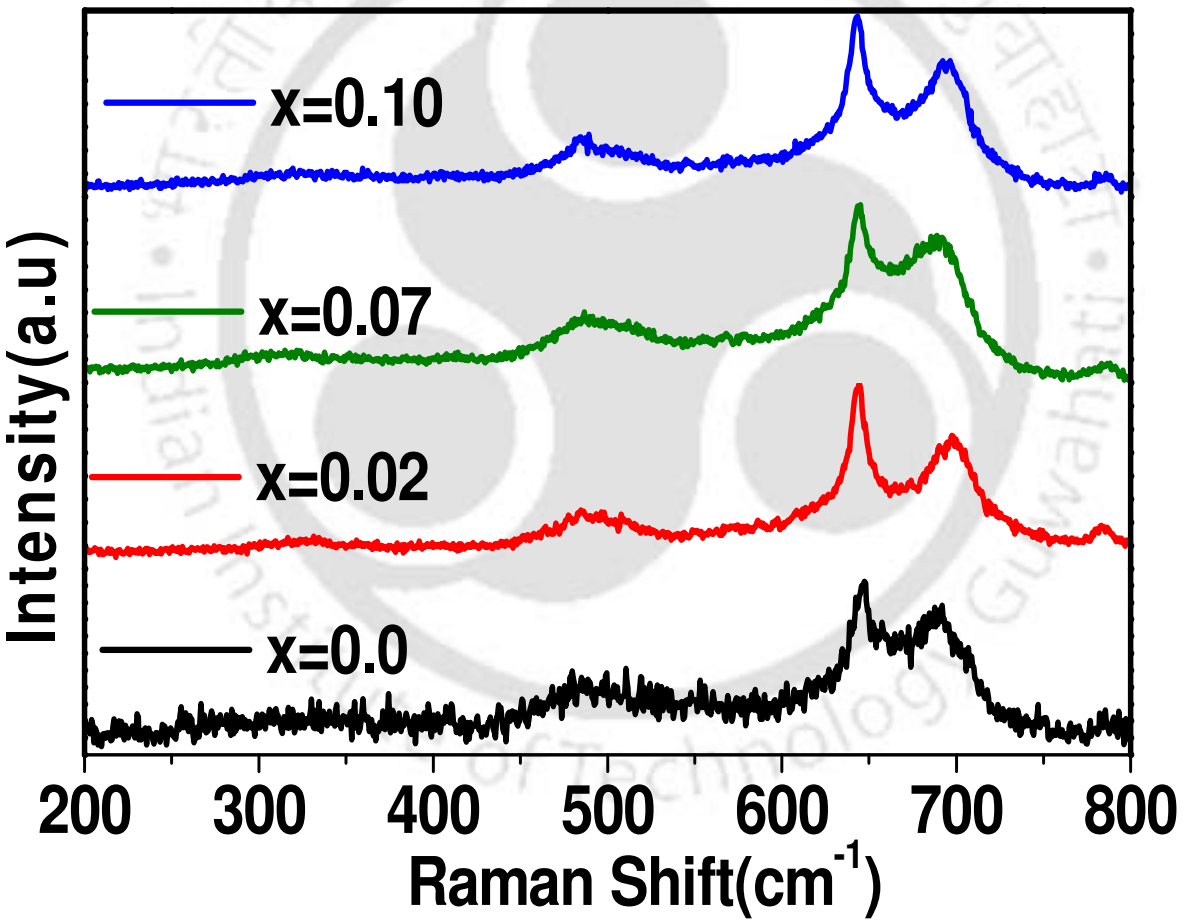

Fig.3.34 Raman Spectra recorded for $Sn_{1-x}Co_xO_2$ x=0.0, 0.02, 0.07, 0.10 samples at room temperature.

3.4.2 Magnetic Properties

The magnetization data of mechanically milled $Sn_{1-x}Co_xO_2$ samples recorded at 290 K for x = 0.0, 0.02, 0.07 and 0.10 are shown in Fig. 3.35(a) for a maximum applied field of 1.5T. They all exhibit ferromagnetic behavior including the x = 0 sample. The M_s value of x = 0 sample is found to be 0.9 emu/g and it is found to increase to 4.4 emu/g for 2 at % of Co doping. The sharp increase in M_s value for x = 0. 02 can be attributed to the FM introduced by Co-substitution in Sn site. However, for further increase in Co-concentration, the M_s value is found to reduce. Such a decrease in M_s value with increase Co concentration has been observed on $(Sn_{1-x}Co_x)O_2$ prepared by solid state route as given in section 3.1.2.

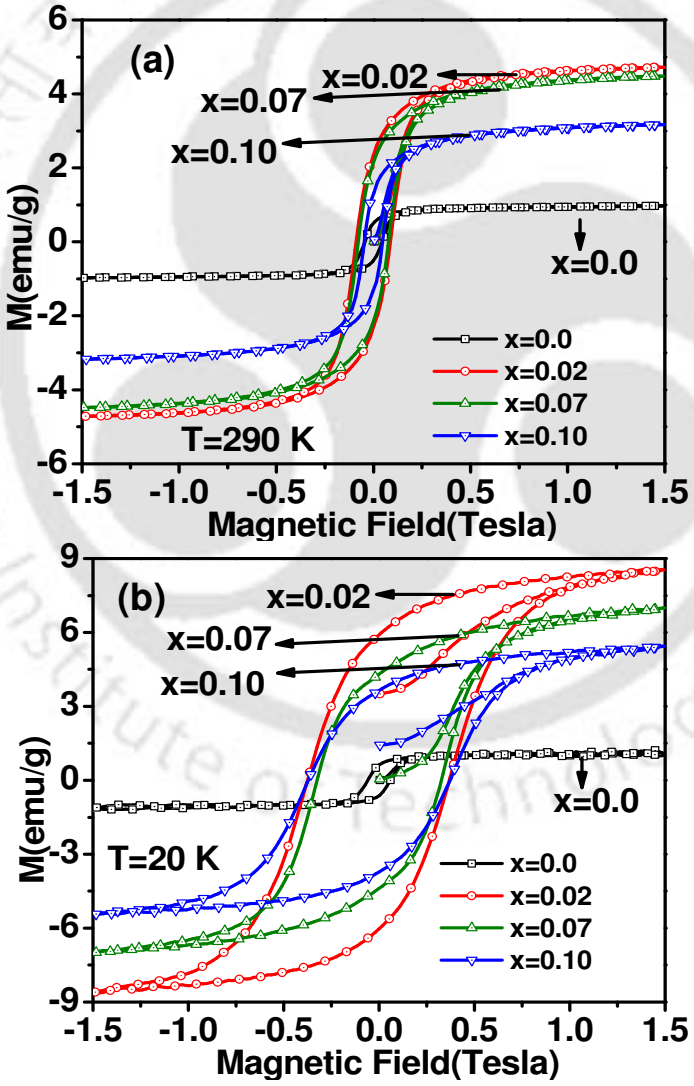

Fig. 3.35 M-H loops of $Sn_{1-x}Co_xO_2$ samples for x = 0.0, 0.02, 0.07 and 0.10 samples at (a) 290 K and (b) 20 K.

However, the magnitude of M_s in the ball milled samples are found to be about two order of magnitude larger than those of solid state synthesized samples for the same concentrations of Co doping. Similar variation of M_s with increase in doping concentration has been reported in literature [198, 265]. The decrease in M_s value with increase in Co-concentration can be understood in terms of enhanced nearest-neighbor antiferromagnetic superexchange interaction. The values of coercive field, H_c are given in Table-3.13. The H_c value is found to be maximum for x=0.02 sample. Similar kind of H_c variation was observed for the Co doped samples prepared by solid state route (section 3.1.2).

Table-3.13 Coercive Field (H_c) and saturation magnetization (M_s) determined for various Co doped SnO_2 samples prepared by ball milling.

Sample/Parameters	**x = 0.0**	**x = 0.02**	**x = 0.07**	**x = 0.10**
M_s(290K) emu/g	0.9	4.4	4.1	3.8
M_s(20K) emu/g	1	7.7	6.4	4.8
H_c(290K)Oe	440	879	786	470
H_c(20K)Oe	590	3735	3727	3245

The M-H loops recorded at 20 K for all the above samples are shown in Fig. 3.35(b). The M_s values were obtained after subtracting the high temperature linear region. The obtained M_s and H_c values are tabulated in Table-3.13. For x = 0 sample, no appreciable variation in M_s and H_c values are observed with decrease in temperature. However for example, x = 0.02 sample exhibits a large increase in M_s and H_c values with decrease in temperature. Similar behavior was observed for other Co-doped samples. So basically, there is a clear difference between the magnetization behavior of x = 0 and other Co doped samples and it leads to the understanding that, the mechanism and the origin of FM in x = 0 sample is quite different from other doped samples. The large increase in H_c value at low temperature can be understood in terms of enhanced magnetic anisotropy due to domain growth. In order to quantitatively analyze the magnetization data due to Co substitution, the contribution from spinel related phase or other extrinsic effect need to be separated out. Since the concentration of spinel phase is almost constant for different samples and the FM behavior of x = 0 sample is found to be distinct compared to rest of the samples, it can be assumed that the observed FM signal of x = 0 sample

is due to lattice defect such as oxygen vacancy, Fe_3O_4 type spinel impurity phase, or due to the small amount of Fe doping in Sn site. The initial M-H curve of x = 0 sample was fitted to the following expression [266],

$$M = M_{so}(1-a/H+b/H^2)+\chi_d H \quad \text{(3.6)}$$

Here M_{so} is the saturation magnetization, a and b are constants and χ_d is the paramagnetic susceptibility. The first term is to account for the FM behavior of x = 0 sample and the second term is to account for the observed paramagnetic contribution at higher field. The data were fitted by varying the parameter M_{so}, a, b and χ_d. The initial curve of x = 0 sample at 290 K along with the fitted data to eq.3.6 are shown in Fig. 3.36(a). The fitted data closely follow the experimental data. The fitted values of M_{so}, a, b and χ_d are found to be 0.915emu/g, 118emu.Oe/g, -1.7×10^5 emu.Oe^2/g, 1.4×10^{-7} emu/g.Oe respectively.

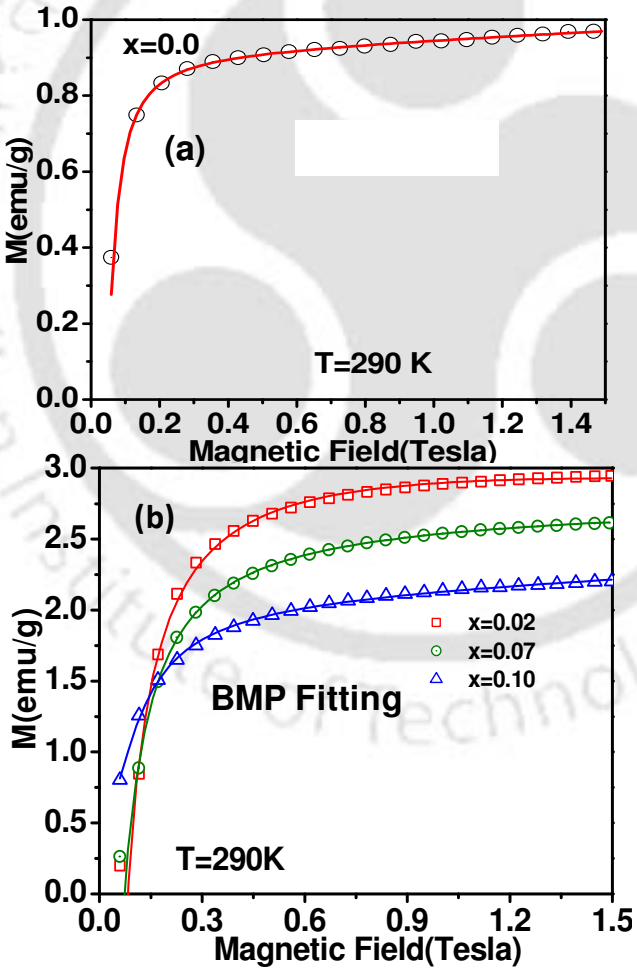

Fig. 3.36(a) Initial M-H curve for x = 0 sample along with fit to eq. 3.6. (b) BMP model fit for x = 0.02, 0.07 and 0.10 sample.

The intrinsic magnetization due to Co-doping was determined by subtracting the magnetization arising from spinel phase or other extrinsic effects. This can be done by estimating the background magnetization by using eq.3.6 and parameters M_{so}, a, b and χ_d corresponding to x = 0 sample. The background magnetization was subtracted from the measured magnetization of Co doped samples. The intrinsic initial magnetization data of x = 0.02, 0.07 and 0.10 samples are shown in Fig. 3.36(b). The intrinsic saturation magnetization, M_{si} was determined from the above plots and are found to be 2.9 emu/g, 2.6 emu/g, 2.2 emu/g for x = 0.02, 0.07 and 0.10 samples respectively at 290 K. Their corresponding values at 20 K are found to be 5.9 emu/g, 4.9 emu/g and 3.3 emu/g. The data were analyzed in terms of bound magnetic polaron model (BMP) [112, 113, 255]. The parameters M_o, m_{eff}, χ_m were varied during the fit to BMP model. The magnetization curves for x = 0.02, 0.07, 0.10 samples at 290 K along with the fitted data are shown in Fig.3.36(b). The fitted data closely follow the experimental data and the fitted parameters M_o, m_{eff} and χ_m are given in Table-3.14. The M_0 value is found to decrease with increase in doping concentration and such a behavior has been reported in Mn-doped SnO_2 compounds [198]. It is mainly due to the reduction in average Co-Co inter-atomic distance, which might contribute to nearest neighbor antiferromagnetic interaction at the expense of ferromagnetism. The paramagnetic susceptibility χ_m is found to increase with increase in doping concentration. The value of spontaneous moment per BMP, m_{eff} is found to be in the order of 10^{-17} emu and increases marginally with increase in Co concentrations. Similar kind of variation was observed for the solid state route prepared Co doped samples and with almost same order of magnitude as given in section 3.1.2. The average radius of the BMP was estimated from the fitted value of m_{eff} and by assuming spherical shape of BMP. The radius of BMP was found to be in the range of 30 Å to 39 Å and is comparable to that reported by Dietl *et al.* in CdMnSe based DMS [267].

Table 3.14: List of parameters obtained from the analysis of M-H data by using BMP model. M_o is the spontaneous magnetization of the system, χ_m is the susceptibility of the matrix and m_{eff} is the effective magnetic moment per bound magnetic polaron.

Sample	***Parameters obtained from BMP Fitting***			
	M_o**(emu/g)**	$\chi_m(10^{-4}$***emu/g.Oe)***	$m_{eff}(10^{-17}$***emu)***	***BMP radius(Å)***
x=0.02	3.34	1.04	5.7	39
x=0.07	2.8	2.1	5.8	31
x=0.10	2.21	5.1	7.8	33

In order to completely understand the magnetic transitions, we have carried out the temperature variation of magnetization for an applied magnetic field of H = 0.2 T and they are shown in Fig. 3.37. M versus T plot of x = 0 sample (sample S2) is shown in Fig. 3.27(c) and for comparison; it is reproduced in Fig. 3.37(a) where we can see the FM transition. The temperature derivative of magnetization as a function of temperature in the expanded scale is shown in Fig.3.37(b), where we can see a sharp negative peak at 690 K and a minor negative peak at 750 K. So, basically the x = 0 sample exhibits two magnetic transitions. The transition observed at 750 K can be attributed to ferrite based structure or extrinsic effect such as oxygen vacancy. However, the observed T_c at 690K could be attributed to the doping of some of Fe-ions into the Sn site. The M-T curves of x = 0.02, 0.07 and 0.10 samples are shown in Fig. 3.37(a) and (c) and they all exhibit single Paramagnetic (PM) to FM transition. The FM T_c is found to decrease with increase in Co-concentration and it is in correlation with a decrease in M_s value observed from M-H data. Unlike x = 0 sample, no secondary transition is observed, and it could be mainly due to the strong FM signal of Co-doped samples.

The paramagnetic susceptibility was fitted to the *modified* Curie-Weiss law,

$$\chi = \chi_0 + \frac{C(x)}{T - \theta_c} \qquad \ldots\ldots\ldots\ldots\ldots\ldots\ldots \qquad (3.7)$$

where, χ_0 is temperature independent susceptibility, $C(x) = xC_0 = xN\mu_{eff}^2/3k_B$ is the Curie constant, where x is the concentration of doped Co-ions, θ_c is Curie temperature. Fig. 3.37(d) shows a typical plot of temperature variation of susceptibility along with fit to eq.3.7 for x = 0.07

sample. The Curie temperature (FM T_c) of x = 0.0, 0.02, 0.07 and x=0.10 samples are found to be 692±0.2K (690 K), 653±0.5K (T_c=640K), 519±0.7 K (T_c=501 K) and 446±0.4 K (T_c=396K) respectively. The observed values suggest that the transition temperature is not due to any Fe or Co related clustering effects or spinel related structures. The μ_{eff} values are found to be 0.94 μ_B/TM-ion, 2.34 μ_B/TM-ion, 3.5 μ_B/TM-ion and 2.15 μ_B/TM-ion respectively for x = 0.0, 0.02, 0.07 and 0.10 samples. The above results suggest that Co doping gives rise to room temperature FM. Strong room temperature FM was observed with a maximum M_{si} value of 2.9 emu/g (3.8 μ_B/Co-ion) and it increases to 5.9emu/g (7.9 μ_B/Co-ion) at 20 K for x = 0.02 sample. Thus the observed giant magnetic moment value is comparable to that reported by Ogale *et al.* [39] for 5 % Co-doped SnO_2 thin film. Such a high M_{si} value can be explained in terms of unquenched d-orbital of the doped Co-ion and due to oxygen vacancy as explained in ref. [45].

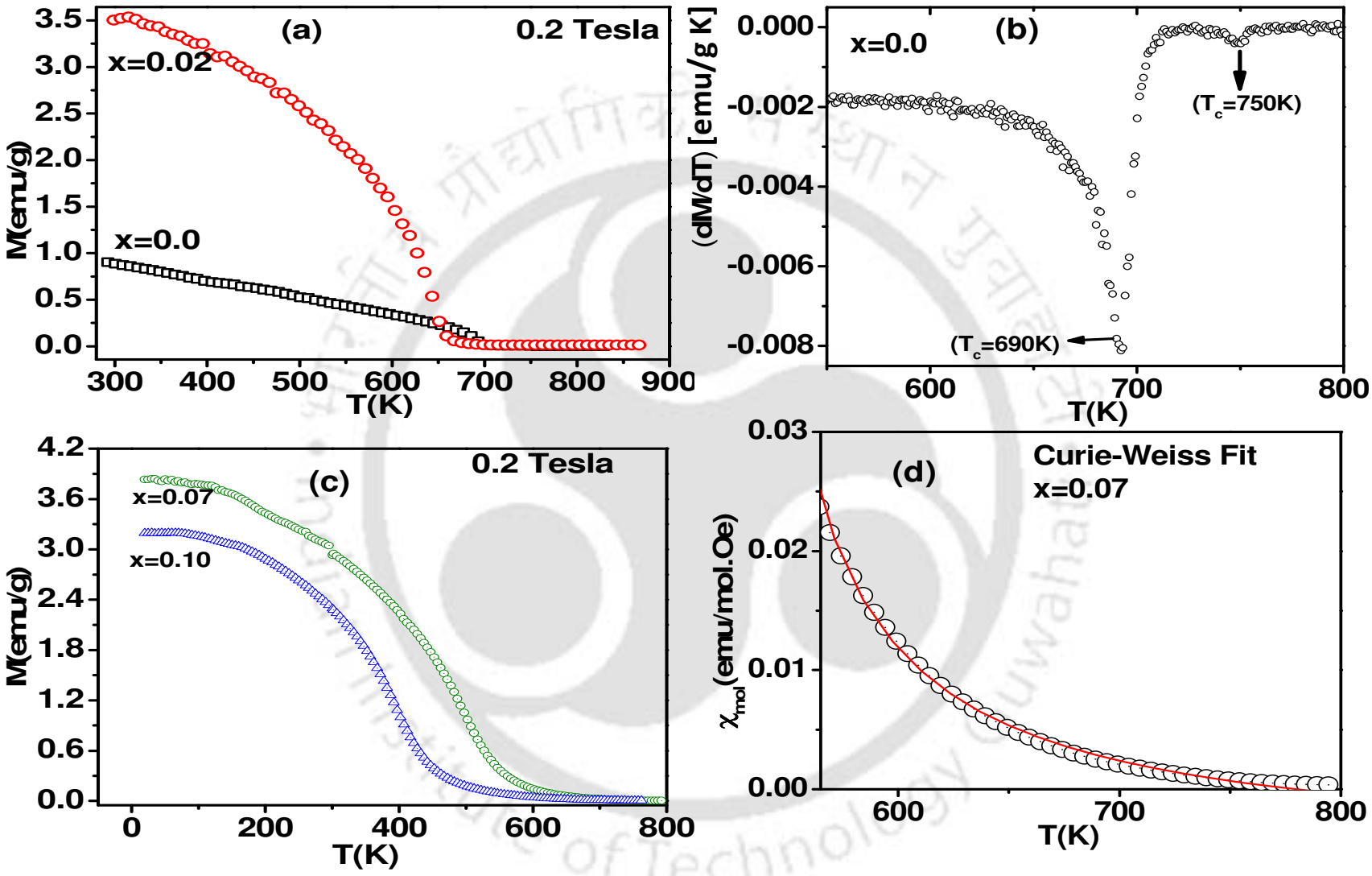

Fig. 3.37 Temperature variations of magnetization M, (**a, b** and **c**) and dM/dT (**d**) for samples T1, S1 and S2.

3.5 Critical Behavior Studies

In order to understand the nature of FM interaction in Co doped SnO_2 sample, a detailed study of critical behavior in the vicinity of PM to FM transition was carried out. For this study, $Sn_{0.98}Co_{0.02}O_2$ sample prepared by mechanical milling process is taken up, because its M versus T plot shows single sharp PM to FM transition. Moreover, it exhibits strong room temperature FM compared to other samples, with a saturation magnetization of $3.8\mu_B$/Co.

The temperature variation of magnetization of mechanically milled $Sn_{0.98}Co_{0.02}O_2$ sample, in an applied field of 2kOe (0.2T) is shown in Fig. 3.37(a) and is reproduced in Fig. 3.38 in the unit of emu/cc for comparison with isothermal magnetization data. The sample exhibits a single PM to FM transition without any trace of secondary transition. The transition can be attributed to the DMS behavior of Co doped SnO_2 because, we have found that the T_c is comparable to the Co-doped SnO_2 prepared by solid state route without any ferrite impurity. The susceptibility in the PM region could be fitted to Curie-Weiss law. The present sample exhibits the highest transition temperature and saturation magnetization compared to other higher doped samples. So, we have taken up a detailed isothermal magnetization study on $Sn_{0.98}Co_{0.02}O_2$ sample to understand the critical behavior.

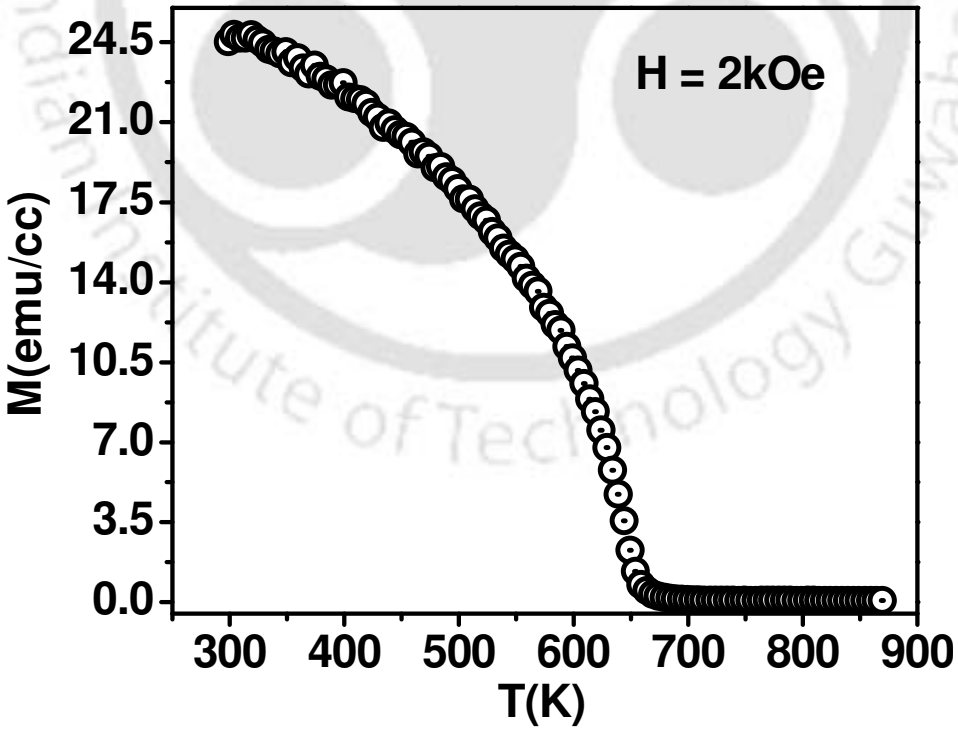

Fig. 3.38 Temperature variation of magnetization for $Sn_{0.98}Co_{0.02}O_2$ sample.

As per the Landau theory and the minimization of Gibb's free energy in the vicinity of magnetic phase transition, the relation between magnetization *M* and magnetic field *H* can be written as,

$$H/M=2a+4bM^2 \quad \ldots\ldots\ldots\ldots\ldots\ldots\ldots\ldots\ldots\ldots\ldots\ldots\ldots\ldots\ldots\ldots \quad (3.8)$$

where the coefficients '*a*' and '*b*' are temperature dependent parameters [120].

Thus the plot of M^2 versus *H/M* should be a straight line [121] . According to Banerjee [122], for a second order phase transition, the plot of *H/M* versus M^2 should be a straight line with positive slope. The thermodynamic parameters, such as spontaneous magnetization, $M_s(T)$, the inverse susceptibility $\chi_0^{-1}(T)$ and the isothermal magnetization at the critical temperature, *M(H)* follow the power law behavior of reduced temperature, $\varepsilon = (T-T_c)/T_c$ as shown below[120],

$$M_S(T) \sim |\varepsilon|^{\beta}, \quad \varepsilon < 0 \ldots\ldots\ldots\ldots\ldots\ldots\ldots\ldots\ldots\ldots\ldots\ldots\ldots\ldots\ldots\ldots \quad (3.9)$$

$$\chi_0^{-1}(T) \sim \varepsilon^{\gamma}, \quad \varepsilon>0 \ldots\ldots\ldots\ldots\ldots\ldots\ldots\ldots\ldots\ldots\ldots\ldots\ldots\ldots\ldots\ldots\ldots\ldots \quad (3.10)$$

$$M(H) \sim H^{1/\delta}, \quad \varepsilon = 0 \quad \ldots\ldots\ldots\ldots\ldots\ldots\ldots\ldots\ldots\ldots\ldots\ldots\ldots\ldots\ldots\ldots \quad (3.11)$$

Here β, γ and δ represent critical exponents associated with M_s, χ_0 and *M(H)*. The critical exponents are related to each other by the Widom scaling relation [125], $\delta = 1+ \gamma/\beta$. According to Arrott and Noakes [123], the mean filed relation (eq.3.8) can be modified, for a more general case as given below,

$$(H/M)^{1/\gamma}=(T-T_C)/T_1+(M/M_1)^{1/\beta} \quad \ldots\ldots\ldots\ldots\ldots\ldots\ldots\ldots\ldots\ldots\ldots\ldots\ldots\ldots\ldots\ldots \quad (3.12)$$

where T_1 and M_1 are sample dependent constants. Eq. (3.12) reduces to eq. (3.8) upon substitution of critical exponents corresponding to mean field model.

The isothermal magnetization curves as a function of applied magnetic field up to H = 20 kOe (2 T) in the temperature range 610 K to 647 K covering the transition temperature are shown in Fig. 3.39. They exhibit a smooth transition from the FM characteristic behavior of magnetization to the PM behavior with increase in temperature. The isothermal magnetization data in the form of Arrott plots (M^2 versus H/M) are shown in Fig.3.40. They all exhibit positive slope and confirm the second order nature of magnetic phase transition. Moreover, the plots at higher fields are found to be almost parallel to each other.

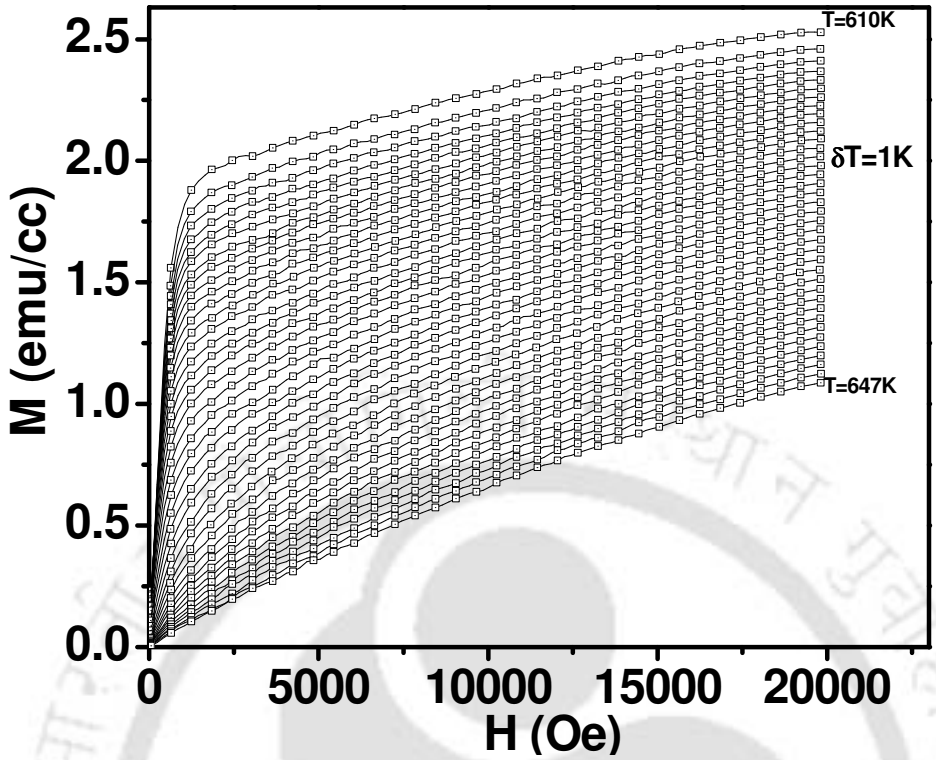

Fig. 3.39 Isothermal magnetization curves for $Sn_{0.98}Co_{0.02}O_2$ sample.

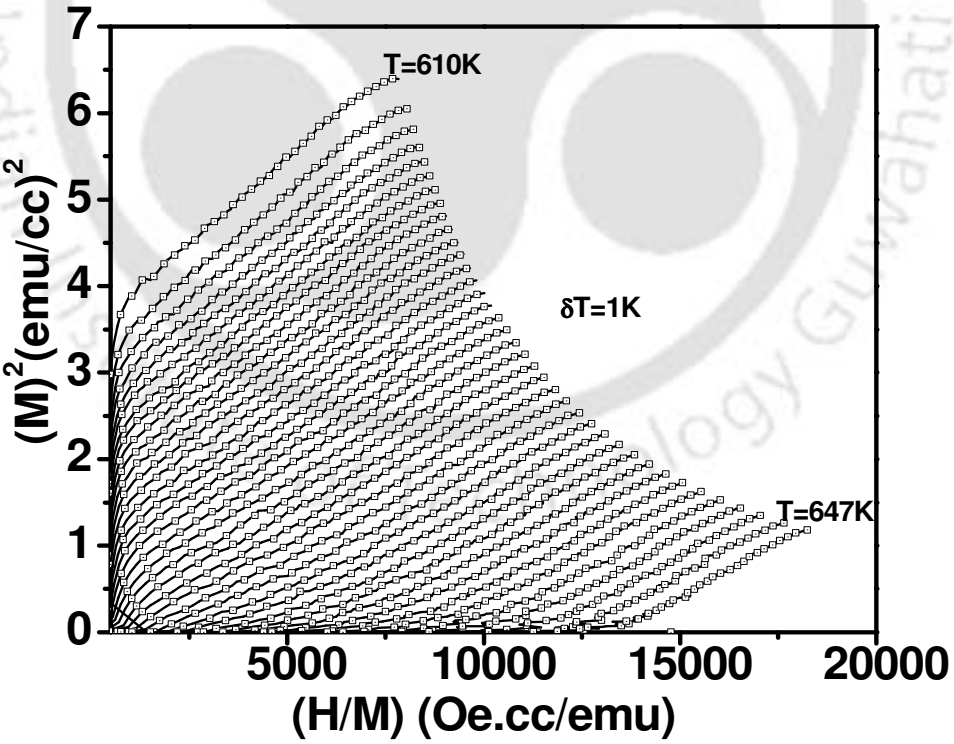

Fig. 3.40. The Arrott plots (M^2 vs. H/M) for 2 at % Co-doped SnO_2 sample in the temperature range of 610-647 K.

In order to determine the reliable critical exponents, we have to determine the accurate values of $M_s(0, T)$ and $\chi^{-1}(0, T)$ at $H = 0$. These thermodynamic experimental data can be obtained from the modified Arrott plots (MAP). The MAP technique [123] requires the prior knowledge of β and γ and however, these $M_s(0,T)$ and $\chi_0^{-1}(0,T)$ data can be obtained by following systematic procedure as reported by Kim *et al.*[268]. Such technique was also used by Samantaray *et al*. [269] in determining the critical exponents of manganites. It is briefly described as follows. MAP was plotted by choosing a trial β and γ values close to one of the known theoretical models such that the plots are linear and from these plots $M_s(T)$ and $\chi_0^{-1}(T)$ were determined by extrapolating the high field data to zero values of horizontal $(H/M)^{1/\gamma}$ and vertical $(M^{1/\beta})$ axis respectively. T_c was taken from the temperature corresponding to the isothermal M-H curve passing through the origin. A new set of β and γ values were obtained by plotting $ln(M_s)$ versus $ln(\varepsilon)$ for $\varepsilon < 0$, and $ln(\chi_0^{-1})$ versus $ln(\varepsilon)$ for $\varepsilon > 0$ and by fitting to linear relation. The above process was repeated by using the new set of β and γ values. This process was repeated until consistent values of β and γ were obtained. By fitting $ln(M)$ versus $ln(H)$ data at $T = T_C$, the exponent δ was determined. The values of critical exponents β, γ and δ determined from the above analysis are given in table-3.15. These values are found to be comparable to those predicted by the mean field model. The set of MAP by using the final refined values of β and γ are shown in Fig. 3.41 and we can see that they exhibit linear behavior at higher field confirming the validity of mean field model. Moreover, the linear plots for different temperature are found to be parallel to each other and they signify the consistency of β and γ values.

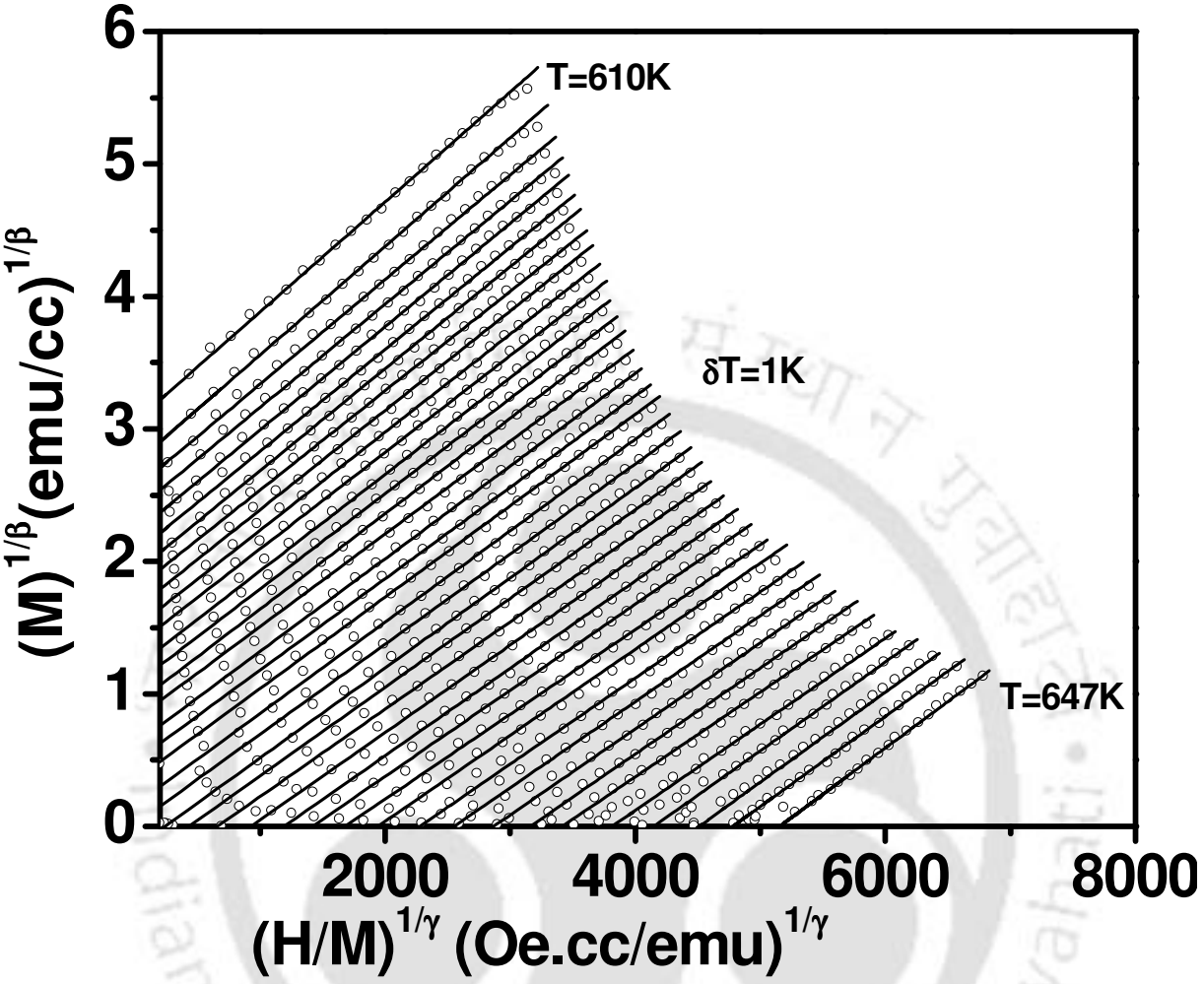

Fig.3.41 Modified Arrott plots, $M^{1/\beta}$ versus $(H/M)^{1/\gamma}$ with $\beta = 0.52$ and $\gamma = 1.1$.

Temperature variation of M_s and χ_o^{-1} determined from the measured data are shown in Fig.3.42 (a) and Fig.3.43 (a) along with theoretical data. The fitted data closely follow the experimental data. The plots of $ln(M_S)$ and $ln(\chi_0^{-1})$ as a function of $ln(\varepsilon)$ are shown in Fig.3.42 (b) and Fig.3.43(b) respectively. We can see that they exhibit linear behavior. The fitted data to the linear relation are shown as solid line and they closely follow the experimental data. The critical exponents β and γ were determined from the linear fit. The isothermal M-H curve at $T = T_C$ along with theoretical fit to eq.3.11 is shown in Fig. 3.44(a). The same data in logarithmic scale along with the fitted data are shown in Fig. 3.44(b). The value of δ was determined from the fit. The value of $\delta - (1+\gamma/\beta)$ was found to be 0.005 and it is close to the expected value of zero as per Widom scaling relation.

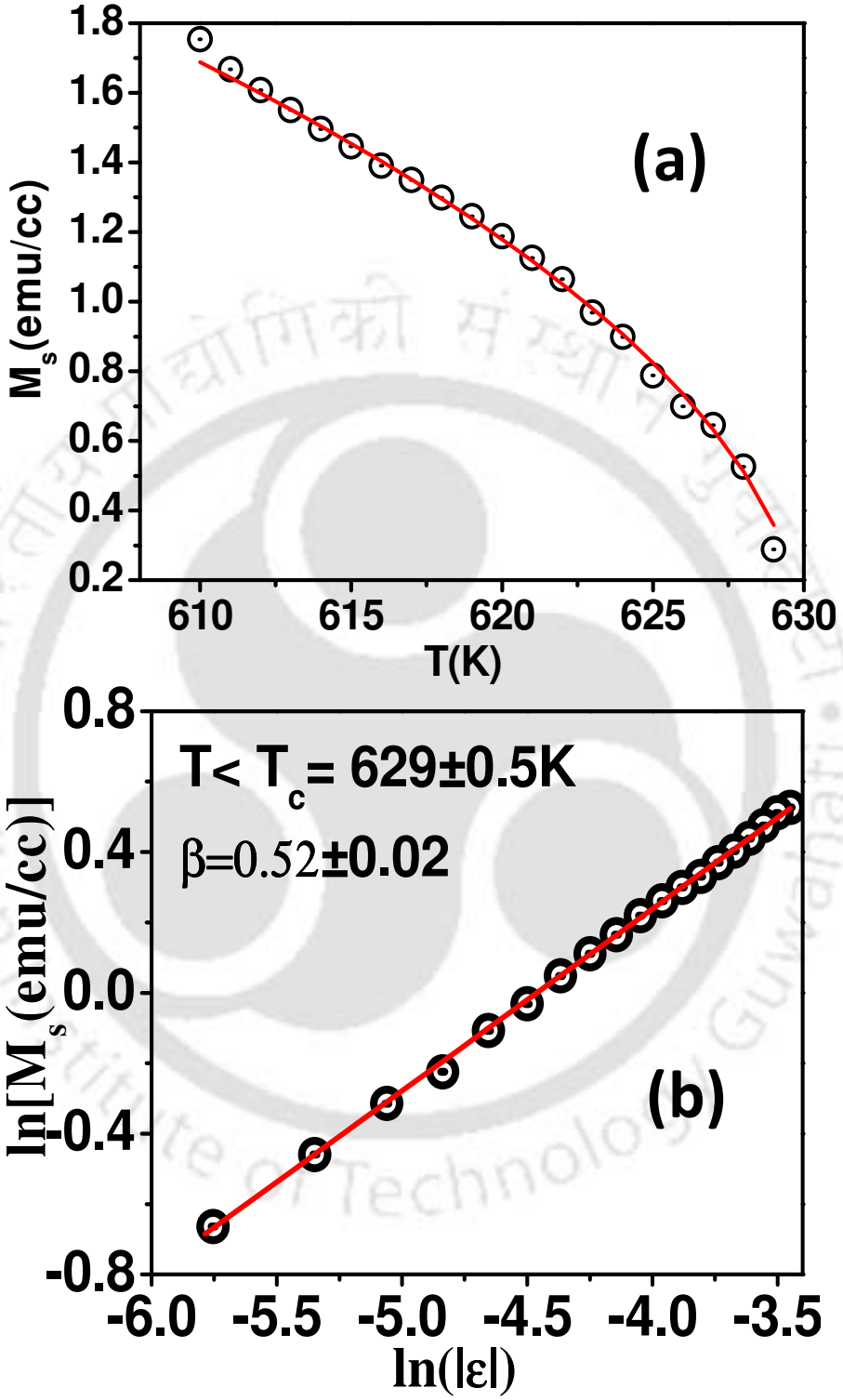

Fig. 3.42 (a) The spontaneous magnetization (M_S) versus Temperature. **(b)** The plot in logarithmic scale along with fitted data.

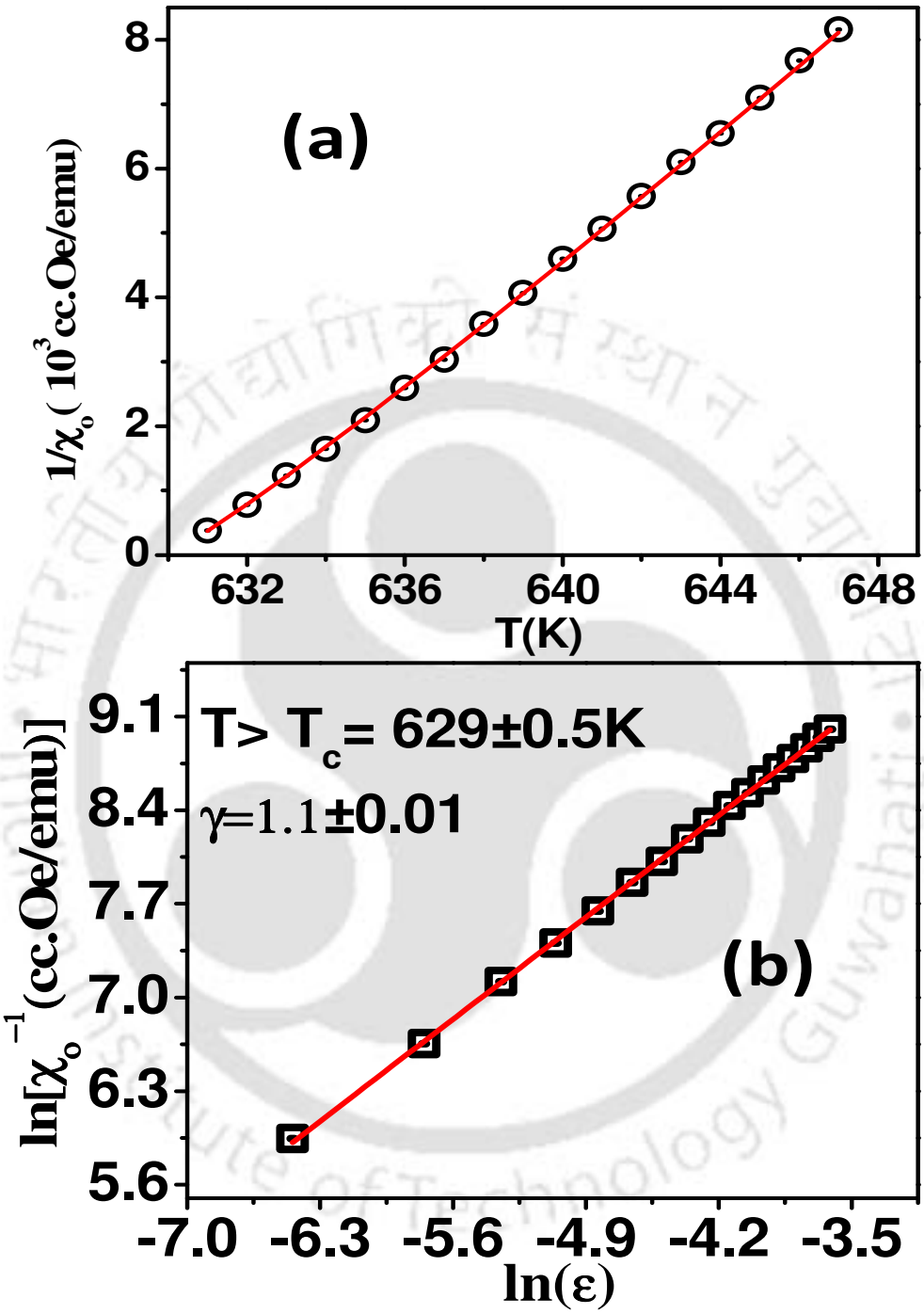

Fig. 3.43 (a) The initial inverse susceptibility $1/\chi_0$ plotted against temperature for 2 at % Co-doped SnO_2 sample. **(b)** The plot in logarithmic scale along with fitted data.

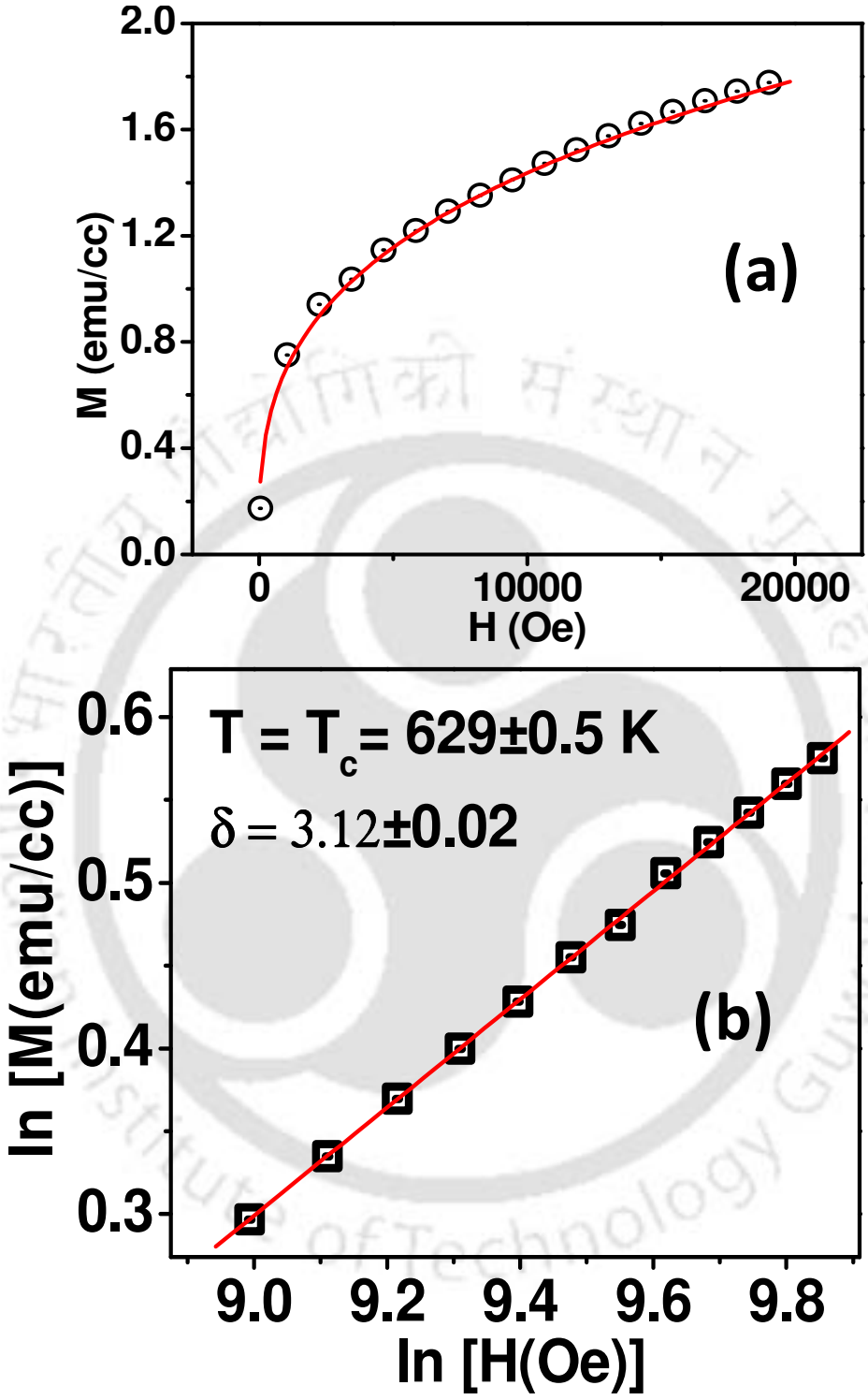

Fig. 3.44. The critical isothermal magnetization at $T = T_C$ for 2 at % Co-doped SnO_2. (b) The plot in logarithmic scale, along with the fitted data shown as solid line.

The static scaling hypothesis predicts that $M(H,\varepsilon)$ is a universal function of ε and H, i.e.

$$M(H, \varepsilon)\,|\varepsilon|^{-\beta} = f_{\pm}(H\,|\varepsilon|^{-(\beta+\gamma)}) \quad \ldots\ldots\ldots\ldots\ldots\ldots\ldots\ldots\ldots\ldots\ldots\ldots \quad (3.13)$$

Here f_+ and f_- are regular analytical functions for $\varepsilon > 0$ and $\varepsilon < 0$ respectively. According to eq. (3.13), plots of $M(H, \varepsilon)|\varepsilon|^{-\beta}$ versus $H\,|\varepsilon|^{-(\beta+\gamma)}$ would lead to universal curves, one for temperatures $T > T_C$ $(\varepsilon > 0)$ and the other for $T < T_C$ $(\varepsilon < 0)$. Fig. 3.45 shows the scaling plot and the inset shows the scaling plot in logarithmic scale. All the data points over the entire range of the variables are found to fall on two branches of a curve depending upon the sign of ε. This suggests that the values of the critical exponents and T_C determined from the analysis are quite accurate.

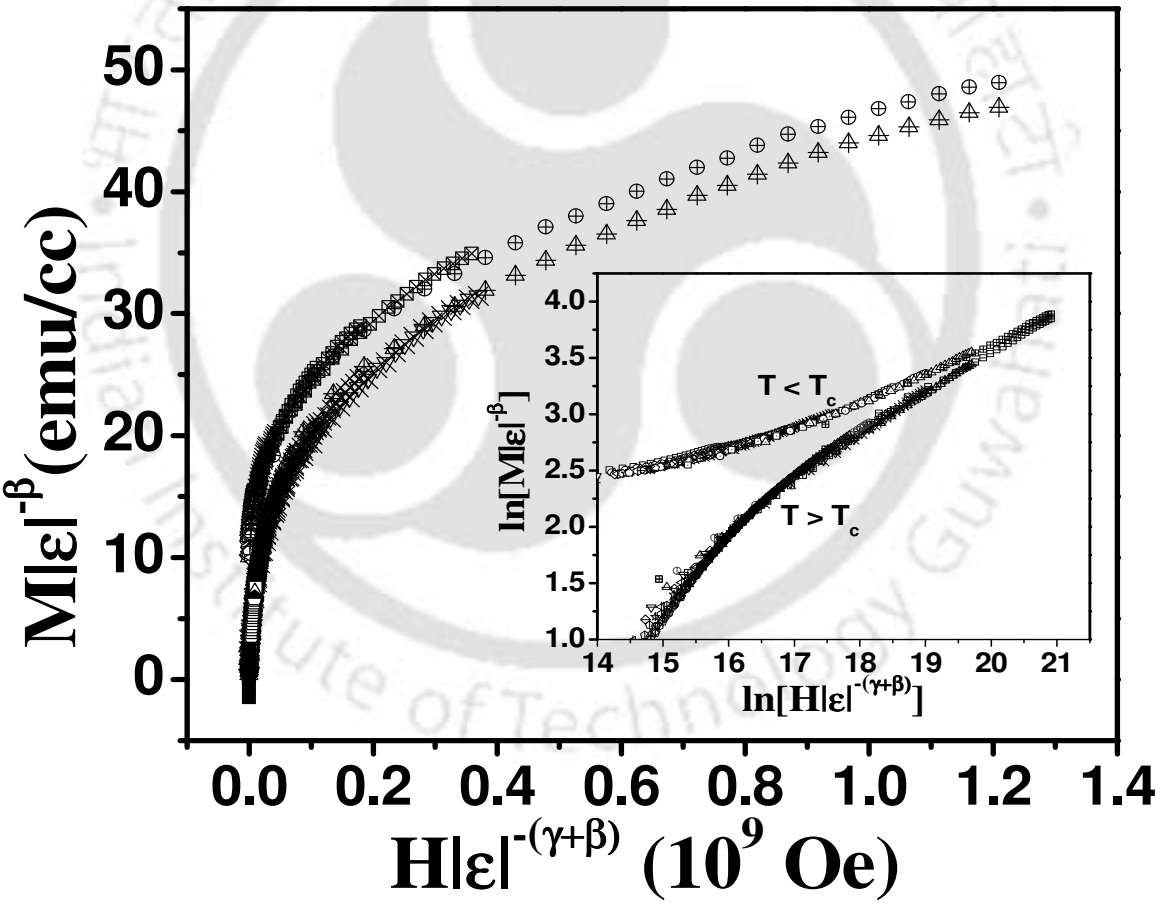

Fig. 3.45 Scaling plot *of* $M\,|\varepsilon|^{-\beta}$ *versus* $H\,|\varepsilon|^{-(\beta+\gamma)}$ with β, γ and δ values from the final iteration for $Sn_{0.98}Co_{0.02}O_2$. Different symbols represent different temperatures. The inset reproduces plots in double logarithmic scale.

The values of critical exponents determined for the present sample along with values predicted for various models such as mean field [120], 3D Heisenberg [120], 3D Ising [120] are listed in table 3.15. The critical exponents *β,* γ and *δ* obtained in the present sample are found to be quite close to those predicted by the mean field model and it reflects the presence of long range magnetic interactions in this material. The main difficulty in arriving at a conclusion regarding the type of magnetic interaction is that the values corresponding to a different universality class of theoretical models are quite close to each other. However, the β and δ values of the mean field model are quite distinct compared to other models in terms of percentage of variation. The experimental values of these critical exponents are also found to quite close to the mean field model. So, we can conclude that the magnetic interaction in the present sample is governed by the mean field model. Even though, the γ-value is found to be slightly larger than the predicted mean field model and however such deviation is well within the ambit of the mean field model, it cannot be identified with any other universality class.

The error inherited in the determination of transition temperature can affect the accuracy of estimated critical exponents. To exclude the possibility of error in T_c obscuring the critical exponents, we have analyzed the χ_o data in terms of Kouvel-Fisher method [127] and according to that, the expression for susceptibility can be written in the following form

$$\chi_o^{-1}\left[\frac{d\chi_o^{-1}}{dT}\right]^{-1} = \frac{T-T_c}{\gamma} \quad \ldots\ldots\ldots\ldots\ldots\ldots\ldots\ldots\ldots\ldots\ldots\ldots\ldots\ldots\ldots\ldots \quad (3.14)$$

So, the plot of $\chi_o^{-1}\left[\frac{d\chi_o^{-1}}{dT}\right]^{-1}$ versus T is expected to exhibit a linear behavior with a slope *1/*γ and the intercept in the *T* axis equal to T_c. Thus T_c and γ can be determined simultaneously. The plot of $\chi_o^{-1}\left[\frac{d\chi_o^{-1}}{dT}\right]^{-1}$ as a function of *T* is shown in Fig.3.46 and the least square fit to the linear relation is shown as solid line. The γ and T_c values determined from the Kouvel-Fisher method are found to be 1.07 and 629.2K respectively and these values are comparable to those obtained from MAP method. So, we can unequivocally say that the present sample exhibits a long range magnetic interaction of the mean field model.

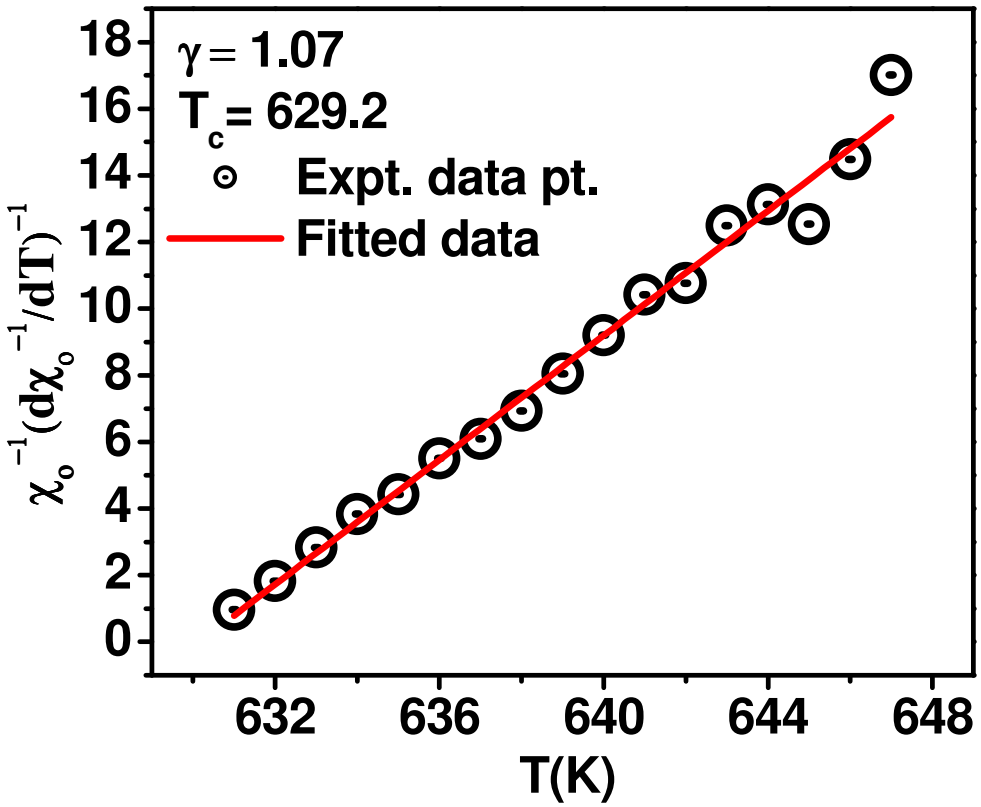

Fig. 3.46 Plot of $\chi_o^{-1}\left[\frac{d\chi_o^{-1}}{dT}\right]^{-1}$ versus temperature along with fitted data.

In order to understand the variation of critical exponents with reduced temperature, we can determine the effective susceptibility critical exponent, γ_{eff} as per the following relation [270]

$$\gamma_{eff} = -\frac{d}{dln\varepsilon}[ln\chi_o(\varepsilon)] \quad \text{.....} \quad (3.15)$$

γ_{eff} value determined from the above technique is found to be quite scattered due to the three points derivative method. To have an idea about the trend of the γ_{eff} as a function of ε, γ_{eff} values were determined by following Padmanabhan *et al.* [270]. The $ln\chi_o$ versus $ln\varepsilon$ data were fitted to the third order polynomial equation and the derivative was obtained analytically. The plot of γ_{eff} as a function ε is shown in Fig. 3.47. Even though, the γ_{eff} values can be identified within the mean field model in the entire ε range, γ_{eff} at $\varepsilon \rightarrow 0$ is found to be closer to the predicted mean field model value of $\gamma_{eff} = 1.0$. It is found to show a broad peak structure with a maximum γ_{eff} value of 1.12 at $\varepsilon = 12.5 \times 10^{-3}$. The broad peak type behavior observed in γ_{eff} versus ε plot is comparable to the theoretical prediction of Priour and Das Sarma [142] in disordered materials, due to the low concentration of magnetic ions. However, they have modeled the magnetic transition in DMS materials in terms of strongly disordered Heisenberg model in 3D lattice. The

present sample, which can be also categorized as strongly disordered system is found to exhibit a long range magnetic interaction.

In the presence of strong disorder, there could be an apparent change in the critical behavior especially at relatively large ε value. In such case, the expression for χ can be written by taking into account the correction to scaling as follows [142]

$$\chi = \chi_o (\varepsilon^{-\gamma} + B\,\varepsilon^{y_1} + C\varepsilon^{y_2} + \cdots) \quad \ldots\ldots\ldots\ldots\ldots\ldots\ldots\ldots\ldots\ldots \quad (3.16)$$

where γ is the genuine critical exponent for χ_o and y_1 and y_2 are the exponents for correction in the scaling relation. The effective exponent, γ_{eff} can be written as

$$\gamma_{eff}(\varepsilon) = \frac{\varepsilon}{\chi_o}\frac{d\chi_o}{dT} = \gamma\left[\frac{1+By_1\varepsilon^{y_1+\gamma}+Cy_2\varepsilon^{y_2+\gamma}}{1+B\varepsilon^{y_1+\gamma}+C\varepsilon^{y_2+\gamma}}\right] \quad \ldots\ldots\ldots\ldots\ldots\ldots \quad (3.17)$$

At $\varepsilon \rightarrow 0$, $\gamma_{eff} \rightarrow \gamma$, the genuine critical exponent of χ_o.

The fit of γ_{eff} versus ε curve, in terms of eq.3.17 is shown in Fig. 3.47 as solid line and it closely follows the experimental data.

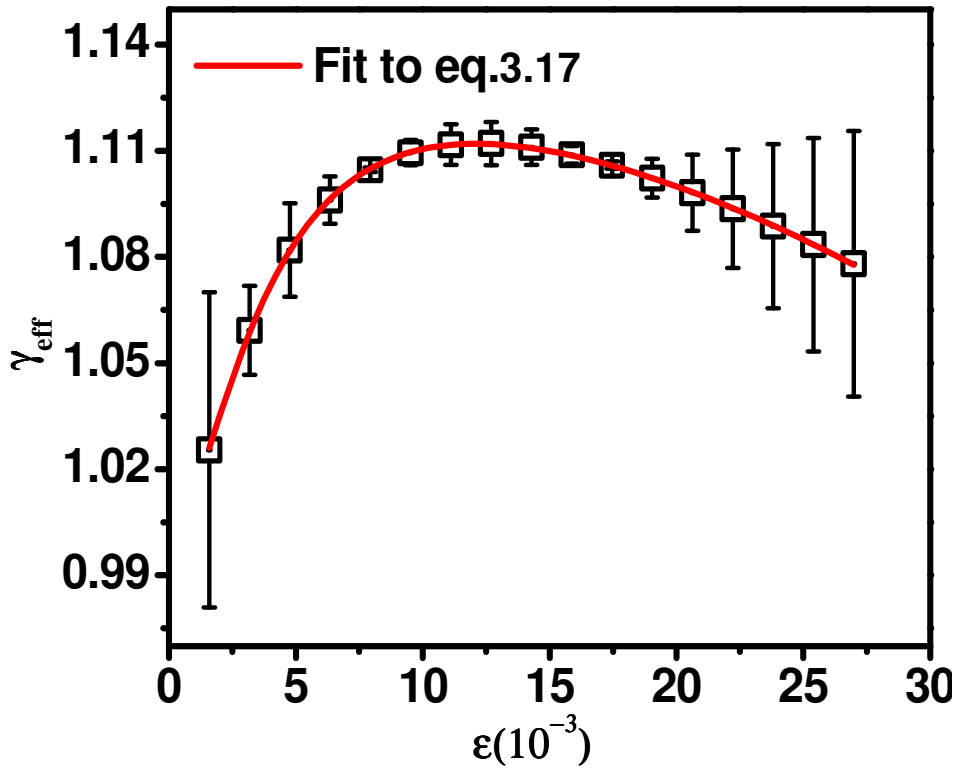

Fig. 3.47 Variation of γ_{eff} with reduced temperature ε.

In order to compare, the obtained critical exponents in the present sample with various theoretical model predictions and on other related materials, the critical exponents β, γ and δ from literature are tabulated in table 3.15.

The critical exponents of the present sample are found to be comparable to those of DMS alloy (Ge,Mn)Te [143] and however, they differ from the values corresponding to (Cd,Mn)Sb and (Cd,Mn)Te [144, 145]. We have also compared with the results of ferrite based materials, where mostly the exponents were comparable to the 3D Heisenberg model. To our knowledge, there is no theoretical prediction on critical exponents of oxide based DMS materials. The possible reason for the observed long range mean field behavior can be discussed by comparing the various mechanisms proposed in literature. Bound magnetic polarons and charge carrier mediated super exchange interaction are quite often used in explaining the FM behavior. In addition to that, defect structure along with charge carrier concentration is found to play a major role on the mechanism of magnetic properties. As per bound magnetic polaron model, each magnetic ion is under the influence of polaron interaction and the overlapping of polarons give rise to long range interaction of magnetic ions, through the polaronic field. So, the observed critical exponents may originate from the long range bound magnetic polaronic interaction. However, theoretical work based on such magnetic interaction would shed further insight into the nature of critical exponents from the above interaction.

Table- 3.15. Comparison of Critical exponent values with different theoretical models for DMS and Ferrite samples.

Sample	Ref.	Technique	T_c (K)	β	γ	δ
$Sn_{0.98}Co_{0.02}O_2$	This work	Bulk (DMS)	629±0.5	0.52±0.02	1.1±0.01	3.12±0.01
Mean Field Model	[120]	Theory	-	0.5	1.0	3.0
3D Heisenberg Model	[120]	Theory	-	0.365	1.336	4.80
3D Ising Model	[120]	Theory	-	0.325	1.241	4.82
$Cd_{0.5}Mn_{0.5}Te$	[145]	Theory	-	-	1.4±0.1	-
$Cd_{0.9}Mn_{0.1}Sb$	[144]	Bulk	536	0.172	-	-
MnSb	[144]	Bulk	514	0.379	-	-
$Ge_{0.12}Mn_{0.88}Te$	[143]	Thin Film	-	0.50	1.00	-
$Ti_{0.2}Fe_{2.8}O_4$	[132]	Single crystal	602	0.47	1.28	-
$MnFe_2O_4$	[131]	polycrystalline	556.2±0.1	0.35±0.04	1.33±0.05	-
Fe_3O_4	[271]	Bulk	853.5	0.379	1.345	-
$Zn_{0.75}Ni_{0.25}Fe_2O_4$	[271]	Bulk	295.2	-	1.420	-

3.6 Summary

Single phase samples of Co doped SnO_2 based diluted magnetic semiconductors were prepared for x=0.02 to 0.10 by solid state route. These samples are found to exhibit room temperature ferromagnetism with the highest magnetic moment of $0.34\mu_B$/Co-ion for x=0.02 sample prepared under N_2 gas atmosphere. The magnetization of x=0.02 sample could be fitted to Brillouin function model by taking into account the ferromagnetic contribution. The magnetization data measured at three different temperatures for $x \geq 0.05$ sample could be fitted to BMP model. The variation of total spontaneous magnetization, M_0 and spontaneous moment per BMP, m_{eff} with temperature has been explained in terms of increase in size of BMP with temperature. The decrease in M_0 and m_{eff} values with increase in doping concentration has been explained on the basis of possible antiferromagnetism due to reduction in average inter-atomic distance of doped Co-ions.

Pure and 2 at % Co doped SnO_2 samples were prepared by co-precipitation technique. The crystallite sizes ranging from 5nm to 15nm have been prepared by choosing different annealing temperature. The homogeneity and single phase nature of the samples have been confirmed from various characterization techniques. Magnetization measurements show the signature of room temperature ferromagnetism. The N_2 gas annealed samples exhibit increase in FM behavior and enhanced conductivity due to the role of N_2 gas in electron doping. We have observed that as the crystallite size reduces, the spontaneous magnetization reduces. This can be explained as a result of restriction in the range of BMP interaction due to smaller crystallites. The resistivity data could be analyzed based on the Mott variable hopping range model (VRH) where the hopping energy and hopping distance are found to be 94 meV and 25Å respectively.

The mechanically milled pure SnO_2 powders were prepared by using two different types of vials and by further annealing at 900^oC. The as milled and annealed samples were characterized by X-ray diffraction, Raman spectroscopy, magnetization and electron spin resonance measurements. Room temperature FM was observed in as milled samples without any transition element doping. They are explained in terms of oxygen vacancy induced localized electrons and the exchange interaction between the spin moment of these electrons. However upon annealing, the FM was

destroyed in one of the samples and partially suppressed in another sample. The measured M-H loops at 20K and 300K were explained in terms of bound magnetic polaron model. The observed ESR spectra and the shift in resonance field upon annealing the samples are found to be consistent with magnetization measurements.

We have shown that bulk Co-doped SnO_2 based diluted magnetic semiconductors prepared by ball milling technique exhibit large saturation magnetic moment with room temperature ferromagnetism. The effective spontaneous moment of BMP was found to be in the order of 10^{-17} emu. The x = 0.02 sample was found to exhibit a maximum FM T_c of 640 K and a effective paramagnetic moment of 2.34 μ_B/TM-ion. The saturation magnetization of 7.9 μ_B/ Co-ion was observed for x = 0.02 sample and is comparable to giant magnetic moment reported by Ogale *et al.* [39]

We have carried out detailed isothermal magnetization measurements in the critical region of $Sn_{0.98}Co_{0.02}O_2$ based DMS material prepared by ball milling technique. The critical exponents corresponding to ferromagnetic to paramagnetic transition were extracted by using modified Arrott plot method. The observed FM transition is found to be of second order in nature. The obtained critical exponents are found to be comparable to the values predicted by mean field model, i.e. with long range interaction. We have also estimated the critical exponent, γ based on Kouvel-Fisher method and it is found to be consistent with the result of MAP method. The critical exponents are also found to follow the Widom scaling relation and universal scaling hypothesis. The characteristic feature of temperature variation of effective critical exponent, γ_{eff} is found to be comparable to the theoretical prediction of disordered system.

Chapter 4

Ni-doped SnO_2 Series

Preparation of Ni doped SnO_2 was carried out by following solid state route and mechanical milling. Their structural characterization and detailed magnetization studies are given. Room temperature FM in thin film samples of Ni doped SnO_2 was reported by Hong *et al.* [272]. The FM T_c was reported to be around 400 K, where the M-T measurement was carried out up to 400 K. Moreover, they have reported that the magnitude of magnetic moment strongly depends on nature of substrate. In order to determine the T_c and to understand the role of Ni in promoting the room temperature FM, without the influence of substrate related ambiguity, we have prepared bulk $Sn_{1-x}Ni_xO_2$ samples for x = 0.0, 0.02, 0.05, 0.07 and 0.10. The temperature variation of magnetic moment was measured up to 1000 K. The M_s value was found to increase up to 7 at % of Ni doping and then decreases with further increase in Ni-doping concentration. The typical M_s value for x = 0.07 sample is found to be 0.023 emu/g (0.01 μ_B/Ni-ion). The effective magnetic moment of the order of 1.4μ_B/Ni-ion with Curie temperature θ_c as high as 770 K has been observed. The magnetization data could be analyzed based on bound magnetic polaron(BMP) model with a typical spontaneous magnetization of 0.06emu/g and a BMP radius of 60 Å.

We have also prepared Ni doped SnO_2 by mechanical milling followed by high temperature annealing. All the prepared samples are found to be in single phase form and could be refined using $P4_2/mnm$ space group. The samples were also characterized by recording Raman spectra. FM ordering above room temperature has been observed for all the Ni doped samples. The samples prepared by ball milling technique also exhibit enhancement in saturation magnetization up to 7 at % of Ni doping similar to the case of solid state synthesized samples. The highest saturation magnetization was found to be 1.13emu/g (0.42 μ_B/Ni ion). The typical value of effective magnetic moment μ_{eff} estimated from the modified Curie-Weiss law analysis is found to be 3.9μ_B/Ni ion and θ_c = 695 K for x = 0.07 sample. The initial magnetization data could be analyzed based on the BMP model. The spontaneous magnetic moment per BMP, m_{eff} was found to be in the order of 10^{-17} emu.

4.1 Ni-doped SnO_2 by solid state route

4.1.1 Preparation and Characterization

Polycrystalline samples of $Sn_{1-x}Ni_xO_2$ (x = 0.0, 0.02, 0.05, 0.07 and 0.10) were prepared by following the standard solid state route. Stoichiometric ratio of SnO_2 and NiO with 99.9% purity were weighed and they were mixed thoroughly for several hours under acetone to have a homogeneous mixture followed by presintering at 400^{o}C for 24 hr. The final sintering in pellet form was carried out at 900^{o}C for 36 hrs in air with several intermediate grindings. Fig.4.1 shows XRD patterns of x = 0.0, 0.02, 0.05, 0.07 and 0.10 samples. Fig.4.2 shows the XRD patterns recorded for all the Ni doped samples along with Rietveld refinement. All the observed peaks could be refined by using $P4_2/mnm$ space group and it suggests the single phase nature of the samples. The typical lattice parameters are found to be a = b = 4.732 Å and c = 3.184 Å for x = 0.0 and a = b = 4.734 Å and c = 3.187 Å for x = 0.07 sample. The parameters obtained from the refinement are tabulated in table-4.1. Fig.4.3 shows the intensity in the logarithmic scale for x=0.0 and x=0.07 sample, where no trace of impurity phase could be identified. The average crystallite size was estimated using the Scherrer's formula, $S=\lambda k/\beta\cos\theta$, where constant k = 0.89, λ = 1.5406Å, β is the full width at half maximum (FWHM) of diffraction peaks and θ is the glancing angle. The experimental β value was corrected for instrumental broadening. The average crystallite size was estimated to be 40 nm for x = 0.07 sample.

The SEM images show uniform surface morphology as shown in Fig.4.4. The cation ratio obtained from EDX analysis are given in table-4.2 and are found to be comparable to that of nominal starting composition.

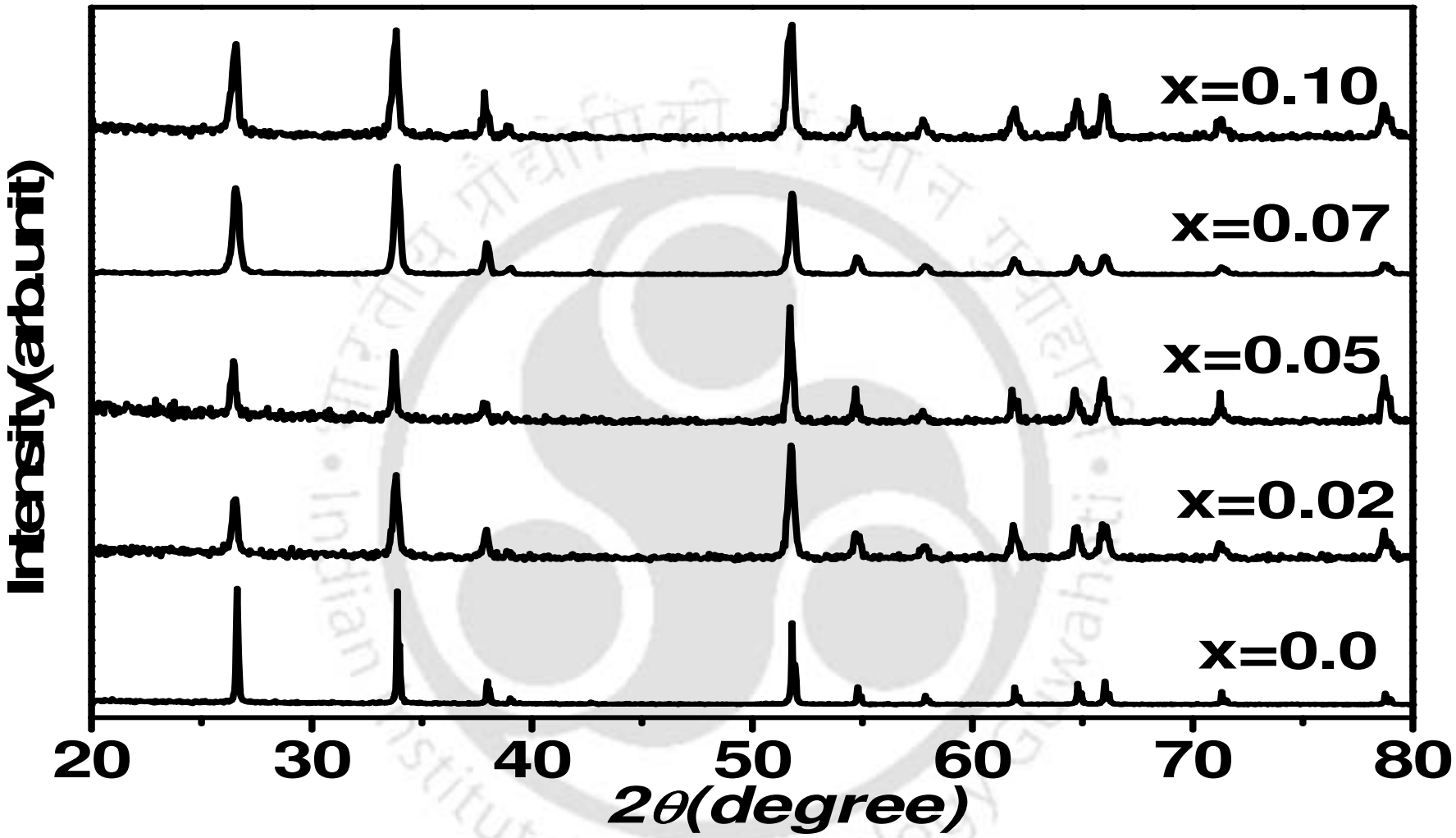

Fig. 4.1. XRD patterns recorded at room temperature for x=0.0, 0.02, 0.05, 0.07 and 0.10 samples of $Sn_{1-x}Ni_xO_2$.

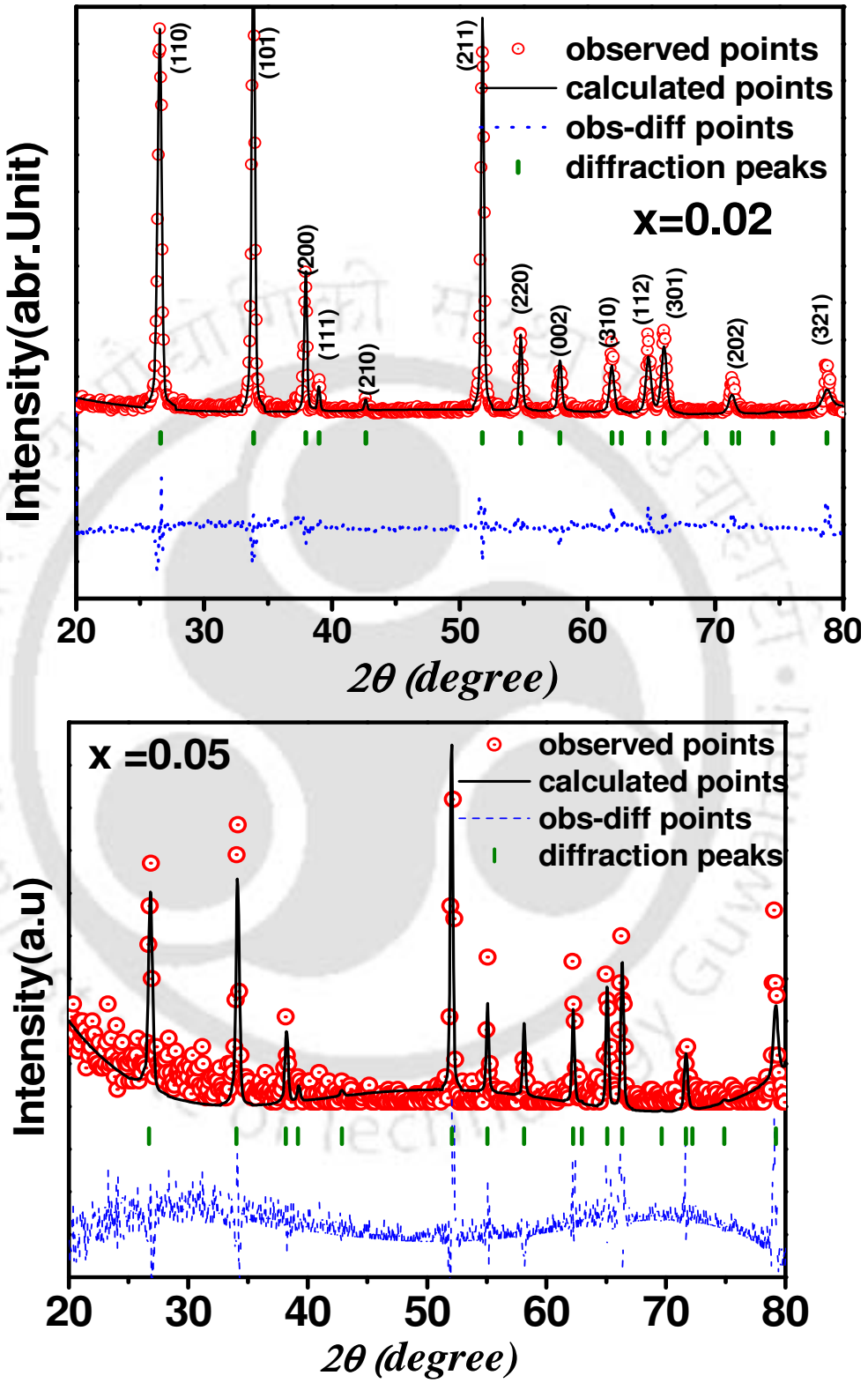

Fig.4.2 (a) XRD patterns along with Rietveld refinement for x=0.02 and 0.05 samples.

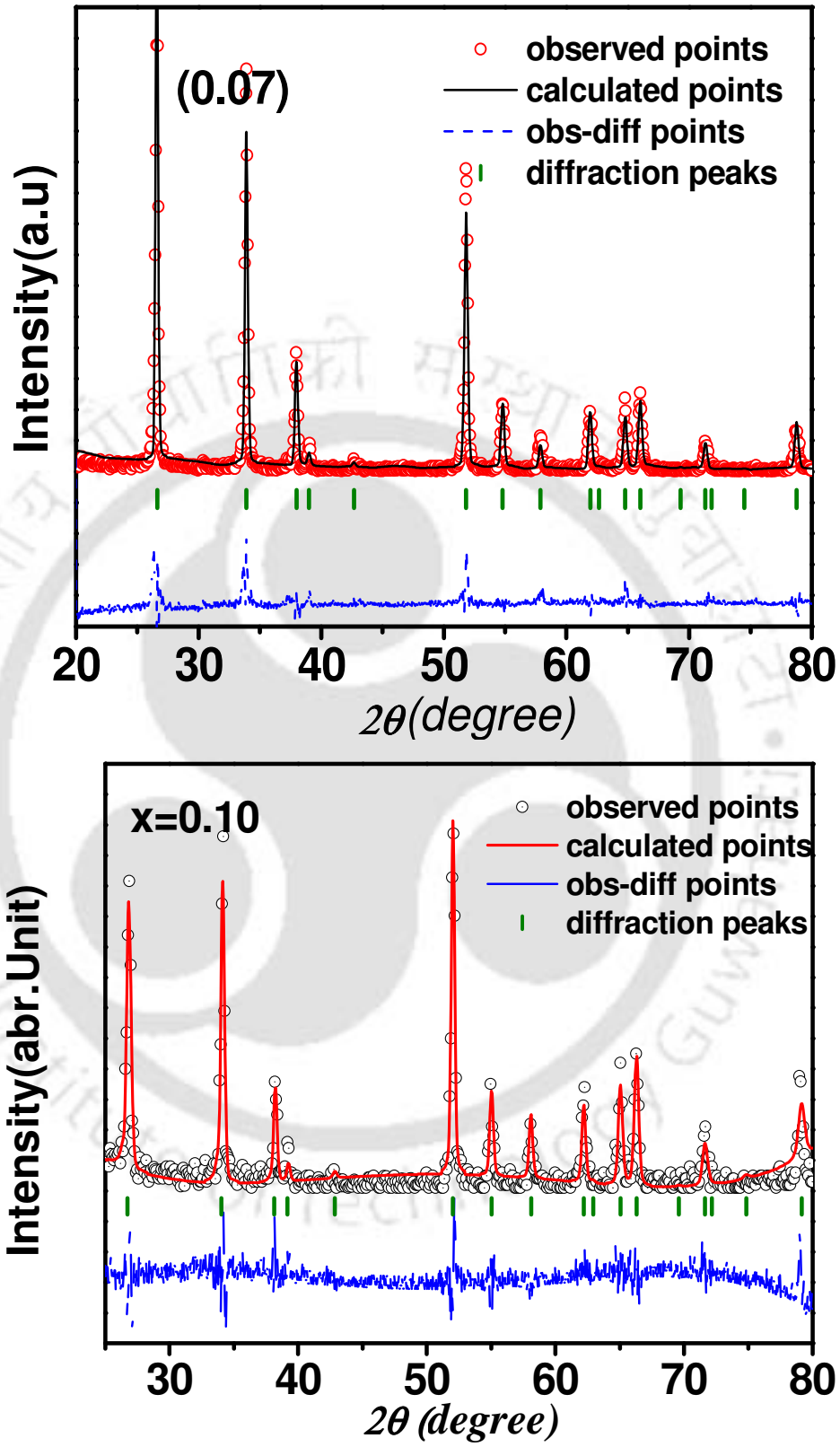

Fig. 4.2(b) XRD patterns along with Rietveld refinement for x= 0.07 and 0.10 samples.

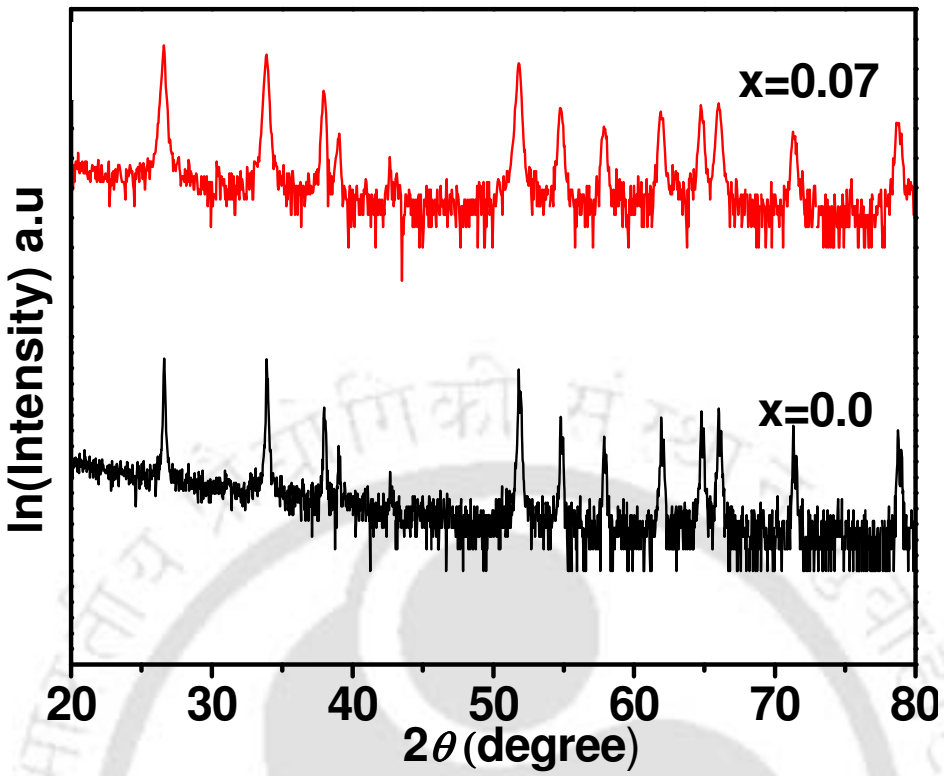

Fig. 4.3 XRD patterns of x =0.0 and 0.07 samples with intensity in logarithmic scale.

Table- 4.1 List of parameters obtained from the Rietveld refinement and analysis of XRD patterns.

Sample/Parameters	**x = 0.0**	**x = 0.02**	**x = 0.05**	**x = 0.07**	**x = 0.10**
Space group	$P4_2/mnm$	$P4_2/mnm$	$P4_2/mnm$	$P4_2/mnm$	$P4_2/mnm$
a = b (Å)	4.732	4.716	4.713	4.712	4.710
c (Å)	3.184	3.172	3.171	3.165	3.162
Volume (Å^3)	71.3	70.5	70.43	70.27	70.14
χ^2 (%)	3.17	2.36	3.07	3	3.02
R_p (%)	28	28	30	25	28
Crystallite size(nm)	66	40	42	42	43

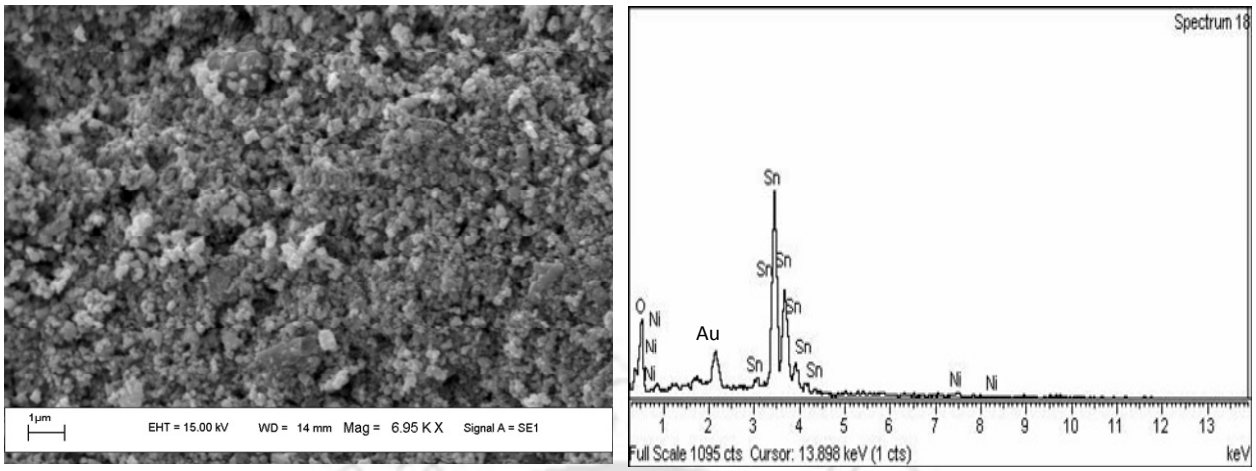

Fig.4.4 SEM image and EDX spectrum of $Sn_{0.95}Ni_{0.05}O_2$.

Table-4.2 Cationic ratio obtained from EDX measurement for different Ni-doped SnO_2 samples.

Sample	**Calculated Cationic Ratio from EDS**	
	Sn	**Ni**
x=0.02	0.98	0.02
x=0.05	0.94	0.05
x=0.07	0.93	0.06
x=0.10	0.90	0.08

Fig.4.5 shows the TEM images of x = 0.07 sample taken in a carbon coated copper grid. The average particle size is found to be around 50 nm. The inset of the Fig. 4.5(a) shows the selected area electron diffraction pattern and it depicts the polycrystalline behavior of the sample. The absence of ring like pattern suggests that the crystalline grains were in some preferred orientation. The high resolution transmission electron microscope (HRTEM) images were recorded at different locations and its typical image is shown in Fig.4.5(b), where we can see the continuous (110) atomic plane. The Fast Fourier Transform (FFT) image and inverse FFT by filtering the noise are shown in the top and bottom insets of Fig.4.5(b), where we can see the

uniform (110) plane. The EDS measurement using TEM facility was carried out and it showed the presence of Ni within the crystallites.

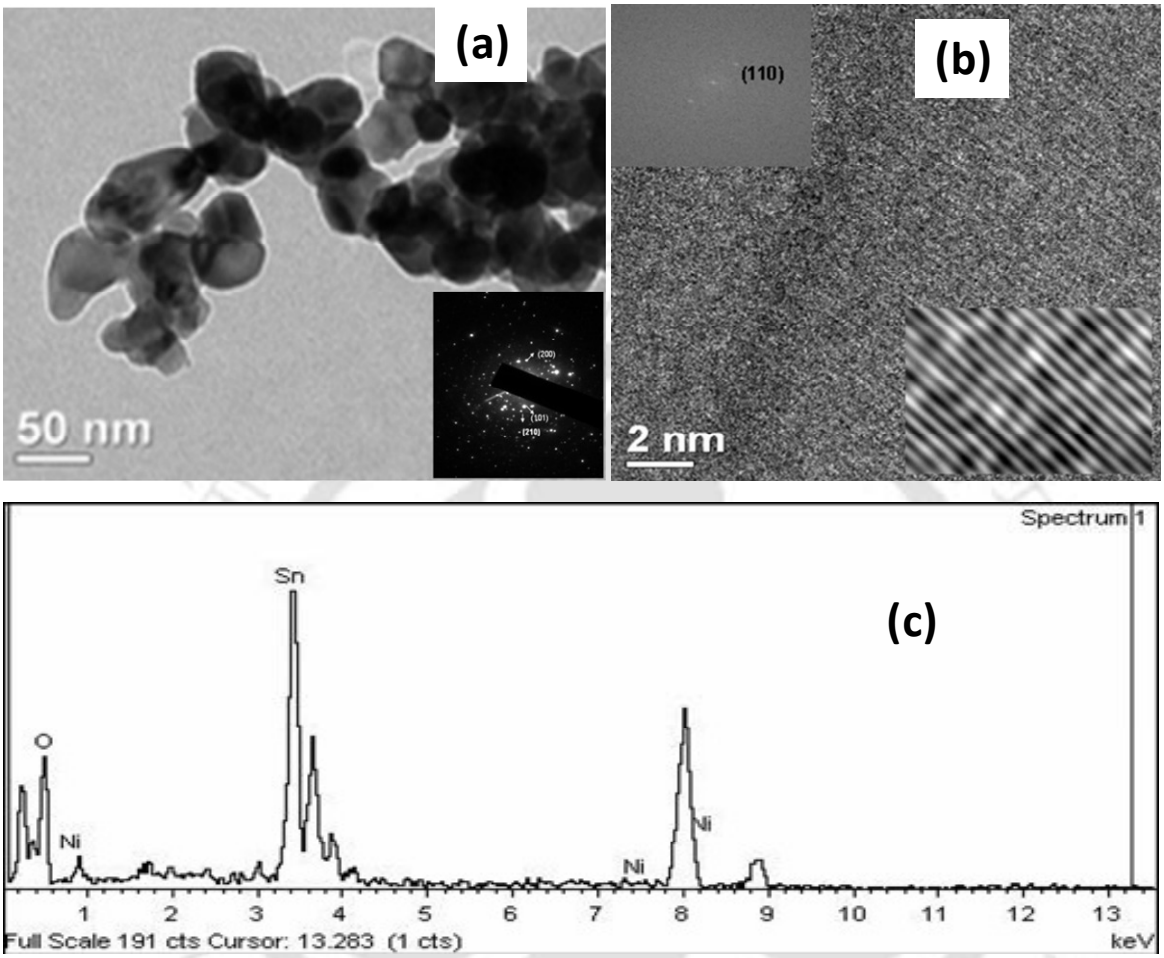

Fig. 4.5 (a) TEM image of x=0.07 sample and the inset shows the selected area diffraction pattern. **(b)** HRTEM image showing the (110) plane. FFT image and inverse FFT image after filtering the background for (110) plane are shown in the top and bottom insets of the Fig (b). **(c)** EDS spectrum of x =0.07 sample showing the presence of Ni.

To further substantiate the doping of Ni ions, FTIR spectra were recorded. Fig. 4.6 shows the absorption spectra for different doped samples along with the parent SnO_2 and NiO compounds. The absorption band observed at 3400 cm^{-1} and 1640 cm^{-1} can be attributed to a hydroxyl group, which is in the O-H mode. The weaker band at, 1370 and 1130 cm^{-1} are basically from C-H vibrations as a result of reaction of atmospheric CO_2 with H_2O as reported in ref.[257]. The bands at around 530 and 680 cm^{-1} correspond to antisymmetric Sn-O-Sn vibrations of SnO_2. So, it is evident from Fig.4.6 that the prepared samples exhibit pure rutile structure without any signature of contribution from NiO cluster.

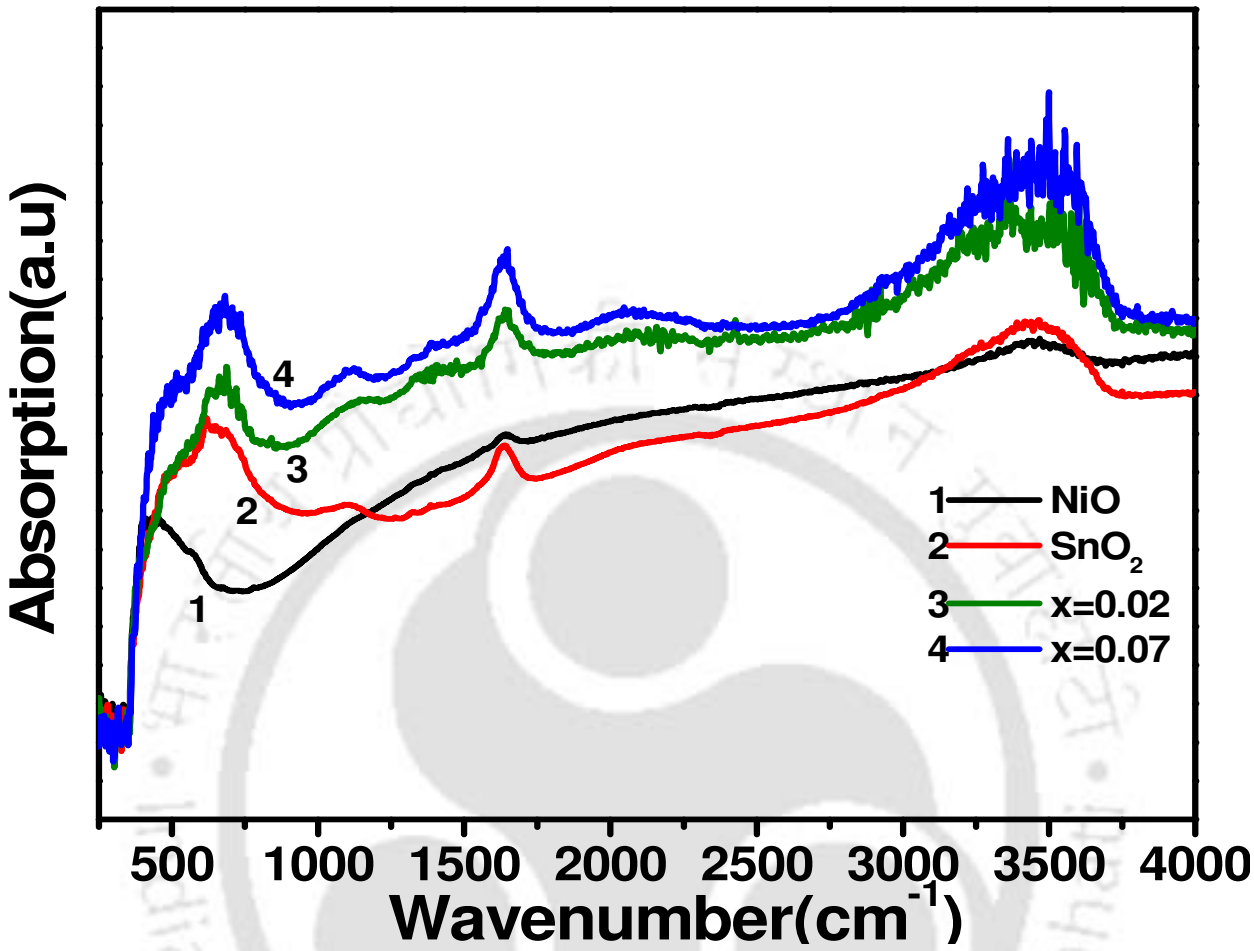

Fig.4.6 FTIR spectrum for x = 0.02 and 0.07 samples along with parent SnO_2 and NiO compounds for comparison.

4.1.2 Magnetic Properties

The magnetic hysteresis loops recorded for x = 0.02, 0.05, 0.07 and 0.10 samples of Ni doped SnO_2 at 85 K and 300 K are shown in Fig.4.7. They demonstrate the presence of room temperature FM. For a comparison, we have also carried out M-H loop measurement on the parent compound SnO_2, and it is found to exhibit weak diamagnetic behavior. The lack of saturation in M-H curves with considerable linear contributions especially at low temperatures highlights the presence of considerable paramagnetic matrix or other competing magnetic interaction. The increase in hysteresis loss with decrease in temperature could be mainly due to

magnetic anisotropy. The observed saturation magnetization is found to be comparable to those reported in literature for ZnO and SnO_2 based DMS materials [273-276]. The values of coercive field, H_c and saturation magnetization, M_s at 85 K and 400K for different samples are tabulated in table-4.3.

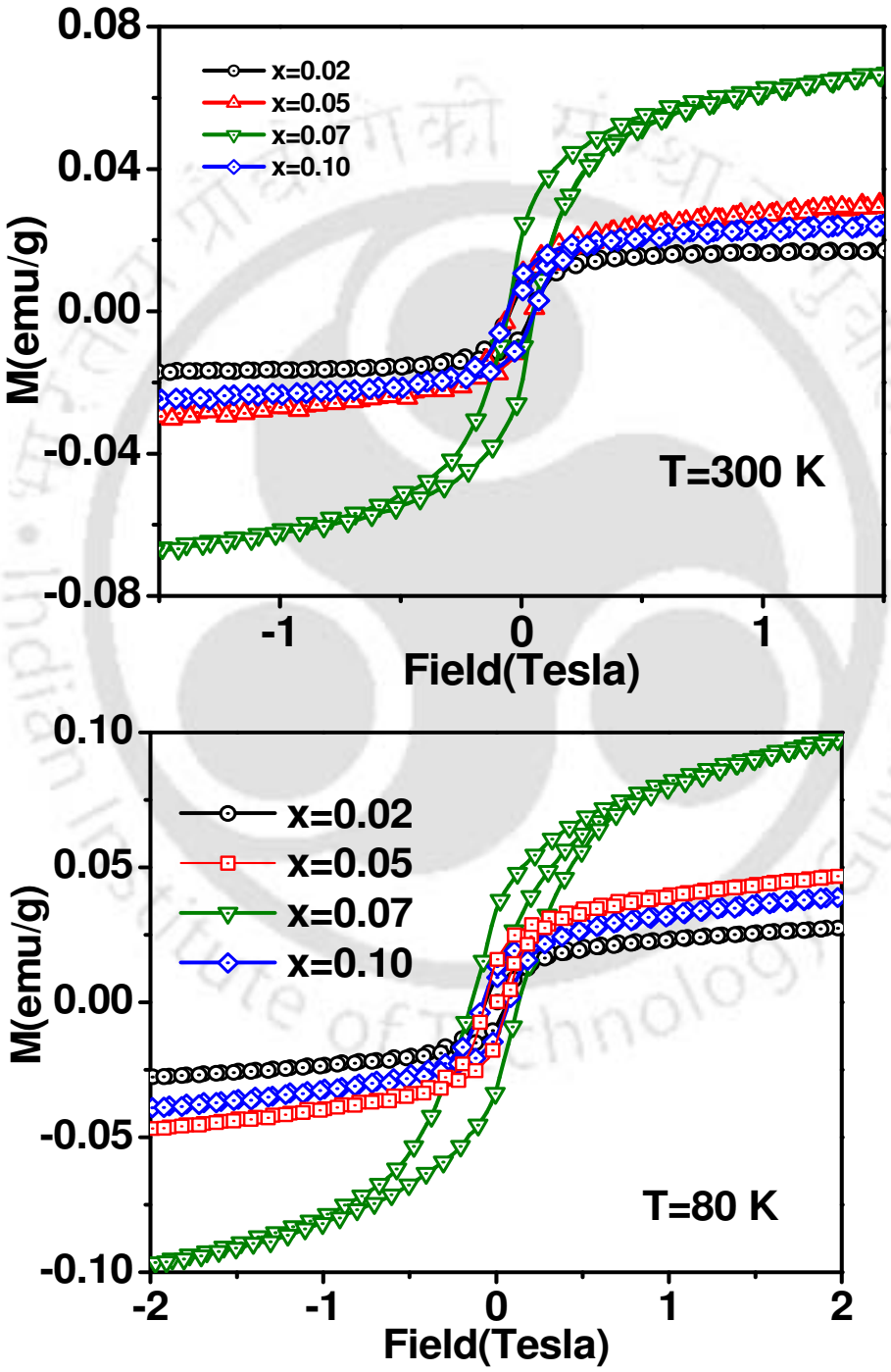

Fig.4.7 M-H loops recorded for x=0.02, 0.05, 0.07 and 0.10 samples at 300K and 80 K.

Table-4.3 Coercive Field (H_c) and saturation magnetization (M_s) values determined for various Ni-doped samples from the magnetization measurements.

Sample/Parameters	**x = 0.0**	**x = 0.02**	**x = 0.05**	**x = 0.07**	**x = 0.10**
H_c Oe (85 K)	diamagnetic	643	650	1314	733
H_c Oe(400 K)	----------	450	490	555	547
M_s emu/gm(85 K)	----------	0.027	0.02	0.025	0.008
M_s emu/gm(400 K)	----------	0.021	0.014	0.023	0.006

The resistivity of these samples is found to be in the order of 10^4 Ω-cm at room temperature and it enhances to 10^7 Ω-cm at around 100 K. The rather large value of resistivity indicates the localized nature of charge carriers. The localized charge carriers are expected to promote the bound magnetic polaron mediated ferromagnetism. Here each trapped charge carrier polarizes the spin of the magnetic ions within its Bohr radius and it leads to ferromagnetic bubble or BMP embedded in a paramagnetic matrix. Ferromagnetism is observed, when these ferromagnetic bubbles start overlapping in such a way that all the magnetic spins are aligned in a particular orientation [112, 113, 255, 267].

In order to further understand the magnetic properties, we have fitted the measured initial M-H curve in terms of the bound magnetic polaron (BMP) model by following refs. [112, 113, 255] and as per eq. 3.2. The parameters M_0, m_{eff}, χ_m were varied during the fit. Plots of magnetization curve for x = 0.02, 0.05, 0.07 and 0.10 samples at 80 K and 300 K along with fitted data to BMP model are shown in Fig.4.8. The theoretical fit closely follows the experimental data and the fitted parameters M_0, m_{eff} and χ_m are given in table-4.4. For a given sample, M_0 is found to increase marginally but m_{eff} is found to reduce with decrease in temperature. The increase in M_0 could be due to interaction between BMP and the paramagnetic matrix and however further analysis is required to verify such interactions. The enhanced hysteresis loop at low temperature can be explained on the basis of magnetic anisotropy. The possible reason for low m_{eff} at low temperature could be due to reduced size of BMP. The origin of such reduced BMP size can be due to the presence of competing magnetic interaction. The considerable increase in χ_m value at low temperature is consistent with smaller size of BMP. The above variation of χ_m cannot be simply explained based on the Curie law for the paramagnetic matrix and it supports the above

argument of BMP size. With the increase in doping concentration; the M_0 and χ_m values are found to increase as a result of higher concentration of magnetic ions. In the present series of samples, the parameter M_0/m_{eff} is found to vary with temperature, so in such condition, one cannot assume $m_s = m_{eff}$. In view of the above restriction, we could not estimate N, the number of BMP per unit volume. The average radius of the BMP was estimated from the fitted value of m_{eff} and by assuming a spherical shape of BMP and, it is found to be 60 Å for x = 0.07 sample at 80 K. The BMP radius is found to be in the same order of magnitude as reported in other magnetic system such as, in CdMnSe by Dietl *et al.* [267]. The main uncertainty in the above calculation is from the estimation of number of transition element ions, Ni within each BMP, especially in weakly doped materials. On the other hand, in other magnetic system following BMP model such as $Cu_2Mn_{0.9}Zn_{0.1}SnS_4$ and $Y_{0.9}Ce_{0.1}MnO_3$ [112, 256] the number of magnetic ions per BMP is large by an order of magnitude. The m_{eff} values are found to increase with temperature and this could be mainly due to change in size of the BMP.

Table 4.4: List of parameters obtained from the analysis of M-H data by using BMP model. M_0 is the spontaneous magnetization of the system, χ_m is the susceptibility of the matrix and m_{eff} is the effective magnetic moment for per BMP.

Sample/ parameter	***x=0.02***		***x=0.05***		***x=0.07***		***x=0.10***	
T (K)	80	300	80	300	80	300	80	300
M_0(emu/g)	0.02	0.02	0.04	0.02	0.07	0.06	0.03	0.02
$\chi_m(10^{-4}$ cgs)	0.04	0.002	0.03	0.002	0.1	0.004	0.02	0.003
$m_{eff}(10^{-17}$ emu)	2.17	5.9	2.3	7.4	1.25	3.6	1.6	7.4
BMP radius (Å)	70	98	52	78	38	54	37	61

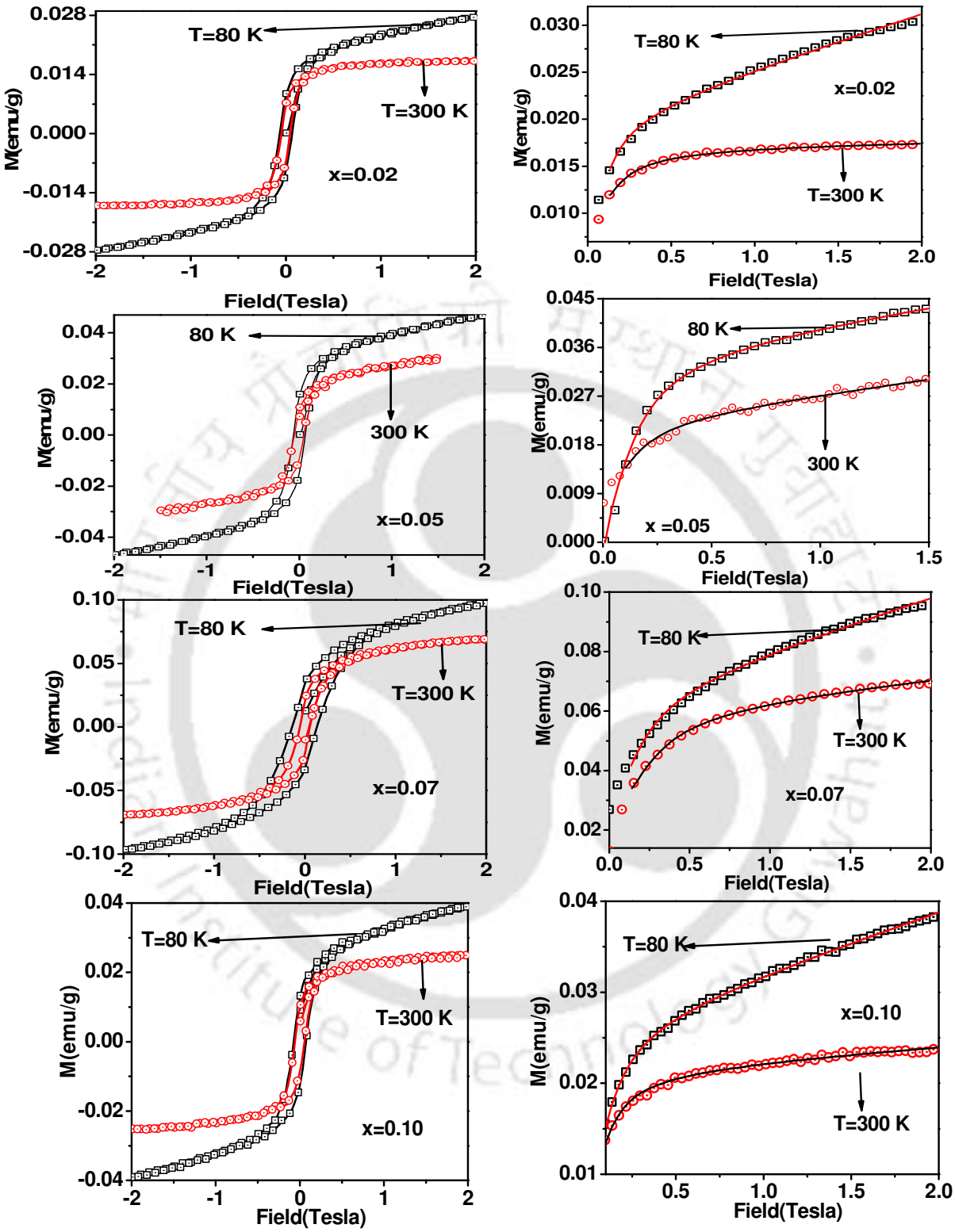

Fig. 4.8 Magnetic hysteresis loops for x = 0.02, 0.05, 0.07 and 0.10 samples at 80 K and 300 K along with fit to BMP model.

In order to study the ferromagnetic transition, the temperature variation of magnetization was measured for a wide temperature range i.e. 300 K to 1000 K. The M-T curves for all the Ni doped samples are shown in Fig.4.9, where a clear PM to FM transition can be seen. The magnetization is found to increase gradually with decrease in temperature. The paramagnetic susceptibility was fitted to modified Curie-Weiss law, i.e. by fitting to eq. 3.7. The paramagnetic susceptibility along with the fit to eq.3.7 are shown in Fig.4.10. The typical values of Curie temperature are found to be 770 K and 730 K respectively for x = 0.02 and x = 0.07 samples. The θ_c and effective magnetic moment μ_{eff} values for all the Ni doped samples are given in table-4.5. The typical value of μ_{eff} estimated from Curie constant is found to be 1.4μ_B/Ni ion for x=0.07 sample and it suggests that the doped Ni ions are expected to be mostly in Ni^{2+} state. If the doped Ni ions are in the Ni^{2+} state, one would expect the μ_{eff} value to be of the order of 2.8μ_B/Ni ion, the observed difference between experimental and theoretical value could be due to only a fraction of Ni ions entering the Sn site.

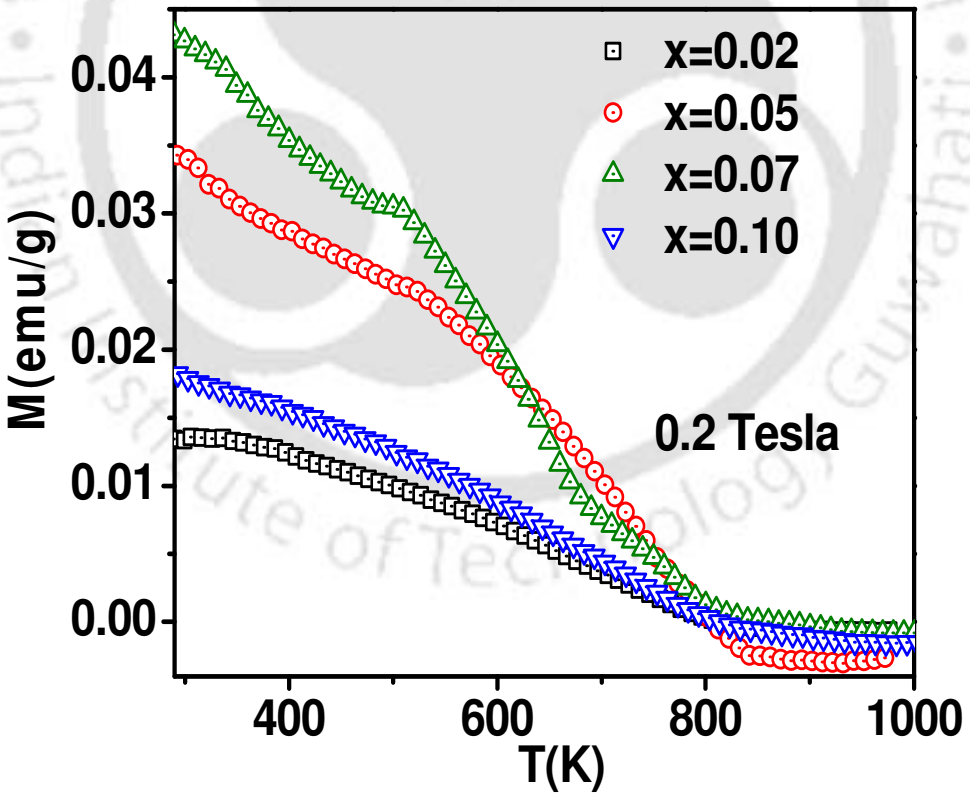

Fig.4.9. Temperature variation of magnetization for x=002, 0.05, 0.07 and 0.10 samples.

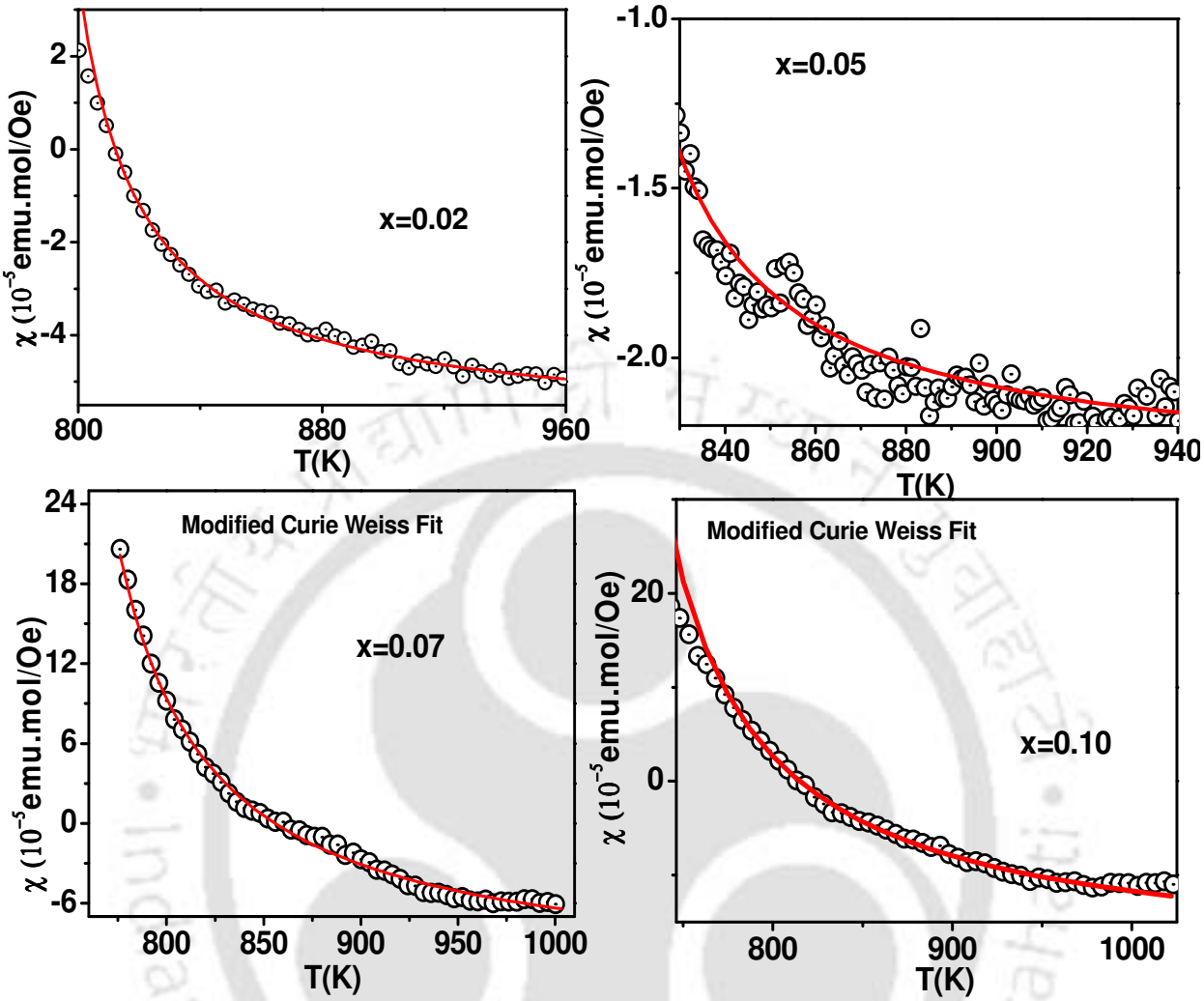

Fig.4.10 paramagnetic susceptibility along with Curie-Weiss law fit for x = 0.02, 0.07 and 0.10 Ni doped SnO_2.

Table-4.5 Parameters obtained from Curie-Weiss fit. Where θ_c is the Curie temperature, μ_{eff} is the effective magnetic moment per Ni-ion.

Sample/Parameters	x=0.02	x=0.05	x=0.07	x=0.10
θ_C (K)	770	750	730	690
μ_{eff} (μ_B)	1.3	1.4	1.43	1.54

4.1.3 Resistivity Analysis

The temperature variation of electrical resistivity was measured down to 100 K for x=0.0, 0.02, 0.05, 0.07and 0.10 samples. The plots of resistivity as a function of temperature for x = 0.0, 0.02 and 0.10 are shown in Fig.4.11. They exhibit semiconducting behavior. The resistivity of x = 0.0 sample at T = 100 K was found to in the order of $10^5\Omega$-cm and it was found to increase up to $10^8\Omega$-cm, upon doping.

The resistivity data could be analyzed based variable range hopping (VRH) model [148] using eq.3.5. The plots of $ln\rho$ as a function of $(1/T)^{1/4}$ for the samples along with VRH model fit are shown in Fig.4.12. The density of states in the vicinity of Fermi level N (E_F), hopping distance R_{hop} and hopping energy E_{hop} was determined by following ref. [148] and they are tabulated in table-4.6. The typical values of density of states, hopping distance and hopping energy are found to be 6.1×10^{24} $eV^{-1}m^{-3}$, 59Å and 215meV respectively for x=0.02. The above parameters for x = 0.07 sample are found to be 1.3×10^{25} $eV^{-1}m^{-3}$, 49 Å and 178meV respectively.

Table-4.6 Parameters obtained from VRH model fit. Here ρ(RT), $N(E_F)$, $R_{hop}(RT)$ and $E_{hop}(RT)$ are resistivity, density of states in the vicinity of Fermi level, hopping distance and hopping energy at room temperature respectively.

Sample Parameters	**x=0.00**	**x= 0.02**	**x=0.05**	**x=0.07**	**x=0.10**
ρ (RT) (10^4 Ω-cm)	0.4	50	65	10	3
$N(E_F)$ 10^{25} $eV^{-1}m^{-3}$	18.0	0.6	0.6	1.3	1.4
R_{hop}(RT) Å	25	59	60	49	48
E_{hop}(RT) meV	92	215	219	178	175

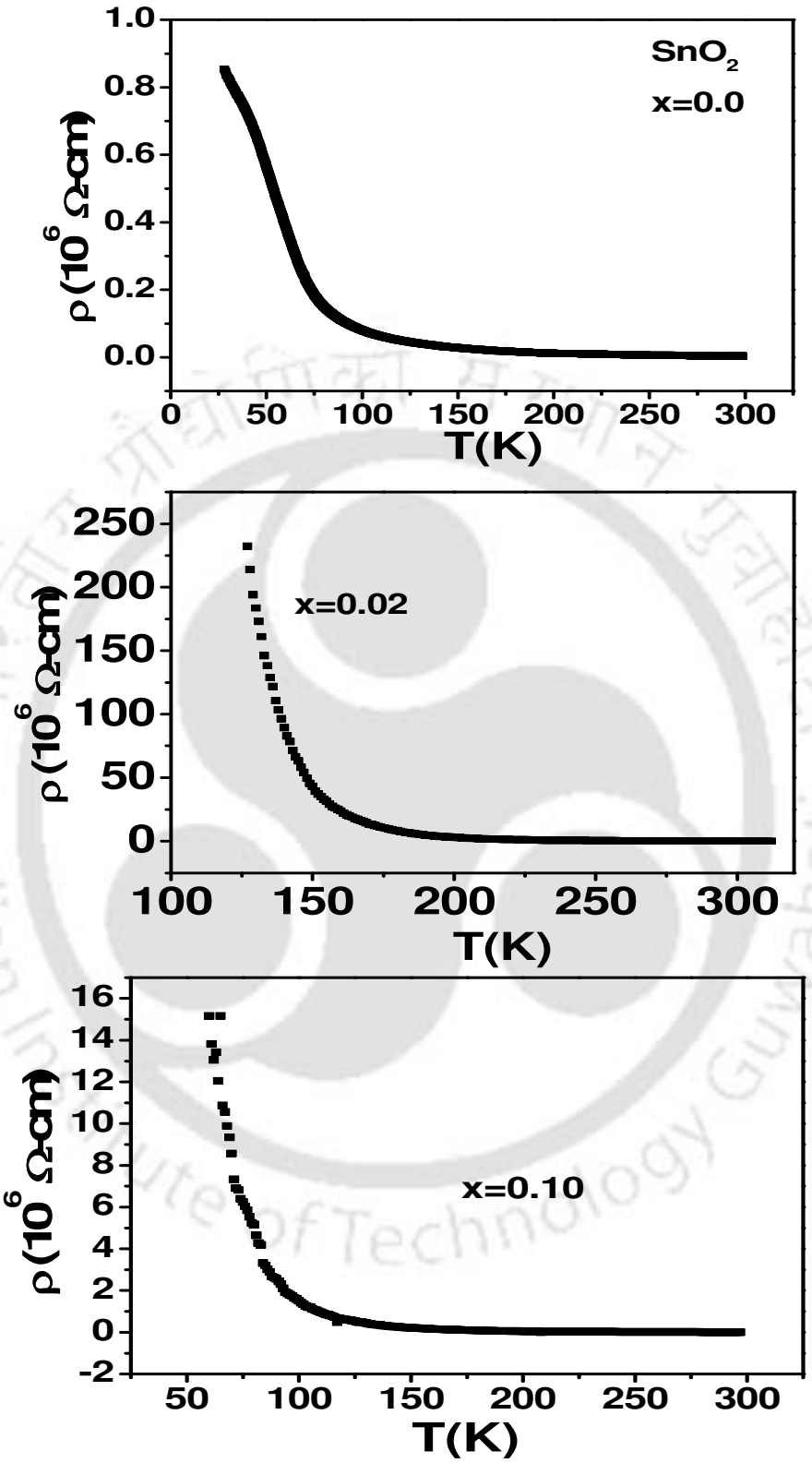

Fig.4.11 Temperature variation of electrical resistivity for x=0.0, 0.02, 0.07 and 0.10 samples.

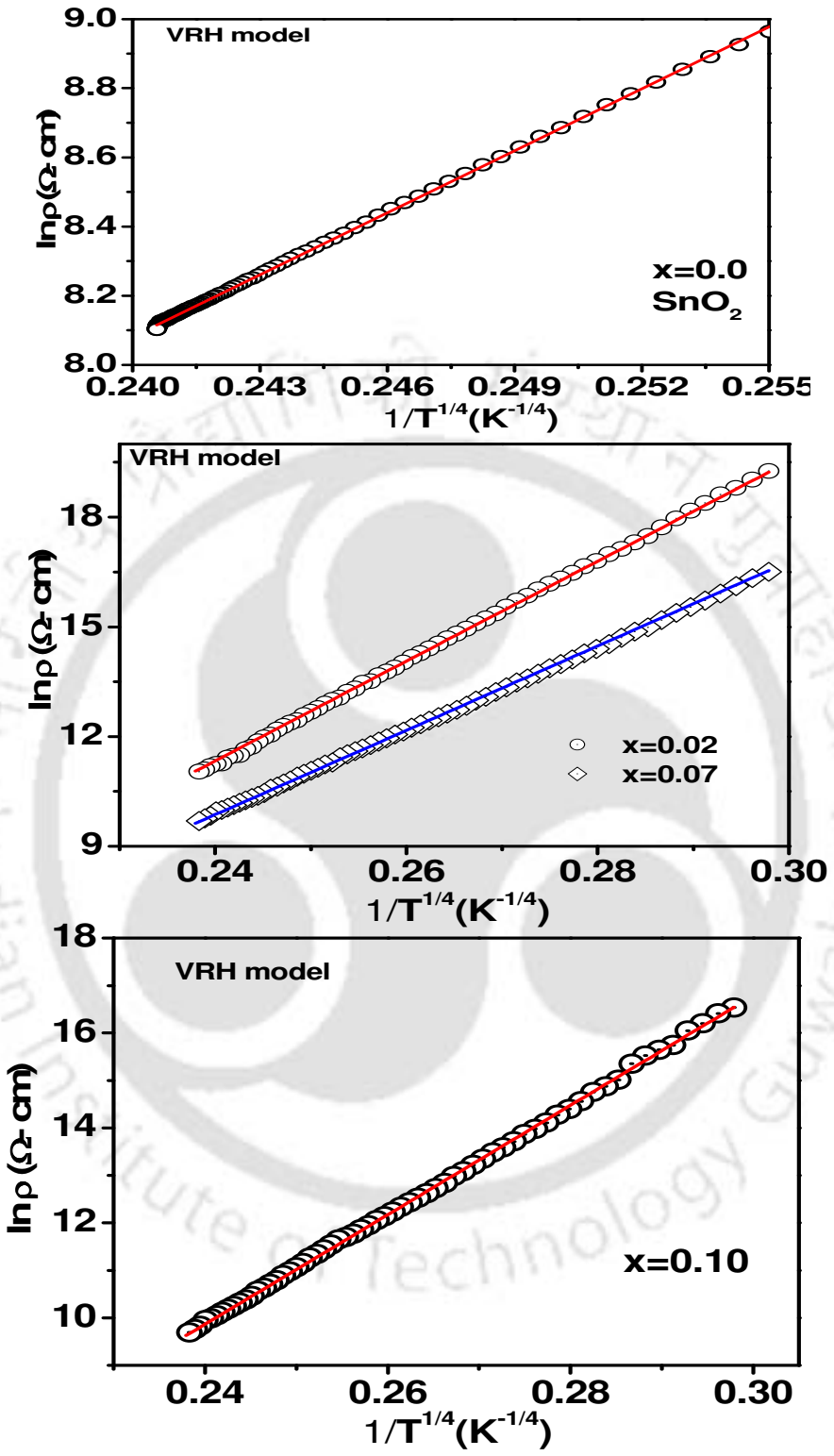

Fig. 4.12 ln ρ versus $(1/T)^{1/4}$ plots along with VRH model fit (solid line).

4.1.4 ESR Measurement

To further investigate the magnetic property of $Sn_{1-x}Ni_xO_2$ samples, ESR spectra were recorded. Fig.4.13 shows the ESR spectra of all the Ni-doped samples at room temperature. The typical resonance field for 2 at % Ni-doped sample is found to be 227 mT (g = 2.84) at 120 K and the value increases to 246 mT at 295K. The values of the resonance peak at room temperature and 120K are given in table-4.7. The integrated intensity of ESR spectra for x = 0.02 and 0.07 and 0.10 samples are shown in Fig.4.14. They show the presence of FM interaction along with the contribution of paramagnetic signal. They could be simulated by using two Gaussian curves as shown in Fig.4.14. The low field shoulder gradually decreases with increase in temperature as the material approaches towards transition temperature.

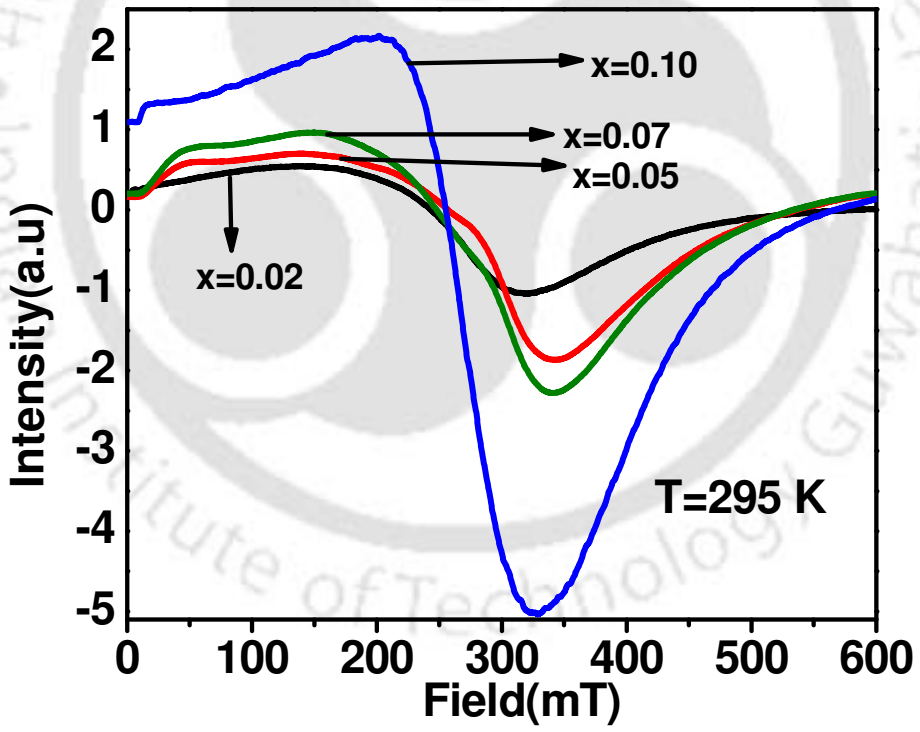

Fig.4.13 ESR data recorded for x = 0.02, 0.05, 0.07 and 0.10 at 295 K.

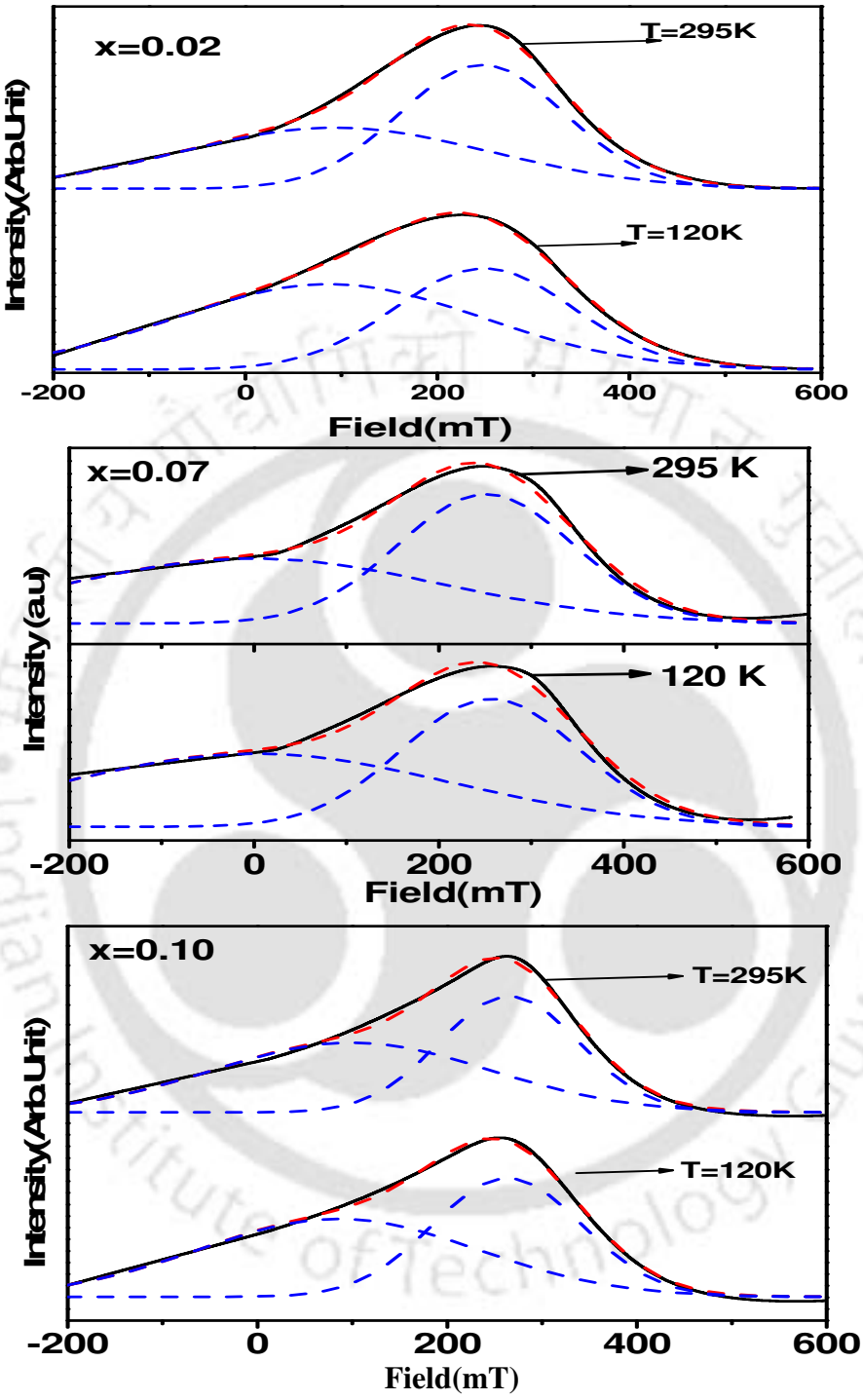

Fig. 4.14 ESR spectra recorded for x = 0.02, 0.07 and 0.10 samples at 295 K and 120 K. The experimental spectrum could be simulated with the help of two overlapping Gaussian profiles.

Table-4.7 Resonance fields (high field and low field) obtained from two overlapping Gaussian profiles at 295 K and 120 K.

Sample	Resonance Field at 295 K (mT)		Resonance Field at 120 K (mT)	
	HF	**LF**	**HF**	**LF**
x=0.02	246	80	246	74
x=0.05	265	55	255	42
x=0.07	274	44	249	31
x=0.10	265	99	263	84

4.2 Ni-doped SnO_2 by ball milling

4.2.1 Preparation and Characterization

$Sn_{1-x}Ni_xO_2$ samples for x = 0.0, 0.02, 0.05, 0.07 and 0.10 were prepared by mechanical milling method. Stoichiometric ratio of SnO_2, NiO with 99.9% purity were weighed and mixed and, then ball milled using a hardened steel vial containing steel balls of 10 mm diameter where the average weight of each ball is approximately 3.5g. The weight of the vial is 5.5 kg and the volume is estimated to be 590 cm^3. The milling speed was 500 rpm and ball to powder weight ratio was 10:1. The milling was carried out for the duration of 10 hrs. The milled powders were pressed into cylindrical pellets and were annealed in air at 900^oC for 10 hrs. Fig.4.15 shows the XRD patterns recorded for all the Ni-doped samples at room temperature. They are found to be in single phase form. The patterns could be refined by using $P4_2/mnm$ space group with the aid of Rietveld refinement technique and Fullprof programme. The XRD patterns along with the Rietveld refinement for all the doped samples are shown in Fig.4.16. No appreciable variation in lattice parameters with Ni doping has been observed and it can be understood in terms of comparable size of Ni^{2+} ions replacing Sn^{4+}ions. The lattice parameters for 2 at % Ni doped sample are found to be a=b=4.739Å and c=3.188Å and they are found to be a=b=4.743Å and c=3.191Å for 10 at % Ni doped sample. All the parameters obtained for different Ni-doped samples are given in table-4.8. No extra impurity phase has been detected from the XRD data. The refined occupancy values of Sn and Ni are found to be comparable to the nominal starting composition. The average crystallite size was calculated using the Scherrer's formula and was found to be in the order of 40 nm.

Fig.4.17 shows the typical SEM image and EDX spectrum for the Ni doped samples. The EDX spectrum shows the presence of Fe along with Ni, Sn and O_2 peaks. The typical ratio of Sn:Ni:Fe for 5 at % Ni doped sample is found to be 0.94:0.05:0.01. The values of cation ratio obtained from the EDX analysis are tabulated in table-4.9. The presence of trace Fe element indicates the inadvertent doping of Fe during the high energetic ball milling process and is found to be within 1 at % for sample x = 0.0 and x = 0.05. No trace of any Fe content was seen in other Ni-doped SnO_2 samples.

The Raman spectra recorded for all the Ni-doped samples are shown in Fig.4.18. All the samples show the Raman shift at ~ 640 cm^{-1} which corresponds to A_{1g} (symmetric Sn-O stretching). This

indicates the tetragonal rutile structure. The other peak observed at 693 cm^{-1} is because of the A_{2u}(LO), LO=longitudinal optic mode; which is basically IR-active but because of some disorder this become Raman active [259-261]. The samples exhibit the peak broadening effect and it depicts the presence of some amorphous phase. The observed peak at 475 cm^{-1} corresponds to the E_g mode of vibration. As the E_g mode is the result of two oxygen atoms vibrating parallel to the c axis, but in opposite direction; it is more sensitive to oxygen vacancies than other modes [262]. So the vacancy related defects are dominant in the samples.

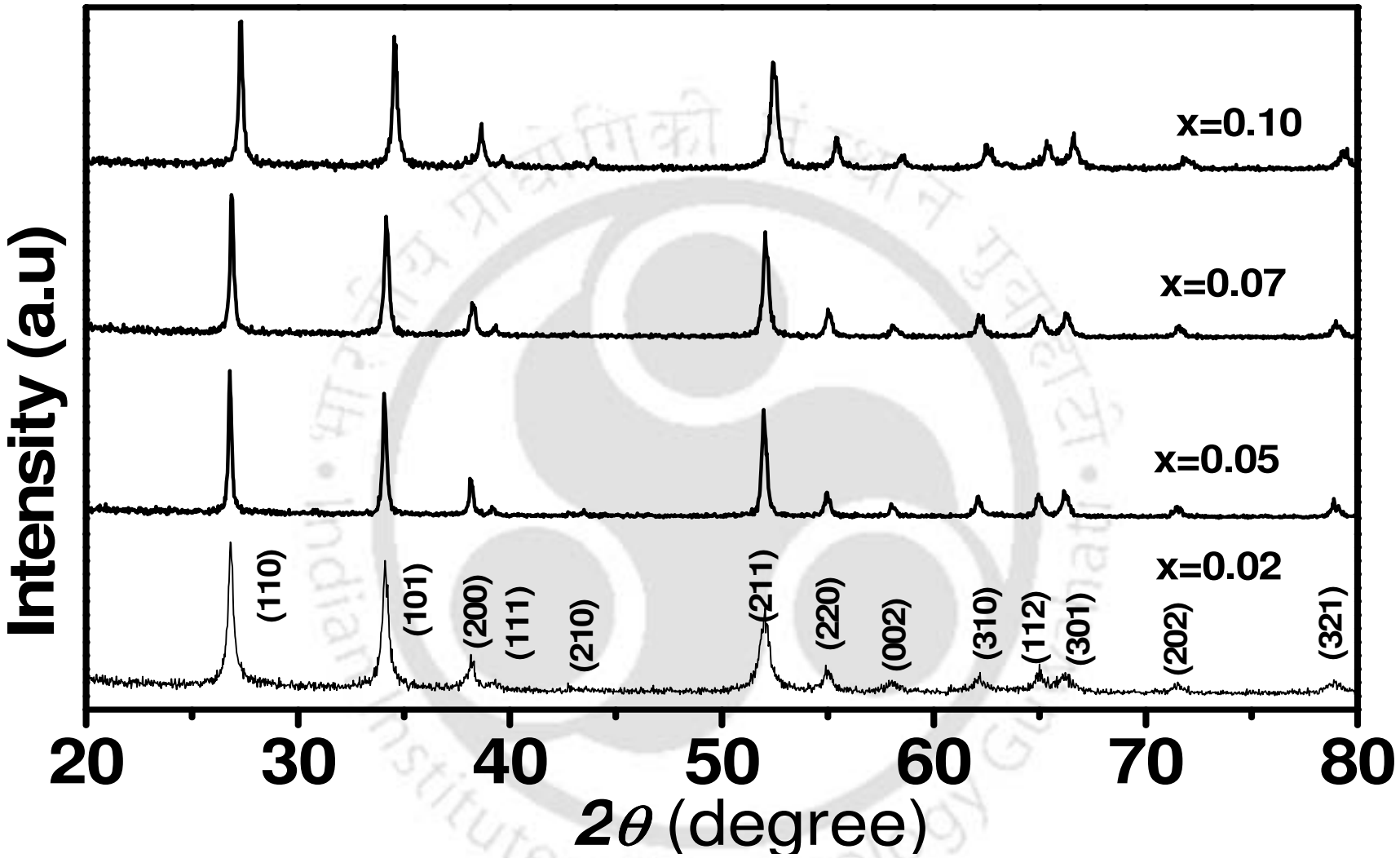

Fig. 4.15 XRD patterns recorded for ball milled x = 0.02, 0.05, 0.07, 0.10 samples.

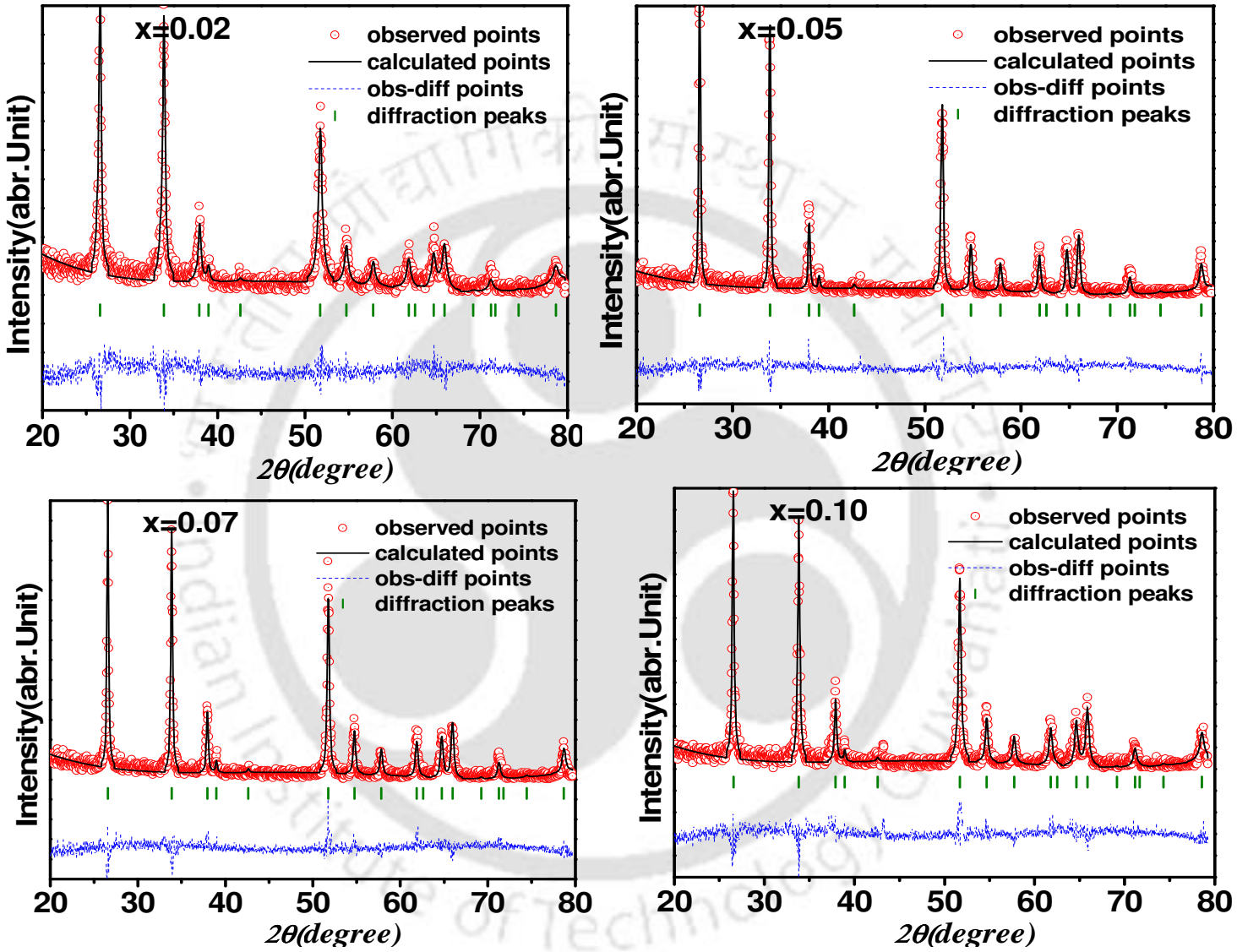

Fig.4.16 XRD patterns of x=0.02, 0.05, 0.07 and 0.10 samples obtained by ball milling method along with the Rietveld refinement.

Table-4.8 List of parameters obtained from the Rietveld refinement and analysis of XRD patterns.

Sample/Parameters	**x = 0.0**	**x = 0.02**	**x = 0.05**	**x = 0.07**	**x = 0.10**
Space group	$P4_2/mnm$	$P4_2/mnm$	$P4_2/mnm$	$P4_2/mnm$	$P4_2/mnm$
a = b (Å)	4.732	4.739	4.736	4.738	4.743
c (Å)	3.184	3.188	3.185	3.186	3.191
Volume ($Å^3$)	71.29	71.59	71.44	71.53	71.82
χ^2 (%)	2	1.9	2.08	1.93	2.05
R_p (%)	19	19.3	22.8	22	22.1
Crystallite size (nm)	38	39	40	38	40

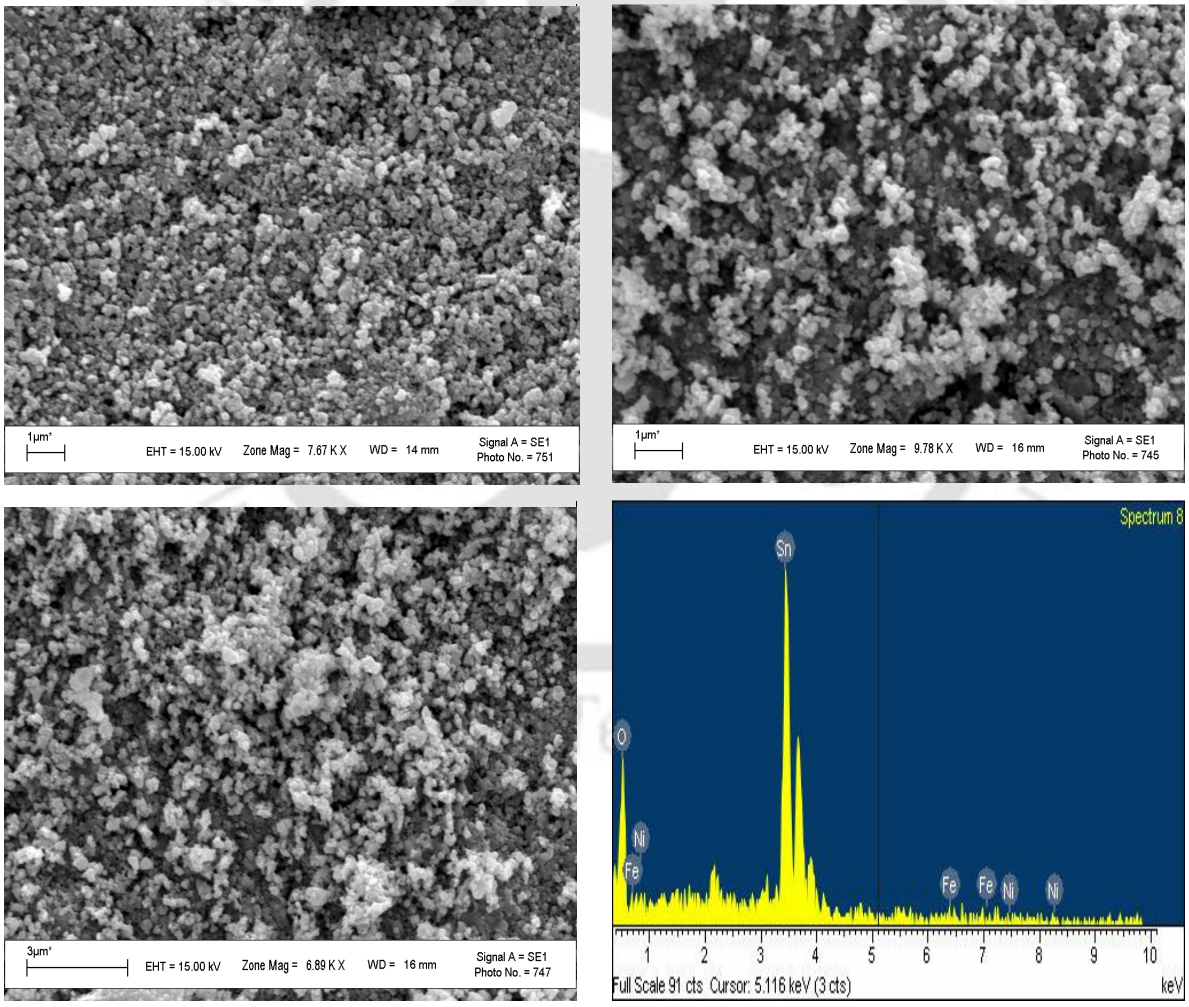

Fig.4.17 SEM and EDX images for x=0.02, 0.05 and 0.010 Ni doped SnO_2 along with the EDX spectra for x=0.10 sample.

Table-4.9 Cationic ratio obtained from EDX measurement for x =0.0, 0.02, 0.05, 0.07 and 0.10 samples

Sample	Calculated Cationic Ratio from EDS		
	Sn	Ni	Fe
x=0.0	0.99	-----	0.01
x=0.02	0.98	0.01	--------
x=0.05	0.94	0.05	0.01
x=0.07	0.93	0.06	--------
x=0.10	0.87	0.09	-----

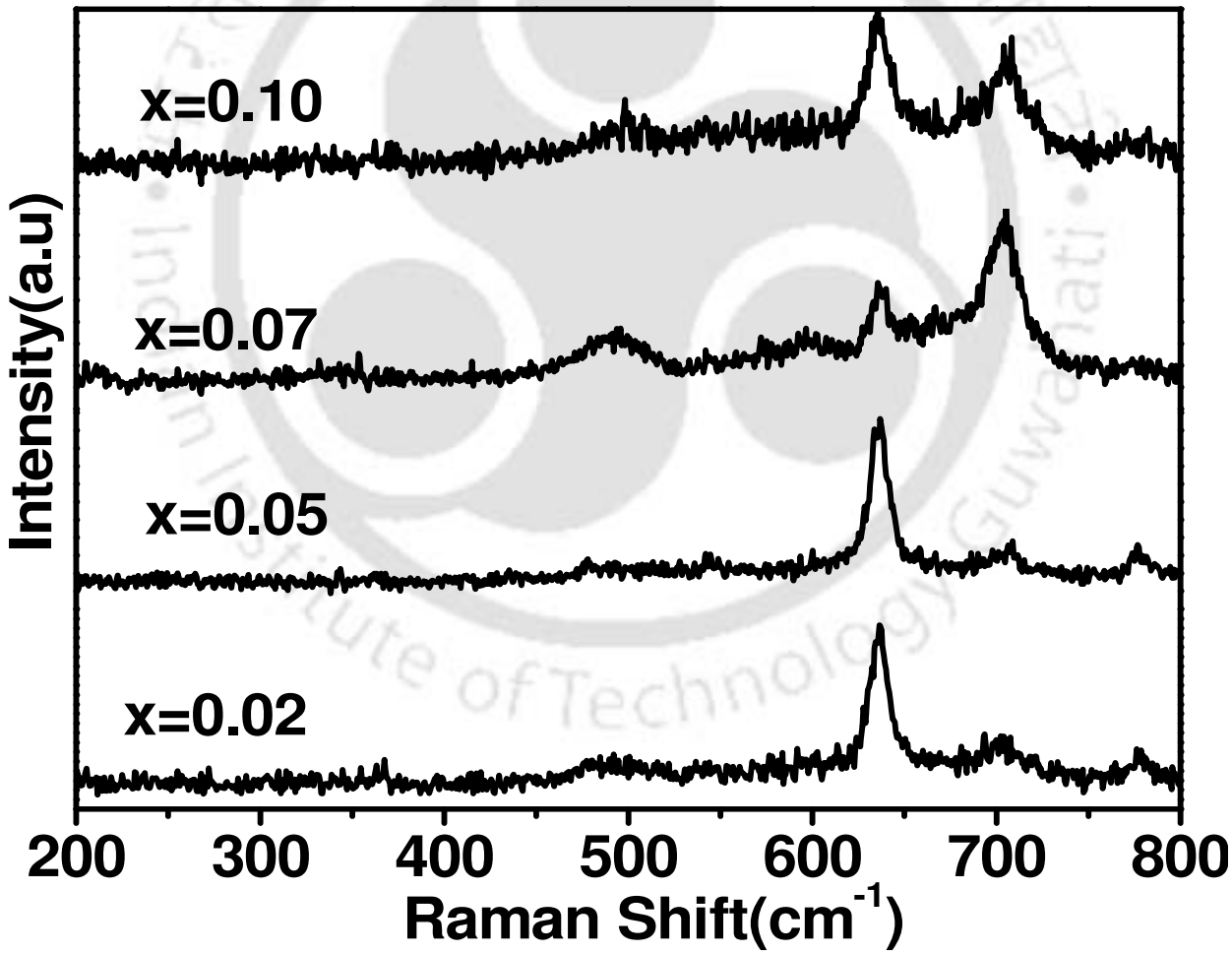

Fig.4.18 Raman spectra recorded for x=0.02, 0.05, 0.07 and 0.10 samples at room temperature.

4.2.2 Magnetic Properties

The magnetization data recorded at 290 K for x = 0.0, 0.02, 0.05, 0.07 and 0.10 samples are shown in Fig. 4.19(a) for a maximum applied field of 1.5T. They all exhibit FM behavior. The M_s value of x = 0.02 sample was found to be 0.7 emu/g and it is found to increase to 1.13 emu/g for 7 at % of Ni doping. Similar to the case of solid state synthesized Ni doped SnO_2 samples, here also we have found a sharp increase in M_s value up to 7 at % of Ni doping and with further Ni doping, the M_s value was found to decrease. The sharp increase in M_s value for x = 0.07 can be attributed to the FM introduced by Ni-substitution in Sn site. The decrease in M_s value with further increase in Ni-concentration can be understood in terms of enhanced nearest-neighbor antiferromagnetic superexchange interaction. The values of coercive field, H_c are given in Table-4.10. The H_c value is found to be maximum for x=0.07 sample and is comparable to that of Ni doped samples obtained from solid state route.

The M-H loops recorded at 80K for all the above samples are shown in Fig. 4.19(b). The M_s values were obtained after subtracting the high temperature linear region. The obtained M_s and H_c values are tabulated in Table-4.10. Unlike the Co-doped samples, here there is no appreciable change in H_c values.

In order to quantitatively analyze the magnetization data due to Ni substitution, the contribution from other extrinsic effect needs to be separated out. In order to study the magnetic properties of Ni doped SnO_2 without the influence of inadvertent Fe doping or defects, the initial M-H curve of x = 0 sample was fitted to eq.3.6. The data were fitted by varying the parameter M_{so}, a, b and χ_d. The initial curve of x = 0 sample at 300 K along with the fitted data to eq.3.6 are shown in Fig. 4.20. The fitted data closely follow the experimental data. The fitted values of M_{so}, a, b and χ_d are found to be 0.134emu/g, 76emu.Oe/g, -1.2×10^{4} emu.Oe^2/g, 1.4×10^{-6} emu/g.Oe respectively.

The intrinsic magnetization due to Ni-doping was determined by subtracting the magnetization arising from other extrinsic effects. This can be done by estimating the background magnetization by using eq.3.6 and parameters M_{so}, a, b and χ_d corresponding to x = 0 sample. The background magnetization was subtracted from the measured magnetization of Ni doped samples. The intrinsic initial magnetization data of x = 0.02, 0.05, 0.07 and 0.10 samples are shown in Fig. 4.21. The intrinsic saturation magnetization, M_{si} was determined from the above

plots and are found to be 0.3 emu/g, 0.5 emu/g, 1.02 emu/g and 0.8emu/g for x = 0.02, 0.05, 0.07 and 0.10 samples respectively at 300 K. Their corresponding values at 80 K are found to be 0.4 emu/g, 0.63 emu/g, 1.34emu/g and 1.05emu/g.

The intrinsic initial magnetization data were analyzed in terms of bound BMP model [112, 113, 255], i.e. by fitting to eq. 3.2. The magnetization curves for x = 0.02, 0.05, 0.07, 0.10 samples at 300 K and 80 K along with the fitted data are shown in Fig. 4.21. The fitted data closely follow the experimental data and the fitted parameters M_o, m_{eff} and χ_m are given in Table-4.11. The M_0 value is found to increase with increase in doping concentration up to 7 at % which is because of the increase in FM interaction with increase in Ni concentration. The value of spontaneous moment per BMP, m_{eff} is found to be in the order of 10^{-17} emu. The m_{eff} values observed in the present samples are comparable to those reported by Quintero *et al.* [114] in p-type $Cu_2FeGeTe_4$ and those of Ni-doped samples from solid state route. The BMP radius calculated from the m_{eff} is found to be around 30 Å and it is found to increase with increase in temperature similar to the case of Co doped SnO_2 and Ni doped SnO_2 samples prepared by solid sate route (section-3.1.2, section-4.1.2).

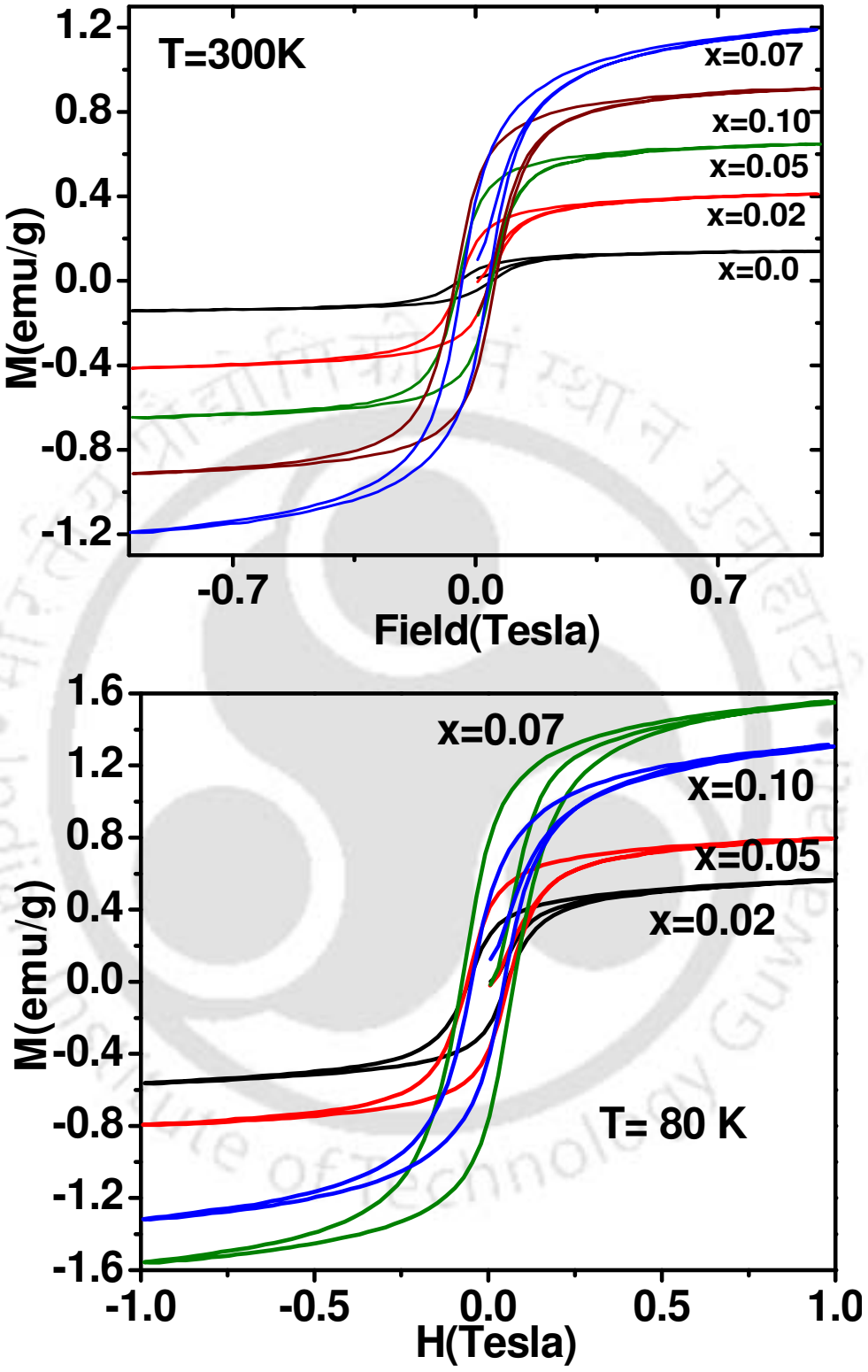

Fig.4.19 M-H loops recorded for x = 0.0, 0.02, 0.05, 0.07 and 0.10 samples at (a) 290 K and (b) 80 K

Table-4.10 M_s and H_c obtained from magnetization measurements.

Sample/Parameters	x = 0.0	x = 0.02	x = 0.05	x = 0.07	x = 0.10
H_c Oe (80 K)	459	548	588	741	467
H_c Oe(300 K)	446	434	477	581	378
M_s (μ_B/Ni) (80 K)	------	0.55	0.4	0.5	0.3
M_s (μ_B/Ni) (300 K)	------	0.4	0.3	0.4	0.2

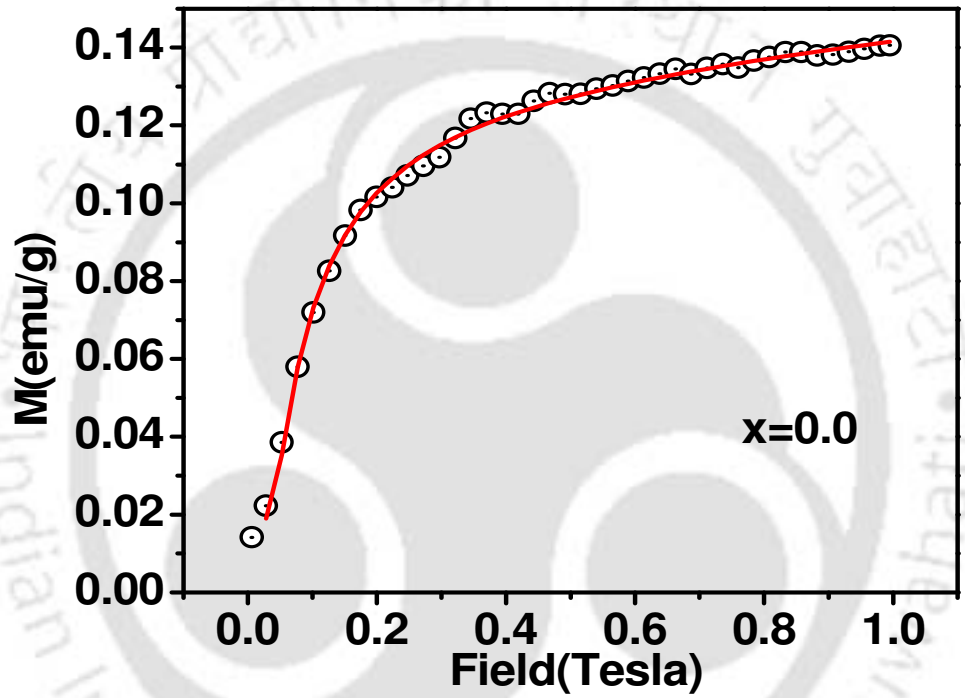

Fig. 4.20 Initial M-H curve of x =0.0 sample along with fit to eq. 3.6.

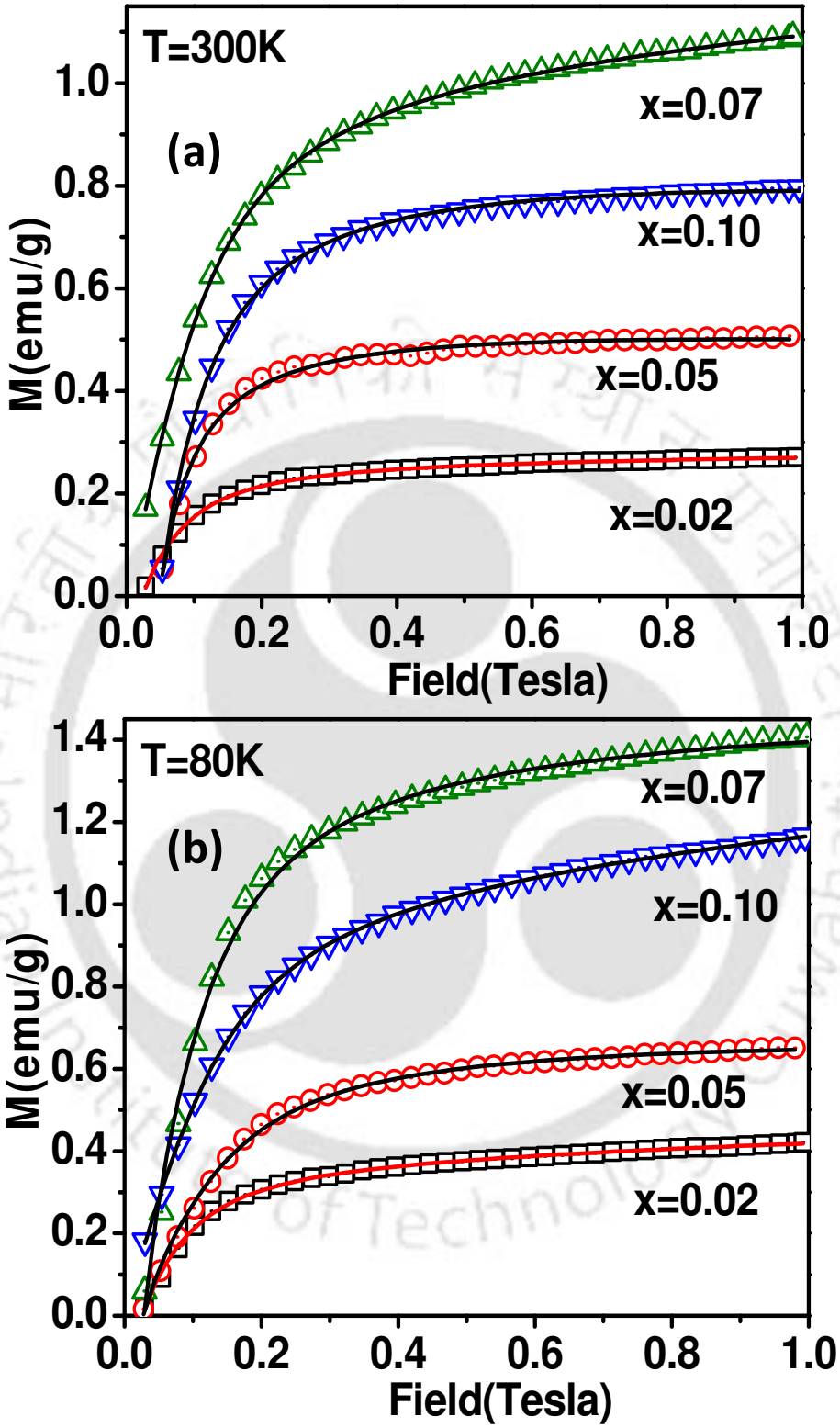

Fig. 4.21(a) Initial M-H curves of x = 0.02, 0.05, 0.07 and 0.10 samples along with BMP model fit at **(a)** 300 K and **(b)** 80

Table-4.11 List of parameters obtained from the analysis of M-H data by using BMP model. M_o is the spontaneous magnetization of the system, χ_m is the susceptibility of the matrix and m_{eff} is the effective magnetic moment for per BMP.

Sample/ parameter	***x=0.02***		***x=0.05***		***x=0.07***		***x=0.10***	
Temperature (K)	**80**	**300**	**80**	**300**	**80**	**300**	**80**	**300**
M_0(emu/g)	0.4	0.3	0.7	0.6	1.5	1.1	1.1	0.9
χ_m(10^{-6} emu/g.Oe)	4.4	0.6	1.8	0.3	1.5	0.9	11.0	4.7
m_{eff}(10^{-17} emu)	2.4	10.0	1.5	15.0	2.0	7.2	1.7	8.5
BMP radius (Å)	60	96	37	81	37	57	31	53

M-T curves for all the Ni doped samples are shown in Fig.4.22, where a clear paramagnetic to ferromagnetic transition can be seen. The FM transition was determined from dM/dT versus T plots as shown in Fig. 4.23 and the T_c values are found to be 789 K, 821 K, 786 K and 825 K for x = 0.02, 0.05, 0.07 and 0.10 samples respectively. The paramagnetic susceptibility was fitted to modified Curie-Weiss law, i.e. by fitting to eq. 3.7. The typical Curie-Weiss fit for x= 0.05 and 0.07 samples are shown in Fig.4.24**.** The Curie temperature and μ_{eff} values are tabulated in table-4.12. Typical Curie temperature was found to be 803±5 K and 774±3 K respectively for x = 0.02 and x = 0.07 samples. The typical value of effective magnetic moment μ_{eff} estimated from Curie constant is found to be 3.7μ_B/Ni ion for 0.07 sample and it suggests that the doped Ni ions are expected to be mostly in Ni^{2+} high spin state.

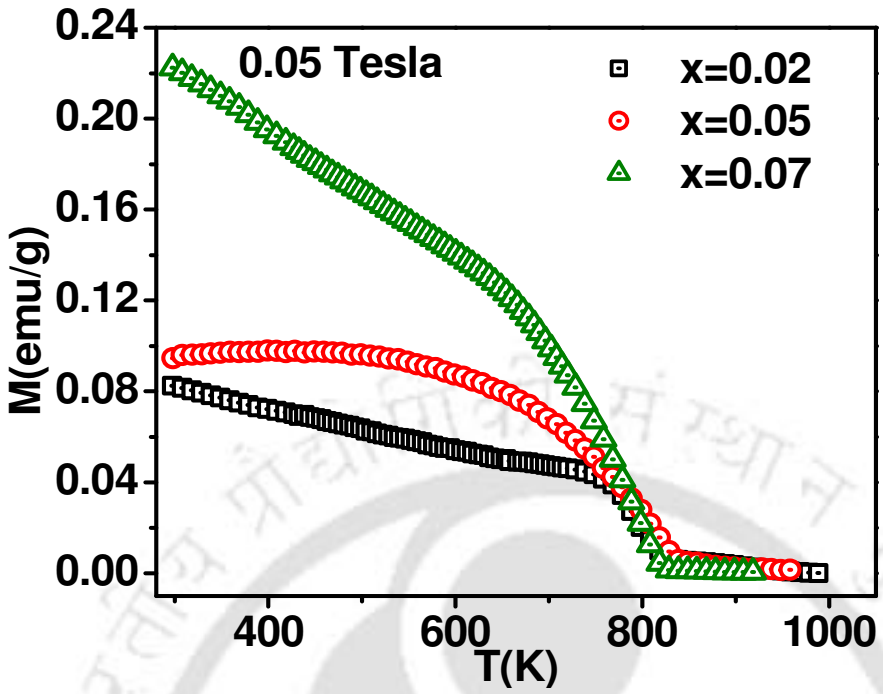

Fig.4.22 (a) M-T curves for x=0.02, 0.05, 0.07 and 0.10 samples.

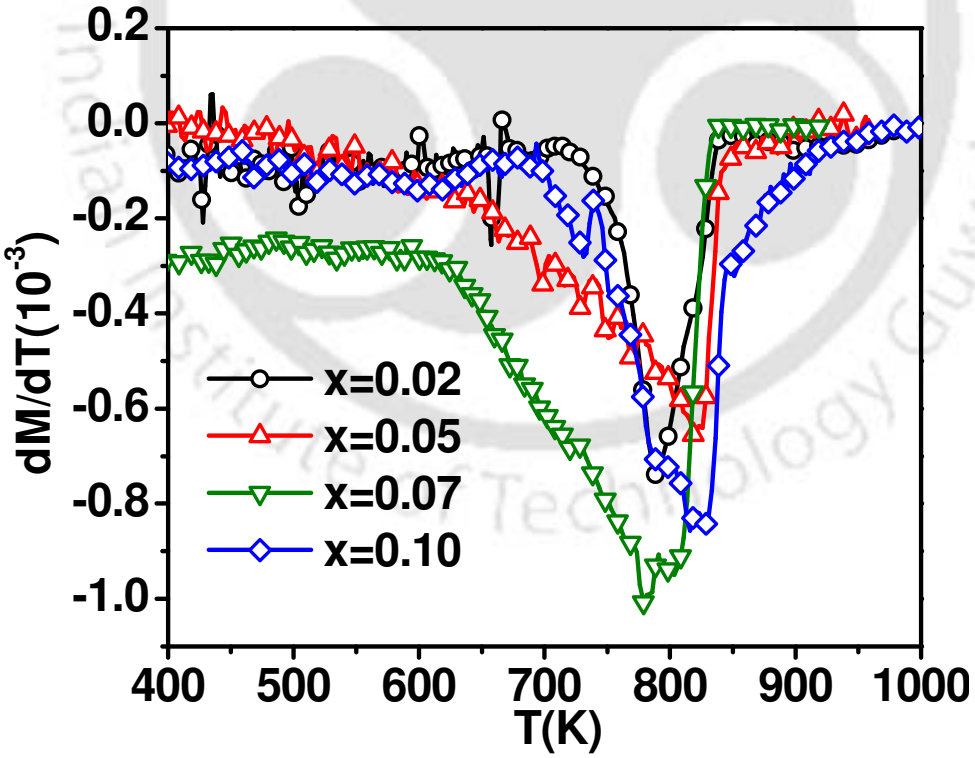

Fig.4.23 dM/dT plot for x = 0.02, 0.05, 0.07 and 0.10 samples.

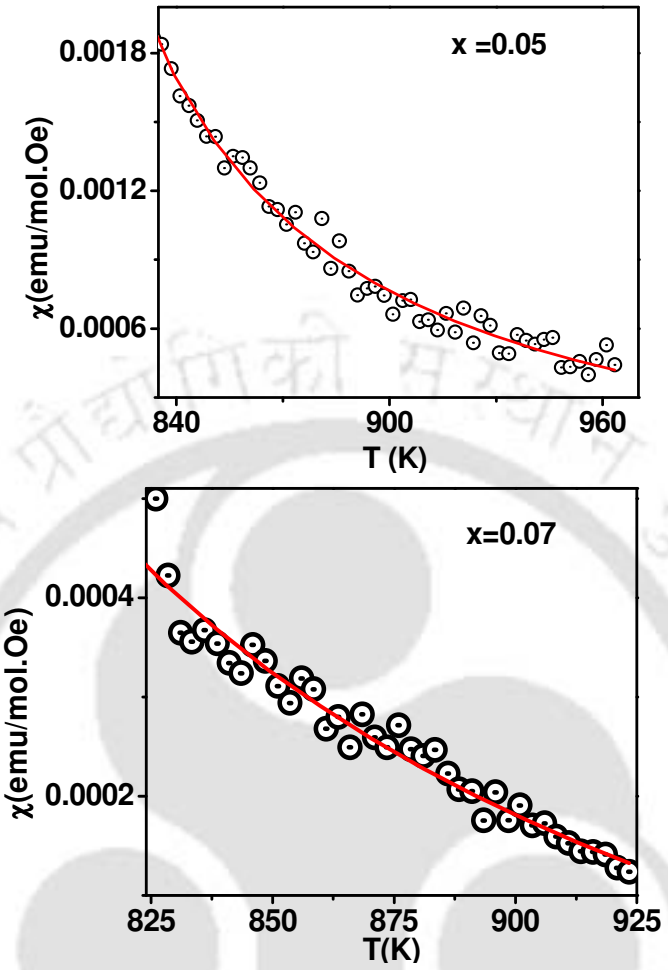

Fig.4.24 Temperature variation of magnetization plot for x=0.05 and 0.07 samples along with modified Curie-Weiss fit in the paramagnetic region.

Table-4.12 Parameters obtained from the fit of susceptibility data to modified Curie-Weiss law and ESR resonance field.

Sample/Parameters	x=0.02	x=0.05	x=0.07	x=0.10
θ_C (K)	803	774	695	-----
μ_{eff} (μ_B)	3.6	4.1	3.9	-----
Resonance Field(mT)	284	281	276	278
g-factor	2.37	2.41	2.44	2.41

4.2.3 ESR Spectra

Fig.4.25 Shows the ESR spectra recorded for x=0.02, 0.05, 0.07 and 0.10 samples at room temperature. The value of resonance field and the corresponding g-value are tabulated in table-4.12. The resonance field shifts towards the lower field with increase in doping concentration up to 7 at %. Further increases in Ni doping concentration, the resonance peak value shifts towards higher field side and it supports the magnetization results of decrease in FM interaction.

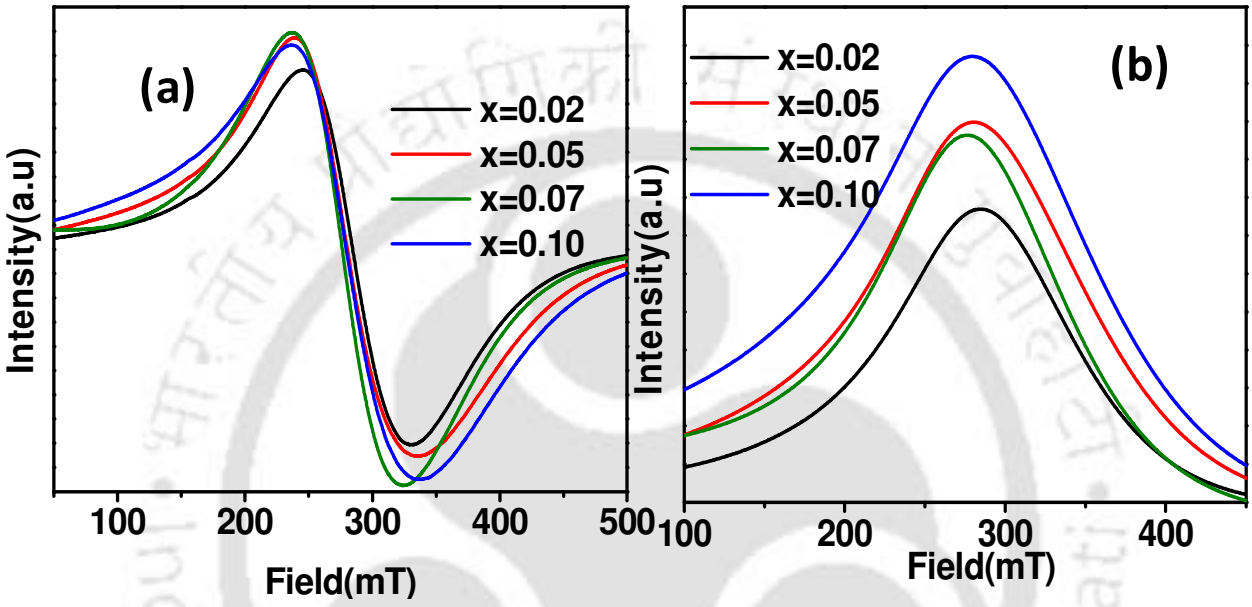

Fig. 4.25 ESR spectra and integrated ESR intensity for x=0.02, 0.05, 0.07 and 0.10 samples of Ni doped SnO_2.

4.3 Summary

The Ni-doped SnO_2 based diluted magnetic semiconductors were prepared in single phase form. They exhibit room temperature ferromagnetism with FM T_c as high as ~ 770 K. The saturation magnetization increases up to 7 at % of Ni doping then it decreases with further increases in Ni concentration. The measured initial M-H loops could be explained based on bound magnetic polaron model. The increase in paramagnetic matrix susceptibility and decrease in effective spontaneous magnetic moment of BMP at low temperature are explained on the basis of reduction in BMP size. The measured magnetization data could be also explained in terms of interaction between BMP and magnetic moments of the matrix.

We have shown that bulk Ni-doped SnO_2 based diluted magnetic semiconductors prepared by ball milling technique exhibit large saturation magnetic moment with room temperature ferromagnetism. The samples are found to be in single phase form and could be refined using the Rietveld refinement technique. Similar to the case of solid state synthesized Ni doped samples, here also the saturation magnetization increases up to 7 at % of Ni doping and then it decreases. The magnetization data after subtracting the contribution from extrinsic effects were analyzed in terms of BMP model. The effective spontaneous moment of the BMP was found to be in the order of 10^{-17} emu. The typical Curie temperature was found to be 803±5 K and 774±3 K respectively for x = 0.02 and x = 0.07 samples. The typical effective magnetic moment μ_{eff} was found to be $3.7\mu_B$/Ni ion for 0.07 sample and it suggests that the doped Ni ions are mostly in Ni^{2+} high spin state.

Chapter 5: CONCLUSIONS

To summarize, two series of SnO_2 based diluted magnetic semiconductors have been prepared in the present thesis work and they are,

1. $Sn_{1-x}Co_xO_2$ (x =0 to 0.10) and
2. $Sn_{1-x}Ni_xO_2$ (x =0 to 0.10)

In both the series, the samples were prepared by following solid state route and ball milling technique. In addition to that on selected Co doped samples, the material preparation was carried out by using a co-precipitation technique and by using alternate vial in ball milling process. The oxide diluted magnetic semiconductors obtained by doping Co and Ni in SnO_2 are found to exhibit room temperature ferromagnetism with high T_c beyond room temperature. The observed ferromagnetism in these samples could be mostly explained on the basis of the formation of bound magnetic polarons. Moreover we have found that along with the transition element doping, defects are also playing a crucial role in tuning the nature of ferromagnetic interaction. In addition to that, for the first time critical exponent analysis has been carried out on oxide based DMS. The important conclusions drawn in Co and Ni doped samples as they are discussed in detail in chapters 3 and 4 are summarized below.

$Sn_{1-x}Co_xO_2$ samples were prepared for x = 0 to 0.10 by using solid state synthesis technique. X-ray diffraction and their analysis in terms of Rietveld technique show that all the Co doped samples are in single phase form. The XRD patterns could be refined by using $P4_2/mnm$ space group with typical lattice parameters a = b = 4.712 Å and c = 3.142 Å for x = 0.10. The average crystallite size was found to 60 nm as per the analysis of XRD pattern. A systematic shifting of (h k l) peaks towards higher 2θ angle and the corresponding decrease in lattice parameters with increase in doping concentration suggest that the doped Co ions indeed enter the Sn site of SnO_2. The cationic ratio obtained from the EDS analysis was found to be comparable to the nominal starting composition. Single phase nature of the samples and their consistent composition and crystal structure down to nanocrystallite level have been confirmed from the recorded Raman spectra and TEM/ HRTEM image at room temperature. As per the magnetization measurement, all the Co doped SnO_2 samples are found to exhibit room temperature ferromagnetism. The saturation magnetization was found to decrease with increase in Co concentration and is

explained in terms of increase in nearest neighbor antiferromagnetic interaction. The saturation moment of 0.036 μ_B/Co-ion (0.027emu/g) was observed for x = 0.02 at 400 K and its value at 85 K was found to be 0.055 μ_B/Co-ion (0.05emu/g). Considerable increase in hysteresis loss with decrease in temperature has been observed due to possible enhancement in magnetic anisotropy or other competing magnetic interaction. Typical increase in coercivity from ~ 500 Oe at 400 K to 4100 Oe at 85 K was observed for $Sn_{0.98}Co_{0.02}O_2$ sample. Large increase in saturation magnetization by an order of magnitude has been observed on a sample prepared by N_2 gas environment at atmospheric pressure. The M-H curves of Co doped samples recorded at three different temperatures could be analyzed based on bound magnetic polaron model. The decrease in spontaneous magnetization, M_0 and increase in spontaneous moment per BMP, m_{eff} with increase in temperature has been explained in terms of increase in BMP size with temperature.
A temperature variation of magnetization up to ~900 K was measured and all the Co doped samples exhibit paramagnetic to ferromagnetic transitions. The FM T_c was found to decrease with increase in doping concentrations. The temperature variation of dc susceptibility obtained from magnetization data in the paramagnetic region could be fitted to Curie-Weiss law. Maximum Curie temperature of 692 K was obtained for x =0.02 sample and it is found to decrease systematically with increase in doping concentrations. ESR spectra measured in the temperature range of 295 K to 445 K show a shift in the resonance field towards the higher field. The resonance field is also found to increase with increase in doping concentration and is in consistent with magnetization results.

In order to study the particle size effect in Co doped SnO_2, nanocrystalline samples of pure and 2 at % Co-doped SnO_2 were prepared by a co-precipitation technique and by annealing at different temperature. Average crystallite size ranging from 5 nm to 15 nm was observed. The homogeneity and single phase nature of the samples were confirmed by using various characterization techniques, such as X-ray diffraction, transmission electron microscope and Fourier infrared spectroscopy. Signature of room temperature ferromagnetism has been observed for 2 at% Co doped samples, however pure SnO_2 was found to be diamagnetic as per the magnetization measurement. The magnetization was found to decrease with decrease in crystallite size. The reduction in magnetization with decrease in crystalline size has been explained as a result of restriction in the range of bound magnetic polaron interaction. The

samples prepared under nitrogen gas environment exhibit improvement in ferromagnetic behavior and enhanced electrical conductivity. The saturation magnetization of samples obtained from co-precipitation technique is found to be quite small compared to solid state synthesized samples. In materials prepared under normal conditions i.e. the samples prepared by solid state route, a relatively large crystallite size of the order of 40nm was found and the magnetization value was also found to be relatively large. Thus crystallite size plays a considerable role in controlling the BMP interactions.

To study the defect induced room temperature FM in SnO_2 based materials, mechanical milling of high purity SnO_2 without any TM element doping was carried out by using two different vials, namely steel and WC. The milled powders were also annealed at 900^oC to study the effect of annealing on defects and hence on the magnetic properties. The XRD patterns could be refined by using $P4_2/mnm$ space group with typical lattice parameters a = b = 4.7322Å and c = 3.1848Å. The Raman spectra recorded for all the samples show dominant vacancy related defects in samples, which exhibit room temperature ferromagnetism. The as-milled powders obtained from both the vials exhibit room temperature ferromagnetism i.e. without any transition element doping. Thus irrespective of the nature of vials used both SnO_2 samples exhibit room temperature ferromagnetism. Typical saturation magnetization values at room temperature for the as-milled samples obtained from steel vial and WC vial are found to be 0.9 emu/g and 0.11emu/g respectively. However upon annealing, the FM was destroyed in WC vial based sample. The observed FM in as-milled samples could be explained in terms of oxygen vacancy and defects induced electrons and exchange interaction between them. The ferromagnetic transition temperature obtained from the temperature variation of magnetization was found to be 915 K for the as-milled samples. The initial magnetization data could be analyzed in terms of bound magnetic polaron model. The resonance field shift in electron spin resonance spectrum is explained in terms of observed ferromagnetism.

In order to study the role of defects and annealing conditions in these materials and in an attempt to have material with large M_s value, Co doped SnO_2 samples were prepared by using ball-milling technique, followed by high temperature annealing. XRD patterns could be refined to $P4_2/mnm$ space group with typical lattice parameters a = b = 4.733 Å and c = 3.184 Å. Presence of minor spinel structure based impurity phase was detected due to contamination from steel vial. All the Co-doped SnO_2 samples were found to exhibit ferromagnetic behavior at room temperature. Decrease in magnetization magnitude with increase in doping concentration has been observed similar to the case of solid state synthesized samples. Typical coercive field, H_c for 2 at % Co-doped SnO_2 sample was found to increase from 879 Oe at room temperature to 3735Oe at 20 K. Strong room temperature FM was observed with a maximum saturation magnetization of 2.9 emu/g (3.8 μ_B/Co-ion) for x = 0.02 sample and is enhanced to 5.9 emu/g (7.9 μ_B/Co-ion) at 20 K. This value is comparable to that reported by Ogale *et al.*[39] for 5 % Co-doped SnO_2 thin film. Such a high saturation magnetization value could be explained in terms of unquenched d-orbital of the doped Co-ion and due to oxygen vacancy. Thus for the first time giant magnetic moment of 7.9 μ_B/Co-ion in bulk Co doped SnO_2 was observed. The magnetization data after subtracting the contribution from the extrinsic effect such as impurity phase could be analyzed based on bound magnetic polaron model. Typical values of M_o, χ_m and m_{eff} for x = 0.02 sample are found to be 3.34 emu/g, 1.04 x 10^{-4} emu/g.Oe and 5.7 x 10^{-17}emu respectively. The BMP radius was found to be in the range of 30 Å to 40 Å. Similar to the case of solid state synthesized samples, the M_o value is found to decrease with increase in doping concentration. Temperature variation of magnetization exhibits clear paramagnetic to ferromagnetic transition with a maximum T_c of 640 K for 2 at % Co-doped sample. Susceptibility in paramagnetic region could be fitted to modified Curie-Weiss law and the typical values of Curie temperature and μ_{eff} for $Sn_{0.98}Co_{0.02}O_2$ sample are found to be 653 K and 2.34 μ_B/TM-ion respectively.

Isothermal magnetization data were plotted as per Arrott–plot method and they are all found to exhibit positive slope with clear FM to PM type magnetization curve with increase in temperature through transition. So, it was confirmed that the observed magnetic transition is second order in nature. The critical exponents corresponding to spontaneous magnetization, susceptibility and isothermal magnetization at T= T_c were determined by performing the analysis

based on modified Arrott plot technique. The estimated values of transition temperature and critical exponents are found to be T_c=629±0.5 K, β=0.52±0.02, γ=1.1±0.01, δ=3.12±0.01. The obtained critical exponent values are found to be comparable to the values predicted by the mean field model, i.e. with long range FM interaction. We have also estimated the critical exponent, γ and T_c based on Kouvel-Fisher method and they are found to be consistent with the result of modified Arrott plot method. The critical exponents are also found to follow the Widom scaling relation and universal scaling hypothesis. The effective critical exponent γ_{eff} as a function of reduced temperature was determined. It was observed that as T tends to T_c, the value of γ_{eff} approaches 1.0, the predicted value for the mean field model. The characteristic feature of temperature variation of effective critical exponent, γ_{eff} is found to be comparable to the theoretical prediction of disordered system.

Polycrystalline $Sn_{1-x}Ni_xO_2$ samples were prepared in single phase form for x = 0.02, 0.05, 0.07 and 0.10 and were characterized by using several experimental techniques. The typical lattice parameters are found to be a = b = 4.734 Å and c = 3.187 Å for x = 0.07 sample. The cationic ratio determined from EDS analysis are found to be comparable to the nominal starting composition. Nano-particles of uniform crystalline phase and composition have been identified from the transmission electron microscope images. All the Ni doped SnO_2 samples were found to exhibit ferromagnetism at room temperature. M_s value was found to increase with increase in Ni concentration up to 7 at % and beyond that it decreases. The initial M-H curves at 80 K and 100K could be fitted to bound magnetic polaron model. The spontaneous magnetization M_o is found to increase with Ni concentration up to 7 at % and the trend is same as that measured saturation magnetization. Increase in M_o and decrease in m_{eff}, the effective spontaneous moment per BMP with decrease in temperature have been observed and is explained in terms of reduced BMP size at low temperature. The typical polaron size at 80 K was estimated to be 60Å for x =0.07 sample. Paramagnetic to ferromagnetic transition with T_c as high as 770 K was observed. The paramagnetic susceptibility could be fitted to Curie-Weiss law and the typical μ_{eff} for x =0.07 is found to be 1.4μ_B/Ni.

Temperature dependence of electrical resistivity was measured. They all exhibit semiconducting behavior. The temperature dependence of resistivity could be explained based on a variable range hopping mechanism. The values of the density of states in the vicinity of Fermi level

$N(E_F)$, hopping distance R_{hop} and hopping energy E_{hop} are found to be 6.1×10^{24} $eV^{-1}m^{-3}$, 59Å and 215meV respectively for x=0.02. The above parameters for x=0.07 sample are found to be 1.3×10^{25} $eV^{-1}m^{-3}$, 49 Å and 178meV respectively.

$Sn_{1-x}Ni_xO_2$ samples for x = 0.0, 0.02, 0.05, 0.07 and 0.10 were also prepared by mechanical milling followed by annealing at 900°C. Unlike, Co doped mechanically milled samples, these samples are crystallized in single phase form as per X-ray diffraction pattern and their analysis. No XRD peak corresponding to Ni metal or Nickel oxide has been notified. XRD patterns could be refined by using $P4_2/mnm$ space group. The typical lattice parameters for 2 at % Ni doped sample are found to be a = b = 4.739Å and c = 3.188Å. The average crystallite size determined from the XRD analysis is found to ~ 40Å. EDS analysis carried out in Ni-doped sample shows cationic ratio comparable to the nominal starting composition. Trace amount of Fe, i.e. within 1 at % was observed in two samples and can be attributed to inadvertent Fe doping in Sn due to vial contamination. The Raman analysis shows the presence of vacancy related peak and it is more prominent for the x = 0.07 sample. All the Ni doped SnO_2 samples were found to exhibit room temperature ferromagnetism. The M_s value of x = 0.02 sample was found to be 0.7 emu/g and the value got increased to 1.13 emu/g for 7 at % of Ni doping. The variation of M_s value with Ni concentration is found to be consistent with the result of solid state synthesized samples. The magnetization data after subtracting the contribution from the extrinsic effects could be analyzed based on bound magnetic polaron model. The size of BMP at 80 K is found to be in the range of 60 Å to 30 Å. Temperature variation of magnetization was measured for all the Ni doped samples prepared by ball milling method. They all exhibit clear paramagnetic to ferromagnetic transition. Unlike the solid state synthesized samples, here the FM T_c is found to be relatively higher. The paramagnetic susceptibility data could be fitted to modified Curie-Weiss law. Typical values of Curie temperature are found to be 803±5 K and 774±3 K for x = 0.02 and x = 0.07 samples respectively. The typical value of effective magnetic moment μ_{eff} estimated from Curie constant is found to be $3.7\mu_B$/Ni ion for 0.07 sample and it suggests that the doped Ni ions are expected to be mostly in the Ni^{2+} high spin state.

Thus in the present thesis, the magnetic properties of Co and Ni doped SnO_2 based diluted magnetic semiconductors prepared by different techniques have been studied in detail.

References

[1] K. Sato and H. K. Yoshida, Mat. Res. Soc. Symp. Proc. **666** (2001) F4.6.1.

[2] Y. Ohno, D. K. Young, B. Beschoten, F. Matsukura, H. Ohno, and D. D. Awschalom, Nature **402** (1999) 790.

[3] Y. Tokura and N. Nagaosa, Science **288** (2000) 462.

[4] K.Sato and H.K.Yoshida, Semicond. Sci. Technol. **17** (2002) 367.

[5] T. Dietl, H. Ohno, F. Matsukura, J. Cibert, and D. Ferrand, Science **287** (2000) 1019.

[6] T.Dietl, J.Spalek, and L.Swierkowski, Phys. Rev. B **33** (1986) 7303.

[7] J.Kossut and W.M.Becker, Phys.Rev.B **33** (1986) 1394.

[8] Y. G. Kusrayev, K. V. Kavokin, G. V. Astakhov, W. Ossau, and L. W. Molenkamp, Phys. Rev. B **77** (2008) 085205.

[9] W. E. Hagston, T. Stirner, J. P. Goodwin, and P. Harrison, Phys. Rev. B **50** (1994) 5255.

[10] P. A. Wolff, R. N. Bhatt, and A. C. Durst, J. Appl. Phys. **79** (1996) 5196.

[11] M. Venkatesan, C. B. Fitzgerald, J. G. Lunney, and J. M. D. Coey, Phys. Rev. Lett. **93** (2004) 177206.

[12] M. S. Green, M. Vicentini-Missoni, and J. M. H. L. Sengers, Phys. Rev. Lett. **18** (1967) 1113.

[13] S. Blundell, Oxford University Press **Chapter 3** (2003)

[14] A. Mauger and C. Godart, Phys. Rep. **141** (1986) 51.

[15] J. K. Furdyna, J. Appl. Phys. **53** (1982) 7637.

[16] J. K. Furdyna, J. Appl. Phys. **64** (1988) R29.

[17] H. Saito, W. Zaets, S. Yamagata, Y. Suzuki, and K. Ando, J. Appl. Phys. **91** (2002) 8085.

[18] J. Blinowski, P. Kacman, and J. A. Majewski, Phys. Rev. B **53** (1996) 9524.

[19] W. Mac, A. Twardowski, and M. Demianiuk, Phys. Rev. B **54** (1996) 5528.

[20] T. Jungwirth, J. Sinova, J. Mašek, J. Kučera, and A. H. MacDonald, Rev. Mod. Phys. **78** (2006) 809.

[21] H. Munekata, H. Ohno, S. von Molnar, A. Segmuller, L. L. Chang, and L. Esaki, Phys. Rev. Lett. **63** (1989) 1849.

[22] H. Ohno, Science **281** (1998) 951.

[23] G. A. Prinz, Science **282** (1998) 1660.

[24] H. Ohno, J. Mag. Magn. Mat. **200** (1999) 110.

[25] A. H. MacDonald, P. Schiffer, and N. Samarth, Nature Materials **4** (2005) 195.

[26] T. Story, R. R. Galstroka-cedillazka, R. B. Frankel, and P. A. Wolff, Phys. Rev. Lett. **56** (1986) 777.

[27] M. P. Mathur, D. W. Deis, C. K. Jones, A. Patterson, W. J. Carr, JR., and R. C. Miller, J. Appl. Phys. **41** (1970) 1005.

[28] C. W. H. M. Vennix, E. Frikkee, P. J. T. Eggenkamp, H. J. M. Swagten, K. Kopinga, and W. J. M. d. Jonge, Phys. Rev. B **48** (1993) 3770.

[29] P. Lazarczyk, T. Story, M. Arciszewska, and R. R. Gatazka, J. Mag. Magn. Mat. **169** (1997) 151.

[30] P. J. T. Eggenkamp, H. J. M. Swagten, T. Story, V. I. Litvinov, C. H. W. Swuste, and W. J. M. d. Jonge, Phys. Rev. B **51** (1995) 15250.

[31] A. J. Nadolny, J. Sadowski, B. Taliashvili, M. Arciszewska, W. Dobrowolski, V. Domukhovski, E. Łusakowska, A. Mycielski, V. Osinniy, T. Story, K.Swiatek, Galazka, and R. Diduszko, J.Mag.Magn.Mat. **248** (2002) 134.

[32] C. Zener, Phys. Rev. **81** (1951) 440.

[33] Y. Matsumoto, M. Murakami, T. Shono, T. Hasegawa, T. Fukumura, M. Kawasaki, P. Ahmet, T. Chikyow, S.-y. Koshihara, and H. Koinuma, Science **291** (2001) 854.

[34] W. K. Park, R. J. Ortega-Hertogs, J. S. Moodera, A. Punnoose, and M. S. Seehra, J. Appl. Phys. **91** (2002) 8093.

[35] J. M. D. Coey, M. Venkatesan, and C. B. Fitzgerald, Nature Materials **4** (2005) 173.

[36] J.-Y. Kim, J.-H. Park, B.-G. Park, H.-J. Noh, S.-J. Oh, J. S.Yang, D.-H. Kim, S. D. Bu, T.-W. Noh, H.-J. Lin, H.-H. Hsieh, and C. T. Chen, Phys. Rev. Lett. **90** (2003) 017401.

[37] P. Sharma, A. Gupta, F. J. Owens, A. Inoue, and K. V. Rao, J.Mag.Magn.Mat. **282** (2004) 115.

[38] K. P. Bhatti, S. Chaudhary, D. K. Pandya, and S. C. Kashyap, Sol. Stat. Commun. **136** (2005) 384

[39] S. B. Ogale, R. J. Choudhary, J. P. Buban, S. E. Lofland, S. R. Shinde, S. N. Kale, V.N.Kulkarni, J. Higgins, C. Lanci, J. R. Simpson, N. D. Browning, S. D. Sarma, H.D.Drew, R. L. Greene, and T. Venkatesan, Phys. Rev. Lett. **91** (2003) 077205.

[40] A. Punnoose, J. Hays, V. Gopal, and V. Shutthanandan, Appl. Phys. Lett. **85** (2004) 1559.

[41] T. Dietl, A. Haury, and Y. M. d'Aubigne, Phys. Rev. B **55** (1997)

[42] H.-T. Lin, T.-S. Chin, J.-C. Shih, S.-H. Lin, T.-M. Hong, R.-T. Huang, F.-R. Chen, and J.-J. Kai, Appl. Phys. Lett. **85** (2004) 621.

[43] K. Gopinadhan, S. C.Kashyap, D. K.Pandya, and S. Chaudhary, J. Phys.: Condens. Matter **20** (2008) 125208.

[44] A. Kaminski and S. D. Sarma, Phys. Rev. Lett. **88** (2002) 247202.

[45] X. L. Wang, Z. X. Dai, and Z. Zeng, J. Phys.: Condens. Matter **20** (2008) 045214.

[46] A. Tiwari, V. M. Bhosle, S. Ramachandran, N. Sudhakar, J. Narayan, S. Budak, and A. Gupta, Appl. Phys. Lett **88** (2006) 142511.

[47] C. Song, K. W. Geng, F. Zeng, X. B. Wang, Y. X. Shen, F. Pan, Y. N. Xie, T. Liu, H. T. Zhou, and Z. Fan, Phys. Rev. B **73** (2006) 024405.

[48] N. A. Spaldin, Cambridge University Press (2003)

[49] S. Datta and B. Das, Appl. Phys. Lett. **56** (1990) 665.

[50] S. Koshihara, A. Oiwa, M. Hirasawa, S. Katsumoto, Y. Iye, C. Urano, H. Takagi, and H. Munekata, Phys. Rev. Lett. **78** (1997) 4617.

[51] H. Munekata, T. Abe, S. Koshihara, A. Oiwa, M. Hirasawa, S. Katsumoto, Y. Iye, C. Urano, and H. Takagi, J. Appl. Phys. **81** (1997) 4862.

[52] S.C.Abrahams and J.L.Bernstein, Acta Cryst. **B25** (1969) 1233.

[53] C. J. Howard, T. M. Sabine, and F. Dickson, Acta Cryst. **B47** (1991) 462.

[54] V. W. H. Baur, Acta Cryst. **9** (1956) 515.

[55] K. L. Chopra, S. Major, and D. K. Pandya, Thin Solid Films **102** (1983) 1.

[56] A. Aoki and H. Sasakura, Japan.J.Appl.Phys. **9** (1970) 582.

[57] A. M. Gheidari, E. A. Soleimani, M. Mansorhoseini, S. Mohajerzadeh, N. Madani, and W. Shams-Kolahi, Mat. Res. Bullet. **40** (2005) 1303.

[58] T. Fukano and T. Motohiro, Sol. EnergyMater. Sol. Cells **82** (2004) 567.

[59] A. Keshavaraja, B. S. Jayashri, A. V. Ramaswamy, and K. Vijayamohanan, Sen. Act. B: Chem. **23** (1995) 75.

[60] U. Betz, M. Kharrazi Olsson, J. Marthy, M. F. Escola, and F. Atamny, Surface and Coatings Technology **200** (2006) 5751.

[61] C. Li, J. Wang, W. Su, H. Chen, W. Wang, and D. Zhuang, Physica B **307** (2001) 1.

[62] J. F. Wang, Y. J. Wang, W. B. Su, H. C. Chen, and W. X. Wang, Mat. Sci. Engg. B **96** (2002) 8.

[63] W. H. Brumage, C. F. Dorman, and C. R. Quade, Phys. Rev. B **63** (2001) 104411.

[64] A. P. Guimaraes and I. S. Oliveira, John Wiley & Sons (1998)

[65] D. Jiles, Chapman & Hall Press (1997)

[66] H. T. Diep, Frustrated Spin System, Chapter1,World Scientific (2004)

[67] K. Binder and A. P. Young, Rev. Mod. Phys. **58** (1986) 801.

[68] C. Y. Huang, J. Mag. Magn. Mat. **51** (1985) 1.

[69] J. A. Mydosh, Spin glasses: an experimental introduction, Taylor & Francis Pub., London (1993)

[70] M. J. P. Gingras, Magnetic system with competing interaction, p. 238, ed. H. T. Diep, World Scientific pub. Singapore (1994)

[71] S. Nagata, P. H. Keesom, and H. R. Harrison, Phys. Rev. B **19** (1979) 1633.

[72] S.Nagata, R.R.Galazka, D.P.Mullin, H.Akbarzadeh, G.D.Khattak, J.K.Furdyna, and P.H.Keesom, Phys.Rev.B **22** (1980) 3331.

[73] Y.F.Chen, W.C.Chou, and A.Twardowski, Solid State Commun. **96** (1995) 865.

[74] E. Marinari, V. Martin-Mayor, and A. Pagnani, Phys. Rev. B **62** (2000) 4999.

[75] P. M. Shand, A. D. Christianson, T. M. Pekarek, L. S. Martinson, J. W. Schweitzer, I. Miotkowski, and B. C. Crooker, Phys. Rev. B **58** (1998) 12876.

[76] H. A. Kramers, Physica **1** (1934) 182.

[77] P. W. Anderson and H. Hasegawa, Phys. Rev. **100** (1955) 675.

[78] P. W. Anderson, Phys. Rev. **109** (1958) 1492.

[79] J. B. Goodenough, Phys. Rev. B **100** (1995) 564.

[80] J. Kanamori, J. Phys. Chem. Solids **10** (1959) 87.

[81] Y. H. Chang, C. H. Park, K. Sato, and H. Katayama-Yoshida, Phys. Rev. B **76** (2007) 125211.

[82] M.A.Ruderman and C.Kittel, Phys. Rev. **96** (1954) 99.

[83] T. Kasuya, Prog.Theor.Phys. **16** (1956) 58.

[84] K.Yosida, Phys. Rev. **106** (1957) 893.

[85] D. Vega, G. Polla, G. Leyva, P. Konig, H. Lanza, A. Esteban, H. Aliaga, M. T. Causa, M. Tovar, and B. Alascio, J. Solid State Chem. **156** (2001) 458.

[86] N. Theodoropouloua, V. Misra, J. Philip, P. LeClair, G. P. Berera, J. S. Moodera, B. Satpati, and T. Som, J.Mag.Magn.Mat. **300** (2006) 407.

[87] X. Li, C. Xia, G. Pei, and X. He, J. Phys. Chem. Solids **68** (2007) 1836.

[88] M. H. F. Sluiter, Y. Kawazoe, P. Sharma, A. Inoue, A. R. Raju, C. Rout, and U. V. Waghmare, Phys. Rev. Lett. **94** (2005) 187204.

[89] A. S. Risbud, N. A. Spaldin, Z. Q. Chen, S. Stemmer, and R. Seshadri, Phys. Rev. B **68** (2003) 205202.

[90] X.-C. Liu, E.-W. Shi, Z.-Z. Chen, T. Zhang, Y. Zhang, B.-Y. Chen, W. Huang, X. Liu, L.-X. Song, K.-J. Zhou, and M.-Q. Cui, Appl. Phys. Lett **92** (2008) 042502.

[91] J. Kudrnovsky´, I. Turek, V. Drchal, F. Ma´ca, P. Weinberger, and P. Bruno, Phys. Rev. B **69** (2004) 115208.

[92] G. Bouzerar, J. Kudrnovsky, L. Bergqvist, and P. Bruno, Phys. Rev. B **68** (2003) 081203(R).

[93] L. Bergqvist, O. Eriksson, J. Kudrnovsky´, V. Drchal, P. Korzhavyi, and I. Turek, Phys. Rev. Lett. **93** (2004) 137202.

[94] W. H. Meiklejohn and C. P. Bean, Phys. Rev. **105** (1957) 904.

[95] B. D. Cullity and C.D.Graham, Introduction to Magnetic Materials, Wiley **Chapter 7** (2007)

[96] R. Skomski, A. Kashyap, J. Zhou, and D. J. Sellmyer, J. Appl. Phys. **97** (2005) 10B302.

[97] R. Skomski, J. Phys,:Condens. Matt. **15** (2003) R841.

[98] Dzyaloshinsky, J.Phys.Chem. Solids **4** (1958) 241.

[99] T. Moriya, Phys. Rev. **120** (1960) 91.

[100] C. Zener, Phys. Rev. **82** (1951) 403.

[101] H. Munekata, A. Zaslavsky, P. Fumagalli, and R. J. Gambino, Appl. Phys. Lett **63** (1993) 2929.

[102] H. Ohno, A. Shen, F. Matsukura, A. Oiwa, A. Endo, S. Katsumoto, and Y. Iye, Appl. Phys. Lett **69** (1996) 363.

[103] C. Zener, Phys. Rev. **83** (1951) 299.

[104] T. Kasuya and A. Yanase, Rev. Mod. Phys. **40** (1968) 684.

[105] J. B. Torrance, M. W. Shafer, and T. R. McGuire, Phys. Rev. Lett. **29** (1972) 1168.

[106] T. Dietl and Z. Spalek, Phys. Rev. Lett. **48** (1982) 355.

[107] A. C. Durst, R. N. Bhatt, and P. A. Wolff, Phys. Rev. B **65** (2002) 235205.

[108] H.Ohno, H.Munekata, T.Penney, S.V.Molnar, and L.L.Chang, Phys.Rev.Lett. **68** (1992) 2664.

[109] D. Chakraborti, S. Ramachandran, G. Trichy, J. Narayan, and J. T. Prater, J. Appl. Phys. **101** (2007) 053918.

[110] Z. L. Lu, H. S. Hsu, Y. H. Tzeng, F. M. Zhang, Y. W. Du, and J. C. A. Huang, Appl. Phys. Lett. **95** (2009) 102501.

[111] J. M. D. Coey, A. P. Douvalis, C. B. Fitzgerald, and M. Venkatesan, Appl. Phys. Lett. **84** (2003) 1332.

[112] G. H. McCabe, T. Fries, M. T. Liu, Y. Shapira, L. R. Ram-Mohan, R. Kershaw, A. Wold, C.Fau, M. Averous, E. J. McNiff, and Jr., Phys. Rev. B **56** (1997) 6673.

[113] E. Quintero, R. Tovar, M. Quintero, J. Gonzalez, J. M. Broto, H. Rakoto, R. Barbaste, J.C.Woolley, G. Lamarche, and A. M. Lamarche, J. Mag. Magn. Mat. **210** (2000) 208.

[114] E.Quintero, M.Quintero, M.Morocoima, G.E.Delgado, L.Lara, J.Gomez, and P.Bocaranda, Rev. Mex. Fis **S53** (2007) 163.

[115] G. Z. Xing, J. B. Yi, D. D. Wang, L. Liao, T. Yu, Z. X. Shen, C. H. A. Huan, T. C. Sum, J. Ding, and T. Wu, Phys. Rev. B **79** (2009) 174406.

[116] D. Mukherjee, T. Dhakal, H. Srikanth, P. Mukherjee, and S. Witanachchi, Phys. Rev. B **81** (2010) 205202.

[117] K. H. Gao, Z. Q. Li, T. Du, E. Y. Jiang, and Y. X. Li, Phys. Rev. B **75** (2007) 174444.

[118] H. Saeki, H. Tabata, and T. Kawai, Sol. Stat. Commun. **120** (2001) 439.

[119] N. H. Hong, J. Sakai, and A. Hassini, Appl. Phys. Lett **84** (2004) 2602.

[120] H. E. Stanley, Introduction to Phase Transition and Critical Phenomena, Oxford University Press, London. (1971)

[121] A. Arrott, Phys. Rev. **108** (1957) 1394.

[122] S. K. Banerjee, Phys. Lett. **12** (1964) 16.

[123] A. Arrott and J. E. Noakes, Phys. Rev. Lett. **19** (1967) 786.

[124] R. V. Chamberlin, Nature **408** (2000) 337.

[125] B. Widom, J. Chem. Phys. **43** (1965) 3898.

[126] P. Weiss and R. Forrer, Ann. Phys. (Paris) **5** (1926) 153.

[127] J. S. Kouvel and M. E. Fisher, Phys. Rev. **136** (1964) A 1626.

[128] S. N. Kaul, J. Mag. Magn. Mat. **53** (1985) 5.

[129] H. Hiroyoshi, A. Hoshi, H. Fujimori, and Y. Nakagawa, J. Phys. Soc. Jpn **48** (1980) 830.

[130] R. V. Colvin and S. Arajs, J. Phys. Chem. Sol. **26** (1965) 435.

[131] V. N. Berzhanskii and V. I. Ivanov, Phys. Stat. Sol. (b) **151** (1989) 259.

[132] A. G. Flores, V. Raposo, J. Iniguez, J. M. Garcia-Beneytez, J. Arcas, and M. Vazquez, Phys. Stat. Sol. (a) **191** (2002) 555.

[133] Y. Motome and N. Furukawa, Phys. Rev. B **68** (2003) 144432.

[134] S. E. Lofland, V. Ray, P. H. Kim, S. M. Bhagat, M. A. Manheimer, and S. D. Tyagi, Phys. Rev. B **55** (1997) 2749.

[135] C. V. Mohan, M. Seeger, H. Kronmüller, P. Murugaraj, and J. Maier, J. Mag. Magn. Mat. **55** (1998) 2749.

[136] A. Schwartz, M. Scheffler, and S. M. Anlage, Phys. Rev. B **61** (2000) R870.

[137] S. Nair, A. Banerjee, and A. V. Narlikar, Phys. Rev. B **68** (2003) 132404.

[138] W. Li, H. P. Kunkel, X. Z. Zhou, G. Williams, Y. Mukovskii, and D. Shulvatev, Phys. Rev. B **70** (2004) 214413.

[139] M. Kar, A. Perumal, and S. Ravi, Phys. Stat. Sol. (b) **243** (2006) 1908.

[140] A. Olega, A. Salazar, D. Prabhakaran, and A. T. Boothroyd, Phys. Rev. B **70** (2004) 184402.

[141] R. Venkatesh, R. Nirmala, G. Rangarajan, S. K. Malik, and V. Sankaranarayanan, J. Appl. Phys. **99** (2006) 08Q311.

[142] D. J. Priour, Jr., and S. D. Sarma, Phys. Rev. B **81** (2010) 224403.

[143] Y. Fukuma, K. Tanaka, H. Asada, and T. Koyanagi, J. Mag. Magn. Mat. **310** (2007) e723.

[144] J. L. Harris, P. M. Shand, L. V. Shapoval, A. VanWaardhuizen, and L. H. Strauss, J. Mag. Magn. Mat. **321** (2009) 1072.

[145] M. Hamedoun, R. Masrour, K. Bouslykhane, A. Hourmatallah, N. Benzakour, and A. Benyoussef, M. J. Condensed Matt. **10** (2008) 31.

[146] M. Jaime, H. T. Hardner, M. B. Salamon, M. Rubinstein, P. Dorsey, and D. Emin, Phys. Rev. Lett. **78** (1997) 951.

[147] N. F. Mott, Conduction in non-crystalline materials (2nd ed.) Oxford: Oxford University Press (1993)

[148] N. F. Mott, Metal- Insulator Transitions 2nd ed. (London, Taylor and Francis) (1990)

[149] A. L. Efros and B. I. Shklovskii, J. Phys. C **8** (1975) L49.

[150] H. Chou, C. P. Lin, H. S. Hsu, and S. J. Sun, Appl. Phys. Lett **96** (2010) 092503.

[151] G. Prathiba, S. Venkatesh, K. K. Bharathi, and N. H. Kumar, J.Appl.Phys. **109** (2011) 07C320.

[152] H. Chou, C. P. Lin, J. C. A. Huang, and H. S. Hsu, Phys. Rev. B **77** (2008) 245210.

[153] P. Sharma, A. Gupta, K. V. Rao, F. J. Owens, R. Sharma, R. Ahuja, J. M. O. Guillen, B. Johansson, and G. A. Gehring, Nat Mater **2** (2003) 673.

[154] Ü. Özgür, Y. I. Alivov, C. Liu, A. Teke, M. A. Reshchikov, S. Doğan, V. Avrutin, S.-J. Cho, and H. Morkoç, J. Appl. Phys. **98** (2005) 041301.

[155] S. J. Pearton, D. P. Norton, K. Ip, Y. W. Heo, and T. Steiner, Prog. Mat. Sci. **50** (2005) 293.

[156] K. Ueda, H. Tabata, and T. Kawai, Appl. Phys. Lett **79** (2001) 988.

[157] S. J. Pearton, C. R. Abernathy, D. P. Norton, A. F. Hebard, Y. D. Park, L. A. Boatner, and J. D. Budai, Mat. Sci. Engg. R **40** (2003) 137

[158] S. J. Pearton, C. R. Abernathy, M. E. Overberg, G. T. Thaler, D. P. Norton, N. Theodoropoulou, A. F. Hebard, Y. D. Park, F. Ren, J. Kim, and L. A. Boatner, J. Appl. Phys. **93** (2003) 1.

[159] W. Prellier, A. Fouchet, and B. Mercey, J. Phys,:Condens. Matt. **15** (2003) R1583.

[160] R.Janisch, P.Gopal, and N.A.Spaldin, J.Phys.Condens.Matt. **17** (2005) R657.

[161] S. A. Chambers, Surf. Sci. Rep. **61** (2006) 345.

[162] F. Pan, C. Song, X. J. Liu, Y. C. Yang, and F. Zeng, Mat. Sci. Engg. R **R 62** (2008) 1.

[163] K. Sato and H. K. Yoshida, Jpn. J. Appl. Phys. **40** (2001) L334.

[164] N. H. Hong, J. Sakai, N. T. Huong, N. Poirot, and A. Ruyter, Phys. Rev. B **72** (2005) 045336.

[165] Z. Jin, T. Fukumura, M. Kawasaki, K. Ando, H. Saito, T. Sekiguchi, Y. Z. Yoo, M. Murakami, Y. Matsumoto, T. Hasegawa, and H. Koinuma, Appl. Phys. Lett **78** (2001) 3824.

[166] H. Liu, X. Zhang, L. Li, Y. X. Wang, K. H. Gao, Z. Q. Li, R. K. Zheng, S. P. Ringer, B. Zhang, and X. X. Zhang, Appl. Phys. Lett. **91** (2007) 072511.

[167] D. C. Kundaliya, S. B. Ogale, S. E. Lofland, S. Dhar, C. J. Metting, S. R. Shinde, Z. Ma, B. Varughese, K. V. Ramanujachary, L. Salamanca-Riba, and T. Venkatesan, Nature **3** (2004) 709.

[168] X. M. Cheng and C. L. Chien, J. Appl. Phys. **93** (2003) 7876.

[169] W. Yan, Z. Sun, Q. Liu, Z. Li, Z. Pan, J. Wang, S. Wei, D. Wang, Y. Zhou, and X. Zhang, Appl. Phys. Lett **91** (2007) 062113.

[170] D. P. Norton, S. J. Pearton, A. F. Hebard, N. Theodoropoulou, L. A. Boatner, and R. G. Wilson, Appl. Phys. Lett **82** (2003) 239.

[171] M. A. Garcia, M. L. Ruiz-Gonzalez, A. Quesada, J. L. Costa-Kramer, J. F. Fernandez, S. J. Khatib, A.Wennberg, A. C. Caballero, M. S. Martin-Gonzalez, M. Villegas, F. Briones, J. M. Gonzalez-Calbet, and A. Hernando, Phys. Rev. Lett. **94** (2005) 217206.

[172] P. Thakur, K. H. Chae, J.-Y. Kim, M. Subramanian, R. Jayavel, and K. Asokan, Appl. Phys. Lett. **91** (2007) 162503.

[173] J.-H. Guo, A. Gupta, P. Sharma, K. V. Rao, M. A. Marcus, C. L. Dong, J. M. O. Guillen, S. M. Butorin, M. Mattesini, P. A. Glans, K. E. Smith, C. L. Chang, and R. Ahuja, J. Phys,:Condens. Matt. **19** (2007) 172202.

[174] S. Venkataraj, N. Ohashi, I. Sakaguchi, Y. Adachi, T. Ohgaki, H. Ryoken, and H. Haneda, J. Appl. Phys. **102** (2007) 014905.

[175] X. X. Wei, C. Song, K. W. Geng, F. Zeng, B. He, and F. Pan, J.Phys.:Condens. Matter **18** (2006) 7471.

[176] S.-J. Han, J. W. Song, C.-H. Yang, S. H. Park, J.-H. Park, Y. H. Jeong, and K. W. Rhie, Appl. Phys. Lett. **81** (2002) 4212.

[177] A.Dinia, G.Schmerber, V.Pierron-Bohnes, C.Me´ny, P.Panissod, and E.Beaurepaire, J. Mag. Magn. Mat. **286** (2005) 37.

[178] J. H. Kim, H. Kim, D. Kim, Y. E. Ihm, and W. K. Choo, J. Appl. Phys. **92** (2002) 6066.

[179] K. Ando, H. Saito, Z. Jin, T. Fukumura, M. Kawasaki, Y. Matsumoto, and H. Koinuma, Appl. Phys. Lett. **78** (2001) 2700.

[180] A. C. Tuan, J. D. Bryan, A. B. Pakhomov, V. Shutthanandan, S. Thevuthasan, D. E. McCready, D. Gaspar, M. H. Engelhard, J. W. Rogers, Jr., K. Krishnan, D. R. Gamelin, and S. A. Chambers, Phys. Rev. B **70** (2004) 054424.

[181] H.-J. Lee, S.-Y. Jeong, C. R. Cho, and C. H. Park, Appl. Phys. Lett. **81** (2002) 4020.

[182] W. Prellier, A. Fouchet, B. Mercey, C. Simon, and B. Raveau, Appl. Phys. Lett. **82** (2003) 3490.

[183] S. Ramachandran, A. Tiwari, and J. Narayan, Appl. Phys. Lett **84** (2004) 5255.

[184] S. Ghoshal and P. S. A. Kumar, J. Mag. Magn. Mat. **320** (2008) L93.

[185] M. Snure and A. Tiwari, J. Appl. Phys. **104** (2008) 073707.

[186] K. P. Bhatti, V. K. Malik, and S. Chaudhary, J Mater Sci: Mater Electron **19** (2008) 849.

[187] K. P. Bhatti, S. Chaudhary, D. K. Pandya, and S. C. Kashyap, J. Appl. Phys. **101** (2007) 103919.

[188] D. Karmakar, T. V. C. Rao, J. V. Yakhmi, A. Yaresko, V. N. Antonov, R. M. Kadam, S. K. Mandal, R. Adhikari, A. K. Das, T. K. Nath, N. Ganguli, I. Dasgupta, and G. P. Das, Phys. Rev. B **81** (2010) 184421.

[189] H.-J. Lee, S.-H. Lee, F. Yildiz, and Y. H. Jeong, J. Mag. Magn. Mat. **310** (2007) 2089.

[190] T. Fukumura, Z. Jin, M. Kawasaki, T. Shono, T. Hasegawa, S. Koshihara, and H. Koinuma, Appl. Phys. Lett. **78** (2001) 958.

[191] T. Mizokawa, T. Nambu, A. Fujimori, T. Fukumura, and M. Kawasaki, Phys. Rev. B **65** (2002) 085209.

[192] A. Tiwari, C. Jin, A. Kvit, D. Kumar, J. F. Muth, and J. Narayan, Sol. Stat. Commun. **121** (2002) 371.

[193] Y. M. Kim, M. Yoon, I.-W. Park, Y. J. Park, and J. H. Lyou, Sol. Stat. Commun. **129** (2004) 175.

[194] S. W. Jung, S.-J. An, G. C. Yi, C. U. Jung, S. I. Lee, and S. Cho, Appl. Phys. Lett. **80** (2002) 4561.

[195] S. Kolesnik, B. Dabrowski, and J. Mais, J.Appl.Phys. **95** (2004) 2582.

[196] O. D. Jayakumar, H. G. Salunke, R. M. Kadam, M. Mohapatra, G. Yaswant, and S. K. Kulshreshtha, Nanotechnology **17** (2006) 1278.

[197] J. B. Wang, G. J. Huang, X. L. Zhong, L. Z. Sun, Y. C. Zhou, and E. H. Liu, Appl. Phys. Lett **88** (2006) 252502.

[198] L. B. Duan, G. H. Rao, J. Yu, Y. C. Wang, G. Y. Liu, and J. K. Liang, J.Appl.Phys. **101** (2007) 063917.

[199] N. A. Theodoropoulou, A. F. Hebard, D. P. Norton, J. D. Budai, L. A. Boatner, J. S. Lee, Z. G. Khim, Y. D. Park, M. E. Overberg, S. J. Pearton, and R. G. Wilson, Sol. Stat. Elec. **47** (2003) 2231.

[200] J. Luo, J. K. Liang, Q. L. Liu, F. S. Liu, Y. Zhang, B. J. Sun, and G. H. Rao, J. Appl. Phys. **97** (2005) 086106.

[201] S. W. Yoon, S.-B. Cho, S. C. We, S. Yoon, B. J. Suh, H. K. Song, and Y. J. Shin, J. Appl. Phys. **93** (2003) 7879.

[202] A. J. Behan, A. Mokhtari, H. J. Blythe, D. Score, X. H. Xu, J. R. Neal, A. M. Fox, and G. A. Gehring, Phys. Rev. Lett. **100** (2008) 047206.

[203] C. B. Fitzgerald, M. Venkatesan, J. G. Lunney, L. S. Dorneles, and J. M. D. Coey, Appl. Surf. Sci. **247** (2005) 493.

[204] L. M. Johnson, A. Thurber, J. Anghel, M. Sabetian, M. H. Engelhard, D. A. Tenne, C. B. Hanna, and A. Punnoose, Phys. Rev. B **82** (2010) 054419.

[205] T. S. Herng, D. C. Qi, T. Berlijn, J. B. Yi, K. S. Yang, Y. Dai, Y. P. Feng, I. Santoso, C. Sanchez-Hanke, X. Y. Gao, A. T. S. Wee, W. Ku, J. Ding, and A. Rusydi, Phys. Rev. Lett. **105** (2010) 207201.

[206] T. Kataoka, Y. Yamazaki, V. R. Singh, A. Fujimori, F. H. Chang, H. J. Lin, D. J. Huang, C. T. Chen, G. Z. Xing, J. W. Seo, C. Panagopoulos, and T. Wu, Phys. Rev. B **84** (2011) 153203.

[207] L. M. C. Pereira, U. Wahl, S. Decoster, J. G. Correia, L. M. Amorim, M. R. da Silva, J. P. J. P. Araujo, and A. Vantomme, Phys. Rev. B **84** (2011) 125204.

[208] H. Tang, H. Berger, P. E. Schmid, and F. Levy, Sol. Stat. Commun. **92** (1994) 267.

[209] S. R. Shinde, S. B. Ogale, S. D. Sarma, J. R. Simpson, H. D. Drew, S. E. Lofland, C. Lanci, J. P. Buban, N. D. Browning, V. N. Kulkarni, J. Higgins, R. P. Sharma, R. L. Greene, and T. Venkatesan, Phys.Rev.B **67** (2003) 115211.

[210] D. H. Kim, J. S. Yang, K. W. Lee, S. D. Bu, T. W. Noh, S.-J. Oh, Y.-W. Kim, J.-S. Chung, H. Tanaka, H. Y. Lee, and T. Kawai, Appl.Phys.Lett. **81** (2002) 2421.

[211] P. A. Stampe, R. J. Kennedy, Y. Xin, and J. S. Parker, J. Appl. Phys. **92** (2002) 7114.

[212] P. A. Stampe, R. J. Kennedy, Y. Xin, and J. S. Parker, J.Appl.Phys. **93** (2003) 7864.

[213] N.-J. Seong, S.-G. Yoon, and C.-R. Cho, Appl. Phys. Lett. **81** (2002) 4209.

[214] S. A. Chambers, C. M. Wang, S. Thevuthasan, T. Droubay, D. E. McCready, A. S. Lea, V. Shutthanandan, and C. F. W. Jr, Thin Solid Films **418** (2002) 197.

[215] S. A. Chambers, T. Droubay, C. M. Wang, A. S. Lea, R. F. C. Farrow, L. Folks, V. Deline, and S. Anders, Appl. Phys. Lett. **82** (2003) 1257.

[216] N. H. Hong, A. Ruyter, W. Prellier, and J. Sakai, Appl. Phys. Lett. **85** (2004) 6212.

[217] T. Droubay, S. M. Heald, V. Shutthanandan, S. Thevuthasan, S. A. Chambers, and J. Osterwalder, J. Appl. Phys. **97** (2005) 046103.

[218] Z. Wang, J. Tang, H. Zhang, V. Golub, L. Spinu, and L. D. Tung, J. Appl. Phys. **95** (2004) 7381.

[219] Z. Wang, W. Wang, J. Tang, L. Tung, L. Spinu, and W. Zhou, Appl. Phys. Lett. **83** (2003) 518.

[220] Y. J. Kim, S. Thevuthasan, T. Droubay, A. S. Lea, C. M. Wang, V. Shutthanandan, S. A. Chambers, R. P. Sears, B. Taylor, and B. Sinkovic, Appl. Phys. Lett. **84** (2004) 3531.

[221] N. H. Hong, W. Prellier, J. Sakai, and A. Hassini, Appl. Phys. Lett. **84** (2004) 2850.

[222] P. Xiaoyan, J. Dongmei, L. Yan, and M. Xueming, J.Mag.Magn.Mat. **305** (2006) 388.

[223] S. Duhalde, M. F. Vignolo, F. Golmar, C. Chiliotte, C. E. R. Torres, L. A. Errico, A. F. Cabrera, M. Rentería, F. H. Sánchez, and M. Weissmann, Phys. Rev. B **72** (2005) 161313(R).

[224] J. A. Marley and T. C. MacAvoy, J. Appl. Phys. **32** (1961) 2504.

[225] S. Samson and C. G. Fonstad, J. Appl. Phys. **44** (1973) 4618.

[226] C. G. Fonstad and R. H. Rediker, J. Appl. Phys. **42** (1971) 2911.

[227] K. J. Button, C. G. Fonstad, and W. Dreybrodt, Phys. Rev. B **4** (1971) 4539.

[228] K. B. Sundaram and G. K. Bhagavat, J. Phys. D: Appl. Phys. **14** (1981) 921.

[229] K. H. Gao, Z. Q. Li, X. J. Liu, W. Song, H. Liu, and E. Y. Jiang, Sol. State. Comm. **138** (2006) 175.

[230] K. Gopinadhan, S. C. Kashyap, D. K. Pandya, and S. Chaudhary, J. Appl. Phys. **102** (2007) 113513.

[231] L. A. Errico, M. Renteria, and M. Weissmann, Phys. Rev. B **72** (2005) 184425.

[232] H. Kimura, T. Fukumura, M. Kawasaki, K. Inaba, T. Hasegawa, and H. Koinuma, Appl. Phys. Lett **80** (2002) 94.

[233] Ç. Kılıç and A. Zunger, Phys. Rev. Lett. **88** (2002) 095501.

[234] A. Thurber, K. M. Reddy, and A. Punnose, J. Appl. Phys. **105** (2009) 07E706.

[235] J. Philip, N. Theodoropoulou, G. Berera, J. S. Moodera, and B. Satpati, Appl. Phys. Lett. **85** (2004) 777.

[236] S. Lany and A. Zunger, Phys. Rev. Lett. **98** (2007) 045501.

[237] G. Peleckis, X. L. Wang, and S. X. Dou, IEEE Trans. Magn. **42** (2006) 2703.

[238] G. Peleckis, X. Wang, and S. X. Dou, Appl. Phys. Lett. **89** (2006) 022501.

[239] S. Qi, F. Jiang, J. Fan, H. Wu, S. B. Zhang, G. A. Gehring, Z. Zhang, and X. Xu, Phys. Rev. B **84** (2011) 205204.

[240] V. Fernandes, J. J. Klein, N. Mattoso, D. H. Mosca, E. Silveira, E. Ribeiro, W. H. Schreiner, J. Varalda, and A. J. A. de Oliveira, Phys. Rev. B **75** (2007) 121304.

[241] Y. Q. Song, H. W. Zhang, Q. Y. Wen, H. Zhu, and J. Q. Xiao, J. Appl. Phys. **102** (2007) 043912.

[242] H. Raebiger, S. Lany, and A. Zunger, Phys. Rev. Lett. **99** (2007) 167203.

[243] P. Kharel, C. Sudakar, M. B. Sahana, G. Lawes, R. Suryanarayanan, R. Naik, and V. M. Naik, J. Appl. Phys. **101** (2007) 09H117.

[244] G. Peleckis, X. L. Wang, and S. X. Dou, Appl. Phys. Lett. **88** (2006) 132507.

[245] R. A. Young, The Rietveld Method, International Union of Crystallography (New York, Oxford University Press)

(1996)

[246] A. Taylor, X – ray Metallography (Wiley, New York) (1961)

[247] R. Kumar, "Atomic and Molecular Spectra" **Chapter-21** (2005)

[248] S. Foner, Rev. Sci. Instr. **30** (1959) 548.

[249] A. Sundaresan, R. Bhargavi, N. Rangarajan, U. Siddesh, and C. N. R. Rao, Phys. Rev. B **74** (2006) 161306.

[250] S. Ghosh, D. D. Munshi, and K. Mandal, J.Appl.Phys. **107** (2010) 123919.

[251] C. M. Liu, X. T. Zu, and W. L. Zhou, J. Phys. Condens. Matt. **18** (2006) 6001.

[252] M. E. Fisher, Phys. Rev. **176** (1968) 257.

[253] A. Bouaine, N. Brihi, G. Schmerber, C. Ulhaq-Bouillet, S. Colis, and A. Dinia, J. Phys. Chem. C **7** (2007) 111.

[254] K.Srinivasan, M. Vithal, B. Sreedhar, M. M. Raja, and P. V. Reddy, J. Phys. Chem. C. **113** (2009) 3543.

[255] C. Chiorescu, J. L. Cohin, and J. J. Neumeier, Phys. Rev. B **76** (2007) 020404 (R).

[256] S.K.Srivastava, M.Kar, S.Ravi, P.K.Mishra, and P.D.Babu, J. Mag. Magn. Mat. **320** (2008) 2382.

[257] L. M. Fang, X.T.Zu, Z.J.Li, S.Zhu, C. M. Liu, W. L. Zhou, and L. M. Wang, J. Alloys Compd. **454** (2008) 261.

[258] J.F.Scott, J. Chem. Phys. **53** (1970) 853.

[259] J.X.Zhou, M.S.Zhang, J. M. Hong, and Z.Yin, Sol. Stat. Commun. **138** (2006) 242.

[260] K.N.Yu, Y. Xiong, Y. Liu, and C. Xiong, Phys. Rev. B **55** (1997) 4.

[261] O.Lupan, L.Chow, G. Chai, H. Heinrich, S.Park, and A. Schulte, J.Crystal Growth. **311** (2008) 152.

[262] J. C. Paker and R. W. Siegel, Appl. Phys. Lett. **57** (1990) 943.

[263] N. T. Lan, N. P. Duong, and T. D. Hien, J.Alloys and Compounds **509** (2011) 5919.

[264] S. Colis, H. Bieber, S. Be´gin-Colin, G. Schmerber, C. Leuvrey, and A. Dinia, Chem. Phys. Lett. **422** (2006) 529.

[265] W. Yu, L. H. Yang, X. Y. Teng, J. C. Zhang, Z. C. Zhang, L. Zhang, and G. S. Fu, J.Appl.Phys. **103** (2008) 093901.

[266] D. Mishra, A. Perumal, and A. Srinivasan, J.Phys.D:Appl.Phys. **41** (2008) 215003.

[267] T. Dietl, J. Spalek, and L. Åšwierkowski, Phys. Rev. B **33** (1986) 7303.

[268] D. Kim, B. L. Zink, F. Hellman, and J. M. D. Coey, Phys. Rev. B **65** (2002) 214424.

[269] B. Samantaray, S. Ravi, and A. Perumal, J. Mag. Magn. Mat. **322** (2010) 3391.

[270] B. Padmanabhan, H. L. Bhat, S. Elizabeth, S. Rößler, U. K. Rößler, K. Dörr, and K. H. Müller, Phys. Rev. B **75** (2007) 024419.

[271] M. Haug, M. Fahnle, and H. Kronmuller, J. Mag. Magn. Mat. **69** (1987) 163.

[272] N. H. Hong, A. Ruyter, W. Prellier, J. Sakai, and N. T. Huong, J. Phys.: Condens. Matter **17** (2005) 6533.

[273] G. Peia, C. Xia, S. Caoc, J. Zhanga, F. Wua, and J. Xua, J. Mag. Magn. Mat. **302** (2006) 340.

[274] L. R. Shah, H. Zhu, W. G. Wang, B. Ali, T. Zhu, X. Fan, Y. Q. Song, Q. Y. Wen, H. W.Zhang, S. I. Shas, and J. Q. Xiao, J. Phys. D, Appl. Phys **43** (2010) 035002.

[275] Y. W. Heo, J. Kelly, D. P. Norton, A. F. Hebard, S. J. Pearton, J. M. Zavada, and L. A.Boatnerd, Electrochemical and Solid-State Letters **7** (2004) G309.

[276] J. Hays, A. Punnoose, R. Baldner, M. H. Engelhard, J. Peloquin, K. M. Reddy, and Phys. Rev. B **72** (2005) 075203.

Manuscript published/ under preparation:

1) "Critical Behavior of Ferromagnetic Transition in SnO_2 based Diluted Magnetic Semiconductor" **Sunita Mohanty** and S. Ravi: (accepted for publication in *Journal of Superconductivity and Novel Magnetism*).

2) "Ferromagnetism in mechanically milled $Sn_{1-x}Co_xO_2$ (x=0 to 0.10) compounds" **Sunita Mohanty** and S.Ravi: J*ournal of Superconductivity and Novel Magnetism*, **25** (2012), 101.

3) "Structural and Magnetic Properties of Nanocrystalline $Sn_{0.98}Co_{0.02}O_2$ under different Annealing conditions" **Sunita Mohanty**, S.Ravi, H.S. Jena and V. Manivannan: *International Journal of Nanoscience,* **10** (2011), 313.

4) "Ferromagnetism and bound magnetic polaron behavior in bulk Sn1-xCoxO2" **Sunita Mohanty** and S. Ravi: *Solid State Communications*, **150** (2010) 739.

5) "Magnetic Properties of Co doped SnO2 Diluted Magnetic Semiconductors" **Sunita Mohanty** and S. Ravi: *Indian J. Phys*. **84** (2010), 735.

6) "Magnetic Properties of Sn_{1-x} Ni_xO_2 based diluted magnetic semiconductors" **Sunita Mohanty** and S. Ravi: *Solid State Communications*, **150** (2010) 1570.

7) " Magnetic Properties of Nanocrystalline SnO_2 Prepared by Mechanical Alloying" **Sunita Mohanty**, M.Kar, S. Ravi: (Submitted).

Other Works

8) "Neutron Powder Diffraction Studies in LaMn1-xCuxO3 (x=0.05,0.10and 0.15)"
B. Samantaray,S. K. Srivastava, **S. Mohanty** and S. Ravi, I. Dhiman and A.Das:
J. Appl. Phys, **107** (2010), 09D719.

9) "Structural, electrical and magnetic properties of Co and Fe co-doped ZnO nanoparticles prepared by solution combustion method."
M.L. Dinesha, H.S. Jayanna, **S. Mohanty** and S. Ravi**:** *J. Alloys and compounds*, **490** (2010) 618-623.

10) "Ferromagnetism and Bound Magnetic Polaron Behavior in $(In_{1-x}Co_x)_2O_3$"
T. Bora, B. Samantaray, **S. Mohanty** and S. Ravi: *IEEE Transaction in Magnetics,* **47** (2011) 10.

School Attended:

Attended Homi Bhabha Centenary DAE-BRNS HRI School on Spintronis and Magnetoelectronics Material and Devices, Jan 5-7, 2009, Toshali Sand, Puri.

Oral/Poster Presentation in National/International conferences:

1) Magnetic Properties of Zn1-xMxO (M Mn, Co) Diluted Magnetic Semiconductors. **S. Mohanty,** K. Manna and S. Ravi
Proceeding/Poster DAE solid state symposium, Dec. 2008, Mumbai

2) Room Temperature Ferromagnetism in Bulk Sn0.95Mn0.05O2 (M = Co, Ni) based Diluted Magnetic Semiconductors. **Sunita Mohanty** and S.Ravi
Oral presentation on Homi Bhabha Centenary DAE-BRNS National Conference on Spintronics and Magnetoelectronics Materials, Jan.08-09, 2009, Tosali Sands, Puri.

3) Magnetic Properties of Co-doped SnO2 Diluted Magnetic Semiconductors
Sunita Mohanty and S.Ravi
Oral presentation on PANE Conference-2009, Tripura

4) Effect of Sb doping in (Sn0.95Fe0.05)O2 based diluted magnetic Semiconductors
Sunita Mohanty, P.Nath and S.Ravi
Proceeding/ Poster presentation in 54th DAE solid state symposium proceedings, Dec. 2009, Baroda.

5) Room Temperature Ferromagnetism in Ni-doped SnO2 based Diluted Magnetic Semiconductor. **Sunita Mohanty** and S.Ravi
Poster Presentation in Discussion meeting on Statistical and Condensed matter physics, IIT Guwahati (Oct- 2009) (Best Poster Award)

6) Structural and Magnetic Properties of Nanocrystalline $Sn_{0.98}Co_{0.02}O_2$ under different Annealing conditions. **Sunita Mohanty** and S. Ravi

Poster Presentation International Conference on Advanced Nanomaterials and Nanotechnology, IITGuwahati (Dec-2009)

7) Effect of Metal doping on the formation of bound magnetic polaron in Transition metal-doped SnO_2. **Sunita Mohanty**, P.Nath and S.Ravi

*Poster presentation in "Recent Advances in Correlated Electron Systems" IITGuwahati (Jan-2010)*Spintronics and Diluted Magnetic Semiconductors

8) S.Ravi and **Sunita Mohanty**

Invited Talk in National Conference on Advanced Materials, Tamilnadu, (Aug-2010)

9) Giant magnetic moment in mechanically milled $Sn_{1-x}Co_xO_2$ compounds

Sunita Mohanty and S. Ravi

Poster presentation in Current Trends in Condensed Matter Physics, Orissa,(Dec-15)

10) Ferromagnetism in mechanically milled $Sn_{1-x}Co_xO_2$ (x=0 to 0.10) compounds

Sunita Mohanty and S.Ravi

Oral presentation in IEEE International Magnetics Conference, Taipei, Taiwan, April-25- 29,2011

11) Magnetic Properties of Nanocrystalline SnO_2 prepared by mechanical synthesis

Sunita Mohanty, M.Kar and S.Ravi ,

ICANN-2011, Guwahati.

.....o.....